

INFORMATION TO USERS

This was produced from a copy of a document sent to us for microfilming. While the most advanced technological means to photograph and reproduce this document have been used, the quality is heavily dependent upon the quality of the material submitted.

The following explanation of techniques is provided to help you understand markings or notations which may appear on this reproduction.

1. The sign or "target" for pages apparently lacking from the document photographed is "Missing Page(s)". If it was possible to obtain the missing page(s) or section, they are spliced into the film along with adjacent pages. This may have necessitated cutting through an image and duplicating adjacent pages to assure you of complete continuity.
2. When an image on the film is obliterated with a round black mark it is an indication that the film inspector noticed either blurred copy because of movement during exposure, or duplicate copy. Unless we meant to delete copyrighted materials that should not have been filmed, you will find a good image of the page in the adjacent frame.
3. When a map, drawing or chart, etc., is part of the material being photographed the photographer has followed a definite method in "sectioning" the material. It is customary to begin filming at the upper left hand corner of a large sheet and to continue from left to right in equal sections with small overlaps. If necessary, sectioning is continued again—beginning below the first row and continuing on until complete.
4. For any illustrations that cannot be reproduced satisfactorily by xerography, photographic prints can be purchased at additional cost and tipped into your xerographic copy. Requests can be made to our Dissertations Customer Services Department.
5. Some pages in any document may have indistinct print. In all cases we have filmed the best available copy.

**University
Microfilms
International**

300 N. ZEEB ROAD, ANN ARBOR, MI 48106
18 BEDFORD ROW, LONDON WC1R 4EJ, ENGLAND

8026204

BLISS, VERNON LEROY

NUMERICAL SIMULATION OF TROPICAL CYCLONE GENESIS

University of Washington

PH.D.

1980

**University
Microfilms
International**

300 N. Zeeb Road, Ann Arbor, MI 48106

18 Bedford Row, London WC1R 4EJ, England

Doctoral Dissertation

In presenting this dissertation in partial fulfillment of the requirements for the Doctoral degree at the University of Washington, I agree that the Library shall make its copies freely available for inspection. I further agree that extensive copying of this dissertation is allowable only for scholarly purposes. Requests for copying or reproduction of this dissertation may be referred to University Microfilms, 300 North Zeeb Road, Ann Arbor, Michigan 48106, to whom the author has granted "the right to reproduce and sell (a) copies of the manuscript in microfilm and/or (b) printed copies of the manuscript made from microform."

Signature Vernon L Bliss
Date 22 Feb 80

TABLE OF CONTENTS

	Page
List of Figures	iv
List of Tables	xii
Chapter I: Introduction	1
CISK and Numerical Hurricane Simulation	2
Wave-CISK	6
Upper Level Effects	6
Cumulus Momentum Transport	9
Atmospheric Moisture	10
Precursor Disturbances	12
The Present Study	15
Chapter II: The Physical Model	20
The Equation of Continuity	22
The Equations of Motion	25
Radiation Parameterization	30
Cumulus Parameterization	31
The Boundary Layer and CISK	32
Diagnosis of the Instability Parameter	37
Mid-tropospheric Equivalent-	
Potential Temperature	41
Upper-tropospheric Equivalent-	
Potential Temperature	41
Boundary-Layer Equivalent-	
Potential Temperature	46
The Forecast Set	50
Chapter III: Numerical Methods	56
Forecast Model Numerical Methods	57
Semi-implicit Calculations	64
Relaxation and other Helmholtz	
Equation Solvers	71
Final Wind Component Prognosis	72
Boundary Layer Prognosis	72
The Integration Cycle	73
Boundary Treatments	73
Noise Control	83
Numerical Stability	84
Initialization Numerical Methods	85
Dirichlet Boundary Initialization	89
Easterly Wave Cyclic Boundary	
Initialization	92

TABLE OF CONTENTS--Continued

	Page
Chapter IV: Results and Discussion	103
Development of a Mature Hurricane	103
Genesis from a Composite Easterly Wave	104
Sea Surface Temperature and Moisture Effects	142
Vertical Wind Shear Effects	149
Cumulus Momentum Transfer	176
Wave-CISK	184
Chapter V: Conclusions	189
Summary	189
Limitations and Suggestions	191
Bibliography	202
Appendix A: Computer Programs	202
Appendix B: Display Notes	202
Appendix C: Model Testing	205

LIST OF FIGURES

Figure	Page
1. Ooyama fluid system	21
2. Stratification of a mean tropical atmosphere	34
3. General flowchart for hurricane model integration	54
4a. Space staggering of gridded variables for even time level and for domain with fixed boundaries	60
4b. Same as 4a but for odd time level	61
5a. Space staggering of gridded variables for even time level and for domain with cyclic boundaries	62
5b. Same as 5a but for odd time level	63
6. E1 and E2 experiments. Levels 0 and 1 initial wind field	78
7. E1 and E2 experiments. Level 2 initial wind field	79
8. E2 experiment. Level 0 and 1 wind field at forecast hour 24	80
9. All V experiments. Levels 0, 1, and 2 initial wind field	93
10. All V experiments. Levels 0, 1, and 2 initialized geopotential	94
11. The variation of Coriolis force in IECB/6 initialization	97
12. EC4, EC6-EC15, EC17-EC20 experiments. Levels 0 and 1 initialized wind	99
13. EC4, EC6-EC15, EC17-EC20 experiments. Levels 0 and 1 initialized geopotential deviations	100
14. EC4, EC6-EC15, EC17-EC20 experiments. Levels 0 and 1 initialized wind. Truncated display	101

LIST OF FIGURES--Continued

Figure		Page
15.	EC4, EC6-EC15, EC17-EC20 experiments. Levels 0 and 1 initialized geopotential deviation. Truncated display	102
16.	V3 experiment. Level 0 wind field for forecast hour 96	105
17.	V3 experiment. Level 2 wind field at forecast hour 48	106
18.	EC4, 9, 11, 16-20 experiments. Level 2 initialized wind field	107
19.	EC4 experiment. Levels 0 and 1 wind field at forecast hour 96	111
20.	EC4 experiment. Levels 0 and 1 divergence field forecast hour 96	112
21.	EC4 experiment. Level 2 divergence field at forecast hour 96	113
22.	EC4 experiment. Level 1 maximum speed versus even time steps	116
23.	EC4 experiment. Level 0 total area kinetic energy versus even time steps	117
24.	EC4 experiment. Level 1 total area kinetic energy versus even time steps	118
25.	EC4 experiment. Level 2 area total kinetic energy versus even time steps	119
26.	EC11 experiment. Level 0 wind field at forecast hour 96	122
27.	EC11 experiment. Level 2 wind field at forecast hour 96	123
28.	EC4 experiment. Level 2 wind field at forecast hour 96.	124
29.	EC11 experiment. Level 0 vertical velocity (m/sec) at forecast hour 96	126
30.	EC11 experiment. Level 2 divergence at forecast hour 96	127

LIST OF FIGURES--Continued

Figure	Page
31. EC11 experiment. Maximum wind speed versus even time steps	128
32. EC17 experiment. Level 0 wind field at forecast hour 96	130
33. EC4, 9, 11, 17-20 experiments. Initial vertical wind shear ($\nabla_2 - \bar{\nabla}_0$)	132
34. V3 experiment. Stability factor η at forecast hour 96	134
35. EC11 experiment. Thermodynamic stability parameter η at forecast hour 96	135
36. EC4-9, 11-15, 17-20 experiments. Levels 0 and 1 initial vorticity	138
37. EC11 experiment. Level 0 vorticity at forecast hour 96	139
38. EC24 experiment. Level 1 wind field at forecast hour 96	146
39. EC24 experiment. Level 1 maximum wind speed versus even time steps	147
40. EC12 experiment. Level 0 wind field at forecast hour 96	152
41. EC13 experiment. Level 0 wind field at forecast hour 96	153
42. EC14 experiments. Level 0 wind field at forecast hour 96	154
43. EC15 experiment. Level 0 wind field at forecast hour 96	155
44. EC12 experiment. Level 1 maximum wind speed versus even time steps	156
45. EC13 experiment. Level 1 maximum wind speed versus even time steps	157
46. EC14 experiment. Level 1 maximum wind speed versus even time steps	158

LIST OF FIGURES--Continued

Figure	Page
47. EC15 experiment. Level 1 maximum wind speed versus even time steps	159
48. EC6 experiment. Levels 0 and 1 wind field at forecast hour 96	161
49. EC7 experiment. Levels 0 and 1 wind field at forecast hour 96	162
50. EC8 experiment. Levels 0 and 1 wind field at forecast hour 96	163
51. EC7 experiment. Level 2 wind field at forecast hour 96	164
52. EC8 experiment. Level 2 wind field at forecast hour 96	165
53. EC6 experiment. Level 1 wind field at forecast hour 48	167
54. EC6 experiment. Level 2 wind field at forecast hour 48	168
55. EC14 experiment. Stability factor η at initial time	170
56. EC15 experiment. Stability factor η at initial time	171
57. EC19 experiment. Level 1 total area kinetic energy versus even time steps	178
58. EC19 experiment. Level 2 total area kinetic energy versus even time steps	179
59. EC19 experiment. Maximum wind speed versus even time steps	180
60. EC18 experiment. Level 2 divergence at forecast hour 96	181
61. EC18 experiment. Level 0 wind field at forecast hour 96	182
62. EC18 experiment. Maximum wind speed versus even time steps	183

LIST OF FIGURES--Continued

Figure	Page
63. EC20 experiment. Level 0 and 1 wind fields at forecast hour 96	186
64. EC20 experiment. Levels 0 and 1 divergence at forecast hour 96	187
65. V2A experiment. Level 1 wind field at forecast hour 240	207
66. V2A experiment. Level 2 wind field at forecast hour 240	208
67. V2A experiment. Level 1 geopotential at forecast hour 240	209
68. V2A experiment. Level 2 geopotential at forecast hour 240	210
69. V2A experiment. Level 1 total area kinetic energy versus odd time steps	211
70. V2A experiment. Level 2 total area kinetic energy versus odd time steps	212
71. V2A experiment. Level 1 total area kinetic energy versus even time steps	213
72. V2A experiment. Level 2 total area kinetic energy versus even time steps	214
73. V2A experiment. Total area potential energy versus odd time steps	215
74. V2A experiment. Total area potential energy versus even time steps	216
75. V2A experiment. Minimum surface pressure deviations versus odd time steps	218
76. V2A experiment. Minimum surface pressure deviations versus even time steps	219
77. V2A experiment. Maximum speed versus even time steps	221
78. V2A experiment. Maximum speed versus odd time steps	222

LIST OF FIGURES--Continued

Figure	Page
79. V2B experiment. Layer 1 geopotential at forecast hour 240	223
80. V2B experiment. Total area potential energy versus even time steps	224
81. V2B experiment. Maximum speed versus even time steps	225
82. V2C experiment. Layer 1 geopotential at forecast hour 240	226
83. V2C experiment. Total area potential energy versus even time steps	227
84. V2C experiment. Maximum speed versus even time steps	228
85. V3 experiment. Level 1 wind field at forecast hour 96	232
86. V3 experiment. Level 0 divergence at forecast hour 96	233
87. V3 experiment. Level 0 divergence at forecast hour 96	234
88. V3 experiment. Level 1 divergence at forecast hour 96	235
89. V3 experiment. Level 2 wind field at forecast hour 96	236
90. V3 experiment. Level 2 divergence at forecast hour 96	237
91. V3 experiment. Level 1 geopotential at forecast hour 96	238
92. V3 experiment. Level 2 geopotential at forecast hour 96	239
93. V3 experiment. Boundary layer χ_0 at forecast hour 96	240
94. V3 experiment. Level 1 maximum wind speed versus odd time steps	242

LIST OF FIGURES--Continued

Figure	Page
95. V3 experiment. Total energy versus even time steps	243
96. V3 experiment. Level 1 wind field at forecast hour 144	244
97. V3 experiment. Level 1 geopotential at forecast hour 144	245
98. V3 experiment. Level 1 maximum wind speed versus even time steps	246
99. V3 experiment. Minimum surface pressure deviation versus even time steps	247
100. EC1 experiment. Levels 0, 1, and 2 initialized wind field	249
101. EC1 experiment. Levels 0, 1, and 2 initialized geopotential	250
102. EC1 experiment. Level 1 wind field at forecast hour 192	251
103. EC1 experiment. Level 1 geopotential at forecast hour 192	252
104. EC2 experiment. Levels 0, 1, and 2 initialized geopotential	254
105. EC2 experiment. Level 1 geopotential at forecast hour 240	256
106. EC2 experiment. Level 1 wind field at forecast hour 240	257
107. EC2 experiment. Level 0 normalized kinetic energy versus even time steps	258
108. EC2 experiment. Level 1 maximum wind speed versus even time steps	259
109. EC3 experiment. Level 1 kinetic energy versus even time steps	261
110. EC3 experiment. Level 0 kinetic energy versus even time steps	262

LIST OF FIGURES--Continued

Figure		Page
111.	EC3 experiment. Level 2 kinetic energy versus even time steps	263
112.	EC3 experiment. Level 1 maximum wind field versus even time steps	264
113.	EC9 experiment. Level 0 total area kinetic energy versus even time steps	265
114.	EC9 experiment. Level 1 total area kinetic energy versus even time steps	266
115.	EC9 experiment. Level 2 total area kinetic energy versus even time steps	267
116.	EC9 experiment. Level 1 maximum speed versus even time steps	268

LIST OF TABLES

Table	Page
1a. Initial profiles of area average vorticity for Ooyama experiments	16
1b. Same as 1a but for point vorticity	16
1c. Development from initial states of 1a and 1b.	17
2. $\bar{\chi}_s$ and $\theta_{e,s}^*$ as a function of sea surface temperature	51
3. Synopsis of model variables and equations . .	52
4. Major fixed boundary experiments	76
5. Model acronyms	82
6. Major cyclic boundary experiments without cumulus effects	109
7. Major cyclic boundary experiments with cumulus effects	120
8. Boundary layer vorticity concentration . . .	137
9. Cyclic boundary experiments with modified cumulus parameterization or boundary-layer moisture changes	144
10. Effects of upper level wind shear on cyclone genesis	151
11. Layer 1 maximum wind speeds for constant η experiments	173
12. Scales for contour and wind vector plots . .	204
13. Spin-down ratios	229

CHAPTER I

INTRODUCTION

What affects the formation and growth of hurricanes? Atmospheric scientists have pondered and studied this question for many years, but the answers are still not complete. Both scientific and practical reasons continue to drive the search for answers. Our scientific curiosity sees the puzzles in the workings of a magnificent and complex heat engine while our practical sense sees one of the most destructive storms on earth. Both reasons compel us to learn as much as possible about hurricanes.

The formation of hurricanes is perhaps a more intriguing question than the maintenance of the mature storm because we are still not very successful in forecasting which tropical disturbances will develop and which will not. Hebert (1978) studied the intensification criteria used by the National Hurricane Center for the years 1968-1972 and found that use of these criteria resulted in a correct development forecast 49% of the time. The criteria, even though they contain many of the generally accepted development factors, are still not adequate. The poor performance can be partially blamed on a lack of data and on the subjectivity inherent in estimating some of the development factors, but that cannot be the whole answer. Certainly we still have much to learn about the physical

mechanisms underlying the development or non-development of a weak tropical disturbance.

1.1 CISK and Numerical Hurricane Simulation

A major difficulty in the hurricane formation problem is that many of the methods of mid-latitude theoretical meteorology do not seem to work as well in the tropics. Mid-latitude analytical quasi-geostrophic theory is very successful in explaining the formation and gross properties of mid-latitude cyclones, but few would argue that any analogous theory is as successful in explaining tropical cyclones.

One of the more successful hypotheses for the tropics has been the CISK (Conditional Instability of the Second Kind) mechanism. Both Ooyama (1964, 1964a) and Charney and Eliassen (1964) developed the idea of a cooperative rather than competitive interaction between cumulus clouds and larger scale tropical disturbances. The impetus for the development of this theory was the conflict between the reality of hurricane existence and the failure of both theory and numerical models to explain or produce a hurricane scale disturbance.

Early numerical models of hurricane development were not successful. Efforts, such as those by Syono (1960), seemed to produce explosively growing small-scale disturbances, and these results appeared to coincide with then

current analytical conclusions which implied that the conditionally unstable atmosphere of the tropics was most unstable to the smallest scale waves (Lilly, 1960). Since hurricanes, as well as small scale cumulus clouds did exist in the tropics, researchers looked for some way to connect the clouds to the larger scale disturbances so that a modeled, conditionally unstable atmosphere would support large- and meso-scale disturbances as well as small-scale convection.

The result of this search was CISK, which parameterizes cumulus heating as a function of synoptic scale parameters. The formulation of these parameters varies from sophisticated to very simple techniques, but a central core is the relationship linking frictionally-forced boundary-layer vertical motions to the quantity of cumulus heating.

The CISK parameterization seemed to be the key to numerically simulating hurricane development. In the years following 1964, many hurricane models employing CISK have been developed and used to explore the hurricane problem.¹ Integrations from weak disturbances have produced mature storms which resemble real hurricanes in many ways, and model experiments have confirmed some of the climatologically gleaned

¹I will not detail all of these simulation models, but a sampling of those not specifically mentioned in the text can be found in the following papers: Anthes (1972), Anthes, et al. (1971a, 1971b), Kasahara (1974), Kurihara and Tuleya (1974), Rosenthal (1971a, 1971b, 1970a, 1970b), Sundquist (1970), and Yamasaki (1968a, 1968b).

development factors such as a warm sea surface and a high Coriolis value.

Hurricane models were also developed for use with real data. Miller (1972), Mathur (1974), and Ceselski (1974) used real data in primitive equation models to forecast the movement and development of hurricanes. Ceselski, in particular, touched upon the problem of development or non-development by using the same model on real data integrations of both an intensifying tropical storm and a non-developing easterly wave. The model produced development in the first case but non-development in the second, thereby supporting CISK as a necessary but not sufficient condition for development.

The use of real data in hurricane models has been successful enough to stimulate the development and use of complex primitive equation models in routine hurricane forecasting. Both the U. S. National Meteorological Center (Hope and Neumann, 1977) and the U. S. Navy's Fleet Numerical Weather Central (Mihok and Hinsman, 1977) have models under evaluation for the dynamical prediction of hurricanes using routine operational data.

Until the recent work of Rosenthal (1978) and Yamasaki (1977), hurricane models continued to use CISK cumulus parameterization schemes of various kinds. Yamasaki developed his model on a fine mesh (400 m) to resolve some aspects of individual clouds, and he discovered that the fears of small

scale instability that had initially led to CISK were unfounded. Although explicitly releasing heat on the resolvable scale, his model integrations gave a hurricane-like disturbance and did not blow up into small scale noise. He also tested the intensification with and without friction in the boundary layer and discovered that a disturbance still developed in the absence of friction; but friction greatly increased the rate of growth, decreased the scale, and allowed an eye to form.

Rosenthal also developed a model with explicit heat release on the resolvable scale and obtained hurricane disturbances from the model integrations. He also questioned a basic CISK tenet of convective control by the synoptic scale. In the early stage of the integration, his model disturbance underwent an organizational period with little growth and with little apparent control of the convection by the large-scale disturbance. Rosenthal's basic thought was that resolvable-scale heating allows a transition to occur from non-synoptic control of the convection during the early stages to a cooperative, synoptic organization and control during the latter stages. With a CISK parameterization, the synoptic control is inherent in the mechanism and so would not realistically simulate this early non-synoptic controlled period. However, similar organizational periods have occurred in other models (Rosenthal, 1970a) which do use a CISK parameterization rather than

direct heat release, and it is not clear that Rosenthal's (1978) early period of little change implies that no organization is occurring and that the synoptic scale has no control.

The ability to perform integrations using resolvable latent heat release is undoubtedly a step forward in hurricane modeling. However, it does not invalidate the use of CISK parameterizations, which are necessary in coarser mesh models that cannot directly resolve cloud-scale heating. In chapter two we will again look briefly at CISK and its justifiable use in the numerical model used in this study.

1.2 Wave-CISK

The CISK mechanism originally incorporated only frictionally forced boundary layer convergence for driving cumulus convection. However, Lindzen (1974) proposed a modified CISK that used the internal convergence of the disturbance itself rather than friction to drive the boundary layer convergence for the cumulus convection. He performed a lengthy theoretical analysis indicating that many tropical disturbances may be consistent with the wave-CISK mechanism, and he hypothesized that even tropical hurricane formation may be partly explained by wave-CISK.

1.3 Upper Level Effects

Recognition of the qualitative effect of the upper troposphere arrived early, and many synoptic studies of

hurricanes have attributed formation and growth effects to the upper levels (1969, Palmen and Newton). Riehl (1954) also hypothesized that the "high tropospheric layer between 300 mb and the tropopause" served as a starter for initiating the development of a pre-existing disturbance.

More recent examples of the strength of upper level effects on tropical disturbances are studies by Ramage (1974), Lewis and Jorgensen (1978), and Sadler (1976, 1978). Ramage studied examples of intensification and decay of typhoons in the South China Sea. Normally, one would expect a negative relationship between sea surface pressure and typhoon intensity because of the large quantities of water vapor that a typhoon consumes in maintaining itself. Ramage, however, frequently found intensity changes in typhoons that behaved in an opposite manner, and he attributed the cause to upper tropospheric influences predominating over the sea surface temperature effects.

Lewis and Jorgensen (1978) documented the dissipation of a hurricane following its interaction with a deep westerly trough while Sadler (1978, 1976) implicated the tropical upper tropospheric trough in typhoon development. Sadler also presented evidence that major tropical cyclone intensification may need a northern outlet to the westerlies as well as a direct outlet to the upper easterlies.

Climatology and composited disturbances have been the basis for a large group of studies by Gray (1977, 1975)

and his students (Zehr, 1976; Erickson, 1977; and McBride, 1979). Gray's initial work supported the idea that the presence of small vertical wind shear was of paramount importance in allowing hurricane formation. However, the recent compositing study of McBride (1979) revealed that a developing disturbance was most likely to have a high shear everywhere except near the center of the disturbance. McBride found a good relationship between the quantity (vorticity 950 mb - vorticity 200 mb) and genesis potential; and this, coupled with the shear observations, produces an ideal model of a developing disturbance as a lower level cyclone overlaid by an upper tropospheric anticyclone. Such a picture would yield a very high value of (ζ 950mb -- ζ 200mb), a low shear in the center, and high vertical shear away from the center.

The presence of significant shear in McBride's developing disturbances reopens the whole question of the effect of shear on development. Gray's (1975) original work was based on climatological parameters, and examination of Gray's maps of genesis parameters reveals a qualitative climatological correlation in the tropics between low vertical wind shear and high positive low level vorticity. Because of this correlation, simple statistical studies such as Gray's would tend to reveal both vorticity and vertical shear as controlling factors even if only one of the two was important to genesis. Thus, although the hypothesis of a vertical

shear effect has survived a long time, a closer look at the effect may be worthwhile.

Only two of the many hurricane simulations have broached the subject of vertical wind shear effect. Madala and Piacsek (1975) added easterly vertical wind shear to a weak barotropic symmetrical vortex ($V_{\max} = 4$ m/sec at $r = 360$ km) and integrated the combined fields. They found that the vertical shear reduced the maximum intensities developed by the disturbances from 46 m/sec for the no-shear case to 20 m/sec for the case with added initial basic easterly currents of 0 m/sec at a height of .5 km, 5 m/sec at 4.0 km, and 15 m/sec at 12 km. However, although the maximum intensity decreased, the rate of development increased with shear; the no-shear case took about 180 hours to reach maximum intensity while the shear case above only took about 80 hours.

The other simulation that incidentally included shear was the work of Jones (1977a, 1977b). He also used a symmetric cyclonic vortex but set the initial intensity to a very high value of 19 m/sec at a radius of 240 km. The addition of an environmental current added a very weak shear with a basic westerly current of 10 m/sec in the boundary layer, 9.4 m/sec in mid-troposphere, and 7.5 m/sec in the upper troposphere. The integration with the basic current and weak shear intensified much faster than the case with no basic current; the basic-current experiment reached

50 m/sec in a little over 30 hours while the no-current case took almost 80 hours to reach the same speed.

1.4 Cumulus Momentum Transport

The vertical motions within and surrounding cumulus clouds move parcels of air between various levels in the atmosphere. One property contained by these vertically moving parcels is horizontal momentum; and if this momentum is at least partially conserved during parcel ascent or descent, then the net result is a transport of horizontal momentum by the cloud-induced vertical motions. This effect is commonly labeled cumulus momentum transport.

Gray (1967) explored this effect and hypothesized that it might ". . . act as a basic mechanism for the generation of tropical easterly waves and other phenomena." Later budget studies by Stevens (1979), Shapiro (1978), and Reed and Johnson (1974) showed apparent upper tropospheric vorticity sources and lower tropospheric sinks that might be explained by cumulus momentum transport. Estoque, et. al. (1977), included transfer effects in a quasi-geostrophic easterly wave simulation and found, contrary to Gray's (1967) hypothesis, that cumulus momentum transfer appeared to decrease wave amplitude in the model.

The results of these studies were not totally consistent with each other. However, they do suggest the possible significance of cumulus momentum transfer in tropical cyclone genesis.

1.5 Atmospheric Moisture

The supply of atmospheric water vapor is important in the development of tropical cyclones because these storms are driven to a large degree by convective clouds. Sea surface temperature in turn plays a crucial role in hurricane or typhoon development because the higher the sea surface temperature, the larger the evaporation rate and the larger the probable moisture supply.

The impact of sea surface temperature has been confirmed both by observations and numerical modeling. Observation shows that a sea surface temperature of at least 26 to 27°C is a necessary condition for hurricane or typhoon development (Palmen and Newton, 1969). The necessity of a sufficiently warm sea surface has also been confirmed by Ooyama (1969), whose simulated hurricane dropped over 20 m/sec in maximum wind speed when the initial sea surface temperature was dropped from 27.5 to 25.6°C.

A developing tropical cyclone also depends upon the initial, local atmospheric water vapor supply. Rosenthal (1970a) details some numerical experiments in which simulated development occurred much sooner in a case with an initial 90% relative humidity than in the case with a lower initial humidity based on the mean tropical atmosphere. Notwithstanding the difference in development rate, both initial humidity conditions produced storms of almost the same final intensity.

Both a high initial moisture and a high sea surface temperature present favorable conditions for tropical cyclone development. By inference, Gray's (1975) development parameter, which was based on climatology, implies that extremely favorable moisture conditions--high atmospheric moisture and high sea surface temperature--may be able to partially compensate for other development factors that are less favorable. Such an idea is reasonable but has not been explored yet by numerical simulation.

1.6 Precursor Disturbances

One hypothesis of long standing is that hurricanes and typhoons form from pre-existing disturbances. Synoptic studies like those of Erickson (1963) and Hawkins and Rubsam (1968) have implicated easterly waves as possible precursors, while a case study by Fett (1968) found pre-typhoon disturbance in the Intertropical Convergence Zone. Still others, like Frank (1963), have studied hurricanes that apparently formed from upper-level cold lows.

A basic problem with many of these synoptic case studies was the lack of data. The sparseness of wind and other observations prevented detailed analysis and weakened many conclusions because the analyst was forced to fill large data void areas with his own conception of the meteorological fields in those areas.

One answer to the data sparseness is to build composite pictures of hurricane and typhoon precursors and non-

developing tropical disturbances. In this manner, data from many disturbances can be combined and averaged, thus isolating some of the mean differences between developing and non-developing systems. Zehr (1976), Erickson (1977), and McBride (1979) used this approach and examined many of the thermodynamic and dynamic variables associated with the disturbances.

Lower tropospheric vorticity was the variable that generally showed the largest, most consistent differences between developing and non-developing tropical disturbances. Weak systems that eventually became hurricanes or typhoons had average lower tropospheric vorticities two to three times higher than those of weak non-developing systems. The vorticity differences were especially evident when looking at the vorticity averages calculated for radii of 6° latitude from the center of each composite disturbance.

Both the above composite data studies and climatological studies by Gray (1975) imply that the low level vorticity field significantly affects tropical storm development. Notwithstanding these observations, only a little information on this effect can be gleaned from past hurricane simulations. Yamasaki (1968b) used two different initial vorticity profiles in experiments with his symmetric hurricane model. His first initial condition carried a peak vorticity of about $15 \times 10^{-5} \text{ sec}^{-1}$ at 30 km radius while the second peaked out at $7 \times 10^{-5} \text{ sec}^{-1}$ at 140 km radius but with a higher vorticity than the

first at all radii outside 100 km. Integration of the two states resulted in totally different development histories. In the first case, the central pressure dropped dramatically between the fourth and fifth day; but in the second case, the rapid pressure drop never came--even by the end of 12 days of integration.

Anthes (1971b) also varied the vorticity in two of his experiments with a circularly symmetric hurricane model. His experiments used two different initial states, one with a peak tangential wind of 18 m/sec at a radius of 240 km and the other with perhaps half that velocity at the same radius. By inference, the first state with the stronger tangential wind had the higher peak vorticity, and a hurricane developed from this state in a little over one day as opposed to the other weaker peak vorticity state that took almost six days to achieve hurricane strength. This result seems to agree with Yamasaki's (1968b) result, which showed faster development of the initial state with the highest peak vorticity.

Ooyama's (1969) model, however, showed longer development times for integrations from initial states with higher vorticity. His experiments involved four different initial vortices, each with its own different vorticity profile but each with the same peak tangential wind speed of 5 m/sec. The radial profiles of these vorticities, both for area average vorticity and for point vorticity, are listed in

Table 1a and 1b, respectively,¹ and some characteristics of the simulated development are contained in 1c. One can see that with Ooyama's model the initial states with higher peak vorticities took longer to develop but eventually developed slightly higher speeds. However, the sequence of development follows the sequence of initial vorticities if the vorticities beyond 100 km radius are considered.

The results of the above simulations confirm that initial vorticity fields may affect the development rate of tropical storms. However, development eventually occurred in all cases, and it is not yet clear whether the low level vorticity field can exert a decisive influence on the final development or non-development of a disturbance.

1.7 The Present Study

Initial conditions used in hurricane simulations have generally reflected relatively strong and organized states. Gray (1975) used the average relative vorticity within the radius of maximum winds to characterize the strength of the vortex used in various simulations. He found that these vorticities were typically an order of magnitude or more greater than actual pre-cyclone cloud cluster vorticities

¹Area average vorticity ζ_a is the average vertical vorticity component about a center point and is $2v_T/r$ in cylindrical coordinates for a symmetric vortex where v_T is the tangential wind speed and r is the radius. Point vorticity, ζ , is the regular vertical component of $\nabla \times \bar{v}$ where \bar{v} is the wind velocity, and ζ is $(1/r)(\partial(v_T r)/\partial r)$ in cylindrical coordinates for a symmetric vortex.

TABLE 1a

INITIAL PROFILES OF AREA AVERAGE VORTICITY
 ($\times 10^5 \text{ sec}^{-1}$) FOR OYAMA (1969) EXPERIMENTS
 $Ai_1, Ai_2, Ai_3, \text{ AND } Ai_4$

Radius	Experiments			
	Ai_1	Ai_2	Ai_3	Ai_4
25	40.00	32.00	24.00	18.82
50	16.00	20.00	18.46	16.00
75	8.00	12.30	13.33	12.80
100	4.71	8.00	9.60	10.00
200	1.23	2.35	3.29	4.00
300	.55	1.08	1.57	2.00

TABLE 1b

SAME AS 1a BUT FOR POINT VORTICITY

Radius	Experiments			
	Ai_1	Ai_2	Ai_3	Ai_4
25	20.00	25.60	21.60	17.72
50	3.20	10.00	12.78	12.80
75	.80	3.79	6.67	8.19
100	.27	1.60	3.46	5.00
200	.02	.13	.41	.80
300		.03	.01	.20

TABLE 1c
 DEVELOPMENT FROM THE INITIAL STATES OF
 TABLES 1b AND 1a

	Experiments			
	Ai ₁	Ai ₂	Ai ₃	Ai ₄
Time to reach max intensity (hr)	530	305	280	270
Time to reach hurricane intensity (hr)	460	240	205	195
Initial radius of max v _T (km)	25	50	75	100
Radius of max v _T at time of max intensity (km)	50	50	70	95
Initial max v _T (m/sec)	5	5	5	5
Max v _T at time of max intensity (m/sec)	55	56	52	46

($1-1.5 \times 10^{-5} \text{ sec}^{-1}$). In addition, the artificial data simulations almost invariably used some form of symmetrical vortex as an initial state. These initial conditions were beyond the point at which a weak tropical disturbance first organizes into a vortex, and model simulations using such conditions could not reveal much about this initial transformation from a weak disturbance into a vortex.

Basically the question of how the initial closed vortex forms and intensifies has been neglected. Gray (1977) describes the situation very succinctly:

The feature of hurricane formation which is least understood is that of how the weak precursor cyclone, that extends through most of the troposphere, is formed from a tropical disturbance with little flow organized circulation. This very early stage in the hurricane formation process will be termed 'cyclone genesis.' By contrast, the question of 'cyclone intensification' or growth of an already formed tropospheric cyclone is much better understood. It is important to make this distinction. Extensive numerical modeling of 'cyclone intensification' has already been accomplished with reasonable success . . . several numerical modelers have simulated the intensification of specified tropical cyclones which extend through the depth of the troposphere. These modeling efforts have been primarily directed towards obtaining realistic simulations of tropical cyclone growth rates from existing cyclones whose inner 100-200km radius vorticities are an order of magnitude larger than those of typical pre-cyclone disturbances. . . . The physical processes responsible for formation of the initial cyclone from which the modelers start their integrations, and the reasons why so few tropical disturbances become tropical cyclones has yet to be satisfactorily enunciated.

Recognition of the above gap in knowledge was the spark for the research described in this dissertation. The result is a numerical simulation study of tropical cyclone genesis and early intensification.

Perhaps the most important considerations in this simulation are the model physics and the initial fields for the model. The model is three dimensional and uses primitive equations, but it does not contain detailed cumulus-scale physics or dynamics. Such additional detail is unwarranted because it would detract from the main research objective of exploring only basic genesis and intensification factors.

Low-level initial circulations for the model fall into two categories. The first is the familiar symmetric vortex, which serves to bridge these simulation studies with other past efforts. The other, major initial circulation, is taken from composited easterly wave data (Reed, et al., 1977). This wave, with an open circulation and a maximum vorticity of about $2.5 \times 10^{-5} \text{ sec}^{-1}$, basically falls into Gray's (1977) category of pre-cyclone disturbances. Simulations using this initial wave state are not expected to reproduce the development of an actual easterly wave, but such simulations are a valid means to study the factors that might generally influence the initial stages of tropical disturbance intensification or vortex development.

Concentration on the details of a single simulation was not the aim of this study. Rather, the objective was to isolate physical factors that affect genesis and intensification. Such isolation was accomplished by evaluating the results of simulations in which the numerical model or the initial condition was modified to reflect change in a basic development factor. Examples of factors that were changed in the experiments are vertical shear of the horizontal wind, CISK, cumulus momentum transfer, eddy diffusion, sea surface temperature, low level moisture, and initial disturbance vorticity and organization. In chapter four we will examine the results of such experiments and discuss their implications for tropical cyclone genesis and intensification.

CHAPTER II

THE PHYSICAL MODEL

The purpose of a numerical simulation basically determines the required complexity of the model. If the purpose of the simulation is to approximate the real atmosphere as closely as possible, then the appropriate model is normally very complex and attempts to incorporate as many physical effects as possible--even if some of the effects are of secondary importance. On the other hand, if the intent of the simulation is to explore specific atmospheric phenomena, then simplicity rather than complexity is a virtue. In this case, retaining only the physical essence of the phenomenon being studied allows an easier analysis and isolation of that phenomenon. Adding additional, non-primary physical mechanisms to the simulation model tends to obscure the basic objectives of the study.

The consideration above stimulated the search for a model that would contain the minimum physics necessary to explore the gross aspects of three dimensional dynamics in tropical cyclone genesis. A suggestion by J. R. Holton and a review of the literature pointed towards the model physics in the Ooyama (1969) hurricane model. The Ooyama (1969) model has the simplest physics of any successful hurricane simulation model, but its balanced dynamics and symmetrical geometry are not appropriate to studying non-symmetrical

initial states nor to studying the effects of basic upper level flows on tropical vortex genesis. However, combination of Ooyama's basic fluid system and CISK mechanisms with the primitive equations presents the quintessential elements needed for the numerical simulations of this investigation.

The simulation model design directly adopts the Ooyama (1969) fluid system, and I refer the reader to that paper for additional details. The model contains three incompressible layers as depicted in Fig. 1: a fixed height planetary boundary layer with density ρ , a lower tropospheric layer with density ρ , and an upper tropospheric layer with density $\epsilon\rho$.

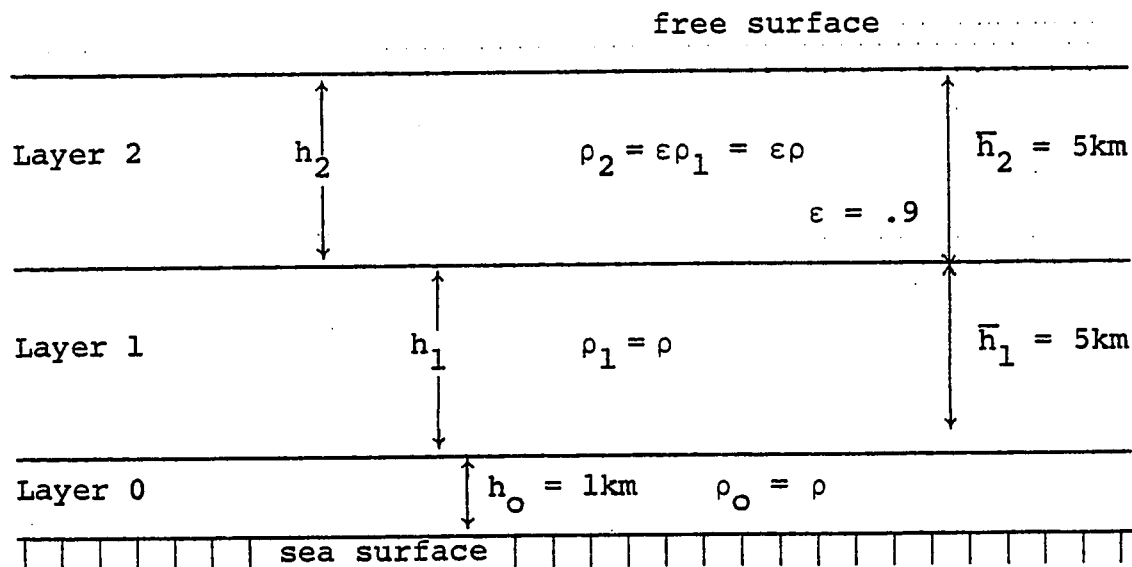


Fig. 1. Ooyama fluid system.

Ooyama's own words best describe the background for this model:

In the construction of a numerical model of such a low vertical resolution, the discretization procedure requires careful attention in order to insure that the

energy and other integral properties of the system of finite difference equations are physically consistent. One method frequently adopted to simplify this problem is the replacement of the atmosphere by a few layers of incompressible homogeneous fluid. In the case of large-scale motions in a stably stratified atmosphere, the incompressible fluid system is dynamically similar to the atmospheric system if the specific volume is interpreted to be analogous to the potential temperature.

One obvious reason for the simplicity of the incompressible fluid system is the absence of true thermodynamics. While this peculiarity is not a serious problem for a study of adiabatic motions in the atmosphere, it may present a difficulty in interpretation if an attempt is made to introduce diabatic processes into the system. In the present study, however, the major diabatic process is associated with unstable moist convection which, for reasons of its own, will require an indirect formulation. In this special situation, the use of an incompressible fluid system does not prove to be a critical disadvantage because the explicit part of the model represents only the cyclone-scale fields which undergo adiabatic changes.

2.1 The Equation of Continuity

With the incompressibility assumption, the equation of continuity initially reduces to:

$$\nabla \cdot \bar{v} = 0 \quad (1)$$

where \bar{v} is the velocity vector.

The incompressibility assumption, together with the hydrostatic equation and the equations of motion, leads further to the conclusion that the velocity is constant with respect to height within an individual layer. This does not mean that there is no vertical shear in the model but only that the shear exists between and not within layers.

The vertical uniformity of u and v within a layer permits vertical integration of the equation of continuity to obtain

$$w = -h_0 \left[\frac{\partial}{\partial x} \left(\frac{u_0}{m} \right) + \frac{\partial}{\partial y} \left(\frac{v_0}{m} \right) \right] \text{ at } z = h_0 \text{ (1km)} \quad (2)$$

$$\frac{\partial h_1}{\partial t} = -m^2 h_1 \left[\frac{\partial}{\partial x} \left(\frac{u_1}{m} \right) + \frac{\partial}{\partial y} \left(\frac{v_1}{m} \right) \right] - m \left(u_1 \frac{\partial h_1}{\partial x} + v_1 \frac{\partial h_1}{\partial y} \right) + w \quad (3)$$

$$\frac{\partial h_2}{\partial t} = -m^2 h_2 \left[\frac{\partial}{\partial x} \left(\frac{u_2}{m} \right) + \frac{\partial}{\partial y} \left(\frac{v_2}{m} \right) \right] - m \left(u_2 \frac{\partial h_2}{\partial x} + v_2 \frac{\partial h_2}{\partial y} \right) \quad (4)$$

where w is the vertical velocity at the top of the boundary layer, h_0 is the constant boundary layer thickness, h_1 is the layer 1 thickness, h_2 is the layer 2 thickness, u_1 is the layer 1 longitudinal wind component, u_2 is the layer 2 longitudinal wind component, v_1 is the layer 1 meridional wind component, v_2 is the layer 2 meridional wind component, and the m is the map factor for a mercator projection (secant of latitude).

In cumulus clouds, condensation heating reduces the density of lower level air, causing it to rise to a higher level where the density again becomes equal to that in the environment. This process is simulated in the present fluid system by a vertical flux of lower tropospheric air across the layer 1, 2 interface to layer 2 where the density is lower.

Labeled $Q+$, the cumulus flux term transfers mass by changing the thickness of layers 1 and 2. $Q+$, as defined, is a positive thickness change rate with units of m/sec. Because of the conservation of mass, a thickness decrease of $-(Q+)$ in layer 1 is reflected as a thickness increase of $+(Q+/\epsilon)$ in layer 2. Such cumulus induced thickness changes are immediately applicable by adding $-(Q+)$ to the right side of (3) as a cumulus-induced thickness sink and by adding $+(Q+/\epsilon)$ to (4) as a compensating thickness source.

Radiative cooling can also be treated in a similar but converse fashion. When radiative cooling occurs in an atmospheric parcel, the parcel becomes denser and tends to sink. This process can be simulated as a downward mass flux across the interface from the lower-density layer 2 to the higher-density region of layers 0 and 1. Like the cumulus-induced transfer term, $Q+$, the radiative-cooling mass flux term, $Q-$, is a positive thickness change rate. Thus, to simulate radiative cooling, $-(Q-/\epsilon)$ is added to the right side of (4) and a compensating $+(Q-)$ added to (3). Combination of these $Q-$ changes to (3) and (4), along with the previous $Q+$ changes, gives the following total result.

$$\frac{\partial h_1}{\partial t} = -m^2 h_1 \left[\frac{\partial}{\partial x} \left(\frac{u_1}{m} \right) + \frac{\partial}{\partial y} \left(\frac{v_1}{m} \right) \right] - m \left(u_1 \frac{\partial h_1}{\partial x} + v_1 \frac{\partial h_1}{\partial y} \right) + w \quad (5)$$

$$-(Q+ - Q-)$$

$$\frac{\partial h_2}{\partial t} = -m^2 h_2 \left[\frac{\partial}{\partial x} \left(\frac{u_2}{m} \right) + \frac{\partial}{\partial y} \left(\frac{v_2}{m} \right) \right] - m \left(u_2 \frac{\partial h_2}{\partial x} + v_2 \frac{\partial h_2}{\partial y} \right) + \frac{1}{\varepsilon} (Q_+ - Q_-) \quad (6)$$

2.2 The Equations of Motion

For the incompressible, hydrostatic fluid system, the primitive equations of motion on a mercator projection become

$$\begin{aligned} \frac{\partial}{\partial t} \left(\frac{u_k}{m} \right) - \left(\frac{v_k}{m} \right) (f + u_k \frac{\partial m}{\partial y}) + u_k \frac{\partial u_k}{\partial x} + v_k \frac{\partial u_k}{\partial m} \\ = - \frac{1}{\varepsilon \rho} \frac{\partial p_k}{\partial x} + \frac{F_{kx}}{m} \end{aligned} \quad (7)$$

and

$$\begin{aligned} \frac{\partial}{\partial t} \left(\frac{v_k}{m} \right) + \left(\frac{u_k}{m} \right) (f + u_k \frac{\partial m}{\partial y}) + u_k \frac{\partial v_k}{\partial x} + v_k \frac{\partial v_k}{\partial y} \\ = - \frac{1}{\varepsilon \rho} \frac{\partial p_k}{\partial y} + \frac{F_{ky}}{m} \end{aligned} \quad (8)$$

where u is the longitudinal wind component, v is the meridional wind component, f is the coriolis parameter, p is the pressure, ρ is the density, F is the dissipation or mixing term, m is the map factor; and where the k subscript indicates the k^{th} vertical level for the respective u , v , p , ρ , or F terms.

Vertical integration of the hydrostatic equation gives the pressure for each layer, and the pressure gradient for each layer becomes:

$$\frac{1}{\rho_0} \nabla p_0 = g \nabla (h_1 + \epsilon h_2) \quad (9a)$$

$$\frac{1}{\rho_1} \nabla p_1 = g \nabla (h_1 + \epsilon h_2) \quad (9b)$$

$$\frac{1}{\rho_2} \nabla p_2 = g \nabla (h_1 + h_2) \quad (9c)$$

where h_1 is the total layer 1 depth, h_2 is the total layer 2 depth, and g is gravitational acceleration. The pressure gradient in layer 0 (9a) is identical to that in layer 1 (9b) because the density in layer 0 is the same as in layer 1 and the height of layer 0 is constant. All three of the above may be appropriately substituted back into (1) and (2) in order to eliminate pressure as a variable.

For the lowest layer ($k = 0$), the F terms consist of simple bulk aerodynamic drag and eddy diffusion:

$$F_{ox} = - \frac{C_D |\bar{v}_0| u_0}{h_0} + \lambda_1 m^2 \nabla^2 u_0 \quad (10a)$$

$$F_{oy} = - \frac{C_D |\bar{v}_0| v_0}{h_0} + \lambda_1 m^2 \nabla^2 v_0 \quad (10b)$$

where C_D is the drag coefficient, h_0 is the constant boundary layer depth (1 km), $|\bar{v}_0|$ is the magnitude of the boundary layer velocity, and λ_1 is the eddy diffusion coefficient (0 or $1000 \text{ m}^2 \text{ sec}^{-1}$).

The F terms in the two higher levels also contain eddy diffusion (A), in addition to cumulus momentum transfer (B), radiative-cooling momentum transfer (C), and shear

stress momentum transfer at the interface between layers 1 and 2 (D):

$$F_{1x} = \lambda_1 m^2 \nabla^2 u_1 \quad (A) \quad - \frac{u_1 Q^+}{\bar{h}_1} + \frac{u_2 Q^-}{\bar{h}_1} \quad (B) \quad - \mu \frac{(u_1 - u_2)}{\bar{h}_1} \quad (D) \quad (11a)$$

$$F_{1y} = \lambda_1 m^2 \nabla^2 v_1 \quad (A) \quad - \frac{v_1 Q^+}{\bar{h}_1} + \frac{v_2 Q^-}{\bar{h}_1} \quad (B) \quad - \mu \frac{(v_1 - v_2)}{\bar{h}_1} \quad (D) \quad (11b)$$

$$F_{2x} = \lambda_2 m^2 \nabla^2 u_1 \quad (A) \quad + \frac{u_1 Q^+}{\epsilon \bar{h}_2} - \frac{u_2 Q^-}{\epsilon \bar{h}_2} \quad (B) \quad + \mu \frac{(u_1 - u_2)}{\epsilon \bar{h}_2} \quad (D) \quad (11c)$$

$$F_{2y} = \lambda_2 m^2 \nabla^2 v_1 \quad (A) \quad + \frac{v_1 Q^+}{\epsilon \bar{h}_2} - \frac{v_2 Q^-}{\epsilon \bar{h}_2} \quad (B) \quad + \mu \frac{(v_1 - v_2)}{\epsilon \bar{h}_2} \quad (D) \quad (11d)$$

where Q^+ is the mass flux from layer 1 to layer 2 (upward), Q^- is the mass flux from layer 2 to layer 1 (downward), \bar{h}_1 is the standard layer 1 thickness (5 km), \bar{h}_2 is the standard layer 2 thickness (5 km), ϵ is the ratio of layer 2 to layer 1 densities (.9), and μ is the shear stress coefficient (0 or 5×10^{-4} m/sec⁻¹).

The shear stress terms above crudely simulate normal down-gradient vertical atmospheric mixing; they do not represent any cumulus induced vertical mixing. With only two forecast thickness layers, the normal eddy diffusion representation requires modification. With dimensional arguments, a vertical eddy diffusion term becomes

$$K \frac{\partial^2 A}{\partial z^2} \approx \frac{K}{\bar{h}} \frac{\partial A}{\partial z} \approx \mu \frac{(A_2 - A_1)}{\bar{h}}$$

where K is the Austausch coefficient, A is any parameter, \bar{h} is a mean layer thickness, and μ is defined to be K/\bar{h} , the interface stress coefficient. The signs of the (D) terms are set so that layer 1 gains positive momentum if the vertical momentum gradient is positive and loses momentum if the vertical gradient is negative. Conversely, just the opposite effects occur in layer 2.

In section 2.1 we looked at the use of $Q+$ and $Q-$ as mass fluxes for simulating cumulus cloud and radiative cooling effects. Because mass carries horizontal momentum, the transfer of mass between layers also implies a transfer of horizontal momentum. In such vertical transfers, the horizontal momentum should be conservative because the time scale for the cumulus scale vertical motion¹ is much shorter than the time scale for the horizontal forces² acting to change the horizontal momentum.

To illustrate this transfer process, consider u_1 and $Q+$. Per unit area and time, the total amount of u_1 momentum transferred from layer 1 to layer 2 is $\rho u_1 Q+$. Spread over the vertical extent of a layer, $\rho u_1 Q+$ transforms to

¹Typical lifetime of a cumulus cloud might be 10 min to 1 hr.

²A weak tropical disturbance may have a length scale of 400 km and a velocity scale of 7 m/sec. This gives a horizontal time scale of about 16 hrs.

$(\rho u_1 Q^+ / h_1)$ for layer 1 or $(\rho u_1 Q^+ / h_2)$ for layer 2. Further approximation represents these as $(\rho u_1 Q^+ / \bar{h}_1)$ and $(\rho u_1 Q^+ / \bar{h}_2)$ where \bar{h}_1 and \bar{h}_2 are the standard thickness values for layers 1 and 2. Acting as a momentum sink in layer 1, the term $(\rho u_1 Q^+ / \bar{h}_1)$ can be incorporated into layer 1 u- component equation of motion:

$$\rho \frac{du_1}{dt} = \dots - \frac{\rho u_1 Q^+}{\bar{h}_1} \quad (12a)$$

or

$$\frac{du_1}{dt} = \dots - \frac{u_1 Q^+}{\bar{h}_1} \quad (12b)$$

where the right side term of (12b) is the same as the (B) term of (11a). The u momentum disappearing via the Q^+ term in layer 1 is vertically transported to layer 2 and appears in the layer 2 u-component equation of motion:

$$\epsilon \rho \frac{du_2}{dt} = \dots + \frac{\rho u_1 Q^+}{\bar{h}_2} \quad (13a)$$

or

$$\frac{du_2}{dt} = \dots + \frac{u_1 Q^+}{\epsilon \bar{h}_2} \quad (13b)$$

where the right side term of (13b) is the same as the (B) term of (11c).

Using analogous reasoning, one can also treat the Q^+ transfer of v_1 momentum and the Q^- transfer of u_2 and v_2

momentum. The final result is the set of cumulus and radiative cooling momentum transfer terms in (11a)-(11d).

2.3 Radiation Parameterization

The impact of radiational cooling on tropical disturbances is controversial. Gray and Jacobson (1977) documented a large diurnal convective cycle in tropical disturbances and hypothesized that the cycle is driven by radiational differences between the cloudy disturbance region and the surrounding clear region. Fingerhut (1978) attempted to model this phenomenon and concluded that "Radiation is fundamental to the maintenance of the cloud cluster." However, his cluster heating function was an inseparable composite of convection and radiative heating and was tuned to fit composited cluster observational data. The inseparability of the radiative-convective heat term seriously weakens Fingerhut's claim that radiation is fundamental for cluster maintenance.

McBride (1979) hypothesized that the diurnal radiational differences between clear and cloudy areas may play a role in tropical cyclone genesis. However, he did not indicate a clear mechanism whereby radiational forcing may cause one disturbance to develop while another does not. Many hurricane simulations have produced realistic fields without any radiation effects, and it is difficult to understand how radiation could play other than a minor role in

tropical cyclone genesis. Based on these observations, radiation effects were neglected by setting the radiation term, Q^- , to zero in all numerical experiments.

2.4 Cumulus Parameterization

Unlike radiative cooling, cumulus clouds are an indisputable part of a hurricane's circulation, and any tropical or hurricane model must account for their effects. As discussed previously, the Q^+ and Q terms simulate the effects of convection by mass transfers from layer 1 to layer 2. In combination with the coarse physical resolution of the model, the Q^+ mechanism with its very simple physics prohibits a treatment of individual clouds. Rather, the Q^+ term represents a net cumulus effect averaged over many clouds. This Q^+ term is then parameterized from large-scale variables with Ooyama's (1969) CISK (Conditional Instability of the Second Kind) treatment:

$$\begin{aligned} Q^+ &= \eta w, \quad w > 0 \\ Q^+ &= 0, \quad w = 0 \end{aligned} \tag{14}$$

where η is a conditional instability parameter and w is the vertical velocity at the top of the boundary layer.

The boundary-layer vertical velocity is the cumulus initiating factor in the above model because almost all tropical marine atmospheres are conditionally unstable, both for cloudy or clear skies. As real cumulus convection

proceeds, decreasing conditional instability may restrain unlimited cloud development. However, the conditional instability, itself, does not provide the initial impetus for most tropical convection because such an instability is not realized until parcels of air reach the level of free convection. Conditionally unstable parcels--most of them in the boundary layer--are forced upward by positive, vertical boundary layer motions; and few parcels would reach the level of free convection without such a boost.

2.4.1 The Boundary Layer and CISK

Deep cumulus convection is generally viewed as a primary factor in tropical disturbance dynamics, and CISK originally appeared as an attempt to parameterize the effects of such convection. Frank (1977) calculated composite typhoons based on a large sample and observed, ". . . generally increasing Cb convection and low-level convergence with decreasing radius. . . ." This relationship between low level convergence and deep convection is seen not only in strong tropical disturbances such as typhoons but also in weaker systems such as easterly waves (Cho and Ogura, 1974), and the evidence for boundary layer forcing of deep convection seems rather good.

Gray (1977) has questioned the CISK mechanism in tropical cyclone genesis. He notes that frictional boundary layer convergence explains only 15-20% of the mass conver-

gence occurring in early-stage intensifying or non-intensifying disturbances and that significant convergence extends all the way to 400 mb. From this, he asserts, "CISK processes thus appear to play only a minor role in the early cyclone genesis and intensification processes." Gray, however, did not recognize all of the pertinent factors.

A key to understanding the relative importance of the boundary layer air lies in Fig. 2, which contains plots of the equivalent and saturated equivalent potential temperature for the mean summer tropical atmosphere (Jordan, 1958). In pseudo-adiabatic ascent the equivalent potential temperature, θ_e , of a rising parcel is conserved. However, a parcel only becomes unstable and rises without external forcing if the parcel θ_e becomes greater than the environmental saturated equivalent potential temperature, θ_e^* . In Fig. 2, the only layer that supports such free convection is the region below 900 mb--in essence, the boundary layer. Any rising parcel originating above this level is characterized by a low θ_e that can never intersect or exceed the θ_e^* of the environment. In other words, parcels originating above 900 mb cannot reach a level of free convection and cannot become unstable.

A major factor in the generation of cumulus clouds is the release of latent vertical instabilities. As we have seen, parcels that originate above the boundary layer

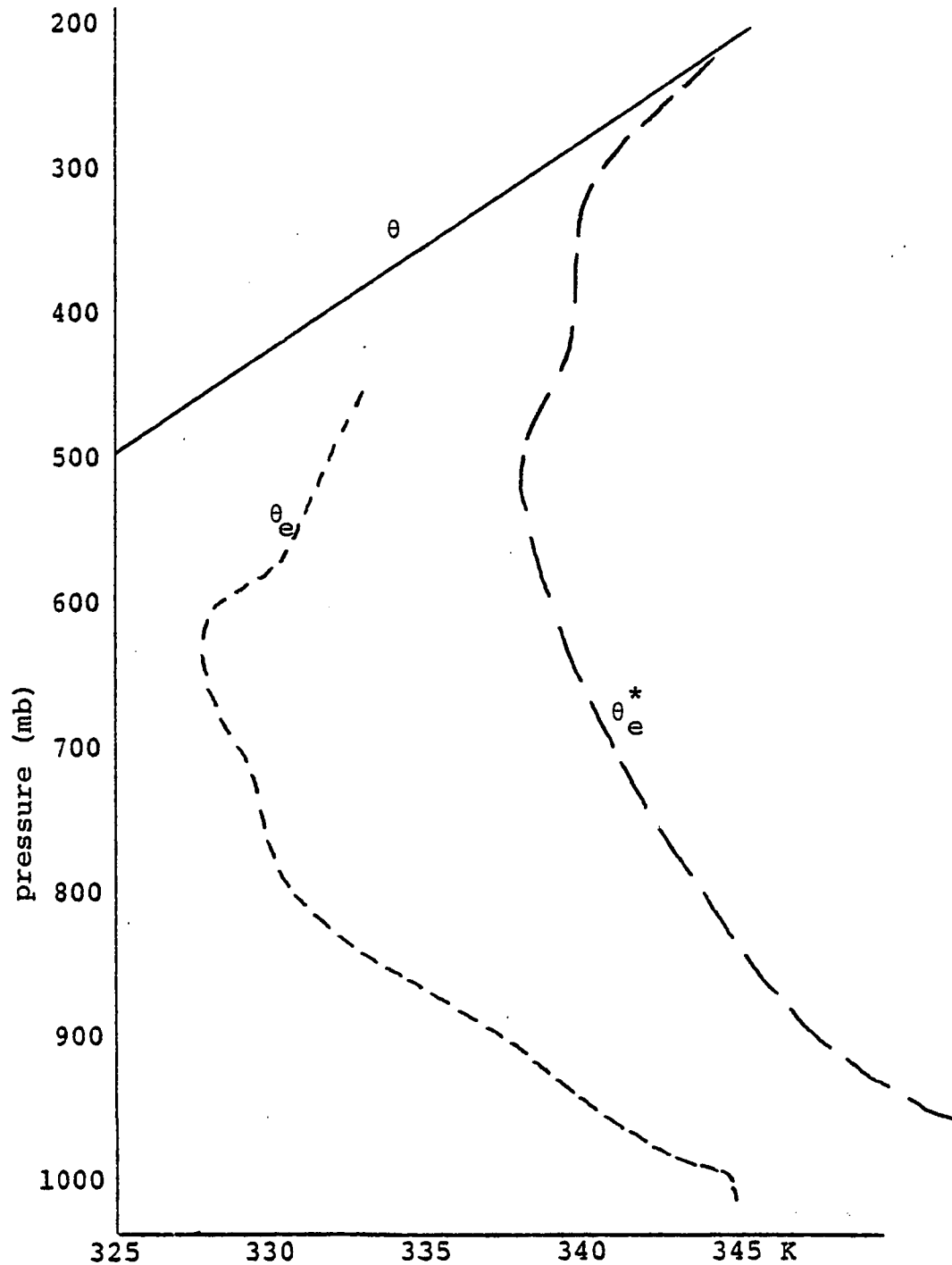


Fig. 2. Stratification of a mean tropical atmosphere (after Jordan, 1958) where θ_e is the equivalent potential temperature, θ_e^* is the saturation equivalent potential temperature, and θ is the potential temperature.

typically cannot reach a layer of free convection and become unstable. Convergence above the boundary layer may force ascent of such parcels, but the net result tends to be stable heating and not the release of cumulus instabilities. Thus, most cumulus clouds should arise from the boundary layer where conditionally unstable air is available.

Release of boundary layer conditional instability requires initial boundary layer vertical motion to force parcels to their levels of free convection. Such vertical motion is generated by boundary layer convergence, which may be separated into frictional and non-frictional parts. For tropical disturbances the ratio of frictional to non-frictional boundary layer convergence varies from about .4 to .7 according to recent estimates by Gray and McBride (1976). By inference then, frictional boundary layer convergence drives about 40-70% of the boundary layer vertical motion that in turn releases the boundary layer instabilities that are the major factor in cumulus production. The magnitude of this frictional boundary layer convergence or CISK effect suggests that this mechanism is not minor, as Gray suggested earlier. On the contrary, the CISK effect probably holds a key role in tropical cyclone genesis and intensification.

Additional observational evidence exists to link boundary layer convergence with cumulus clouds in weak tropical disturbances. The composite easterly wave of Reed, et al.

(1977) indicates a much closer correlation between convective cloudiness and surface convergence than between the same cloudiness and convergence at the higher levels of 850 and 700 mb. Frank (1978) also found a close connection between low-level convergence and convection in the 1974 GATE data. In a special Florida observational study, Ulanski and Garstang (1978) found excellent correlation between surface convergence and convective rainfall. This study, conducted on a relatively fine observational grid, dealt primarily with very weak disturbances, and so the results definitely support the applicability of a CISK type mechanism even for weak convection.

Not all studies have shown a neat relationship between convective clouds and boundary layer convergence. As stated before, Cho and Ogura (1974) showed a connection between deep cumulus convection and synoptic boundary layer convergence, but they were unable to find any clear connection between the same convergence and the total cumulus mass flux.

Although occasionally questioned, the CISK concept is supported by extensive evidence as illustrated above. Certainly, the relationship of boundary layer convergence to cumulus is real, and the frictional part of this convergence appears to be significant. These and other factors discussed previously support the cumulus parameterization scheme used in this model.

2.4.2 Diagnosis of the Instability Parameter

The formulation of η , the instability parameter in (14), depends upon the behavior of the static energy within cumulus clouds. This static energy, H , is defined as $gZ + CpT + rL$ where g is gravitational acceleration, Z is altitude, Cp is specific heat capacity at constant pressure, T is the temperature, r is the mixing ratio, and L is the latent heat of condensation. Like the equivalent potential temperature, the static energy has a mid-tropospheric minimum in the tropics and is roughly conserved in pseudo-adiabatic ascent. Either H or θ_e can be used to represent the gross thermodynamics in cumulus convection, but the static energy is initially chosen here because the relationship for static energy mixing is much simpler than that for θ_e .

To illustrate these mixing properties, we consider two masses of air, m_1 and m_2 , both at the same height or pressure, but each having different temperatures and mixing ratios. When the masses are combined, the average static energy easily reduces to the mass weighted average of the individual static energies:

$$\begin{aligned} \bar{H} &= \frac{gZ(m_1+m_2) + Cp(m_1T_1+m_2T_2) + L(m_1r_1+m_2r_2)}{(m_1+m_2)} & (15) \\ &= \frac{m_1H_1 + m_2H_2}{(m_1+m_2)} \end{aligned}$$

where the overbar signifies an average and the subscripts simply indicate properties relating to air mass 1 or air mass 2. Because the equivalent potential temperature is a nonlinear function, a mass averaged $\bar{\theta}_e$ is not as simple as an \bar{H} :

$$\bar{\theta}_e = \frac{m_1 \theta_1 + m_2 \theta_2}{m_1 + m_2} \exp \frac{L}{C_p \bar{T}_s} \frac{m_1 r_1 + m_2 r_2}{m_1 + m_2} \quad (16)$$

$$\neq \frac{m_1 \theta_{e,1} + m_2 \theta_{e,2}}{(m_1 + m_2)}$$

where the subscripts 1 and 2 again designate air mass 1 and air mass 2 and where \bar{T}_s is the temperature at which the mixed parcel reaches saturation.

Mixing plays an important role in cumulus convection. In a typical convective cloud, unstable boundary layer air does not remain undiluted as it rises. On the contrary, it normally mixes with some of the mid-tropospheric air entrained by the cloud, and the parcels reaching the upper troposphere have average properties reflecting this mixing. In the cumulus parameterization of this model, (14) implies that for every unit mass of boundary layer air rising in a cumulus cloud, $(\eta - 1)$ units of mass of mid-tropospheric layer air are entrained, resulting in a total of (η) units of mass of mixed, saturated air entering the upper tropospheric layer 2. With the simple averaging properties of H , this process can be represented as

$$\begin{aligned}\bar{H} &= \frac{(1)H_0 + (\eta-1)H_1}{(\eta-1) + (1)} \\ &= \frac{H_0 + (\eta-1)H_1}{\eta}\end{aligned}\tag{17}$$

where \bar{H} is the average static energy value of the cumulus air entering the upper layer, and H_0 and H_1 are the representative static energies of the boundary and mid-tropospheric layers.

In parcel theory, a buoyant mass of air will rise as long as its H (or θ_e) of the environment. In the current cumulus scheme, this implies that \bar{H} , the static energy of cloud air entering the upper layer, should be equal to the saturated static energy value for the layer 2 environment. Equating this environmental H_2^* to the \bar{H} relationship in (17) gives

$$H_2^* = \frac{H_0 + (\eta-1)H_1}{\eta}\tag{18}$$

Rearrangement then leads to an equation for the instability parameter:

$$\eta = 1 + \frac{H_0 - H_2^*}{H_2^* - H_1}\tag{19}$$

Although the use of static energy in deriving (19) was advantageous, further development of η is more convenient in terms of equivalent potential temperature. Conversion of (19) to θ_e draws upon the observations that (19) is in terms of H differences and that the following approximate differ-

ential relation holds between θ_e and H:

$$dH = \left(\frac{C_p T}{\theta_e}\right) d\theta_e \quad (20)$$

Use of the finite difference form of (20) in (19) gives:

$$\eta = \frac{\bar{T}_{0,2}}{\bar{\theta}_{e,0,2}} \frac{\bar{\theta}_{e,2,1}}{\bar{T}_{2,1}} \frac{\theta_{e,0} - \theta_{e,2}^*}{\theta_{e,2}^* - \theta_{e,1}^*} + 1 \quad (21)$$

where $\bar{T}_{0,2}$ is an average temperature between the boundary layer (950 mb) and layer 2 (300 mb), $\bar{T}_{2,1}$ is an average temperature between layer 2 (300 mb) and layer 1 (700 mb), $\bar{\theta}_{e,2,1}$ is an average equivalent potential temperature between layer 2 and layer 1, and $\bar{\theta}_{e,0,2}$ is an average equivalent potential temperature between layer 2 and layer 0. On the right side of (21), the first set of brackets encloses a quantity that is approximately equal to 1 in Jordan's (1958) mean tropical atmosphere. This quantity is relatively constant because a slight variation in the numerator implies a similar variation in the denominator in the same direction. Following Ooyama (1969), we neglect this variation and set the magnitude to a constant 1, thus yielding the following from (21):

$$\eta = 1 + \frac{\theta_{e,0} - \theta_{e,2}}{\theta_{e,2}^* - \theta_{e,1}^*} \quad (22)$$

In order to reduce the use of subscripts and to aid later calculations, a new set of variables are introduced into (22) to give:

$$\eta = 1 + \frac{\chi_0 - \chi_2}{\chi_2 - \chi_1} \quad (23)$$

where χ_0 , χ_1 , and χ_2 are defined to be $(\theta_{e,0} - \Delta)$, $(\theta_{e,1} - \Delta)$, and $(\theta_{e,2}^* - \Delta)$, respectively. The factor Δ is an arbitrary constant that will be chosen later to facilitate the derivation of χ_2 in section 2.4.2.2.

2.4.2.1 Mid-tropospheric Equivalent Potential Temperature

For simplicity, horizontal and temporal variations in (χ_1) , are neglected as in Ooyama (1969). Ooyama argued that this approximation was not a serious detriment, and his successful symmetric model¹ integrations tend to confirm his reasoning. As in Ooyama's symmetric model, the value of χ_1 , was set to a constant -10 K, which is equivalent to a constant $\theta_{e,1}$ of 330 K.

2.4.2.2 Upper Tropospheric Equivalent Potential Temperature

The variable χ_2 represents an upper level saturated equivalent potential temperature deviation in the present model. However, because this model uses incompressible fluid layers, the calculation of χ_2 depends upon the development of an analog from a similar compressible system.

In a compressible fluid, the hydrostatic equation, in conjunction with potential temperature, yields the following:

¹Using Ooyama's 1969 article, I have independently programmed the symmetric model and run baseline versions that confirm Ooyama's results.

$$\frac{\partial (gZ)}{\partial \pi} = -C_p \theta \quad (24)$$

where θ is potential temperature, Z is altitude, and π is defined as $(p/1000)^{R/C_p}$ with p as pressure in mb, R as the gas constant for dry air, and C_p as the specific heat at constant pressure. Equation (24) can be further separated into a horizontal mean and perturbation with the result:

$$\frac{\partial g\bar{Z}}{\partial \pi} = -C_p \bar{\theta} \quad (25a)$$

$$\frac{\partial \phi'}{\partial \pi} = -C_p \theta' \quad (25b)$$

where $\phi' = (gZ - g\bar{Z})$, $\theta' = (\theta - \bar{\theta})$, and the overbar designates horizontal averaging. Conversion of (25b) to finite difference form gives:

$$\frac{\phi'_2 - \phi'_1}{(\pi_1 - \pi_2)} = C_p \theta'_m \quad (26)$$

where the subscripts 1 and 2 represent levels 1 and 2, respectively and where the m subscript stands for a vertical averaging between layers 1 and 2.

Ooyama (1969) noted that in a tropical cyclone, a typical range of variation of $\theta_{e,2}^*$ is from 340 to 370 K while θ_m varies approximately from 324 to 339 K. Assuming simple linear interpolation, we can reform the $\theta_{e,2}^* - \theta_m$ relationship into:

$$(\theta_{e,2}^* - 340) = 2(\theta_m - 324) \quad (27)$$

The variable χ_2 was earlier defined as a $\theta_{\rho,2}^*$ deviation from an arbitrary constant Δ ; and letting $\Delta = 340$ in (27) gives:

$$\chi_2 = 2(\theta_m - 324) \quad (28)$$

If we assume pressures of 700 mb and 300 mb for levels 1 and 2, respectively, then data from Jordan (1958) gives a mean annual $\bar{\theta}_m$ of about 324 K. This result, in conjunction with the previously defined θ_m^1 and (28), yields:

$$\frac{\chi_2}{2} = \theta_m^1 \quad (29)$$

This simple relationship is substituted back into (26), and rearrangement presents:

$$\chi_2 = \frac{2}{C_p(\pi_1 - \pi_2)} (\phi_2^1 - \phi_1^1)$$

The further use of 700 mb and 300 mb to represent levels 1 and 2 allows π_1 and π_2 to be calculated, and (30) becomes:

$$\chi_2 = \frac{10.3}{C_p} (\phi_2^1 - \phi_1^1) \quad (31)$$

Equation (31) is a crude link between the thermodynamic parameter χ_2 and the geopotential deviation. It is, strictly speaking, only valid for a compressible atmosphere. However, the similar dynamical role of geopotential deviation in both compressible and incompressible atmospheres will allow definition of a (31) analog for use in the current incompressible model.

This dynamical similarity can be seen by looking at the pressure gradient terms in the current incompressible model and in an analogous compressible model in isobaric coordinates. In both models, the horizontal pressure gradient term can be replaced by the horizontal gradient of geopotential deviations. In the compressible case, the applicable geopotential deviations are;

$$\phi'_1 = g(Z_1 - \bar{Z}_1) \quad (32a)$$

$$\phi'_2 = g(Z_2 - \bar{Z}_2) \quad (32b)$$

where ϕ'_1 and ϕ'_2 are geopotential deviations for levels 1 and 2, respectively, Z_1 and Z_2 are the actual heights of the level 1 and 2 pressure surfaces, and \bar{Z}_1 and \bar{Z}_2 are the mean heights of the level 1 and 2 pressure surfaces. For the incompressible case, the geopotential deviations are:

$$\phi'_1 = g[(h_1 - \bar{h}_1) + \epsilon(h_2 - \bar{h}_2)] \quad (33a)$$

$$\phi'_2 = g[(h_1 - \bar{h}_1) + (h_2 - \bar{h}_2)] \quad (33b)$$

where ϕ'_1 and ϕ'_2 are geopotential deviations for layers 1 and 2, h_1 and h_2 are actual layer 1 and layer 2 thicknesses, \bar{h}_1 and \bar{h}_2 are mean layer thicknesses, and ϵ is the ratio of layer 2 to layer 1 density.

This dynamical similarity suggests that we may calculate a χ_2 for the incompressible model by replacing the compressible geopotential deviations in (31) with the analogous

geopotential deviations from the incompressible model. Thus, by substituting (33a) and (33b) into (31), (34) yields χ_2 in terms of incompressible model variables:

$$\chi_2 = \frac{1.03}{C_p} h_2 \quad (34)$$

where h_2 is the layer 2 thickness. In (34), the representative pressures for incompressible layers 1 and 2 are implicitly assumed to be 700 and 300 mb because of the calculation of $(\pi_1 - \pi_2)$ for (31). The factor 1.03 arises from the product of the number 10.3 from (31) and the factor $(1 - \epsilon)$, which resulted from the substitution for $(\phi_2' - \phi_1')$. χ_2 exhibits much the same behavior from parameterized cumulus convection in either a compressible model or the current incompressible one. In a compressible model, cumulus direct or indirect heating tends to warm the upper troposphere resulting in an increase in χ_2 and an accompanying increase in the thickness of the upper tropospheric layers. Likewise, in the incompressible model, the effect of cumulus convection--as reflected in the Q term of (6)--increases the thickness of h_2 and consequently increases the value of χ_2 as diagnosed from (34). This similarity in behavior of the compressible and incompressible cases suggests that the use of (34) to diagnose χ_2 is reasonable--especially when viewed against the overall sophistication of the entire model.

2.4.2.3 Boundary Layer Equivalent Potential Temperature

The only heat-related prognostic variable in this model is χ_0 , the boundary layer equivalent potential temperature deviations. The tendency equation for χ_0 basically follows the treatment by Ooyama (1969) and includes horizontal advection (A), one-side vertical advection (B), horizontal diffusion (C), and sea-air transfer (D):

$$\begin{aligned} \frac{\partial \chi_0}{\partial t} = & \quad (A) \quad \quad \quad (B) \\ & -m(u_0 \frac{\partial \chi_0}{\partial x} + v_0 \frac{\partial \chi_0}{\partial y}) - w \frac{-(\chi_1 - \chi_0)}{h_0} \\ & \quad \quad \quad (C) \quad \quad \quad (D) \\ & + \lambda_1 m^2 \nabla^2 \chi_0 \quad + \frac{C_E |\bar{v}_0|}{h_0} (\chi_s - \chi_0) \end{aligned} \quad (35)$$

where m is a map factor, the subscripts 0 and 1 indicate boundary layer and layer 1, respectively, h_0 is the constant boundary layer thickness (1 km), λ_1 is the diffusion coefficient for either layer 1 or the boundary layer, C_E is the sea-air exchange coefficient, $|\bar{v}_0|$ is boundary layer speed, χ_s is a sea-surface saturation-equivalent-potential-temperature deviation, and w^- is defined as $(|w| - w)/2$ so as to allow import of layer 1 air to affect the boundary layer χ_0 . The use of w^- rather than w is questionable, but w^- was retained in order to conform to Ooyama's (1969) treatment of that term.

In (35) we used χ_s , the saturation-equivalent-potential-temperature deviation at the sea surface. In consonance with past definitions, χ_s is taken as $(\theta_{es}^* - \Delta)$ where θ_{es}^* is the saturation-equivalent-potential temperature at the sea surface and Δ is the same constant used in the development of χ_0 , χ_1 , and χ_2 in (23). The value of Δ , as chosen earlier, is 340 K.

χ_s is typically a function of both sea surface temperature and surface pressure. In this model, as in Ooyama (1969), the sea surface temperature is preset and temporally constant, thus allowing the effect of different sea surface temperatures to be implicit in the initial setting of χ_s . Surface pressure, on the other hand, changes throughout the forecast period of the model and plays an explicit role in the diagnostic calculation of χ_s .

The derivation of a simple diagnostic equation for χ_s begins with the saturated-equivalent-potential temperature, θ_e^* :

$$\theta_e^* = \theta \exp \left[\frac{Lq_s}{CpT} \right] \quad (36)$$

where θ is the potential temperature, θ_e^* is the saturation-equivalent-potential temperature, L is the latent heat of condensation, q_s is the saturation mixing ratio, C_p is the specific heat at constant pressure, and T is the temperature. Taking the logarithm of each side and differentiating partially with respect to pressure yields:

$$\frac{\partial \theta_e^*}{\partial p} = \frac{-\theta_e^*}{C_p} \left[-\frac{R}{C_p} - \frac{Lq_s}{T} \frac{1}{(p-e_s)} \right] \quad (37)$$

where p is pressure, R is the gas constant for dry air, and e_s is the saturation vapor pressure. In order to reduce (37) to a simple form, we assume mean values of $p = 1015$ mb and $T = 28^\circ\text{C}$ for the right hand side of (37). These values, in conjunction with an expression for e_s from Iribane and Godson (1973) and the definition of mixing ratio from Hess (1959), allow (37) to be reduced to:

$$\frac{\partial \theta_{es}^*}{\partial p_s} \approx -\frac{1.80}{C_p} \quad (38)$$

where the subscript s indicates that the calculation applies at the sea surface. In finite difference form, (38) becomes:

$$\theta_{es}^* - \overline{\theta_{es}^*} \approx -\frac{1.80}{C_p}(p_s - \overline{p_s}) \quad (39)$$

where the overbar indicates the value of a variable at a standard surface pressure. In terms of χ_s , (39) transforms to:

$$\chi_s = \overline{\chi_s} - \frac{1.80}{C_p}(p_s - \overline{p_s}) \quad (40)$$

In (40), χ_s directly varies as a function of surface pressure. Integration of the hydrostatic equation yields the surface pressure as a function of the thickness of the model layers:

$$p_s = g\rho(h_0 + h_1 + \epsilon h_2) \quad (41)$$

where ϵ is the density, g is gravitational acceleration, h_1 is the layer 1 thickness, h_2 is layer 2 thickness, h_0 is the constant boundary layer thickness and ϵ is the ratio of layer 2 to layer 1 density (.9). From (41) we can get;

$$(p - \bar{p}_s) = g\rho[(h_1 - \bar{h}_1) + \epsilon(h_2 - \bar{h}_2)] \quad (42)$$

Substituting (42) into (40) and assuming a lower layer density of 1.04 kgm^{-3} gives the final equation for the saturation-equivalent-potential-temperature deviations at the sea surface:

$$\chi_s = \bar{\chi}_s - 1.87 \frac{g}{C_p} [(h_1 - \bar{h}_1) + \epsilon(h_2 - \bar{h}_2)] \quad (43)$$

With (43) χ_s can be diagnosed and then used in (35) for the forecast of χ_0 .

Variations in sea surface temperatures cause changes in $\bar{\chi}_s$ because χ_s is $(\theta_{\rho_s}^* - \Delta)$ and $\bar{\theta}_{\rho_s}^*$ is a function of sea surface temperature at the previously selected standard pressure. Using (36) and the standard pressure of 1015 mb, we can obtain values of $\bar{\theta}_{\rho_s}$ as a function of sea surface temperature. Some of these values, along with the associated $\bar{\chi}_s$ values, are shown in Table 2. In experiments with this hurricane model, $\bar{\chi}_s$ is typically set to some constant value, and this value may be roughly correlated to the sea surface temperature via Table 2. Varying the value of $\bar{\chi}_s$, in effect, varies the sea surface temperature that the model sees.

2.5 The Forecast Set

The purpose of the preceding pages was to develop the equations and variables necessary for a model solution. Table 3 recapitulates the 14 variables and equations that form the basis for the integration of this hurricane model. This set of equations cannot be solved analytically, and the numerical methods of solutions will be detailed in the next chapter. However, Fig. 3 is a rough, overall flow-chart that shows one manner of using the equations to integrate the model forward in time. With the model developed in this chapter and the numerical techniques of the next chapter, we will be equipped to explore some of the questions addressed in Chapter I.

TABLE 2

$\bar{\chi}_s$ AND $\bar{\theta}_{es}^*$ AS A FUNCTION OF THE
SEA SURFACE TEMPERATURE T_s

T_s °C	$\bar{\theta}_{es}^*$ K	$\bar{\chi}_s$ K
22	338.7	-1.3
23	342.7	2.7
24	347.0	7.0
25	351.6	11.6
26	356.3	16.3
27	361.3	21.3
28	366.6	26.6
29	372.2	32.2
30	378.1	38.1
31	384.3	44.3

TABLE 3

SYNOPSIS OF MODEL PROGNOSTIC AND DIAGNOSTIC
VARIABLES AND EQUATIONS

Name	Type of Variable			
	Symbol	Diag- nostic	Prog- nostic	Calculated atom equation(s) number(s)
boundary layer vertical velocity	w	x		(2)
cumulus mass transfer factor	Q+	x		(14)
instability parameter	η	x		(23)
upper-level (2) saturated equivalent-potential-temperature derivation	χ_2	x		(34)
sea surface saturated-equivalent potential temperature deviation	χ_s	x		(43)
lower layer (1) thickness	h_1		x	(5)
upper layer (2) thickness	h_2		x	(6)
u component boundary layer (0) velocity	u_0		x	(7), (9a), (10a)
u component lower layer (1) velocity	u_1		x	(7), (9b), (11a)
u component upper layer (2) velocity	u_2		x	(7), (9c), (11c)

TABLE 3--Continued

Name	Type of Variable			
	Symbol	Diag- nostic	Prog- nostic	Calculated from equa- tion(s) number(s)
v component boundary layer (0) velocity	v_0		x	(8), (9a), (10b)
v component lower layer (1) velocity	v_1		x	(8), (9), (11b)
v component upper layer (2) velocity	v_2		x	(8), (9c), (11d)
boundary layer (0) equivalent-potential temperature deviation	χ_0		x	(35)

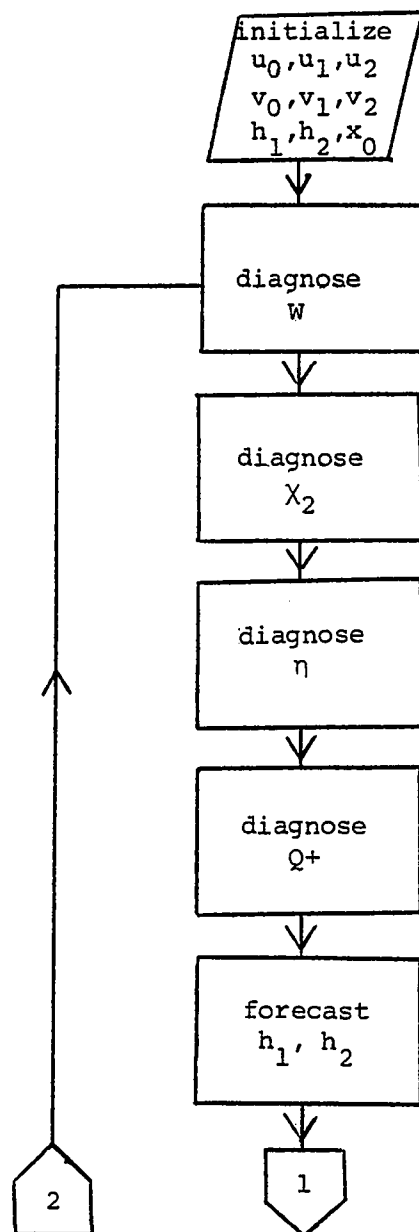


Fig. 3. General flowchart for hurricane model integration. Diagnostic steps designated as time level t , prognostic steps as $t + \Delta t$, where Δt is the time step interval.

(continued)

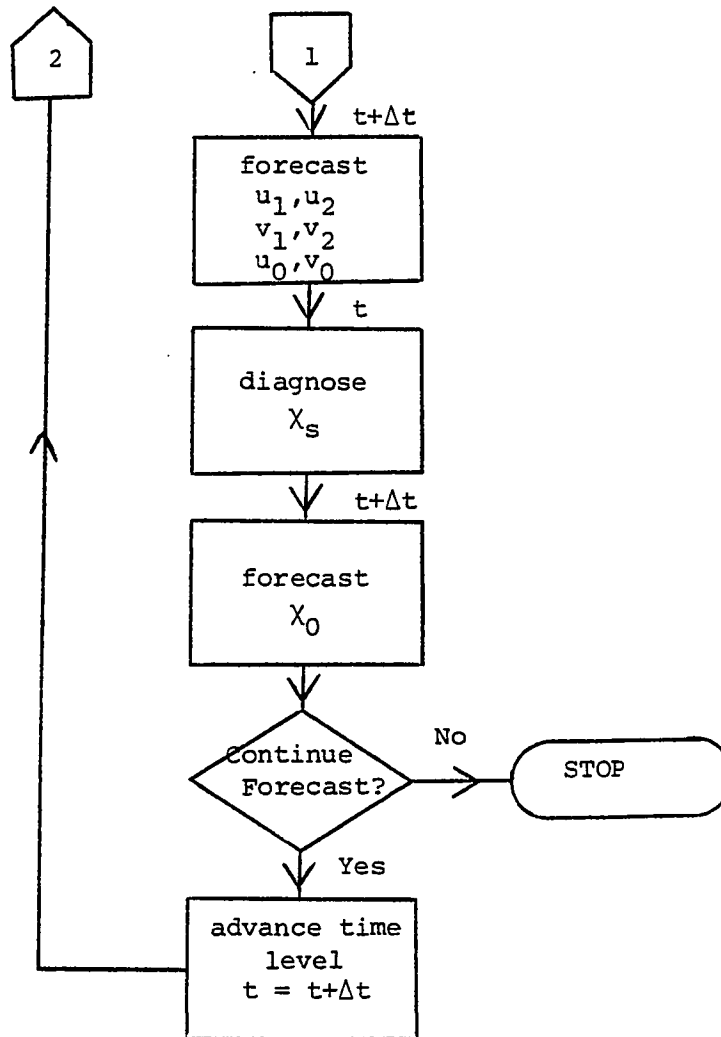


Fig. 3. General flowchart for hurricane model integration. Diagnostic steps designated as time level t , prognostic steps as $t + \Delta t$ where Δt is the time step interval.

CHAPTER III

NUMERICAL METHODS

The hurricane model of the previous chapter can only be integrated with the use of numerical methods and a computer. Selection of the numerical method of solution hinges upon several important factors: (1) accuracy of the solution, (2) available computer facilities, (3) ease in programming the method and insuring an error-free program (i.e., simplicity), and (4) the cost of computing the solution. Ideally, only the first factor should be important, but limited resources and time often make the other factors of equal significance. Unfortunately, these four factors are often contradictory. For example, solution accuracy typically requires very high numerical resolution (e.g., small grid size), but such high resolution increases the computer execution time and consequently the cost to integrate the model. Conflicts such as this are common among the selection criteria, and final numerical method selection depends upon a careful balance of competing factors.

The first major choice in developing the numerical model was to decide the type of spatial representation; finite difference, spectral, or finite element. Finite difference techniques have been used and studied for many years, but the newer spectral and finite element methods appeared to offer some advantages: the spectral method has higher

accuracy and the finite element method is readily adaptable to almost any geometric domain or boundary condition. On the other hand, the very newness of these methods argued against their use because their properties and eccentricities, when used in atmospheric models, have not been as fully documented as those of the finite difference technique. Because investigating the numerical technique itself was not the major research goal, finite differences were selected as the representation least likely to develop major numerical surprises.

A second major choice was the type of time integration scheme. An explicit time scheme is generally easy to program on the computer, but the explicit schemes only allow relatively small time steps and hence require a relatively large amount of computer time. The extra complexity in programming a semi-implicit time scheme was outweighed by such a scheme's ability to allow much larger time steps than explicit methods. Thus, the semi-implicit technique was chosen to fulfill the requirement for a time integration method.

3.1 Forecast Model Numerical Methods

Gerrity and McPherson (1971) combined several numerical techniques to solve a hemispheric primitive equation, barotropic model. Their numerical methods were based on a semi-implicit time scheme in combination with finite differences on space-time staggered grids. A time filter on the

advection terms was also included to control non-linear instability. Although simple, the time filter appeared to be sufficient to allow integrations of several days length. In addition, their methods were readily adaptable to the current model. Thus, their techniques were chosen as the basis for the numerical solution of the current model.

The Gerrity and McPherson finite difference system uses a grid system staggered in space. All variables do not appear at each grid point at a given time step but are staggered in space in order to minimize the number of required points while still retaining most of the accuracy inherent in carrying every variable at each grid point.

Other studies have affirmed the excellent numerical characteristics of this staggered grid system. Mesinger and Arakawa (1976) reported that this particular spatial grid gave more accurate inertia-gravity wave phase speeds than others studied and that it ". . . is the best lattice to simulate the geostrophic adjustment process." In addition, McGregor and Leslie (1977) showed that this spatial configuration helped to prevent spatial solution separation in semi-implicit time differenced models.

The variables are staggered not only in space but also in time. An even time step spatial grid contains variables at different points than the odd time step spatial grid. Without such time staggering, additional spatial averaging

would be required in developing the semi-implicit finite-difference equations.

Figures 4 and 5 illustrate both the time and space staggering of variables: Figure 4 for fixed boundary conditions and Figure 5 for cyclic boundary conditions. The physical grid space in the figures is the same for all variables at a given time step. For example, the physical grid coordinates of a geopotential (ϕ) variable carried on the physical grid could never be the same as the coordinates of a horizontal wind component (u or v) variable carried on the same time level physical grid. For computational purposes, however, each variable can be considered to be on a separate computational grid where all grid points not containing that particular variable have been eliminated and the grid renumbered. For example, on such computational grids, both a $u_{2,2}$, a $v_{2,2}$, and a $\phi_{2,2}$ exist, but they do not represent the same physical point. On the physical grid of Figure 4a, these variables in fact, would exist at the quite disparate physical points of (4,3), (3,4), and (3,3).

At this point it will aid the discussion to define some basic finite difference operators for the staggered grids:

$$F_x \equiv \frac{1}{\Delta x} [F(x + \frac{\Delta x}{2}) - F(x - \frac{\Delta x}{2})], \quad (44)$$

$$\overline{F^x} \equiv \frac{1}{2} [F(x + \frac{\Delta x}{2}) + F(x - \frac{\Delta x}{2})],$$

$$\overline{F^r} \equiv \frac{1}{4} (\overline{F^{nxx}} + \overline{F^{nyy}} + 2 \overline{F^{n-1xy}}),$$

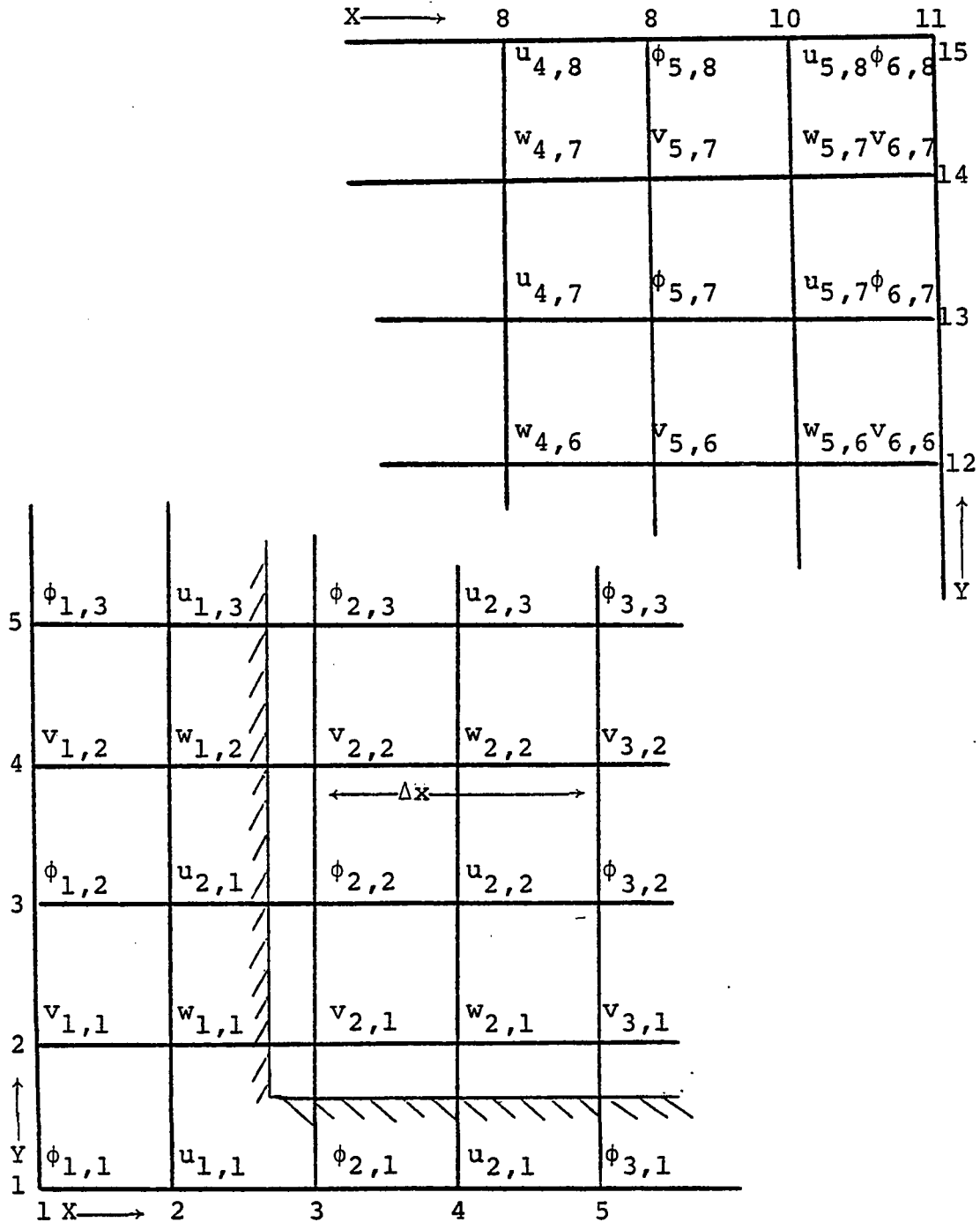


Fig. 4a. Space staggering of gridded variables for even time level and for domain with fixed boundaries. Grids shown are physical space. Subscripts indicate the placement of variables on the computational grid. X and Y along the border delineate physical grid numbering. Both XMAX and YMAX must be odd (e.g., 11, 15). Points outside the hashed region are fixed. Variables $\chi_2, \chi_1, \chi_0, Q, h_1,$ and h_2 are also carried at the ϕ points.

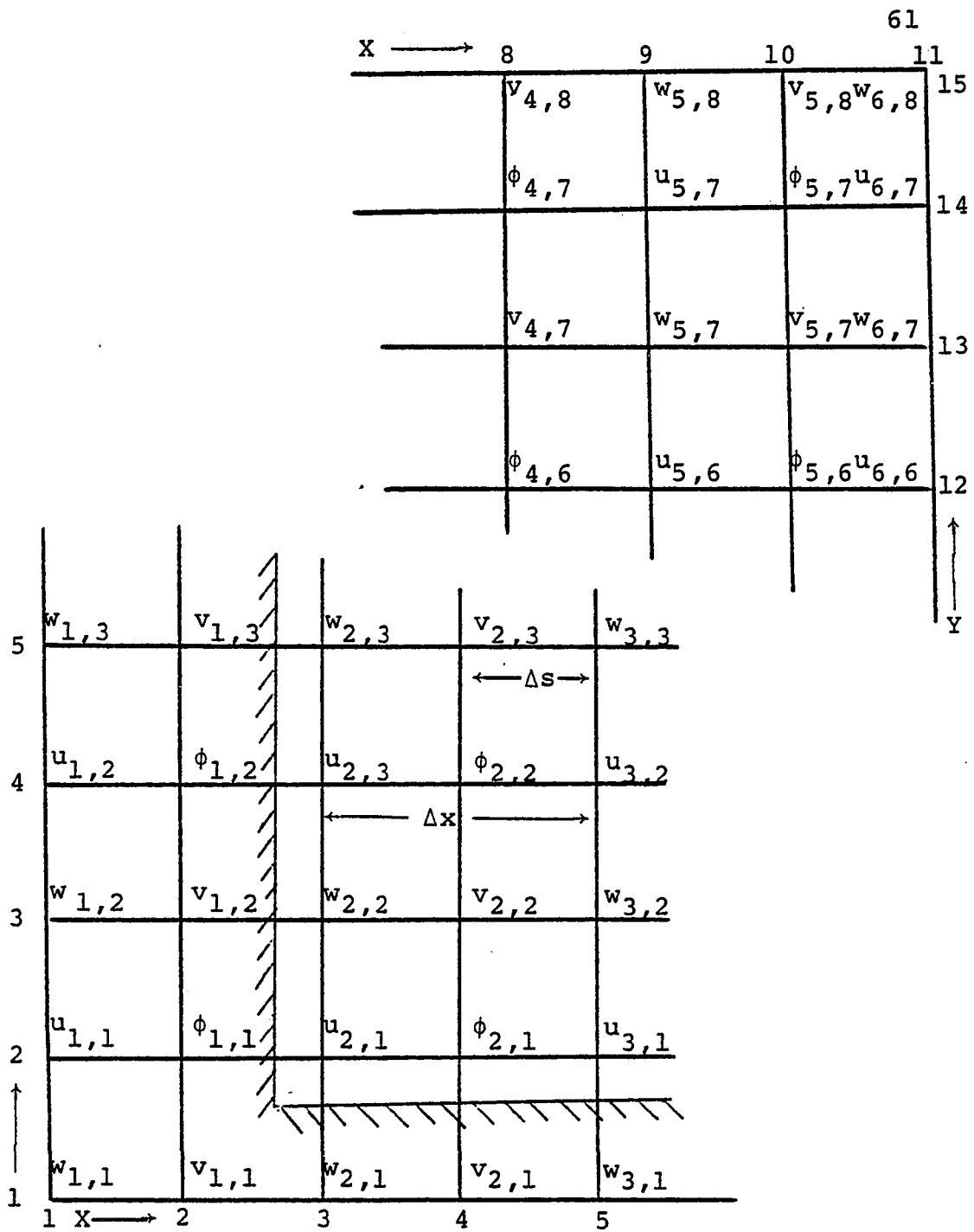


Fig. 4b. Same as 4a but for odd time level.

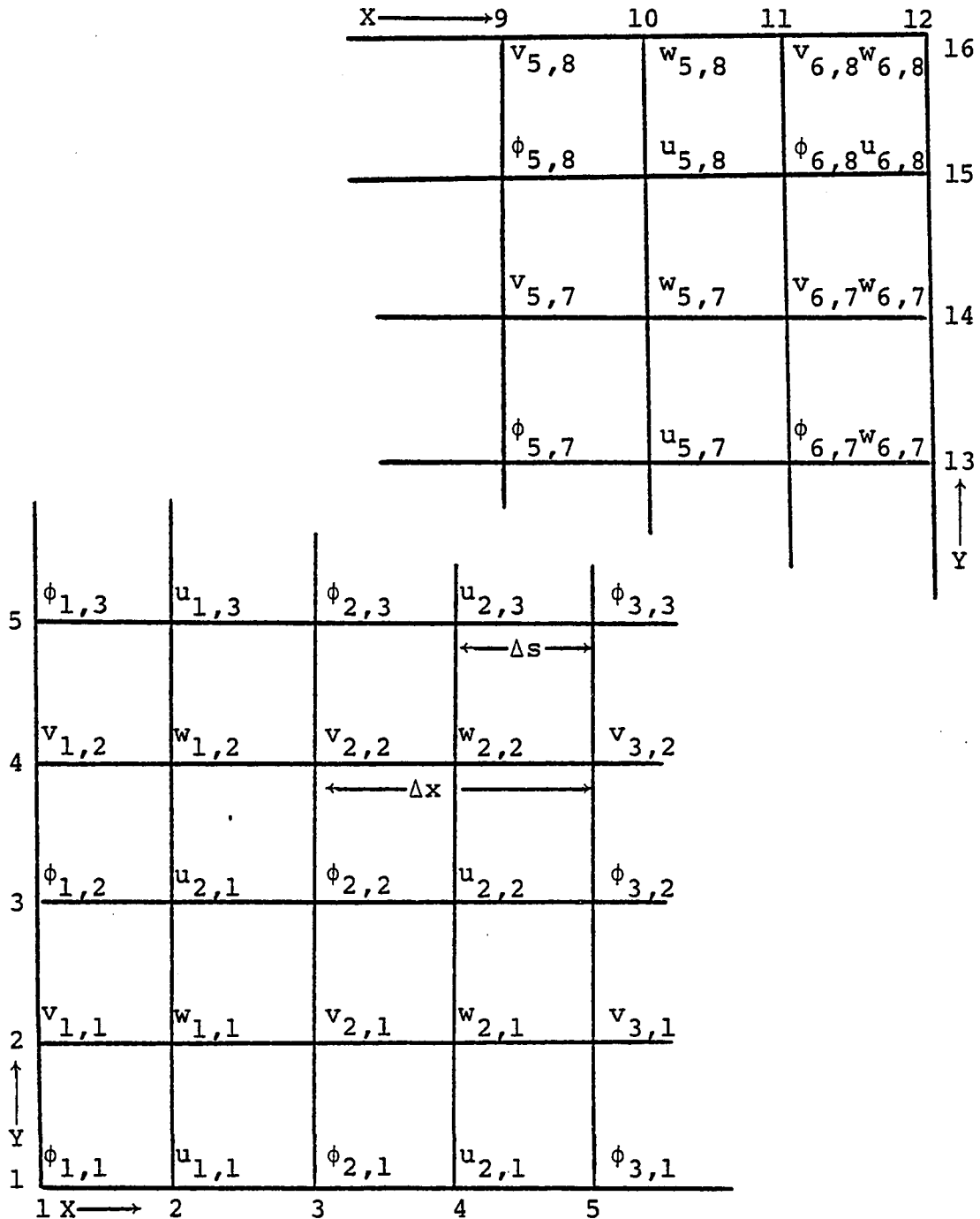


Fig. 5a. Space staggering of gridded variables for even time level and for domain with cyclic boundaries. Grids shown are physical space. Subscripts indicate the placement of variables on the computational grid. X and Y along the border delineate physical grid numbering. Both XMAX and YMAX must be even (e.g., 12,16). Variables $\chi_2, \chi_1, \chi_0, Q, h_1$, and h_2 are carried at ϕ points whereas vorticity, ζ , is carried at w points.

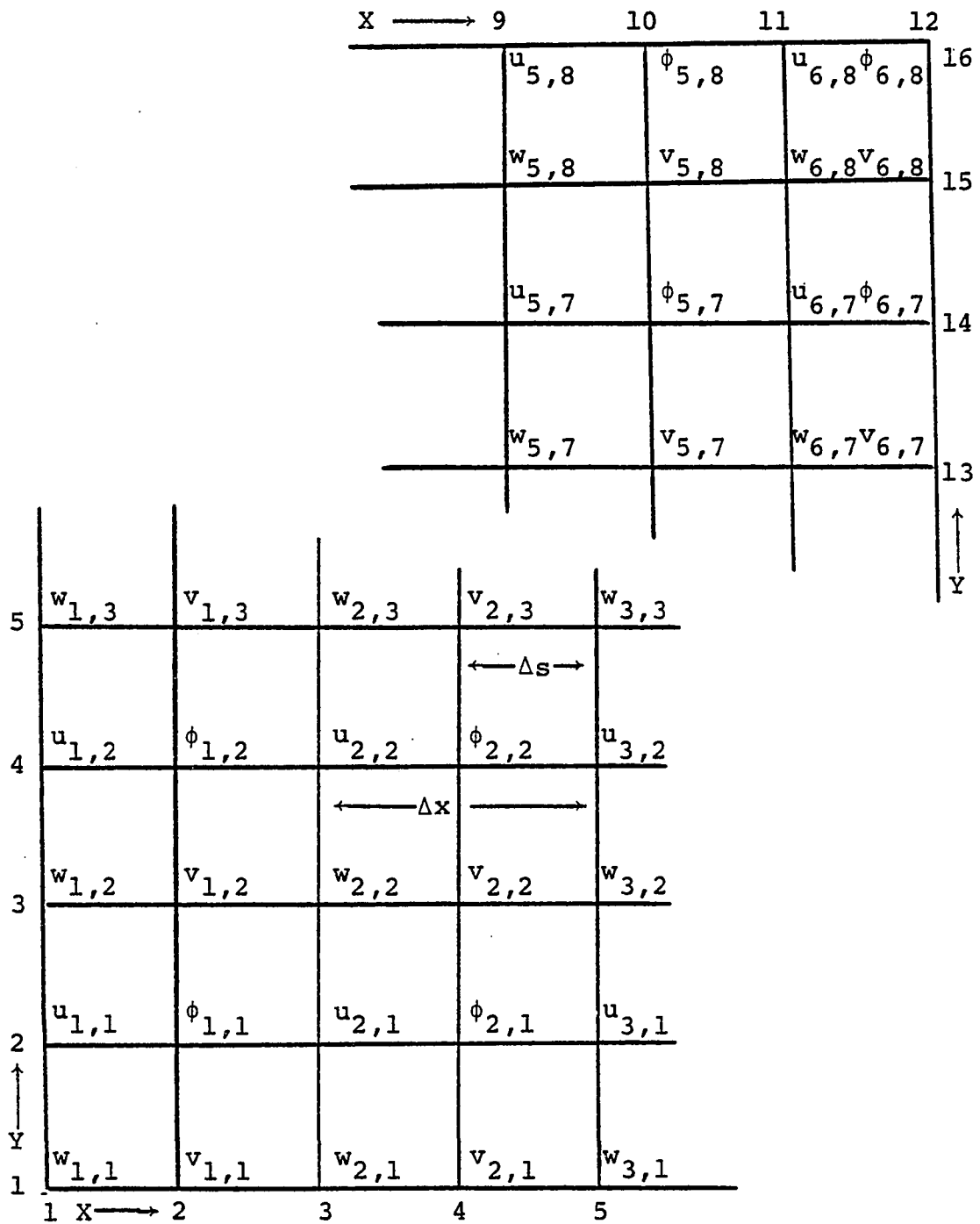


Fig. 5b. Same as 5a but for odd time level.

$$\begin{aligned}\overline{F^S} &\equiv \frac{1}{4} (\overline{F^{n-1xx}} + \overline{F^{n-1yy}} + 2\overline{F^{nxy}}) \\ \hat{F} &\equiv \frac{1}{4} (\overline{F^{ny}} + \overline{F^{n-1x}}), \\ \tilde{F} &\equiv \frac{1}{2} (\overline{F^{n-1y}} + \overline{F^{nx}}),\end{aligned}$$

where $\Delta x/2$ or Δs is the physical grid spacing and $n-1$, n , and $n+1$ stand for past, present, and future time levels, respectively. The operators in (44) are basically defined for the physical grid, but analogous operators would also exist for the computational grids. Using Figures 4 and 5, one can visualize the use of the operators in practice.

3.1.1 Semi-implicit Calculations

Gravity wave phase speed severely limits the time step size in explicit time integrations of primitive equations. The basis for this impact lies in linear stability requirements where the maximum allowable time step is inversely proportional to the maximum speed of waves represented by a given set of explicitly-formulated equations. With the primitive equations, gravity waves have phase speeds on the order of 300 m/sec and are, by far, the fastest waves represented by the equations. Thus, gravity wave phase speed becomes the limiting factor in setting the maximum-allowable, stable time step by linear stability criteria.

In order to increase the maximum-allowable time step, the primitive equations can be integrated with a semi-implicit time scheme. With this technique, the components that control

the motion of the gravity waves are implicitly treated and the rest of the variables are treated explicitly. Such a treatment allows a much greater time step for the primitive equations because the linear stability criterion is then a function of meteorological wave speeds that are much slower than gravity wave speeds. The increase in time step is gained at the expense of some additional complexity in calculation, but this half-implicit, half-explicit formulation still avoids the horrendous practical problems that would be encountered with a totally implicit formulation for all variables.

In the following pages, the model equations of Chapter II are framed for semi-implicit solution on the staggered grids of Figure 4 and Figure 5. Careful attention to these figures will help the reader visualize the rationale behind many of these formulations. In addition, reference to Gerrity and McPherson (1971) may also aid the reader because a much simpler, barotropic model was solved with analogous numerical techniques in that paper.

The first step in the integration process is to calculate the non-linear advective terms from (5), (6), (7), and (8):

$$\frac{u_k^*}{m} = \frac{u_k^{n-1}}{m} + 2\Delta t \left[\frac{\bar{v}_k^r}{m} \bar{u}_k^s \bar{u}_k^m \bar{u}_k^y - \bar{u}_k^s \bar{u}_k^x \bar{u}_k^y \middle|_k - \bar{v}_k^r \bar{u}_k^x \bar{u}_k^y \middle|_k \right] \quad (45)$$

$$\frac{v_k^*}{m} = \frac{v_k^{n-1}}{m} - 2\Delta t \left[\frac{\bar{u}_k^r}{m} \bar{u}_k^s \bar{u}_k^m \bar{u}_k^y + \bar{u}_k^r \bar{v}_k^s \bar{u}_k^x \bar{u}_k^y \middle|_k + \bar{v}_k^s \bar{v}_k^x \bar{u}_k^y \middle|_k \right] \quad (46)$$

and

$$h_k^* = h_k^{n-1-2m\Delta t} (\hat{u}_k \bar{h}_x^y |_{k} + \tilde{v}_k \bar{h}_y^x |_{k}). \quad (47)$$

where the * variables are intermediates, the k subscripts represent vertical level, n-1 represents past time level, and the other super- and subscripts represent the operations previously defined. Note also that terms such as \bar{u}_x^y , etc., are defined for the n or present time level.

In addition to (45)-(47), the rest of the terms in (5)-(8) can be converted to finite differences and the variables at the future or n+1 time level collected on the left:

$$\left(\frac{u_1}{m}\right)^{n+1} + \frac{2\Delta t}{2} g(h_x^{n+1} |_{1} + \varepsilon h_x^{n+1} |_{2}) = U_1 \quad (48)$$

$$\left(\frac{u_2}{m}\right)^{n+1} + \frac{2\Delta t}{2} g(h_x^{n+1} |_{1} + h_x^{n+1} |_{2}) = U_2 \quad (49)$$

$$\left(\frac{v_1}{m}\right)^{n+1} + \frac{2\Delta t}{2} g(h_y^{n+1} |_{1} + \varepsilon h_y^{n+1} |_{2}) = V_1 \quad (50)$$

$$\left(\frac{v_2}{m}\right)^{n+1} + \frac{2\Delta t}{2} g(h_y^{n+1} |_{1} + h_y^{n+1} |_{2}) = V_2 \quad (51)$$

$$h_1^{n+1} + \frac{2\Delta t}{2} m^2 \bar{h}_1^{xy} \left[\left(\frac{u_1}{m}\right)_x^{n+1} + \left(\frac{v_1}{m}\right)_y^{n+1} \right] = H_1 \quad (52)$$

$$h_2^{n+1} + \frac{2\Delta t}{2} m^2 \bar{h}_2^{xy} \left[\left(\frac{u_2}{m}\right)_x^{n+1} + \left(\frac{v_2}{m}\right)_y^{n+1} \right] = H_2, \quad (53)$$

where

$$\begin{aligned}
U_1 \equiv & \frac{u_1^*}{m} + 2\Delta t \left(\frac{v_1}{m} \right) f - \frac{2\Delta t}{2} g (h_x^{n-1} |_1 + \epsilon h_x^{n-1} |_2) \\
& + 2\Delta t \{ \lambda_1 m (u_{xx}^{n-1} |_1 + u_{yy}^{n-1} |_1) - \frac{1}{m\bar{h}_1} \bar{Q}^x u_1^{n-1} \\
& - \frac{\mu}{m\bar{h}_1} (u_1^{n-1} - u_2^{n-1}) \} \tag{54}
\end{aligned}$$

$$\begin{aligned}
U_2 \equiv & \frac{u_2^*}{m} + 2\Delta t \left(\frac{v_2}{m} \right) f - \frac{2\Delta t}{2} g (h_x^{n-1} |_1 + h_x^{n-1} |_2) \\
& + 2\Delta t \{ \lambda_2 m (u_{xx}^{n-1} |_2 + u_{yy}^{n-1} |_2) + \frac{1}{m\epsilon\bar{h}_2} u_1^{n-1} \bar{Q}^x \\
& + \frac{\mu (u_1^{n-1} - u_2^{n-1})}{m\epsilon\bar{h}_2} \} \tag{55}
\end{aligned}$$

$$\begin{aligned}
V_1 \equiv & \frac{v_1^*}{m} - 2\Delta t \left(\frac{u_1}{m} \right) f - \frac{2\Delta t}{2} g (h_y^{n-1} |_1 + \epsilon h_y^{n-1} |_2) \\
& + 2\Delta t \{ \lambda_1 m (v_{yy}^{n-1} |_1 + v_{xx}^{n-1} |_1) - \frac{1}{m\bar{h}_1} v_1^{n-1} \bar{Q}^y \\
& - \frac{\mu}{m\bar{h}_1} (v_1^{n-1} - v_2^{n-1}) \} \tag{56}
\end{aligned}$$

$$\begin{aligned}
V_2 \equiv & \frac{v_2^*}{m} - 2\Delta t \left(\frac{u_2}{m} \right) f - \frac{2\Delta t}{2} g (h_y^{n-1} |_1 + h_y^{n-1} |_2) \\
& + 2\Delta t \{ \lambda_2 m (v_{xx}^{n-1} |_2 + v_{yy}^{n-1} |_2) + \frac{1}{m\epsilon\bar{h}_2} v_1^{n-1} \bar{Q}^y \\
& + \frac{\mu}{\epsilon\bar{h}_2} (v_1^{n-1} - v_2^{n-1}) \} \tag{57}
\end{aligned}$$

$$\begin{aligned}
H_1 \equiv h_1^* - m \frac{2\Delta t}{2} \overline{h_1^{nxy}} \left[\left(\frac{u_1}{m}\right)_x^{n-1} + \left(\frac{v_1}{m}\right)_y^{n-1} \right] \\
+ 2\Delta t(w-Q), \tag{58}
\end{aligned}$$

$$\begin{aligned}
H_2 \equiv h_2^* - m \frac{2\Delta t}{2} \overline{h_2^{nxy}} \left[\left(\frac{u_2}{m}\right)_x^{n-1} + \left(\frac{v_2}{m}\right)_y^{n-1} \right] \\
+ \frac{2\Delta t}{\epsilon} Q, \tag{59}
\end{aligned}$$

The boundary layer vertical velocity and cumulus term are formulated from (2) and (14), respectively:¹

$$w = -h_0 \left[\left(\frac{\overline{u_0}}{m}\right)_x^{xy} + \left(\frac{\overline{v_0}}{m}\right)_y^{xy} \right], \tag{60}$$

$$Q = \begin{cases} \overline{\eta^{xy} w} & w > 0 \\ 0 & w \leq 0 \end{cases} \tag{61}$$

In (52) we can substitute for the divergence at the $n + 1$ time level after having taken the combination $\partial(48)/\partial x + \partial(50)/\partial y$. Similarly, one can also substitute for the divergence in (53) using $\partial(49)/\partial x + \partial(51)/\partial y$. With these substitutions (52) is relabeled (62), and (53) becomes (63.) We further reduce the equations by the subtractions

¹Note that the χ variables and consequently η are carried on the same grid points as h . The averaging here is necessary because η is needed at the η time level but on the h points of the $n-1$ time grid.

[(53) - (52)] and [(52) - ε(53)]. Rearrangement then yields the matrix equation:¹

$$\nabla^2 \begin{pmatrix} h_1^{n+1} \\ h_2^{n+1} \end{pmatrix} - a \begin{pmatrix} +1/h_1^{\overline{nx}} & -\epsilon/h_2^{\overline{ny}} \\ -1/h_1^{\overline{ny}} & +1/h_2^{\overline{nx}} \end{pmatrix} \begin{pmatrix} h_1^{n+1} \\ h_2^{n+1} \end{pmatrix} = \begin{pmatrix} D_1 \\ D_2 \end{pmatrix} \quad (64)$$

where

$$a \equiv 1/[\sigma g(\Delta t m)^2],$$

$$\sigma \equiv 1 - \epsilon,$$

$$D_1 \equiv 1/(\sigma g \Delta t) [U_{1x} + V_{1y} - \epsilon(U_{2x} + V_{2y})] \\ - 1/[\sigma g(\Delta t m)^2] [H_1/h_1^{\overline{nx}} - \epsilon H_2/h_2^{\overline{ny}}]$$

$$D_2 \equiv 1/(\sigma g \Delta t) (U_{2x} + V_{2y} - U_{1x} - V_{1y}) \\ - 1/(\sigma g(\Delta t m)^2) [H_2/h_2^{\overline{nx}} - H_1/h_1^{\overline{ny}}].$$

Because two dimensional Helmholtz equations are easier to solve, (64) is transformed from three to two dimensions before solution. Using the method of Sela and Sconik (1972) and letting h , A , and F stand for the matrices in (64), we can rewrite (64) as:

¹The ∇^2 operator, operating on a function F , is just $F_{xx} + F_{yy}$ in the previously defined notation.

$$\nabla^2 h + Ah = F \quad (65)$$

Premultiplication by the 2x2 inverse matrix p^{-1} and slight rearrangement gives:

$$\nabla^2 p^{-1}h + (p^{-1}Ap)p^{-1}h = p^{-1}F \quad (66)$$

If $p^{-1}Ap$ is diagonal, the system has been separated into two 2D equations:

$$\begin{aligned} \nabla^2 W_1 + \lambda_1 W_1 &= D_1 \\ \nabla^2 W_2 + \lambda_2 W_2 &= D_2 \end{aligned} \quad (67)$$

where λ_1 and λ_2 are the eigenvalues of A,

$$W \equiv \begin{pmatrix} W_1 \\ W_2 \end{pmatrix} = p^{-1}h$$

and

$$D \equiv \begin{pmatrix} D_1 \\ D_2 \end{pmatrix} = p^{-1}F$$

The two-by-two nature of these matrices allows an exact calculation of the eigenvalues λ_1 and λ_2 and construction of P and P^{-1} :

$$P = \begin{pmatrix} 1 & 1 \\ (\lambda_1 - a_{11})/a_{12} & (\lambda_2 - a_{11})/a_{12} \end{pmatrix} \quad (68)$$

$$P^{-1} = \frac{a_{12}}{\lambda_2 - \lambda_1} \begin{pmatrix} (\lambda_2 - a_{11})/a_{12} & -1 \\ (a_{11} - \lambda_1)/a_{12} & 1 \end{pmatrix} \quad (69)$$

where A is represented as

$$A = \begin{pmatrix} a_{11} & a_{12} \\ a_{21} & a_{22} \end{pmatrix}.$$

Thus, (64) is transformed to the two independent equations of (67). These 2D Helmholtz equations in (67) are solved by relaxation, and the W variables are then used in the inverse matrix transformation $h = pW$ to obtain h_1 and h_2 at the $n + 1$ time level.

3.1.1.1 Relaxation and Other Helmholtz Equation Solvers

The Helmholtz equations in (67) were numerically solved by relaxation, primarily because relaxation is a simple method to program. There are several direct methods for solving elliptic equations, and these are generally faster and more accurate than relaxation. However, until recently, all of these faster methods required the elliptic equations to be separable. Because the Helmholtz coefficients of λ_1 and λ_2 are functions of x and y , the equations in (67) are not totally separable; and consequently, the direct equations are not directly applicable to (67). Such techniques could still be used in some kind of iterative scheme, but such use would reduce the direct solver speed and accuracy advantages.

Madala (1978) has reported an elliptic equation solution technique that works on any elliptic equation of the form:

$$\begin{aligned}
 A(x,y) \frac{\partial^2 R}{\partial x^2} + B(x,y) \frac{\partial^2 R}{\partial x \partial y} + C(x,y) \frac{\partial^2 R}{\partial y^2} + D(x,y) \frac{\partial R}{\partial x} \\
 + E(x,y) \frac{\partial R}{\partial y} + G(x,y)R = F(x,y)
 \end{aligned} \tag{70}$$

where R is the unknown function of x and y . This technique, labeled stabilized error vector propagation or SEVP, appears to be at least 10 times faster than overrelaxation and would be a logical successor to the relaxation scheme in any future model versions.

3.1.2 Final Wind Component Prognosis

After solving for h_1 and h_2 at the $n + 1$ time level, we can return to rearranged versions of (48), (49), (50), and compute u_1 , u_2 , v_1 , and v_2 . In addition, u_0 and v_0 can be calculated by:

$$\begin{aligned} \left(\frac{u_0}{m}\right)^{n+1} = & -g\Delta t (h_x^{n+1}|_1 + h_x^{n-1}|_1 + \epsilon h_x^{n+1}|_2 + \epsilon h_2^{n-1}|_2) \\ & + \frac{u_0^*}{m} + 2\Delta t \left(\frac{v_0}{m}\right) f \end{aligned} \quad (71)$$

$$+ \frac{2\Delta t}{m} \{ \lambda_1 m^2 (u_{xx}^{n-1}|_0 + u_{yy}^{n-1}|_0) - \frac{C_D}{D_{10}} |\bar{v}_0| u_0 \} \quad (72)$$

$$\begin{aligned} \left(\frac{v_0}{m}\right)^{n+1} = & -g\Delta t (h_y^{n+1}|_1 + h_y^{n-1}|_1 + \epsilon h_y^{n+1}|_2 + \epsilon h_y^{n-1}|_2) \\ & + \frac{v_0^*}{m} - 2\Delta t \left(\frac{u_0}{m}\right) f \end{aligned} \quad (73)$$

$$+ \frac{2\Delta t}{m} \{ \lambda_1 m^2 (v_{xx}^{n-1}|_0 + v_{yy}^{n-1}|_0) - \frac{C_D}{h_0} |\bar{v}_0| v_0 \}. \quad (74)$$

3.1.3 Boundary Layer Prognosis

The variable χ_0 is forecast by a simple, explicit, finite difference formulation of (35):

$$\begin{aligned}
\chi_0^{n+1} = \chi_0^{n-1} &- 2\Delta t m [\hat{u}_0 \bar{\chi}_x^y |_0 + \tilde{v}_0 \bar{\chi}_y^x |_0 \\
&+ \frac{\bar{w}}{h_0} (\chi_0 - \chi_1) \\
&+ 2\Delta t \{ \lambda_1 m^2 (\chi_{xx}^{n-1} |_0 + \chi_{yy}^{n-1} |_0) \\
&+ \frac{C_E}{h_0} |\bar{v}_0| (\chi_s^{n-1} - \chi_0^{n-1}) \},
\end{aligned} \tag{75}$$

where \bar{w} is defined as in section 2.4.2.3 and where χ_s is calculated from (43).

3.1.4 The Integration Cycle

At the $n + 1$ time level, all of the prognostic variables are now available: $u_0, v_0, u_1, v_1, u_2, v_2, h_1, h_2,$ and χ_0 . From these variables at the $n + 1$ time, one can obtain other needed variables by diagnostic calculations. For example, w is calculated by (60), χ_2 by (34), η by (23), and Q or Q^+ by (61). Such calculations complete a time step cycle: the n time level becomes the $n - 1$ time level, the $n + 1$ level becomes the n , and the $n + 1$ becomes the new future time level. Integration can then proceed again to a new time level $n + 1$ by using the new n and $n - 1$ time level data in the same sequence of calculations outlined earlier in sections 3.1.1 to 3.1.4.

3.1.5 Boundary Treatments

The first versions of the forecast model held forecast variables constant on the boundaries. Fixed boundaries are sometimes not satisfactory because the actual atmosphere is

laterally unbounded and has no real fixed lateral boundaries. The error inherent in these numerically fixed boundary conditions tends to propagate inward from the boundaries, and it eventually destroys the whole forecast. However, if the forecast region is large enough and the forecast period short enough, a fixed boundary model may allow reasonable forecasts in the interior.

Fixed boundaries were used initially in the model for two major reasons. The first and foremost reason was that fixed boundary conditions are simple. The second reason was that a fixed boundary model could be readily modified and adapted to a telescoping grid system if extremely high spatial resolution became necessary.

The fixed boundary version (FDB/B) of the forecast model was used successfully in integrations of an Ooyama (1969) type vortex (appendix C). This particular version used Gerrity and McPherson's (1971) treatment of the points next to the boundary. For the penultimate boundary points, this treatment changed the calculations of u^* , v^* , and h^* from that of (45), (46), and (47) to those below:

$$\left(\frac{u^*}{m}\right) = \left(\frac{\bar{u}_k^n}{m}\right) + \Delta t \left[\frac{\bar{v}_k^r}{m} \bar{u}_k^s \bar{m}_y - \bar{u}_k^s \bar{u}_k^y \Big|_k - \bar{v}_k^r \bar{u}_k^x \Big|_k \right] \quad (76)$$

$$\left(\frac{v^*}{m}\right) = \left(\frac{\bar{v}_k^{nxy}}{m}\right) + \Delta t \left[\frac{\bar{u}_k^r}{m} \bar{u}_k^r \bar{m}_y + \bar{u}_k^r \bar{v}_k^y \Big|_k + \bar{v}_k^s \bar{v}_k^x \Big|_k \right] \quad (77)$$

$$h_k^* = \bar{h}_k^{nxy} - m \Delta t \left(\hat{u}_k^r \bar{h}_k^y \Big|_k + \tilde{v}_k^r \bar{h}_k^x \Big|_k \right). \quad (78)$$

In later fixed boundary experiments (FDB/D model version), the boundary treatment was changed to the method suggested by Chen (1973; also Chen and Miyakoda, 1974). This technique, involving smoothing the penultimate boundary points, damps all waves to some extent, but it most severely damps the shorter wavelengths and completely eliminates the two-grid wave. In this method all interior points, including those next to the boundary, use the same forecast scheme. Following the calculation of a new time level $n + 1$, the points next to the boundary are smoothed in a direction normal to the boundary. For example, near the west boundary, the penultimate smoothing for any forecast variable F would be:

$$F_{2,J}^{n+1}(\text{smoothed}) = \frac{1}{2}F_{2,J}^{n+1} + \frac{1}{4}(F_{1,J} + F_{3,J}) \quad (79)$$

where the subscripts stand for the X and Y positions in the physical grid.

The fixed boundary easterly wave integrations were unsatisfactory. Over a four-day forecast period, the easterly waves jammed into the northern boundary. These boundary effects can be observed in the E2 experiment (Table 4). This experiment was initialized with the easterly wave conditions shown in Figures 6 and 7; and the integration, with all sinks and sources disconnected, proceeded to 96 hours. The impact of the boundary is immediately felt on the westward wave, which has mostly disappeared by the 24 hour forecast time (Fig. 8). Even the eastward wave becomes quickly

TABLE 4
MAJOR FIXED BOUNDARY EXPERIMENTS

Designator	Initial ¹ Model	Initial Conditions		Forecast ¹ Model	Domain Size (km)	Δs (km)	Δt (sec)	Integration Length (hrs)	Coriolis	Filter Parameter
		Level 0,1	Level 2							
V1	IVDB ²	vortex	vortex	FDB/B	3800 x 3800	100	3600	96	f-plane (5x10-5)	0
V2A	IVDB	vortex	vortex	FDB/B	3800 x 3800	100	1800	240	f-plane (5x10-5)	0
V2B	IVDB	vortex	vortex	FDB/B	3800 x 3800	100	3600	240	f-plane (5x10-5)	0
V2C	IVDB	vortex	vortex	FDB/B	3800 x 3800	100	7200	240	f-plane (5x10-5)	0
V3	IVDB	vortex	vortex	FDB/B	3800 x 3800	100	1200	blow-up at 175	f-plane (5x10-5P)	.01
E1	IEDB	700mb GATE	300mb GATE	FDB/D	4835 x 2565	49.33	900	96	eq. B-plane	.01

¹See Table 5 for acronym explanations.

²This initialization model actually assumed no motion in level 2. Barotropic initialization was completed in a special version of the forecast model FDB/B.

TABLE 4--Continued

Designator	Air-Sea ³ Heat Transfer?	CE, transfer Coefficient	Boundary Layer Connected to Upper Level? ⁴	CD, drag Coefficient	μ Vertical Shear Stress Coefficient	λ_1, λ_2 Horizontal Diffusion Coefficients	Cumulus Heating?	Cumulus Momentum Transfer?
V ₁	yes	.0015	yes	.0015	0	0	no	no
V _{2A}	yes	.0015	no	.0015	0	0	no	no
V _{2B}	yes	.0015	no	.0015	0	0	no	no
V _{2C}	yes	.0015	no	.0015	0	0	no	no
V ₃	yes	.0015	yes	.0015	0	0	yes	no
E ₁	yes	.0015	yes	.0015	0	0	yes	no
E ₂	no	0	no	0	0	0	no	no

³ Although the forecast model could handle spatial variations in X_s , a measure of sea surface temperature, the X_s for all experiments in this table was set to uniform constant 30. In addition, X_0 , a measure of boundary layer equivalent-potential temperature, was set to an initially uniform 10.

⁴ A no answer means that layers 1 and 2 are independent of the direct boundary layer effects (w), although positive answers in the cumulus blocks would still imply some indirect connection.

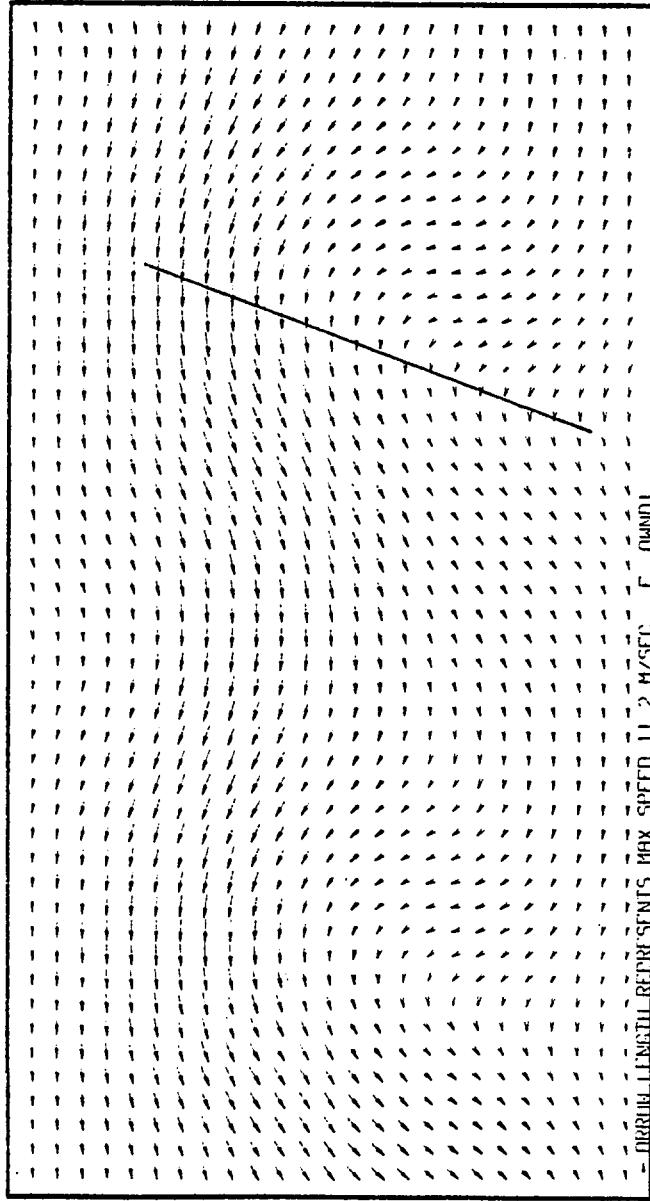


Fig. 6. E1 and E2 experiments. Levels 0 and 1 initial wind field.

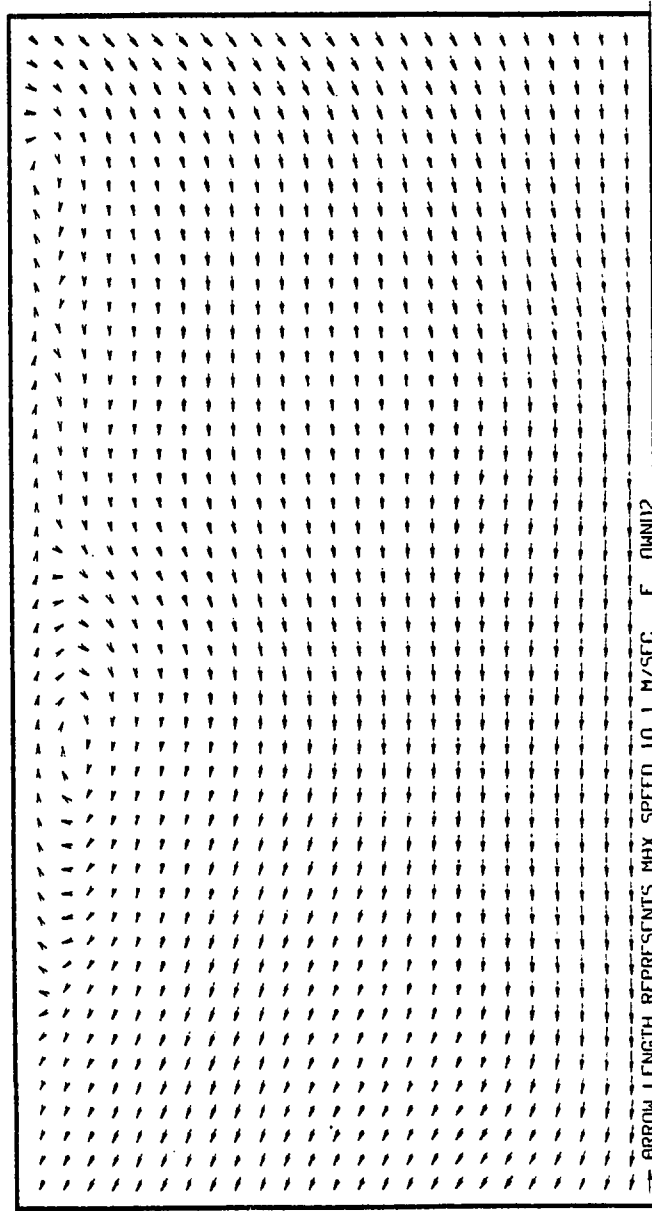


Fig. 7. E1 and E2 experiments. Level 2 initial wind field.

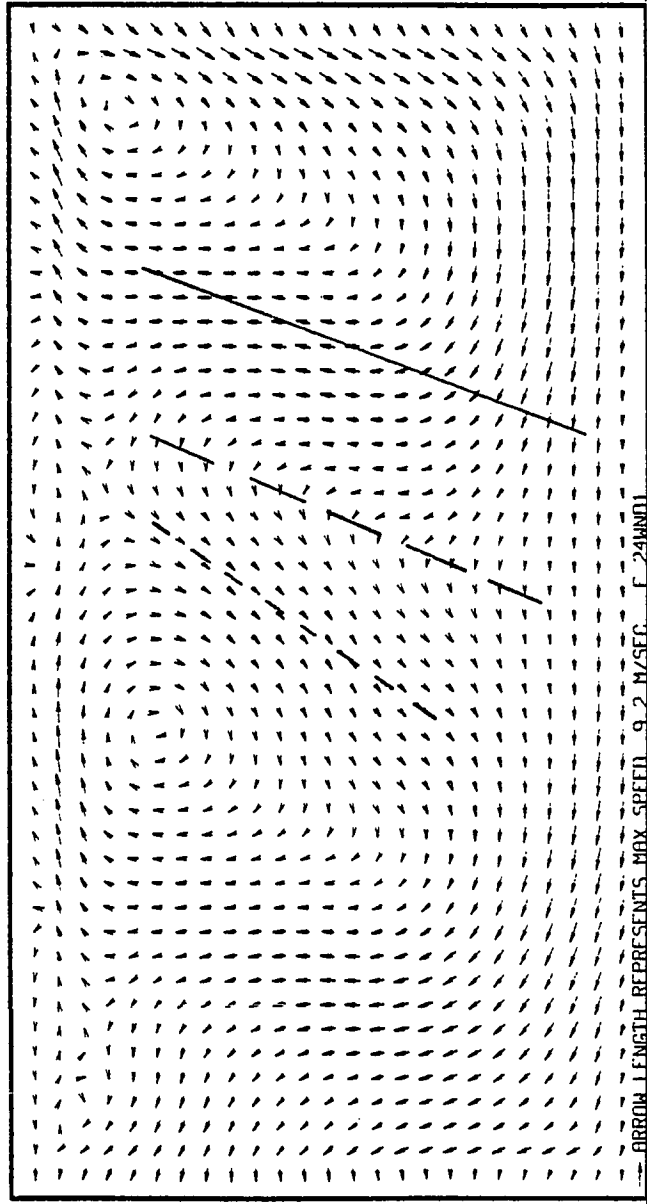


Fig. 8. E2 experiment. Level 0 and 1 wind field at forecast hour 24. Continuous line is initial trough position. Short dashed line is trough position at forecast hour 48.

affected as its average westward propagation speed is cut from over 8 m/sec during the first 24 hours to under 5 m/sec during the second 24 hours. Because of such drastic effects, the fixed boundary conditions were dropped in favor of cyclic boundaries that would not impede the movement of the waves.

The cyclic boundary conditions were incorporated in a new forecast model version FCB (Table 5). This version retained all of the basic physics and numerics of the previous forecast versions except for computations surrounding the boundaries. These changes basically treated any variable F at the edge of the domain in the following manner:

$$\begin{aligned}
 F(IMAX+1,J) &= F(1,J), \\
 F(0,J) &= F(IMAX,J), \\
 F(I,JMAX+1) &= F(I,1), \\
 F(I,0) &= F(I,JMAX),
 \end{aligned}
 \tag{80}$$

Where I and J are grid point counters in either the physical or computational domains of Figures 4 and 5, $IMAX$ is the most eastward longitudinal grid coordinate, and $JMAX$ is the most northern meridional grid coordinate.

Basically, the addition of cyclic boundaries cured the boundary impact problems. Easterly wave no-source, no-sink integrations with the cyclic boundaries gave smooth wave propagation and no sudden slowing as the boundary was approached as had happened in the fixed boundary version. Energy conservation was also much better in the cyclic model,

TABLE 5
MODEL ACRONYMS

Acronym	Explanation
IVDB	Initialization model using a Vortex and Dirichlet Boundary conditions.
IEDB	Initialization model using an Easterly wave and Dirichlet Boundary conditions.
FDB/B	Forecast model using Dirichlet Boundary conditions with Gerrity and McPherson (1971) near-boundary treatment.
FDB/D	Forecast model using Dirichlet Boundary conditions with Chen (1973) near-boundary treatment.
IECB/5	Initialization model using an Easterly wave and Cyclic Boundary conditions. Geopotential calculation does not allow mean u or v component in domain.
IECB/6	Initialization model using an Easterly wave and Cyclic Boundary conditions. Allows mean u field in the wave part of the domain.
FCB	Forecast model using Cyclic Boundary conditions.

and the meteorological fields looked better, subjectively, in the cyclic forecasts than in the fixed boundary forecasts.

3.1.6 Noise Control

A time filter was added to the forecast model for additional control of extraneous numerical noise. The use of time filters in controlling noise is now relatively common, and the one used in the forecast model follows Asselin (1972). Asselin's original form of the filter is:

$$\tilde{F}(t) = F(t) + .5\nu[F(t-(n-1)\Delta t) - 2F(t) + F(t+(n+1)\Delta t)] \quad (81)$$

where the tilde represents the time filter function F , ν is the filter factor, t is time, n represents the time step number, and Δt is the time step. In the current forecast model, (81) must be modified somewhat because of the alternating time and space grids:

$$F(t) = F(t) + .5\nu[\overline{F(t-(n-1)\Delta t)}^{xy} - 2F(t) + \overline{F(t+(n+1)\Delta t)}^{xy}] \quad (82)$$

where the bar is an averaging operator as previously defined. The averaging is necessary because a particular variable is not held at the same grid point on alternate time steps (see Figures 4 and 5). This version of the filter smooths both in time and space; and when used, it smooths each of the basic forecast fields.

3.1.7 Numerical Stability

In an atmospheric numerical model, the two prime numerical stability factors are labeled linear and non-linear. The linear stability criterion approximately measures the maximum time step that one can use in a time integration scheme without causing numerical instability and a consequent blowup of the scheme. All models must reckon with linear instability because it occurs very quickly when the model integration exceeds the criterion.

Elvius and Sundstrom (1973) analyzed basically the same numerical scheme used in this model. They found a linear stability criterion of

$$\Delta t > \frac{\Delta s}{\max(|U|, |V|)} \quad (83)$$

where Δs is the distance shown on Figure 2 and Figure 3. Use of (83) with a $\max(|U|, |V|)$ of 10 m/sec and a Δs of 100 km gives a maximum Δt of 167 minutes. Integration of a barotropic 10 m/sec vortex in experiment V2C (Table 4) confirmed that a Δs of 100 km combined with a time step of 120 minutes stayed within the actual model's linear stability (see appendix C). For a smaller Δs of 50 km and a $\max(|U|, |V|)$ of 50 m/sec, the maximum Δt , according to (83), becomes less than 17 minutes. Based on these estimates, a time step of 15 minutes was selected for the forecast experiments that had cumulus heating effects included. This time step was adequate in practice as evidenced by a lack of linear stability problems.

Non-linear stability is not so well defined as linear, and there are no simple formulas for guidelines. Non-linear stability is also not quite so crucial to short-period forecast models because the instability normally appears to slowly grow and only explodes after several forecast time steps. The model used in this work is in a borderline category as far as the importance of non-linear stability: it is not a climate model and so does not require very stringent stability control; and yet, it is integrated normally for periods of four to six days and is therefore not really a short-period forecast model. Fortunately, the advective term (Gerrity and McPherson, 1971) is a compromise between a very stringent control, such as an Arakawa-type conservative advection scheme, and a no-control system such as a simple centered-difference advection scheme. Although it is not as complicated as an Arakawa scheme (Arakawa and Mesinger, 1976), the Gerrity and McPherson scheme appears to be perfectly satisfactory for use in the current forecast model. Ten-day no-source, no-sink integrations of both vortex and easterly wave states resulted in no significant changes in energy (see appendix C) or meteorological patterns and confirmed that the non-linear stability control in the model was sufficient for the current experiments.

3.2 Initialization Numerical Methods

Formulating the initial fields for a primitive equation (PE) model is a delicate task because a bad initialization

may cause unwanted gravity wave and noise generation. In order to lessen such noise, the mass and the wind field are frequently balanced in some manner so that gravity waves are absent in the initial fields. These so-called balanced fields contain only rotational winds, and the geopotential fields are linked to the winds by either a linear or non-linear balance equation. Such balance equations are derived from the divergence equation by neglect of the divergence and other small terms (Haltiner, 1971). Gravity waves, which are basically waves driven by divergence, cannot exist in such balanced, non-divergent fields.

Non-divergent, balanced initial fields were used in the present research because of the noise reduction characteristics discussed above. For real forecasts, some other, more sophisticated initialization techniques might be necessary. However, the present research simulations were aimed at qualitative and not quantitative observations, and the simpler balance equation technique appeared to be adequate for these purposes.

In the tropics the balance equation is used to diagnose the geopotential. This is the converse of mid-latitude modeling practice that diagnoses the non-divergent wind from the geopotential field. A basis for this difference lies in the relative magnitude of gradients in the tropics versus mid-latitudes. Tropical geopotential gradients are typically much smaller than those in mid-latitudes; thus tropical geopotential fields are, relatively speaking, more prone to

obscuration by observational errors than mid-latitude fields. Wind field gradients are more or less comparable in both regions, indicating that wind field accuracy relative to geopotential accuracy increases greatly from mid-latitude to tropical regions. Thus, in the tropics the wind rather than the geopotential is the better defined field; and consequently, the geopotential is diagnosed from the wind.

The basic outline of the initialization used in this research is fairly simple. The first step involves computation of the stream function from the equation:

$$m^2 \nabla^2 \psi = \zeta \quad (84)$$

where ψ is the stream function, ζ is the vorticity, and m is the mercator-projection map factor. This Poisson equation is transformed into simple second-order finite differences and solved for ψ on the entire physical grid. In the Dirichlet (fixed) boundary case, relaxation is the method of solution whereas the NCAR program POIS (Adams, 1975) is used in the cyclic boundary case.

The derived stream function is an intermediate in the preparation of both rotational (non-divergent) winds and geopotential. In particular, the rotational winds are calculated on the entire physical grid from simple finite difference versions of the following:

$$\begin{aligned} u &= -m \frac{\partial \psi}{\partial Y} \\ v &= m \frac{\partial \psi}{\partial X} \end{aligned} \quad (85)$$

To obtain the geopotential from the stream function, the non-linear balance equation (Haltiner, 1971) is used:

$$\nabla^2 \phi = f \nabla^2 \psi + \nabla \psi \cdot \nabla f - 2m^2 \left(\frac{\partial^2 \psi}{\partial x \partial y} \right)^2 + 2m^2 \frac{\partial^2 \psi}{\partial x^2} \frac{\partial^2 \psi}{\partial y^2} \quad (86)$$

where f is the Coriolis factor and ϕ is the geopotential. Equation (86), which is a Poisson equation like (84), was solved by numerical methods analogous to those used on (84).

The rotational winds and balanced geopotential were calculated for layers 1 and 2 separately and for every grid point on the entire physical grid. However, the forecast model does not carry variables at each point; and so u , v , and ϕ data at the appropriate points were extracted from the physical grid data and placed into the requisite odd or even initial computational grids.

Other necessary grid fields were either set with uniform values or diagnosed from the already initialized u , v , and ϕ :

- (a) Grids for χ_0 and χ_s were each typically initialized with a separate uniform value, although either or both fields could be readily initialized with spatially non-uniform states.
- (b) Grids for layer thickness were initialized with h_1 and h_2 values diagnosed from ϕ_1 and ϕ_2 by means of a rearranged (33):

$$h_1 = (\phi_1 - \epsilon \phi_2) / [g(1-\epsilon)] + \bar{h}_1 \quad (87a)$$

$$h_2 = (\phi_2 - \phi_1) / [g(1-\epsilon)] + \bar{h}_2 \quad (87b)$$

After computation, the h_1 and h_2 grids replaced the geopotential grids, and geopotential was not included in the final set of gridded variables necessary to begin the forecast model program.

- (c) Grids for boundary layer winds were initialized with layer 1 winds because of the constant boundary layer thickness.

Besides the variables discussed above, initial values of w , χ_2 , χ_s , η , and Q^+ were also required. However, these variables were diagnosed, as needed, in the forecast program and were not supplied to the forecast model by the initialization program.

3.2.1 Dirichlet Boundary Initialization

The Dirichlet-boundary forecast model was used in development simulations with both Ooyama (1969) type vortices and with a composite easterly wave derived from GATE data (Reed, et al., 1977). As noted earlier, the fixed boundary experiments with the easterly wave were discontinued because of boundary effects. For that reason, the initialization of those experiments (E1 and E2) will not be discussed further except to note that their initialization generally followed the scheme outlined earlier.

The Ooyama vortex, unlike the easterly wave, behaved well in fixed boundary integrations. This vortex was used in extensive forecast model testing (appendix C) and in

the results of Chapter IV; and its initialization deserves a few brief comments. The analytical form of the vortex is:

$$v_T = \frac{\hat{v}_T 2(r/\hat{r})}{[1 + (\frac{r}{\hat{r}})^2]} \quad (88)$$

where v_T is the tangential velocity, r is the radius from the center, \hat{r} is 3×10^5 m, and \hat{v}_T is 10 m/sec.

In the easterly wave case, the vorticity for use in (84) must be obtained by finite differences. However, for the Ooyama vortex, an analytical formula for vorticity can be obtained from (88):

$$\zeta = \frac{4\hat{v}_T}{\hat{r}[1 + (\frac{r}{\hat{r}})^2]^2} \quad (89)$$

Thus, the vorticity was calculated directly at each grid point for the vortex, and then the finite difference form of (84) used to solve for ψ .

A major part of the Dirichlet initialization was setting reasonable, consistent boundary conditions. At each boundary, the velocity components normal to the boundary were set to zero (constant ψ all around the boundary). Such a closed region generally has fewer numerical problems in the forecast than a region with fixed boundaries that allow advection into or out of the region.

The constant ψ on the boundary required a constant geopotential on the boundary in order for the wind and mass

fields to remain in balance. These constant values for layers 1 and 2 were derived from the standard geopotentials for 700 and 300 mb, respectively. The link between the constant boundary ψ and geopotential was through the geostrophic stream function:

$$\psi_B = \frac{\phi_B}{f_0} \quad (90)$$

where ψ_B is a boundary stream function constant, ϕ_B is a boundary geopotential constant, and f_0 is a constant Coriolis factor of $5 \times 10^{-5} \text{ sec}^{-1}$.

One other item of note is the placement of the initial vortex center on the grid. Initially, the vortex was centered on a physical grid point, but such placement caused numerical problems in the forecast. The numerical symptoms were a separation of the χ_0 odd and even grid solutions by the end of a three day forecast. A tentative explanation for the problem was that the low grid resolution ($\Delta x = 200 \text{ km}$, $\Delta s = 100 \text{ km}$) and the small initial vortex ($\hat{r} = 300 \text{ km}$) combined to produce inconsistent odd and even initial grids when initial data was extracted from the physical grid. In essence, because of the low grid resolution, the odd and even computational grids represented disturbances that were very different near the vortex center. When the center of the initial vortex was redirected to a spot equidistant from grid points, both odd and even grids extracted more consistent data; and the solution separation problem disappeared.

Aside from the discussion in this section, the vortex initialization followed the path outlined earlier in 3.2. This combination produced the basic fields that are displayed in Figure 9 and Figure 10. This wind field is on a geopotential grid because it was necessary to interpolate the staggered grid u and v components to common grid points for wind vector display. For convenience the geopotential is displayed in Figure 10 as a deviation from a standard value. Figures 9 and 10 together provide subjective verification that the vortex initialization procedures produce reasonable and consistent fields.

3.2.2 Easterly Wave Cyclic Boundary Initialization

As discussed in section 1.7, wind data from a composite easterly wave was used in these experiments. Again, as mentioned in 1.7, the experiments involving this composite wave (Reed, et al., 1977) were not intended to simulate an actual easterly wave's development. The composite easterly wave merely served as a reasonable, convenient example of a relatively weak, unclosed tropical disturbance for qualitative simulations concerning tropical development.

The GATE composite wave was defined on an 8×7 horizontal grid at several vertical levels. The 8 longitudinal coordinates were spaced at 3° longitude, but implied a 24° regional length rather than 21° because of the cyclic nature of the wave. The 7 latitudinal points were equally spaced in 4° latitude increments from the equator to 24° north latitude.

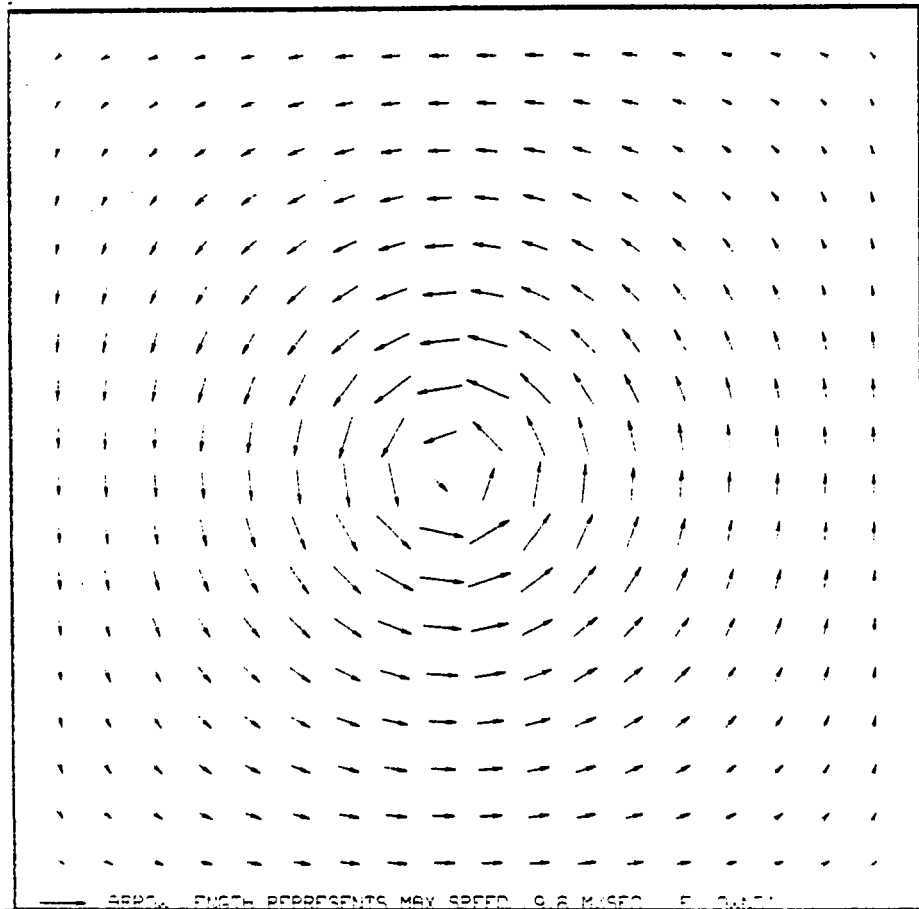


Fig. 9. All V experiments. Levels 0, 1, and 2 initial wind field.

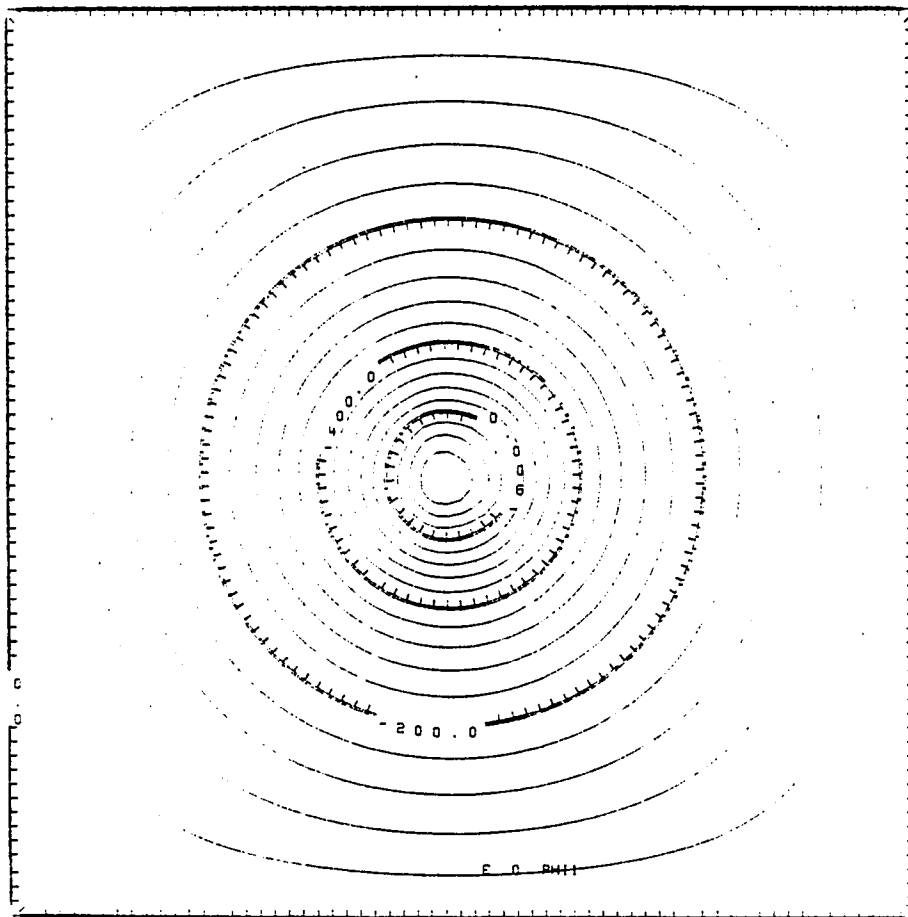


Fig. 10. All V experiments. Levels 1, 2, and 2 initialized geopotential (m^2/sec^2).

The initialization grid was on a finer mesh than the composite data, and some interpolation was necessary to obtain u and v at the additional required grid points. Because the composite was already an average, it appeared unnecessary to be very sophisticated about the interpolation scheme. Consequently, a simple bilinear method was used to interpolate composite grid point data to additional points.

Experiments with the composite wave basically used the wind data from 700 mb and 300 mb. This composite wind data was either used together or one level was used in combination with a zonal wind for the other level. Such zonal wind-composite wave combinations were used primarily in the experiments to study vertical shear of the horizontal wind.

The cyclic boundary conditions of (80) dictated some obvious changes to fixed-boundary initialization techniques, and these obvious changes led to the IECB/5 (Table 5) program. This program cured forecast distortions caused by constant, fixed boundaries; but it created two new problems: (1) how to properly treat the Coriolis parameter, which is not physically cyclic in the north-south direction, and (2) how to retain a mean u flow field in the initialization.

IECB/5 treated the Coriolis parameter very simply: f simply increased from the equator to the northern boundary. This simple expedient implied a very large negative f gradient at the north-south boundary; and while this gradient did not create total havoc in the forecast, it did not appear to be

totally satisfactory. A comparison of EC1, an f-plane integration, and EC2, a β -plane integration, revealed that the large north-south f gradient did add extra noise to the forecast and suggested that a better boundary treatment was appropriate (see appendix C).

The cyclic boundaries do not permit a mean ψ difference across the north-south distance, and one cannot force such a difference as with fixed ψ boundaries. With no difference, $\Delta\psi/\Delta Y$ between the north and south boundaries is zero, and consequently, the mean u field is zero. This same ψ field is the basis of the geopotential field through the non-linear balance equation. Simply adding a mean u field to the ψ -derived wind is not successful because the wind field then becomes inconsistent with the geopotential field, which is still based on the no-mean-flow stream function.

A solution to both the Coriolis gradient and the no-mean-flow problems was to extend the northern boundary with an additional computational region of points. For the Coriolis force, this extra computational region is symmetric as in Figure 11: the Coriolis rises to a peak at the boundary of the easterly wave region and then declines back to zero as one approaches the northern boundary of the added computational region. The technique was simple, but a physical justification is difficult. However, the technique probably does not significantly contaminate the forecasts in the easterly wave region.

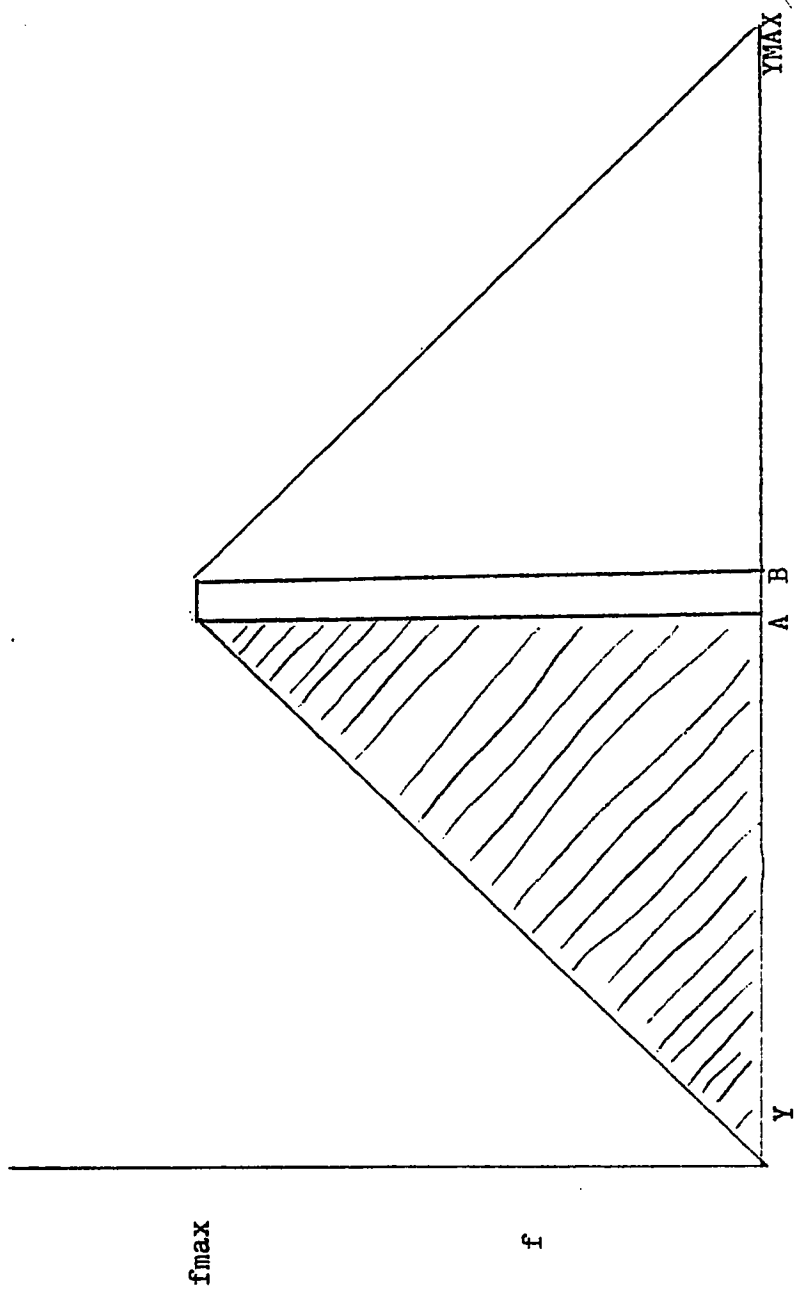


Fig. 11. The variation of Coriolis force in IECB/6 initialization (not to scale). $A = (\Delta s)(M)/2$, $B = \Delta s(M+1)/2$ where M is the number of physical grid points in the y direction. Hatched region is region of real data. $f(YMAX + \Delta s) = f(0)$, $f(-\Delta s) = f(YMAX)$.

The Coriolis treatment was symmetric, but the treatment to add mean flow is essentially antisymmetric. The true mean u flow is added to the stream-function-derived u in the easterly wave region, and the negative of this same mean u makes up the total flow field in the attached computational region. In this way the u still averages out to zero over the total combined easterly wave and computational regions. The geopotential diagnosed over this combined region will then support a mean flow in the easterly wave region because the total region mean flow remains zero.

A new cyclic initialization was designed to incorporate the above Coriolis and mean-flow specifications. In addition the program (IECB/6) also included other cyclic-specific details discussed earlier in the section. Basically, however, the initialization still follows the same general path outlined earlier in 3.2. Examples of initialized fields from this program are displayed in Figure 12 and Figure 13. Figures 12 and 13 shows the total-region level 1 wind and geopotential, respectively, and we can qualitatively see the antisymmetry in the mean fields of both figures. Figure 14 and Figure 15 also show the easterly wave region evident in Figures 12 and 13; but Figures 14 and 15 do not show most of the computational region, which is of little interest. Because they are more legible and concentrate attention on the region of interest, analogous truncated displays will be used frequently in displaying later cyclic wave experiments.

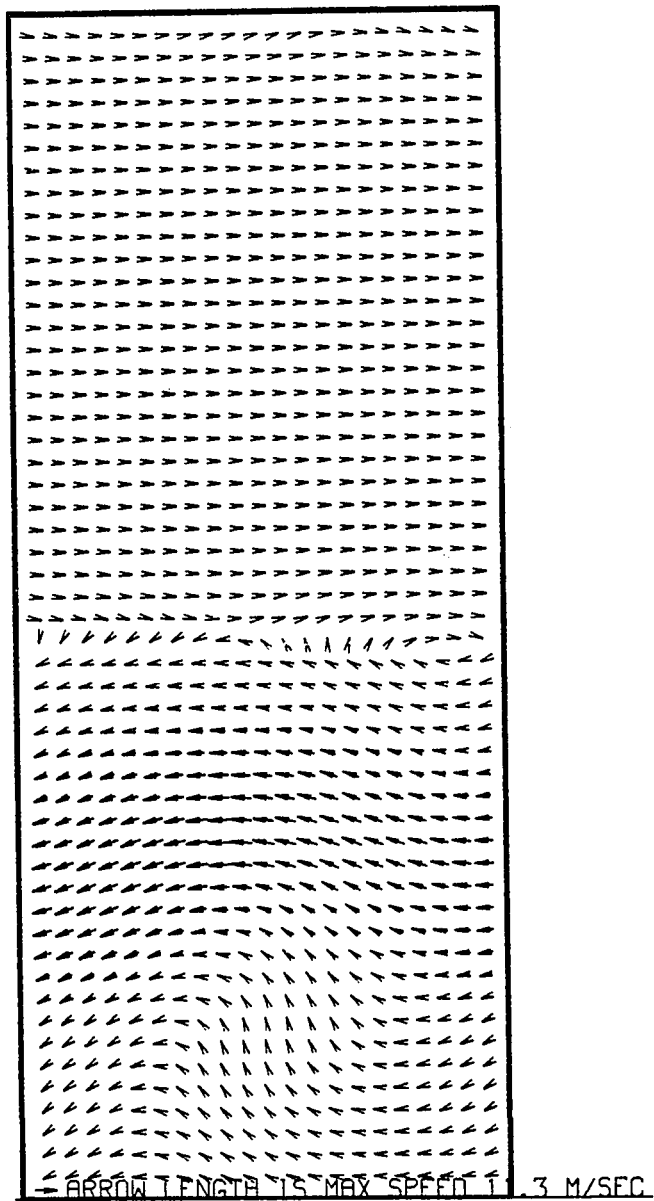


Fig. 12. EC4, EC6-EC15, EC17-EC-20 experiments.
Levels 0 and 1 initialized wind.
Max speed is 11.3m/sec.

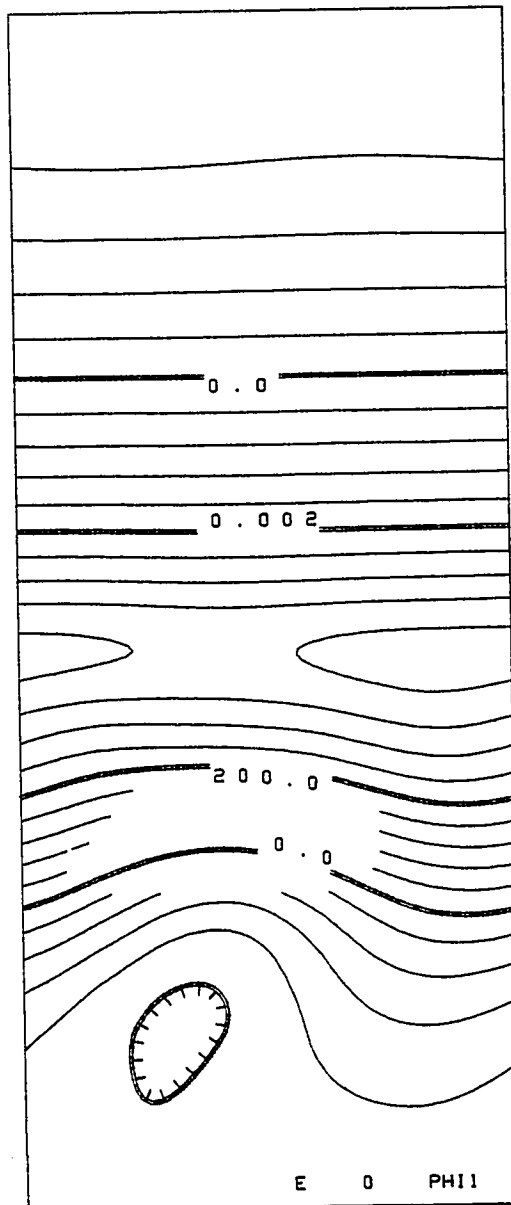


Fig. 13. EC4, EC6-EC15, EC17-EC20 experiments.
Levels 0 and 1 initialized geopotential
deviations (m^2/sec^2).

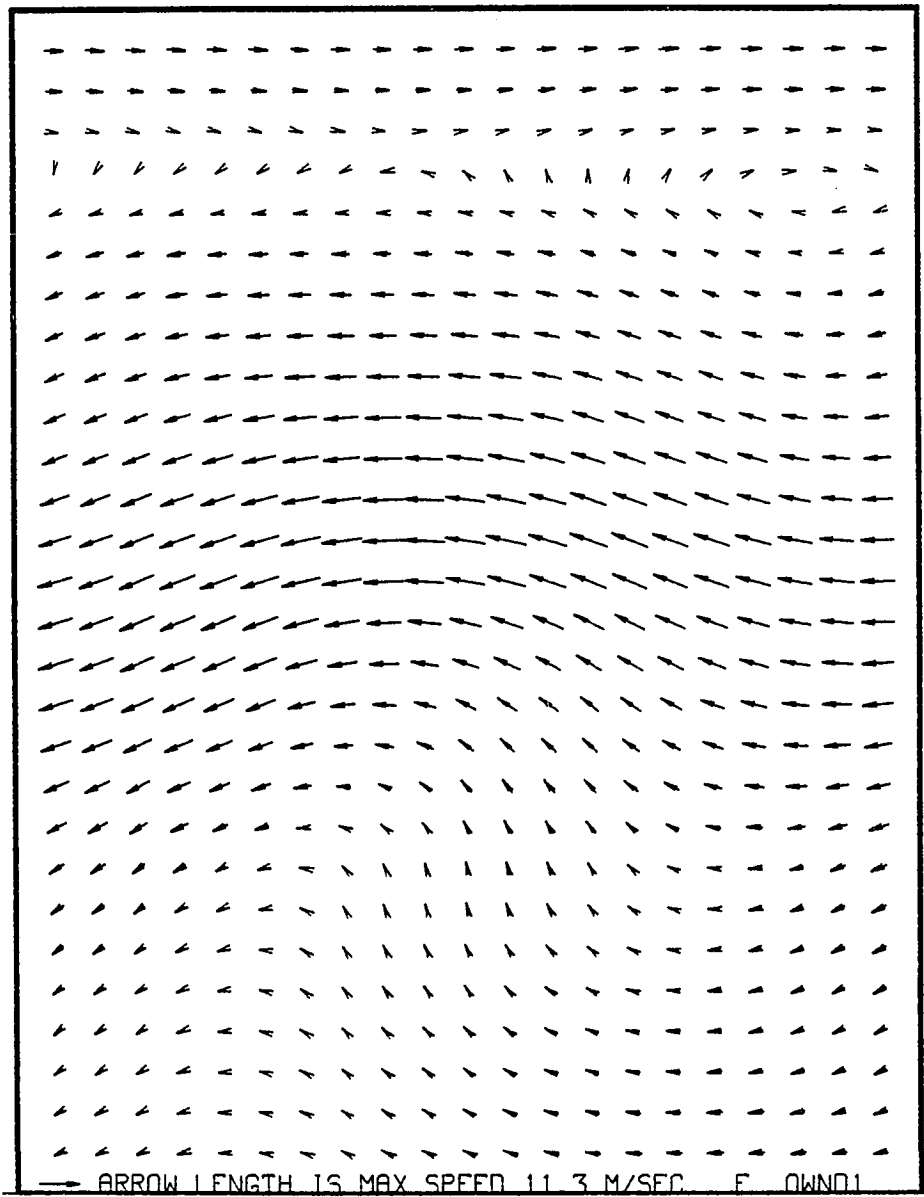


Fig. 14. EC4, EC6-EC15, EC17-EC20 experiments.
Levels 0 and 1 initialized wind.
Truncated display.

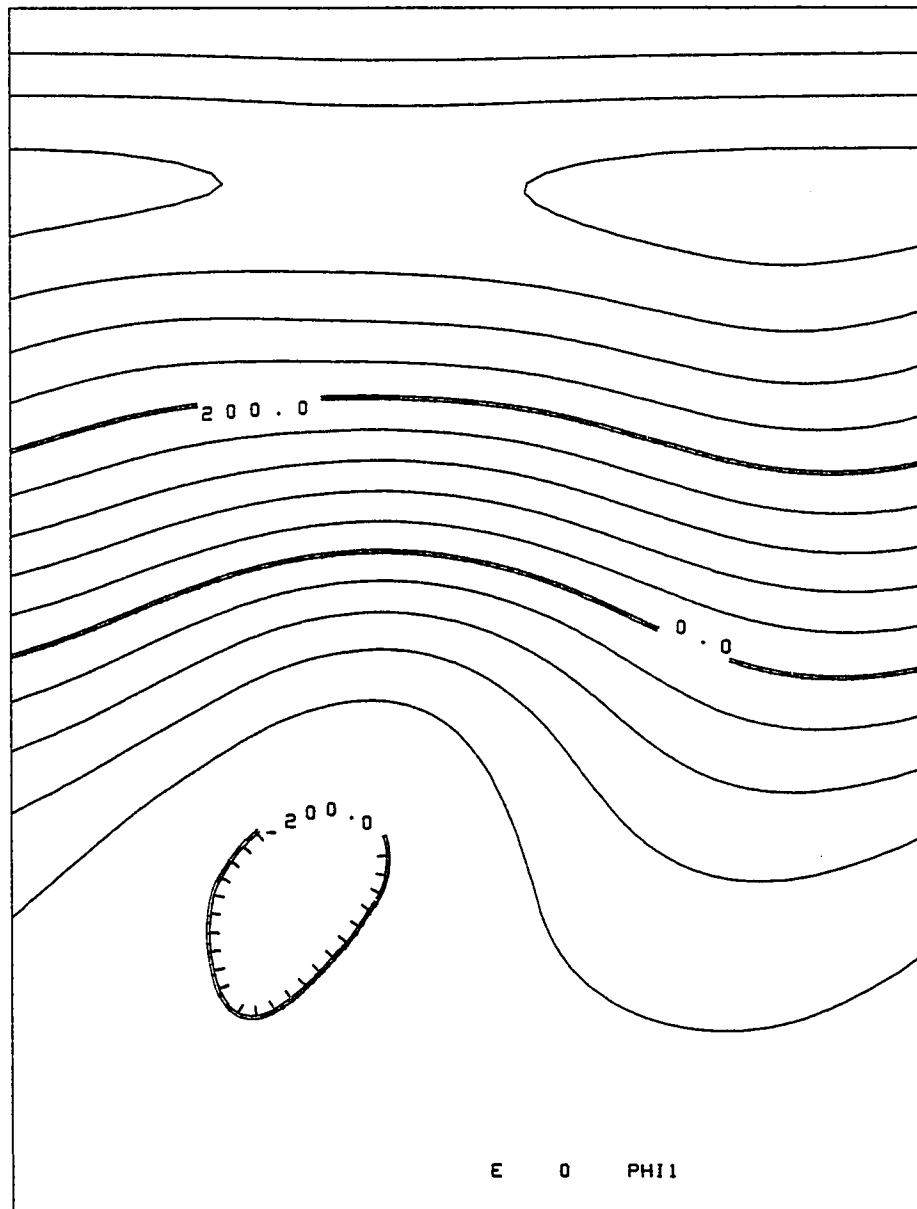


Fig. 15. EC4, EC6-EC15, EC17-EC20 experiments.
Levels 0 and 1 initialized geopotential
deviations. Truncated display.

CHAPTER IV

RESULTS AND DISCUSSION

The models and techniques of Chapters II and II could be used for a wide range of investigations and experiments. A premium on time and computer availability, however, narrowed the range of experiments to those in Tables 4, 6, 7, and 8. The experiments in these tables can be generally separated into the following categories: (1) model testing, (2) general development simulation, (3) boundary-layer moisture effects, (4) vertical shear effects, (5) cumulus momentum transfer effects, and (6) wave-CISK effects.

The forecast model has undergone severe testing to lessen the chance that computer program errors might obscure or invalidate the experiments. Several of these tests, but not all by any means, are discussed in appendix C.

4.1 Development of a Mature Hurricane.

One of the first diabatic experiments (V3) was used to substantiate the capacity of the model to simulate hurricane development for comparison with later experiments. Experiment V3 (Table 4) included a constant $\bar{\chi}_s$ of 30°C, an initial χ_0 field of 10°C, and a χ_1 of -10°C (values used in Ooyama, 1969). Both top and bottom layers had the same initial Ooyama (1969) type vortex (see Figures 9 and 10) with a maximum tangential wind of 10 m/sec of 300 km and a concomitant

area vorticity of $6.6 \times 10^{-5} \text{ sec}^{-1}$ at the same radius. The resolution was very coarse in V3, but the vortex still grew to hurricane strength, 33.4 m/sec, by the end of the 96 hour integration. Figure 16 shows the boundary layer, which has the spiral inflow typical of hurricanes. The initial upper level vortex also has completely disappeared and been replaced by the characteristic hurricane upper level anticyclone (Figure 17). Appendix C details further aspects of this experiment, but Figures 16 and 17 basically verify the fact that the forecast model is capable of producing a hurricane when given both the proper dynamic and thermodynamic conditions.

4.2 Genesis from a Composite Easterly Wave

As described in Chapter II, most of the simulations in this study were based upon the use of initial wind fields from a composited easterly wave (Reed, et al., 1977; Thompson, et al., 1979). These fields are shown in Figures 12 through 15, and Figure 18. The 700 mb level of the composite wave serves as the input to the balanced, non-divergent initialization for the boundary layer (level 0) and level 1. The reason for the dual use of 700 mb arises from the boundary layer constant height assumption and consequent boundary layer driving by the layer 1 geopotential gradient. The upper level, layer 2, follows with initialized winds from the 300 mb composite wave level.

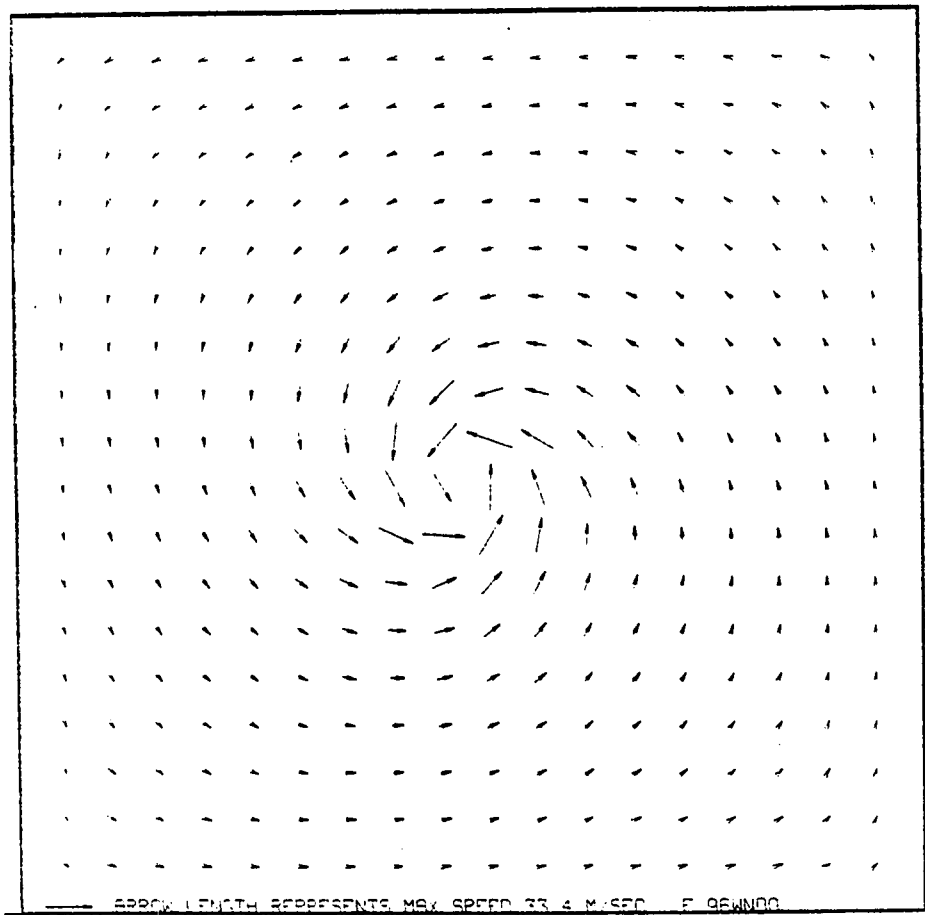


Fig. 16. V3 experiment. Level 0 wind field for forecast hour 96.

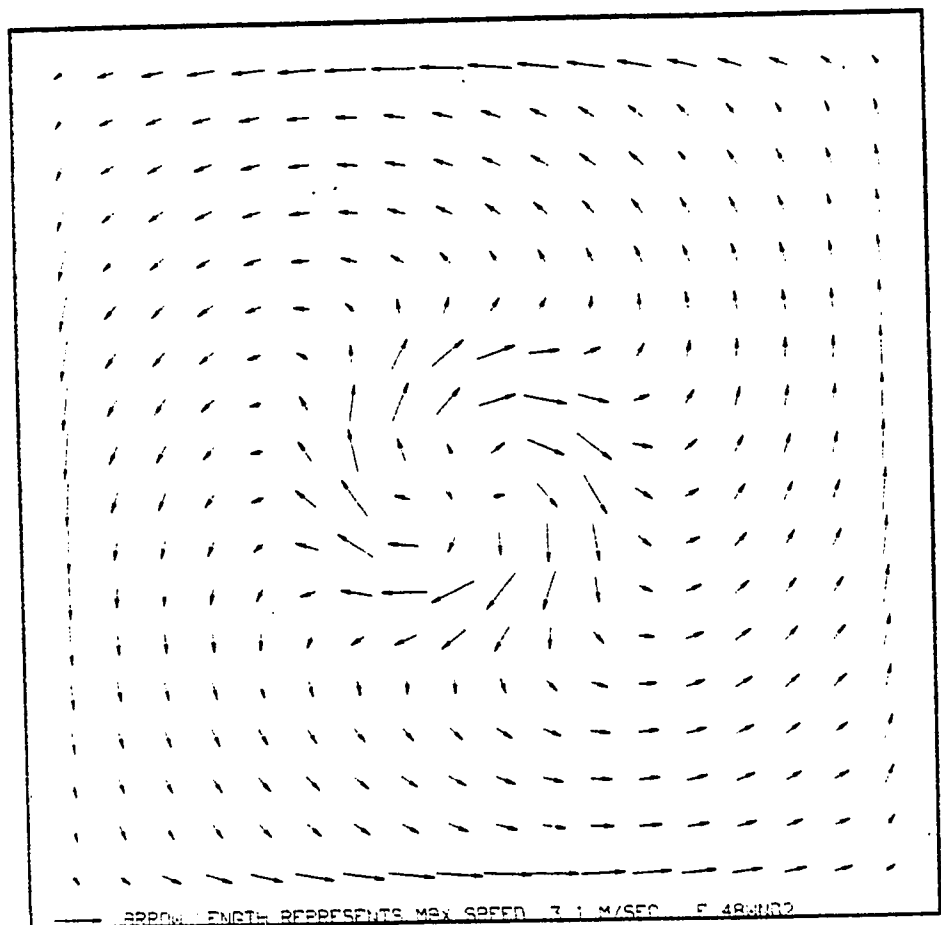


Fig. 17. V3 experiment. Level 2 wind field at forecast hour 48.

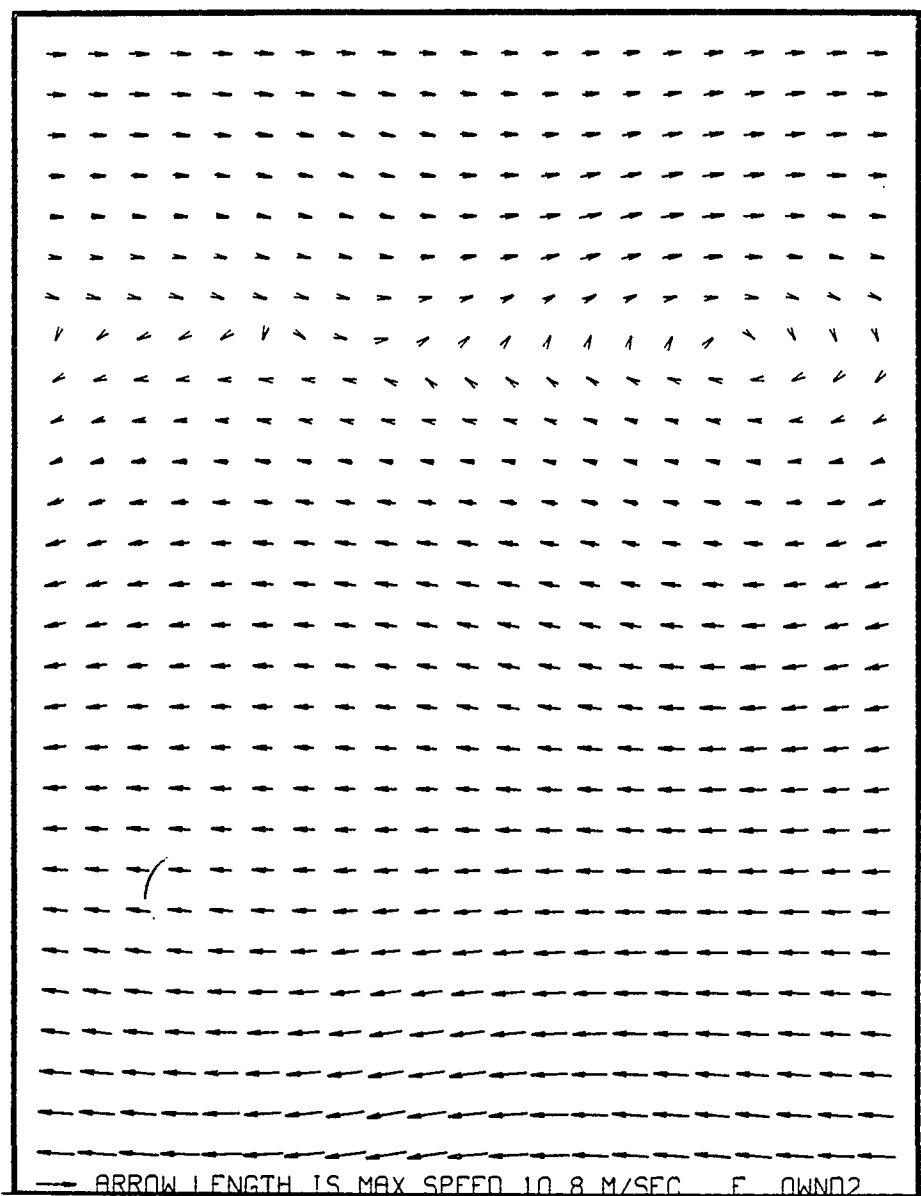


Fig. 18. EC4, 9, 11, 16-20 experiments.
Level 2 initialized wind field.

Prior to reviewing the CISK-driven development, we need to briefly look at a coasting wave forecast for comparison. Experiment EC4 (Table 6) has no sources or sinks and runs to 96 hours. Although it starts with no divergence fields, the wave does develop a weak but semi-organized field by 96 hours. Comparison of the divergence fields (Figures 20 and 21) with the wind field (Figure 19) shows that the level 1 is convergent and level 2 divergent to the east of the wave trough. The level 0, 1 convergence agrees with the positioning of the divergence field at the 700 mb level in the original GATE composite wave (Reed, et al., 1977), but the 300 mb divergence field in the original GATE wave is opposite to that in this 96 hour forecast. Actually, Figures 20 and 21 show divergence fields reminiscent of the classical easterly wave (Riehl, 1954), which has clouds basically to the east of the wave trough.

The differences between the 96 hour EC4 divergence fields and the original composite wave may arise from two sources. The first is undoubtedly due to the fact that the EC4 initial fields used only two levels from the GATE wave and could not capture the whole essence of the wave.

The second source involves the natural evolution of the wave. The average phase speed of the wave is 8.1 m/sec, which is in the normally observed speed range; and the wave travels westward about 2800 km or 25.2 degrees longitude during the 96 hour simulation. This distance is almost

TABLE 6

MAJOR CYCLIC BOUNDARY EXPERIMENTS WITHOUT CUMULUS EFFECTS

Designator	Initial ¹ Model	Initial Conditions		Forecast ¹ Model	Domain Size (km)	Δs (km)	Δt (sec)	Integration Lg. (hrs)	Coriolis	Filter Parameter
		Level 0,1	Level 2							
EC1	IECB/5	700mb GATE	700mb GATE	FCB	2590x 3108	51.8	900	240	f-plane (5x10 ⁻⁵)	0
EC2	IECB/5	700mb GATE	700mb GATE	FCB	2590x 3108	51.8	900	240	eq. β -plane	0
EC3	IECB/5	700mb GATE	700mb GATE	FCB	2590x 3108	51.8	900	96	f-plane (5x10 ⁻⁵)	0
EC4	IECB/6	700mb GATE	300mb GATE	FCB	2623x 6159	57.0275	900	96	eq. β -plane	0
EC5	IECB/6	u=-10 v=0	300mb GATE	FCB	2623x 6159	57.0275	900	96	eq. β -plane	0
EC6	IECB/6	700mb GATE	u=0 v=0	FCB	2623x 6159	57.0275	900	96	eq. β -plane	0
EC7	IECB/6	700mb GATE	u=0 v=0	FCB	2623x 6159	57.0275	900	96	eq. β -plane	0
EC8	IECB/6	700mb GATE	u=-20 v=0	FCB	2623x 6159	57.0275	900	96	eq. β -plane	0
EC9	IECB/6	700mb GATE	300mb GATE	FCB	2623x 6159	57.0275	900	96	eq. β -plane	0

¹See Table 5 for acronym explanations.

TABLE 6--Continued

Designator	Air-Sea ² Heat Transfer?	C_T , Transfer Coefficient	Boundary ³ Layer Connected to Upper Level?	C_D , drag Coefficient	μ Vertical Shear Stress Coefficient	λ_1, λ_2 Horizontal Diffusion Coefficients	Cumulus Heating?	Cumulus Momentum Transfer?
EC1	no	0	no	0	0	0	no	no
EC2	no	0	no	0	0	0	no	no
EC3	no	0	yes	.0015	0	0	no	no
EC4	no	0	no	0	0	0	no	no
EC5	no	0	no	0	0	0	no	no
EC6	no	0	no	0	0	0	no	no
EC7	no	0	no	0	0	0	no	no
EC8	yes	.0015	no	.0015	0	0	no	no
EC9	no	0	no	0	5×10^{-4}	10000, 10000	no	no

²Although the forecast model could handle spatial variations in \bar{X}_s , a measure of sea surface temperature, the \bar{X}_s for all experiments in this table was set to a uniform, constant 30. In addition, X_0 , a measure of boundary layer equivalent-potential temperature, was set to an initially uniform 10.

³A no answer means that layers 1 and 2 are independent of the direct boundary layer effects (w), although positive answers in the cumulus blocks would still imply some indirect connection.

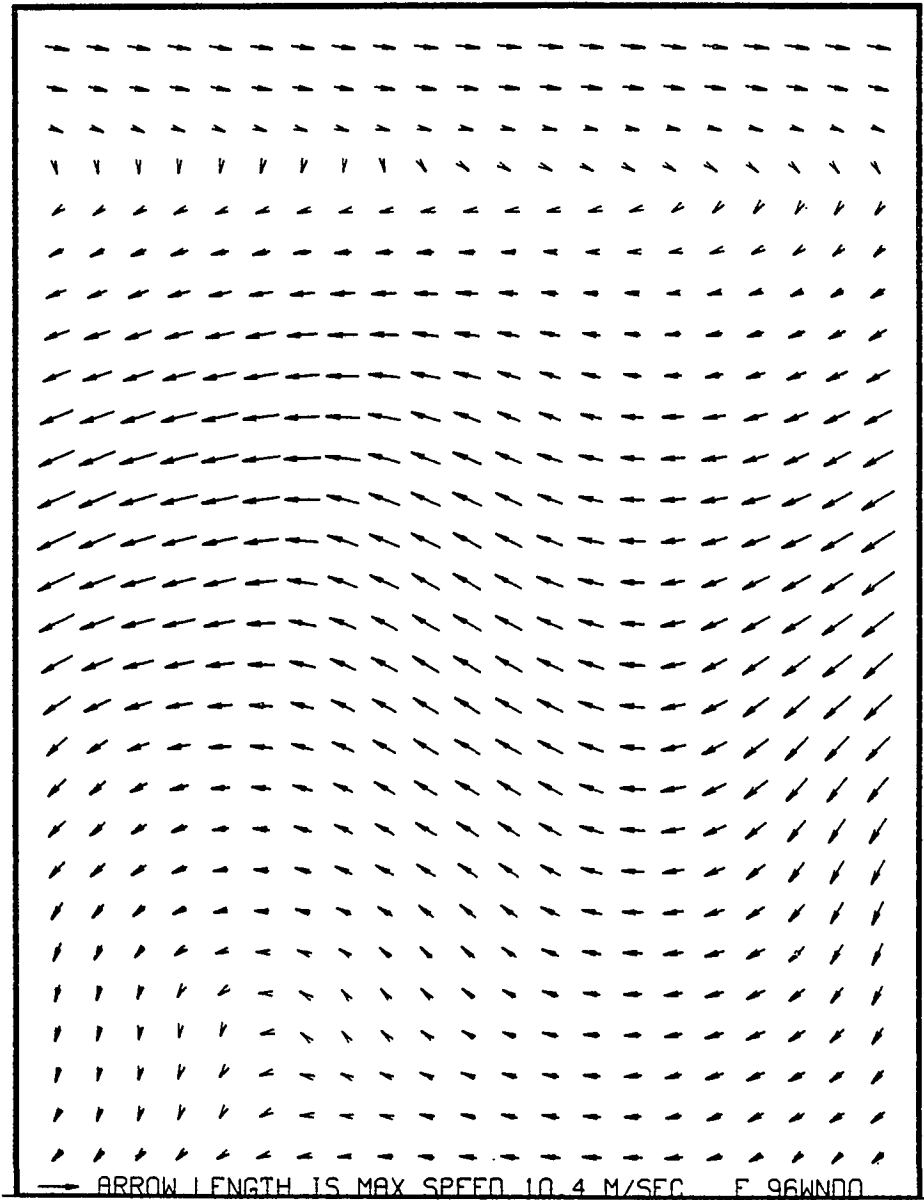


Fig. 19. EC4 experiment. Levels 0 and 1 wind field at forecast hour 96.

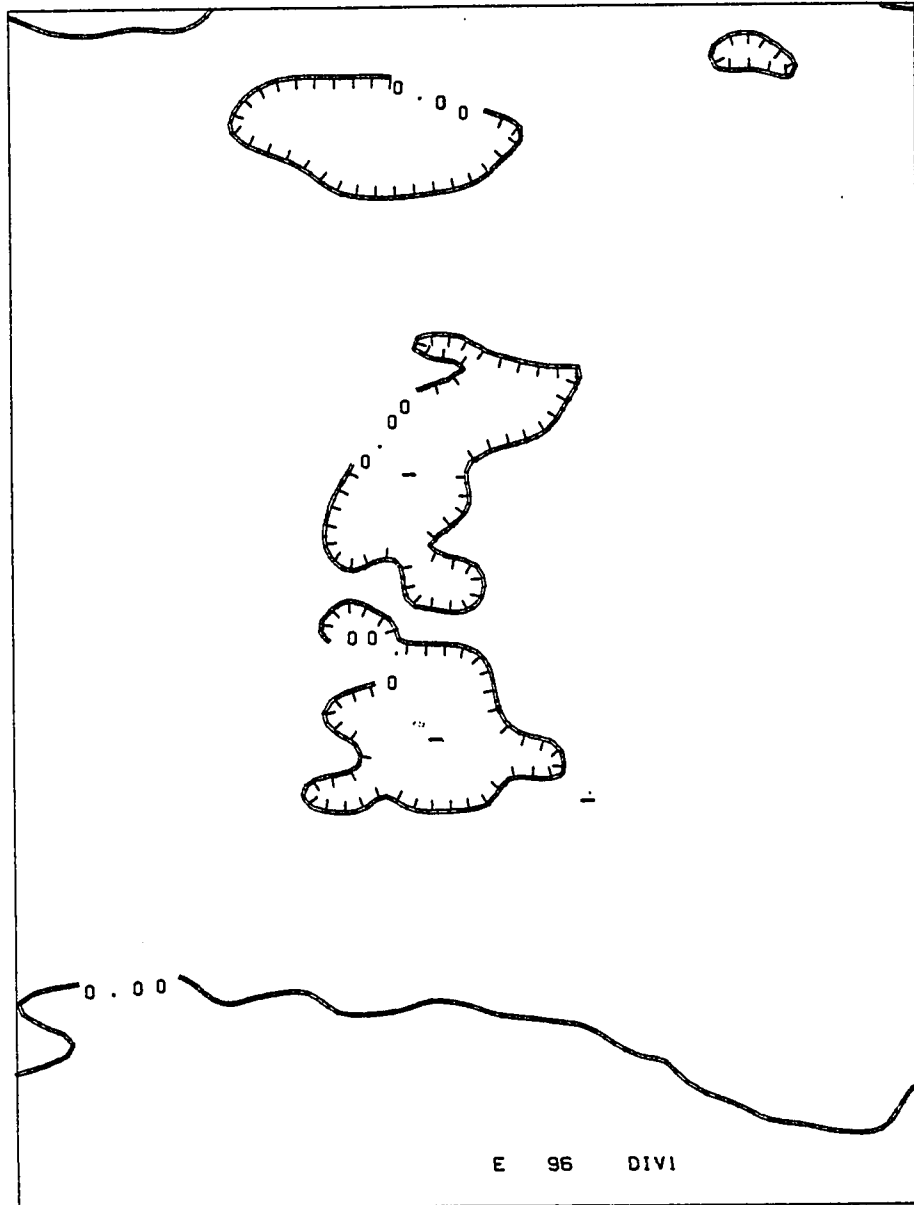


Fig. 20. EC4 experiment. Level 0 and 1 divergence field at forecast hour 96 (sec^{-1}).

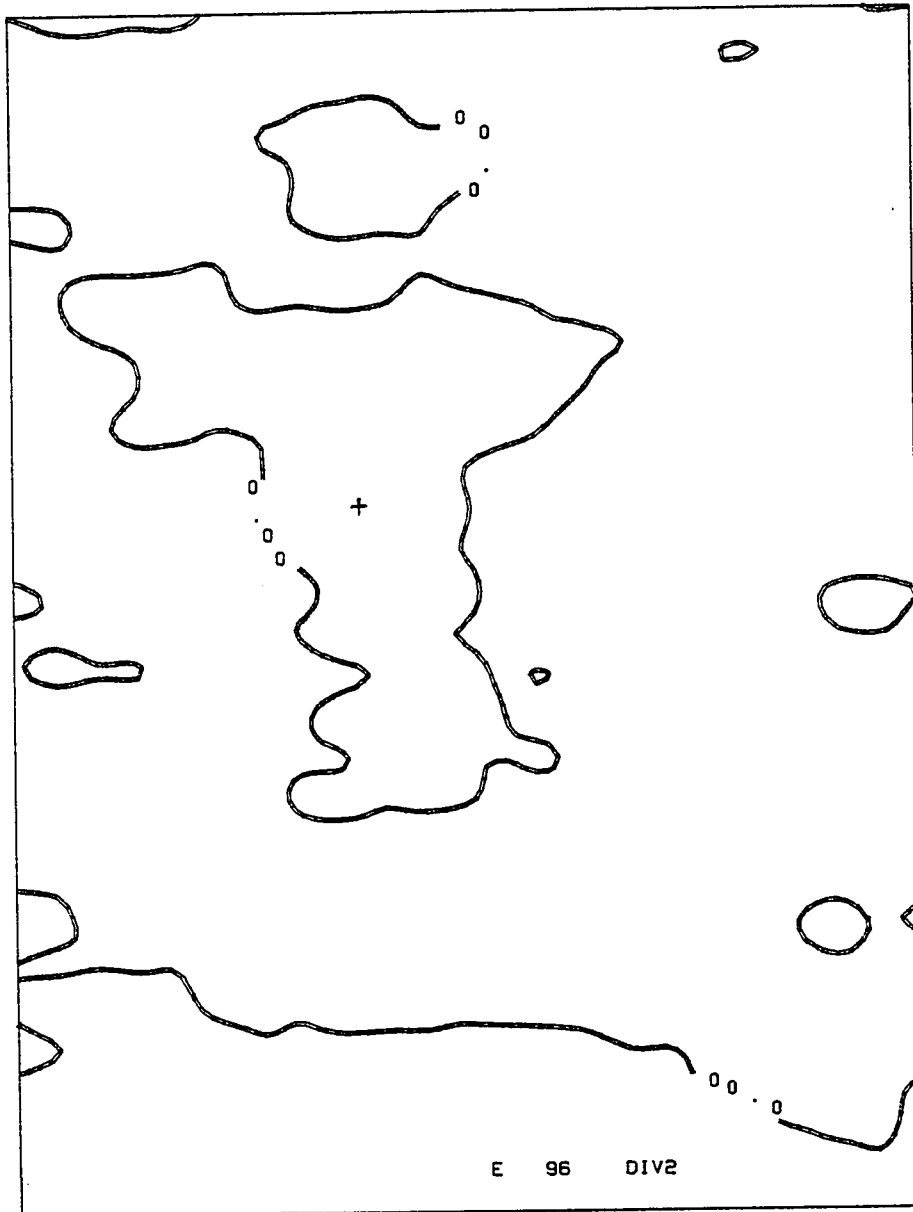


Fig. 21. EC4 experiment. Level 2 divergence field at forecast hour 96.

equivalent to that from the GATE region to the Eastern Caribbean. Since the classical Caribbean easterly wave is more similar to the 96 hour forecast than the original GATE composite, it is tempting to infer that the 96 hour simulation is the natural, dynamical evolution of a non-forced GATE easterly wave.

The coasting EC4 easterly wave does develop one eccentricity. The tilt of the trough reverses from the original southwest-northeast (Figure 20) to one of southeast-northwest. This tilt reversal is apparently an artifact of the model, and the two pertinent factors are the decrease in the mean easterlies toward the southern boundary and the phase speed of the wave.

As discussed in section 3.2.2, an additional computational region with westerly flow was added to the cyclic model in order to retain a mean (longitudinal average) easterly flow in the easterly wave region. However, such an arrangement implies that the mean easterlies must begin to decrease as the southern boundary is approached because the southern boundary separates mean easterlies from the mean westerlies of the computational region.

Application of the above observation can be made with a crude estimate of the easterly wave phase speed (Rossby wave formula):

$$c = U - \frac{\beta L^2}{4\pi^2} \quad (91)$$

where c is the phase speed of the wave, U is the mean longitudinal flow, β is the partial derivative of the Coriolis factor with respect to meridional distance, and L is the wavelength. In the EC4 experiment, both β and L are essentially constant over the easterly wave region. However, U decreases to the south as the southern boundary is approached; and consequently c has a smaller easterly value to the south than to the north. Thus, over a period of time, the faster wave speed to the north moves the northern portions of the trough further eastward and results in the trough reversal.

Other fields indicate that the basic coasting easterly wave is fairly docile. The maximum wind speed in the wave field goes through a small, long-period oscillation (Figure 22). The level 0 and 1 kinetic energies (Figures 23 and 24) do appear to climb slightly over the 96 hour period, but this climb is in phase with a drop in kinetic energy in level 2 (Figure 25). Overall, we can conclude that the no source-sink EC4 integration yields a reasonable result.

Unlike the coasting wave, the CISK-driven wave of EC11 (Table 7) intensifies over a 96 hour period and develops a closed vortex circulation (Figure 26). Comparing the level 2 initial fields of Figure 19 with the 96 hour EC11 (Figure 27) and with the 96 hour EC4 field (Figure 28), we find that the EC11 field displays a much better defined anticyclone. This EC11 anticyclone is just east of the lower level vortex and

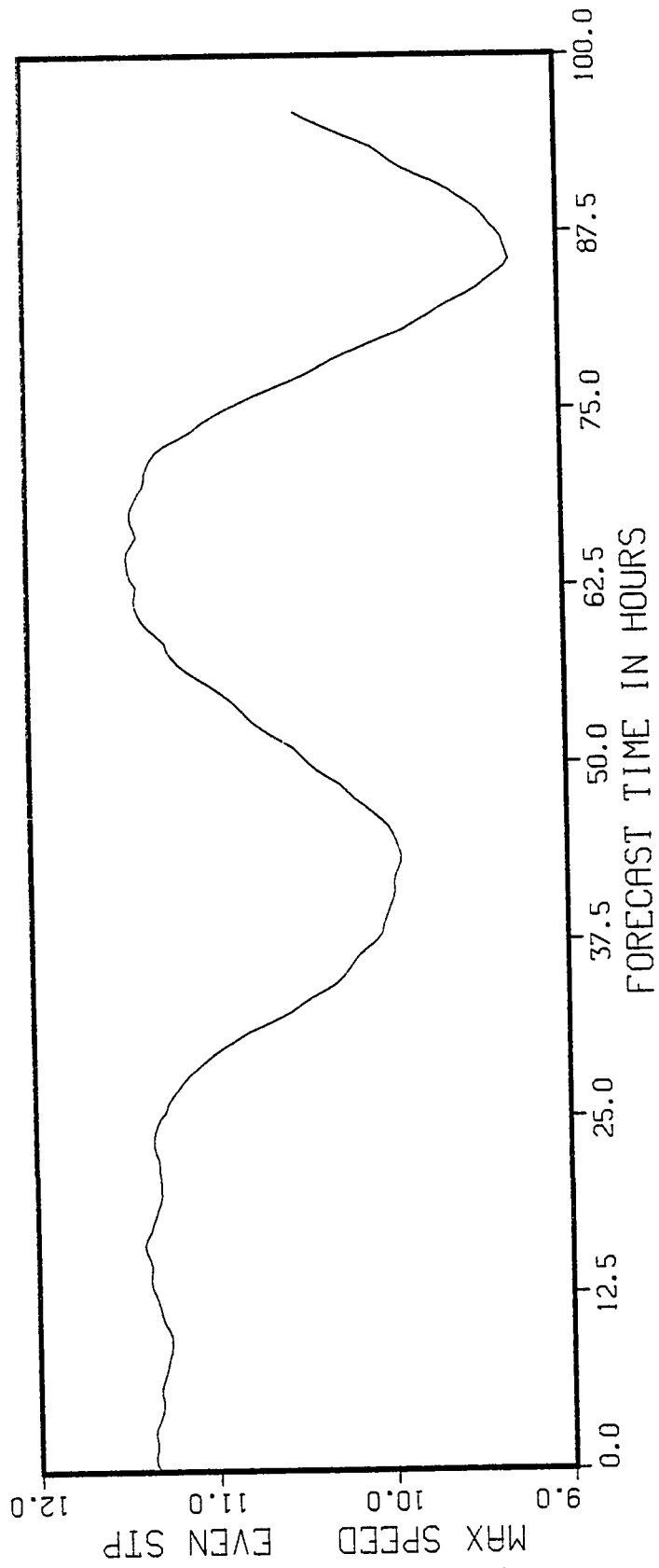


Fig. 22. EC4 experiment. Level 1 maximum speed (m/sec) versus even time steps.

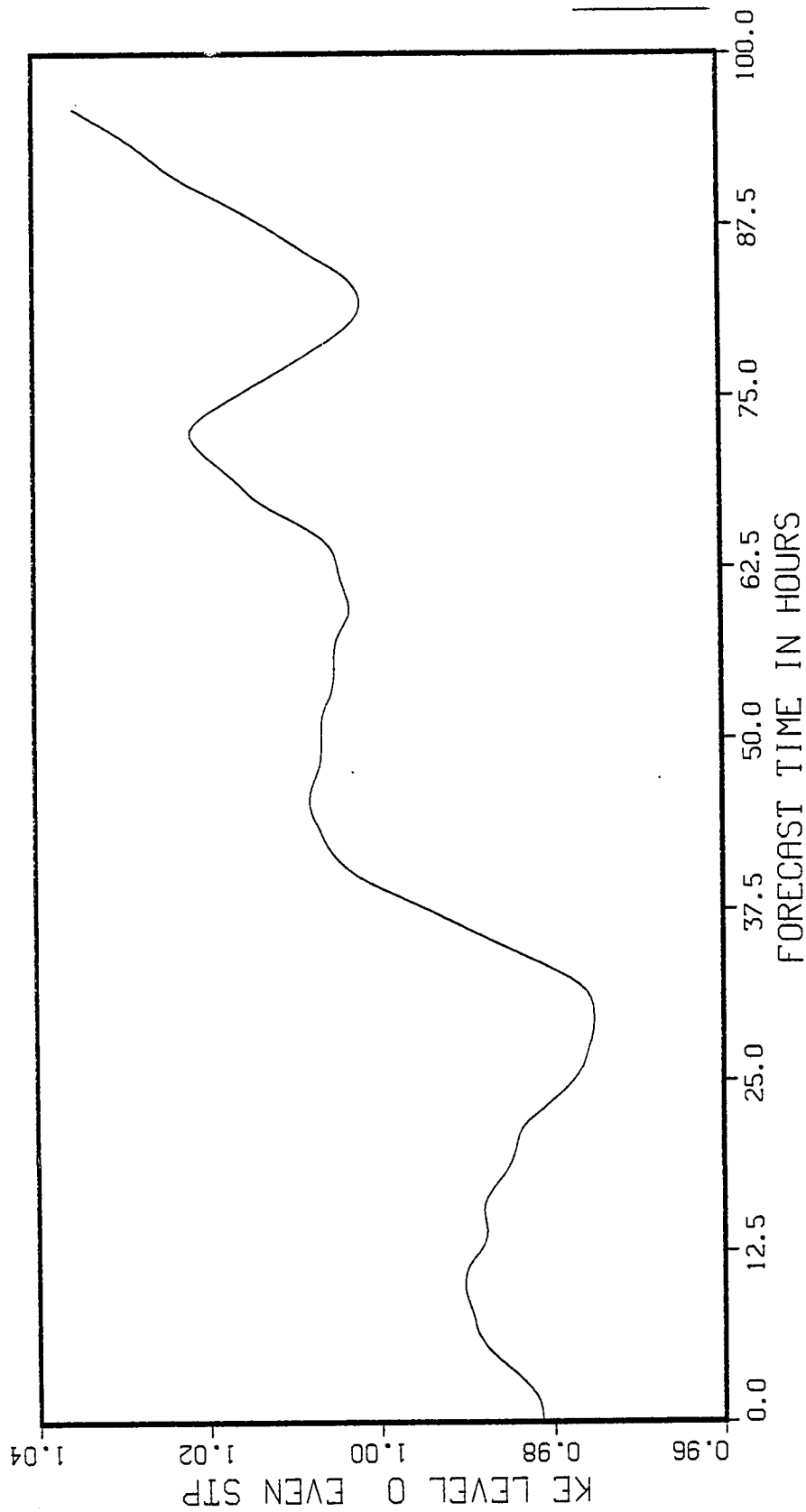


Fig. 23. EC4 experiment. Level 0 total area kinetic energy versus even time steps.

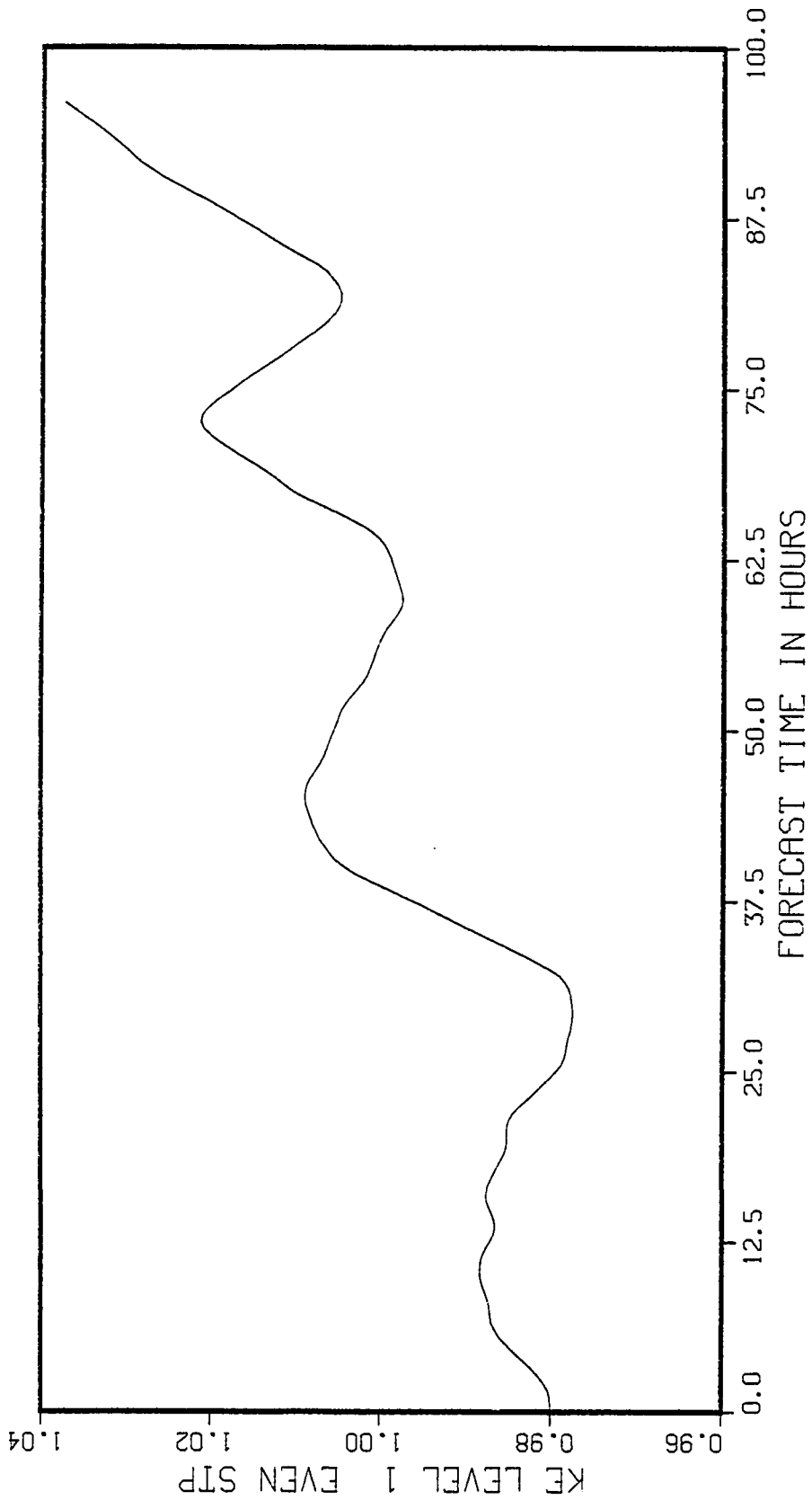


Fig. 24. EC4 experiment. Level 1 total area kinetic energy versus even time steps.

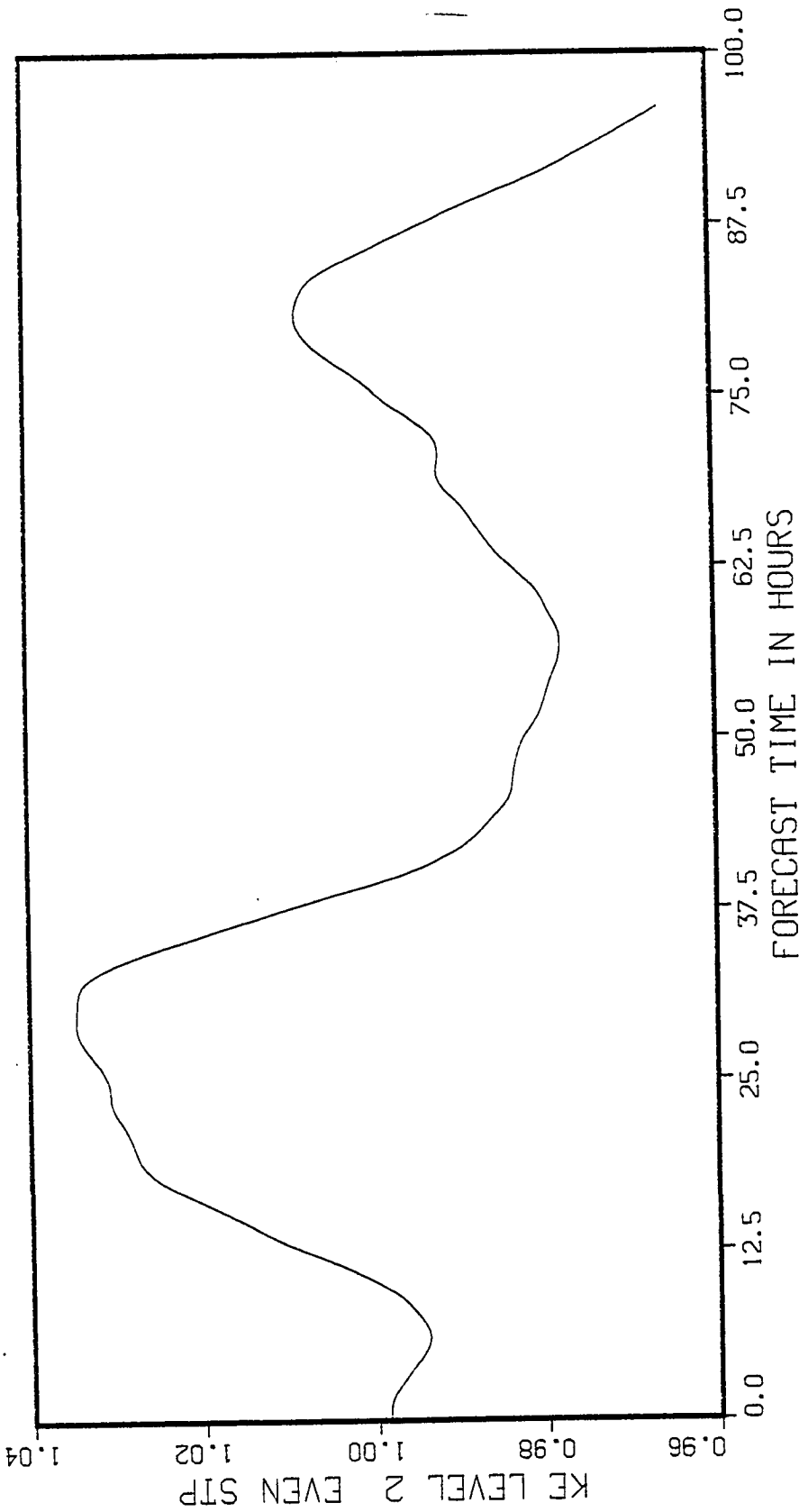


Fig. 25. EC4 experiment. Level 2 total area kinetic energy versus even time steps.

TABLE 7

MAJOR CYCLIC BOUNDARY EXPERIMENTS WITH CUMULUS EFFECTS

Designator	Initial ¹ Model	Initial Conditions		Forecast ¹ Model	Domain Size (km)	Δs (km)	Δt (sec)	Integration (Lg) hrs	Coriolis	Filter Parameter
		Level 0,1	Level 2							
EC11	IECB/6	700mb GATE	300mb GATE	FCB	2623x 6159	57. 0275	900	144	eq. β - plane	0
EC12	IECB/6	700mb GATE	u=+9.47 v=0	FCB	2623x 6159	57. 0275	900	96	eq. β - plane	0
EC13	IECB/6	700mb GATE	u=0 v=0	FCB	2623x 6159	57. 0275	900	96	eq. β - plane	0
EC14	IECB/6	700mb GATE	u=-10 v=0	FCB	2623x 6159	57. 0275	900	96	eq. β - plane	0
EC15	IECB/6	700mb GATE	u=-20 v=0	FCB	2623x 6159	57. 0275	900	96	eq. β - plane	0
EC16	IECB/6	u=-10 v=0	300mb GATE	FCB	2623x 6159	57. 0275	900	96	eq. β - plane	0
EC17	IECB/6	700mb GATE	300mb GATE	FCB	2623x 6159	57. 0275	900	96	eq. β - plane	0
EC18	IECB/6	700mb GATE	300mb GATE	FCB	2623x 6159	57. 0275	900	96	eq. β - plane	0
EC19	IECB/6	700mb GATE	300mb GATE	FCB	2623x 6159	57. 0275	900	96	eq. β - plane	0
EC20	IECB/6	700mb GATE	300mb GATE	FCB	2623x 6159	57. 0275	900	96	eq. β - plane	0

¹See Table 5 for acronym explanations.

TABLE 7--Continued

Designator	Air-Sea ² Heat Transfer	C _E , transfer coefficient	Boundary ³ Layer Connected to Upper Level?	C _D , drag coefficient	μ Vertical Shear Stress Coefficient	λ ₁ , λ ₂ Horizontal Diffusion Coefficients	Cumulus Heating?	Cumulus Momentum Transfer?
EC11	yes	.0015	yes	.0015	0	0	yes	no
EC12	yes	.0015	yes	.0015	0	0	yes	no
EC13	yes	.0015	yes	.0015	0	0	yes	no
EC14	yes	.0015	yes	.0015	0	0	no	no
EC15	yes	.0015	yes	.0015	0	0	no	no
EC16	yes	.0015	yes	.0015	0	0	yes	no
EC17	yes	.0015	yes	.0015	5x10 ⁻⁴	10000, 10000	yes	no
EC18	yes	.0015	yes	.0015	0	0	yes	yes
EC19	yes	.0015	yes	.0015	0	0	no	yes
EC20	yes	.0015	yes	0	0	0	yes	no

² Although the forecast model could handle spatial variations in \bar{X}_s , a measure of sea surface temperature, the \bar{X}_s for all experiments in this table was set to a uniform, constant 30. In addition, X_0 , a measure of boundary layer equivalent potential temperature was set to an initially uniform 10.

³ A no answer means that layers 1 and 2 are independent of the direct boundary layer effects (w), although positive answers in the cumulus blocks would still imply some indirect connection.

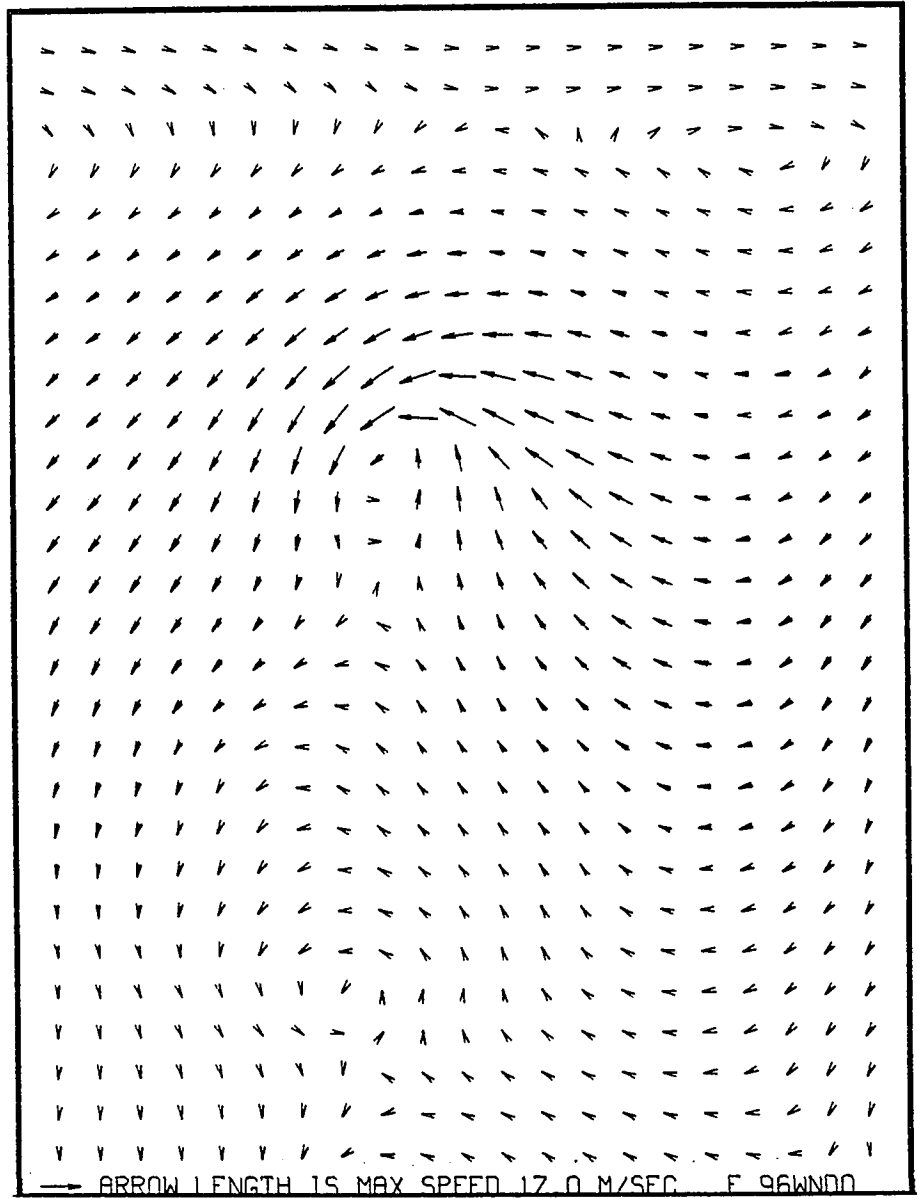


Fig. 26. EC11 experiment. Level 0 wind field at forecast hour 96.

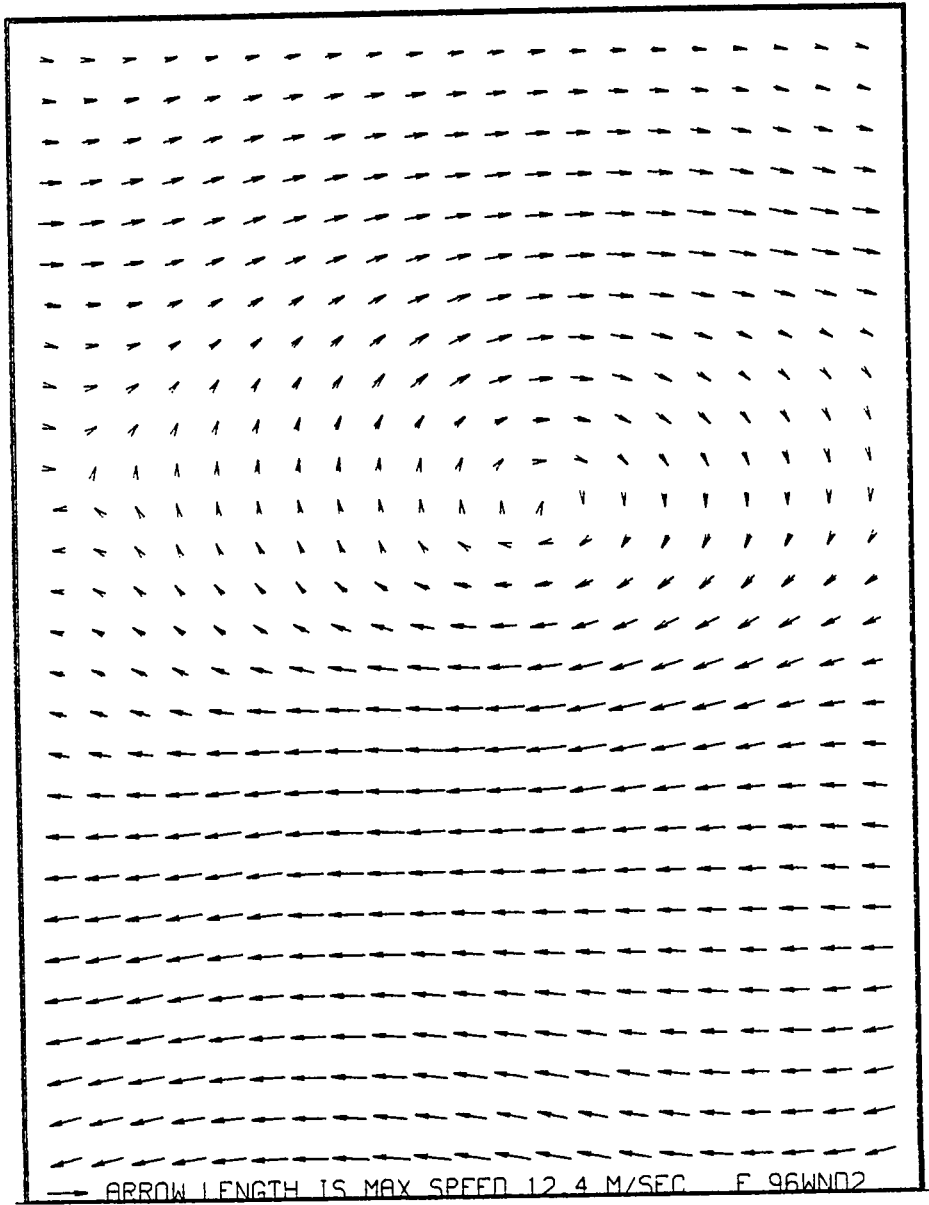


Fig. 27. EC11 experiment. Level 2 wind field at forecast hour 96.

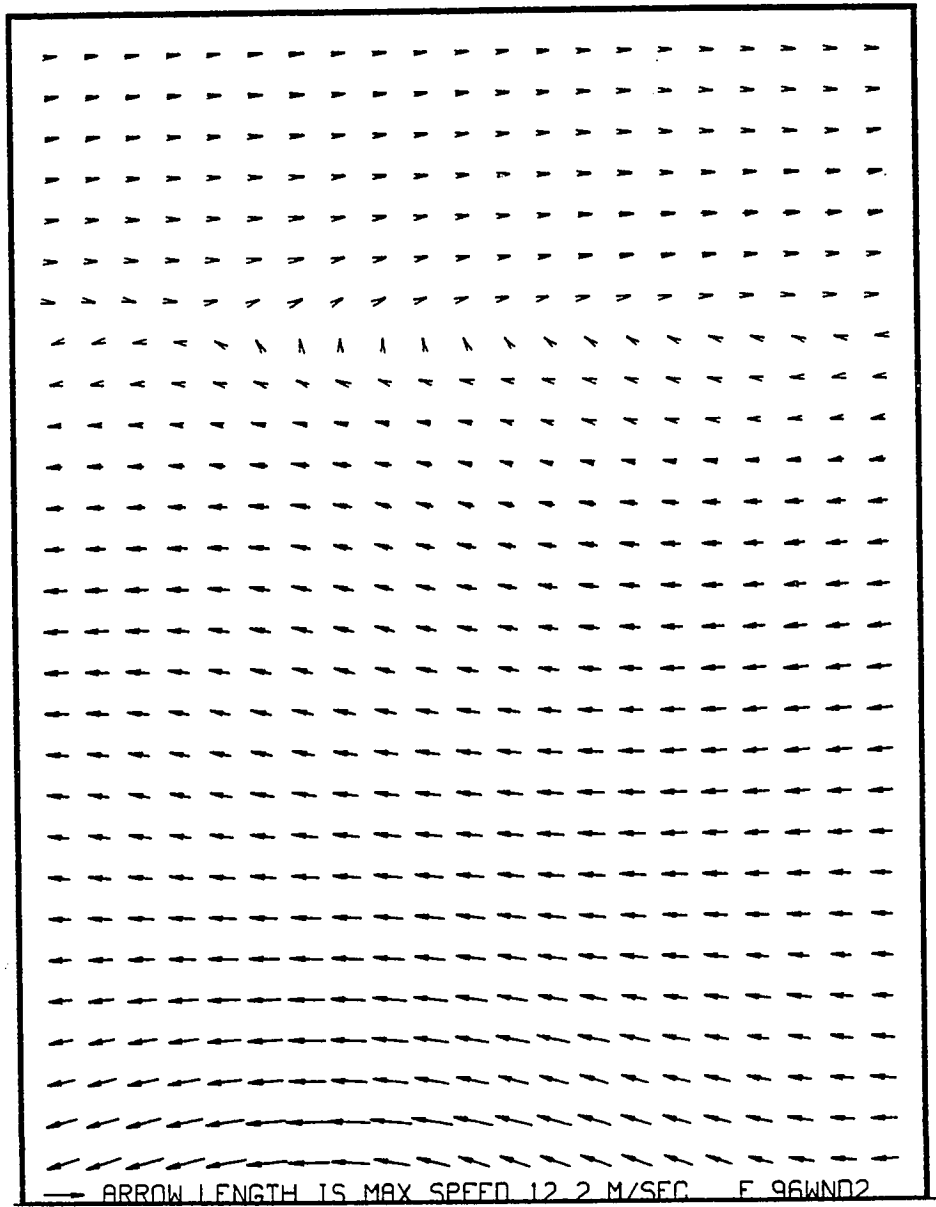


Fig. 28. EC4 experiment. Level 2 wind field at forecast hour 96.

implies that the CISK driven convection below is generating its own upper level, anticyclonic support.

The closed vortex¹ develops in the northern portion of the wave and in the center of the wave trough. This does not agree with the position of the maximum convective activity associated with the original GATE wave (Payne and McGarry, 1977), which had maximum activity further south and slightly to the west of the trough axis. However, the 17.8° latitude of development in EC11 is reasonably close to McBride's (1979) observed average genesis latitude for non-developing Atlantic easterly wave clusters.

Boundary layer vertical velocity and upper level divergent fields are in the pattern of an inverted V (Figures 29 and 30). This pattern is suggestive of the inverted V cloud pattern which has frequently been observed in Atlantic easterly waves (Barrett, 1974).

Although the easterly wave does form a vortex, its intensification does not continue indefinitely. The model integration for EC11 was extended to six days and revealed that the vortex did not continue to intensify to hurricane strength. A look at Figure 31, the maximum wind speed, confirms this and shows that the maximum wind speed peaked at under 20 m/sec, which is still considerably below hurricane strength.

¹The exceedingly weak vortex to the south is probably an artifact due to the initial cyclonic shear across the southern boundary created by the IECB/6 initialization.

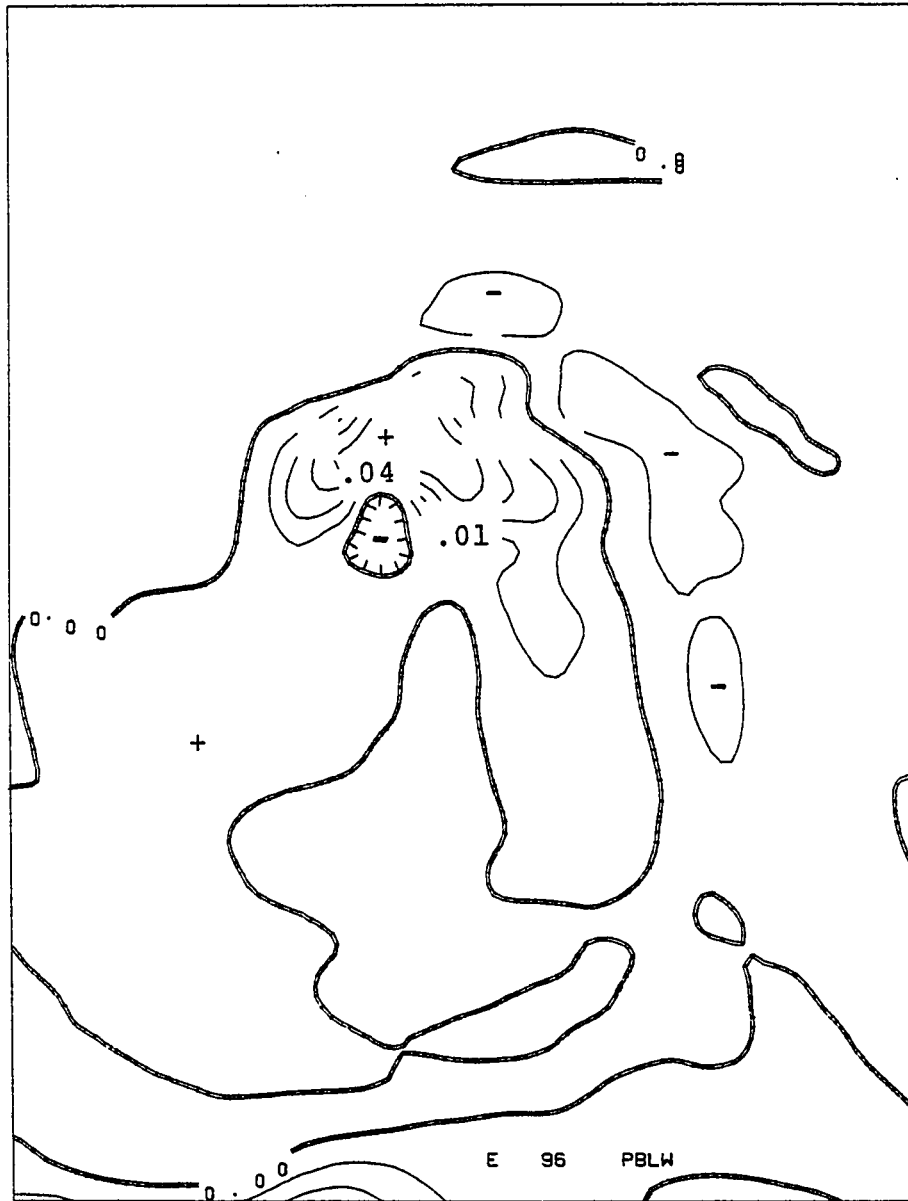


Fig. 29. EC11 experiment. Level 0 vertical velocity (m/sec) at forecast hour 96.

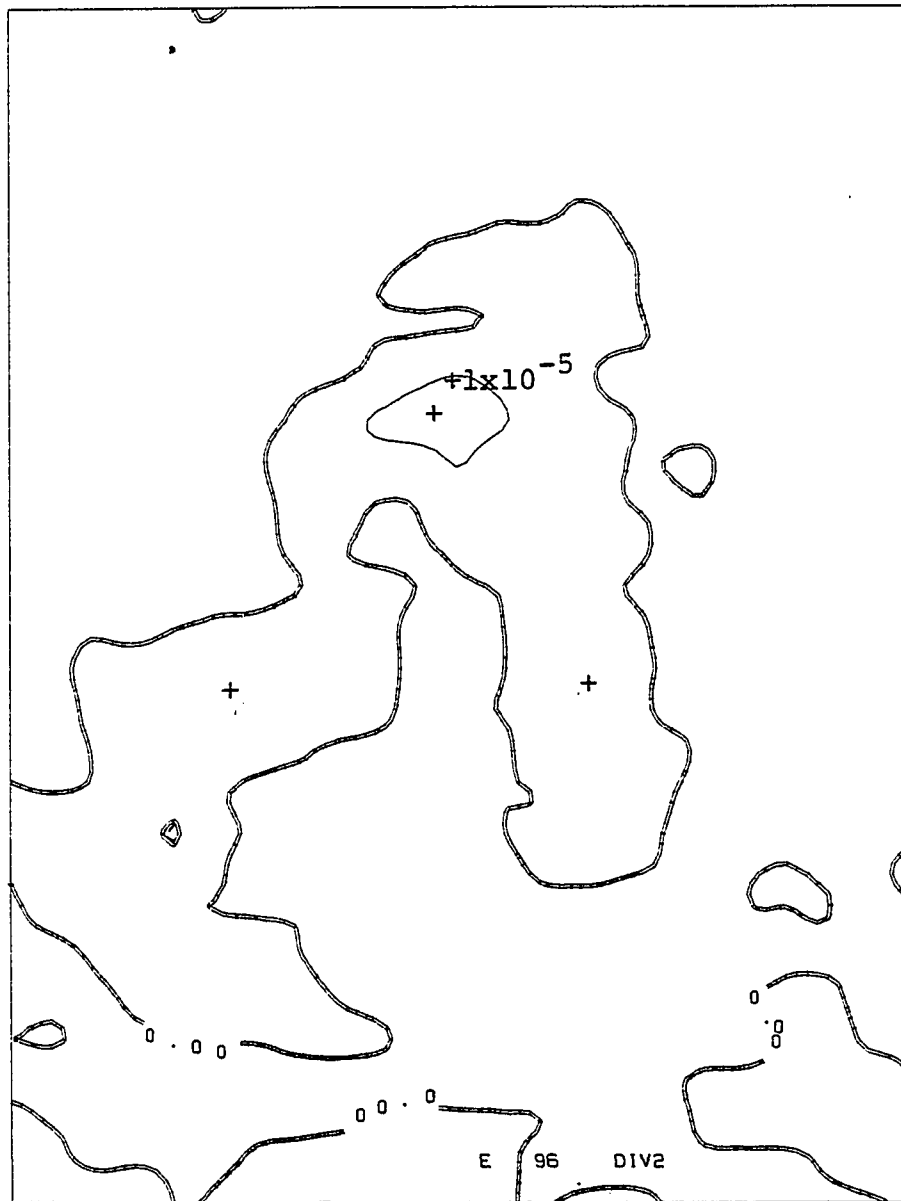


Fig. 30. EC11 experiment. Level 2 divergence at forecast hour 96.

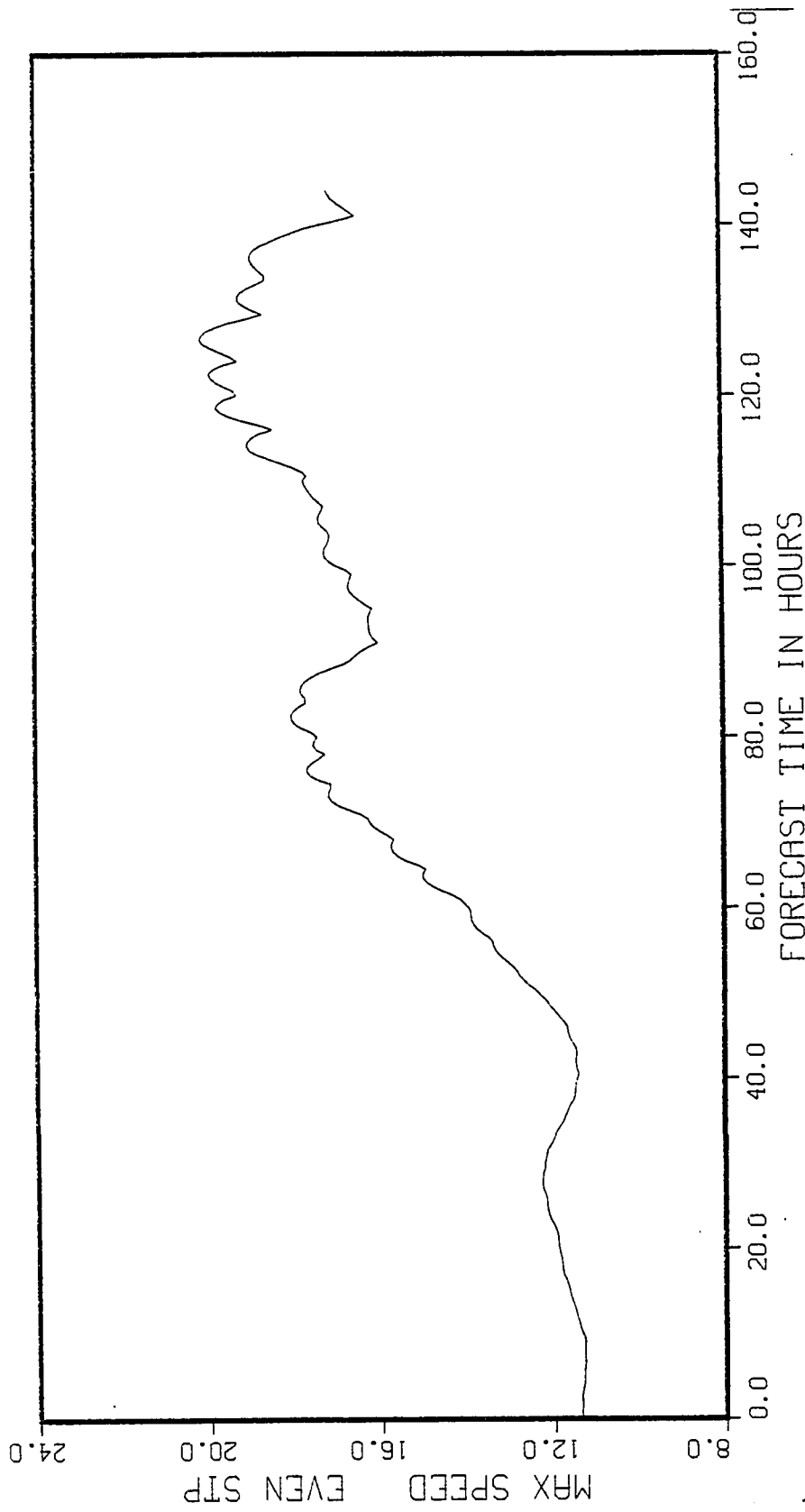


Fig. 31. EC11 experiment. Maximum wind speed versus even time steps.

One can see from Tables 4, 6, and 7 that most of the experiments used zero diffusion. This was deliberate because diffusion terms are sometimes used to mask forecast noise or other forecast model problems and to tune the results. In this sense diffusion is often employed as a numerical filter and not as a physical mechanism. The use of diffusion terms always involves a decision as to the value of the diffusion coefficient. Much debate still exists as to the proper value for atmospheric models. With diffusion in a model, a non-developing integration result might be attributed to the use of too much diffusion. In order to prevent that type of obscuration, most experiments did not contain diffusion.

Notwithstanding the above comments, the atmosphere does indeed contain some sub-grid scale mixing, and it is perhaps prudent to at least run a sample of comparative experiments in order to look at its gross effects on genesis. For these experiments, the values of λ_1 , λ_2 , and μ used by Ooyama (1969) were adopted. EC9 was a repeat of EC4 except for diffusion, and the results showed the expected decay in energy and motion (see Appendix C). EC17 conditions duplicated those of EC11 except for the addition of diffusion. In this instance the diffusion decreased the intensification rate; and, unlike the no-diffusion case (Figure 26), the diffusion did not allow a vortex to completely form in EC17 (Figure 32). Basically, however, EC17 was simply a weaker version

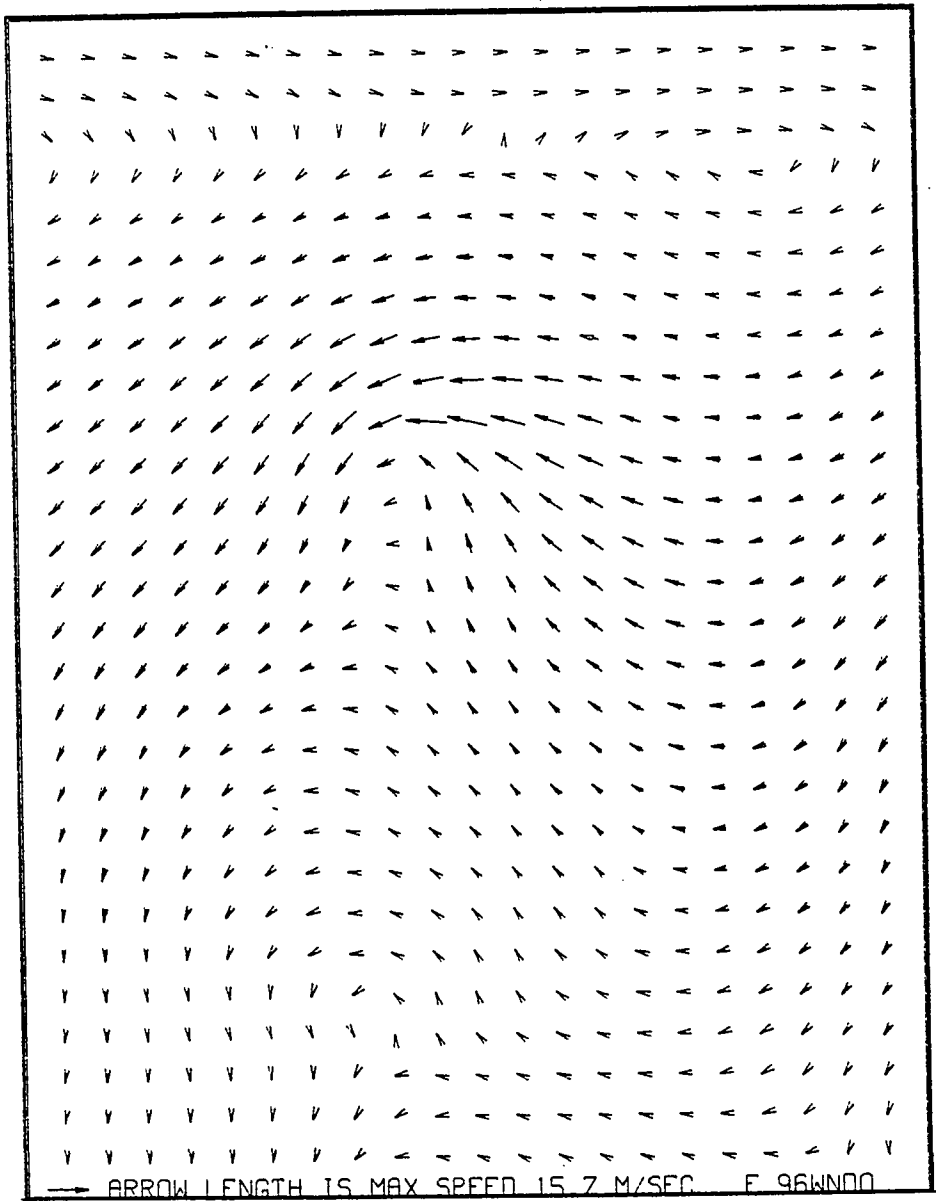


Fig. 32. EC17 experiment. Level 0 wind field at forecast hour 96.

of the no-diffusion experiment, thus confirming the expected result.

In a previous section we saw that the vortex in the V3 experiment attained hurricane force winds. The easterly wave in EC11 intensified somewhat but peaked at a speed below 20 m/sec. What differences allowed one to greatly intensify while the other did not? The basic thermodynamic initial fields of χ_0 and χ_1 were the same in both cases. The initial convective parameter η was uniformly equal to 2 because of the vortex's barotropic state, and this was slightly greater than the values for the easterly wave initial η , which ranged between about 1.6 and 2. This slightly greater convective potential of the vortex should have been offset by its cyclonic upper level circulation as opposed to the hypothetically more favorable slightly anti-cyclonic upper level flow over the easterly wave. In fact, according to McBride's (1979) criteria, the barotropic state of the initial V3 vortex should have prevented its development because the equivalent of $\zeta_{950 \text{ mb}} - \zeta_{200 \text{ mb}}$ was zero.

The vertical wind shear in the vortex (V3) initial fields differed significantly from the wave (EC11) fields, but this was not a significant factor. In the V3 initial state, vertical wind shear is zero because of the barotropic vortex. The easterly wave also has zero shear near the center of the wave vorticity (see Figure 33), but there is westerly vertical wind shear to the north and easterly wind

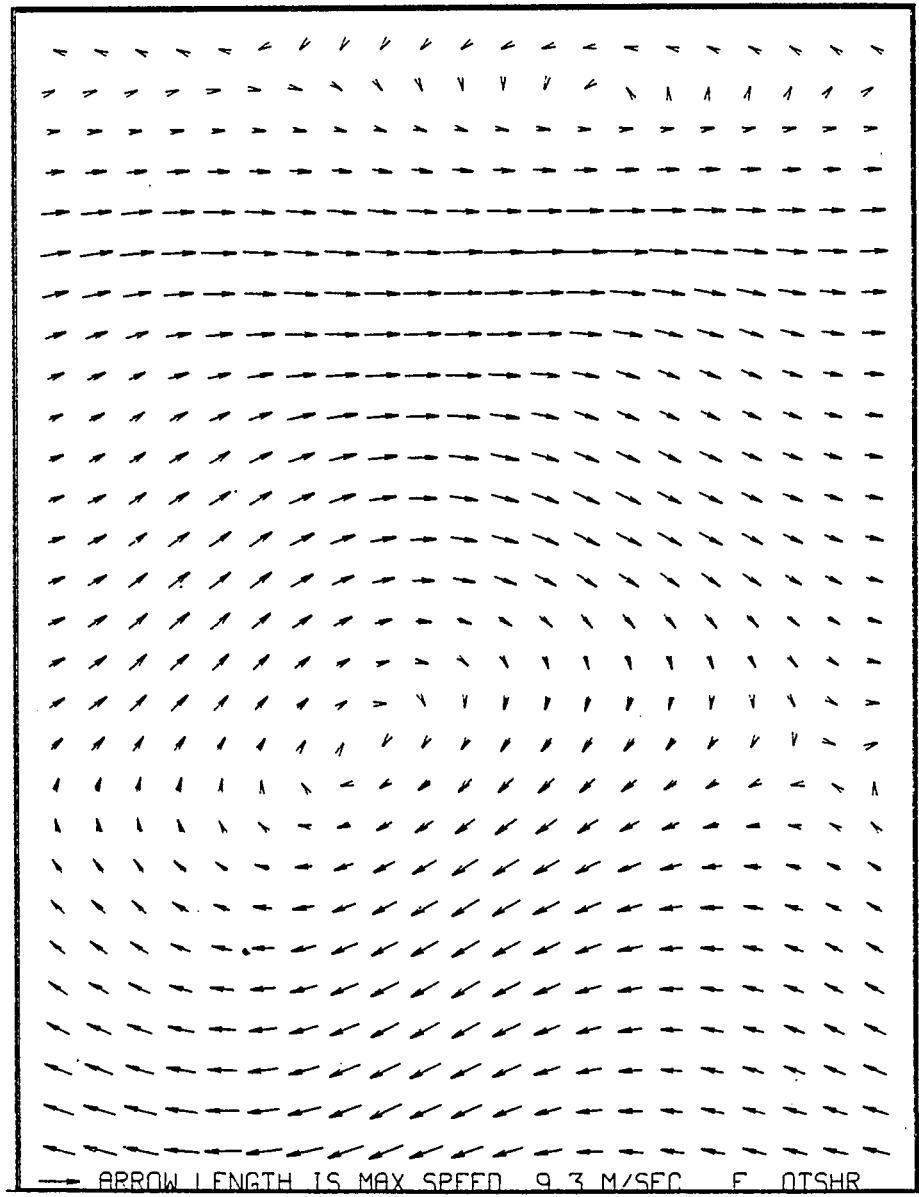


Fig. 33. EC4, 9, 11, 17-20 experiments.
Initial vertical wind shear ($\bar{V}_2 - \bar{V}_0$).

shear to the south. However, as we will discover in a later section, large vertical wind shear, by itself, does not appear to inhibit tropical cyclone genesis. Hence, the differences between the V3 vortex shear and the wave shear are not major factors in determining why V3 greatly intensified and why the wave did not.

At the 96 hour point, the convective stability has significantly increased (η decreased) in the disturbance regions for both the V3 vortex (Figure 34) and the easterly wave (Figure 35). In V3, η has decreased from the initial value of 2.0 to values below 1.2 near the vortex center. The η in the easterly wave has also developed regions of values of less than 1.2 in several areas around the vortex (Figure 35), and this is a decrease from the initial η , which was greater than 1.6 throughout the region. This decrease in η (increase in stability) helped to cap the intensification of both the V3 vortex and the wave vortex because a smaller η in the model tends to reduce the cumulus convection.

A brief look at the initial wind and geopotential fields of V3 and EC11 shows large differences in organization between the two experiments (see Figures 9, 10, 14, and 15). Such differences are implicit in the initial vorticity fields of both V3 and EC11 because the non-divergent winds and the geopotential are directly linked to the vorticity through the stream function and the associated equations (84) to (86). With such connections, the vorticity fields, by themselves,

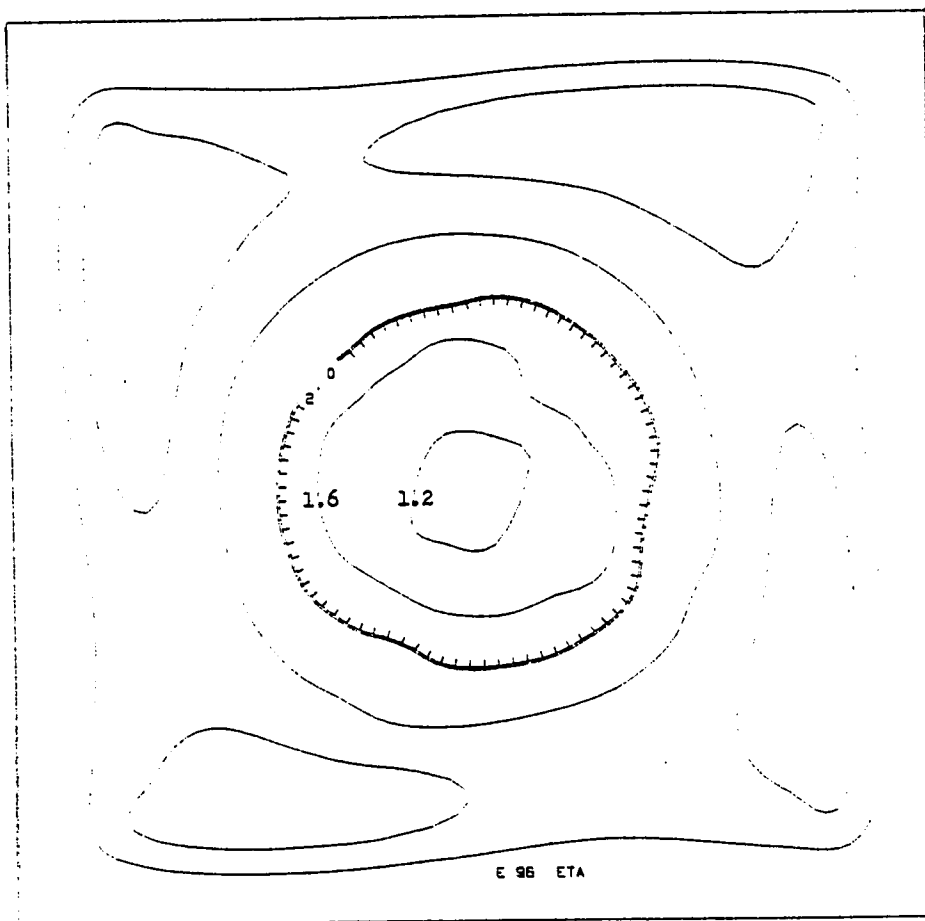


Fig. 34. V3 experiment. Stability factor η at forecast hour 96.

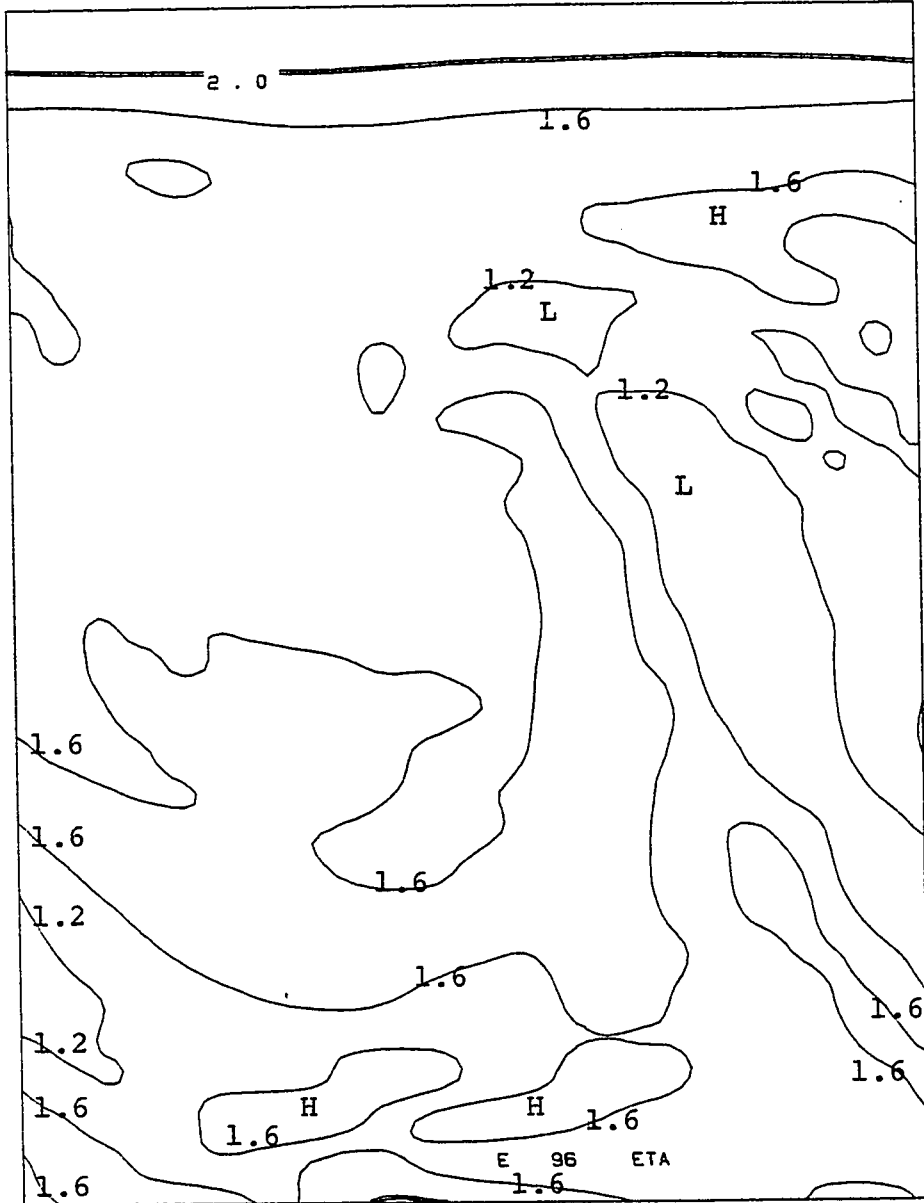


Fig. 35. EC11 experiment. Thermodynamic stability parameter η at forecast hour 96.

should reasonably characterize major differences in organization between V3 and EC11.

Examination of the vorticity fields of V3 and EC11 shows telling differences between the two experiments. From Table 8 we see that the initial easterly wave actually has a higher areal coverage for the low values of positive vorticity $1 \times 10^{-5} \text{ sec}^{-1}$ and $2 \times 10^{-5} \text{ sec}^{-1}$ (see also Figure 36). However, the wave vorticity does not have any area with vorticity greater than $3 \times 10^{-5} \text{ sec}^{-1}$, whereas the vortex has a significant area with vorticity above that value. The initial V3 vortex vorticity actually exceeds $10 \times 10^{-5} \text{ sec}^{-1}$ within a radius of about 118 km and reaches a maximum of $13.33 \times 10^{-5} \text{ sec}^{-1}$ at the center. In other words, in the central part of the disturbance, within at least the inner 300 km from the center, the initial vorticity in V3 greatly exceeds that in the initial wave of EC11.

Table 8 and Figure 37 reveal that the vorticity of the wave vortex at 96 hours is only slightly greater than the initial V3 vortex field. Yet the increased convective stability at the 96 hour point is a significant damper on further intensification.

A consistent explanation for why V3 greatly intensified and the wave did not may rest in the initial vorticity fields. Although both intensified due to CISK, the intensification itself increased convective stability and eventually brought both intensifications to a halt within

TABLE 8
BOUNDARY LAYER VORTICITY CONCENTRATION

Experiment	Time of Data (hr)	Radius (km)	$\zeta_0 (10^{-5} \text{sec}^{-1})$	Area ($\text{km}^2 \times 10^5$) $\zeta > \zeta_0$
V3 ¹	0	488.5	1	7.50
V3 ¹	0	377.33	2	4.48
V3 ¹	0	315.81	3	3.13
V3 ¹	0	117.995	10	.44
V3 ¹	0	0	13.33	0
EC11 ²	0		1	10.3
EC11 ²	0		2	3.5
EC11 ²	96		2	2.8
EC11 ²	96		10	.4
EC11 ²	96		15	.2

¹Vortex vorticities calculated from analytical formulas describing the initial vortex. The tangential velocity of the symmetric vortex is defined

$$v = \frac{\hat{v}(r/\hat{r})}{1 + (r/\hat{r})^2}$$

where \hat{r} is the radius at which the maximum wind \hat{v} occurs. Since the vorticity for a symmetric vortex is $\zeta = (1/r) \partial(vr)/\partial r$, the vorticity for the initial V3 vortex becomes

$$\zeta = 4 (\hat{v}/\hat{r}) / \{ [1 + (r/\hat{r})^2]^2 \}$$

²Wave vorticities and plots estimated from displays.

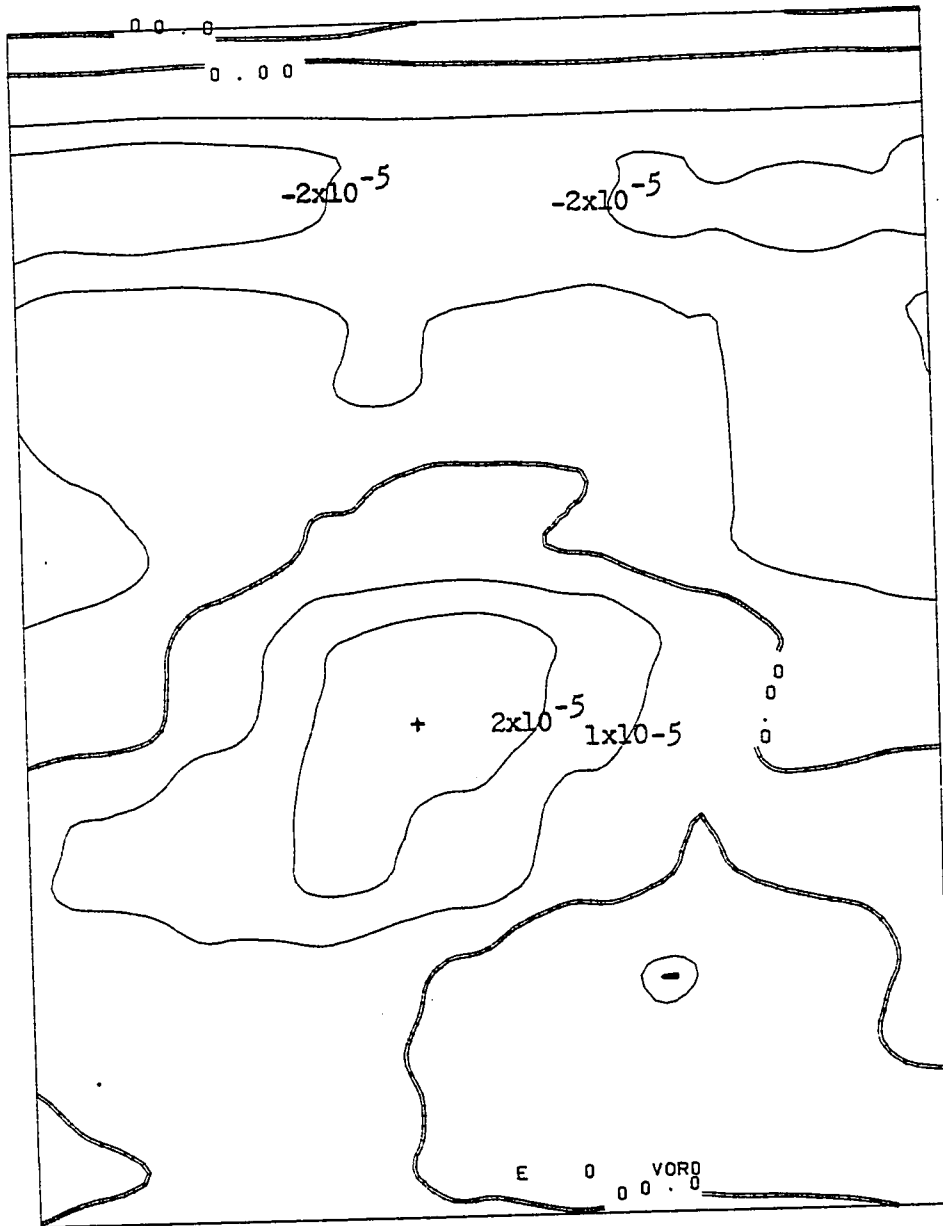


Fig. 36. EC4-9, 11-15, 17-20 experiments.
Levels 0 and 1 initial vorticity.



Fig. 37. EC11 experiment. Level 0 vorticity at forecast hour 96.

approximately the same time scale. However, during that time, V3 had a much larger initial supply of low level vorticity to concentrate than did EC11. We can see the effect of this larger vorticity supply by looking at the symmetric angular momentum equation:

$$\frac{\partial r v_T}{\partial t} = -ru(\zeta + f) - r C_D |\bar{v}| v_T \quad (92)$$

where ζ is vorticity, r is radius, v_T is tangential velocity, u is radial velocity, $|\bar{v}|$ is wind speed, and f is the Coriolis parameter. Given a period of time Δt and a negative u (inflow), a larger value of initial vorticity will result in a larger increase in positive relative angular momentum and a net larger intensification. V3 had larger initial low level vorticity; and it intensified more, suggesting that the larger vorticity may have been a large factor in the different intensification rates of V3 and EC11.

The emphasis on low level flow as being more critical than the upper levels is supported by Shapiro's work (1977, 1977a). He developed an easterly wave intensification criterion based upon a scaling of the potential vorticity equation and using low level (1000-600 mb average) wind data to calculate the critical parameter ϵ' . Although ϵ' is not simply a relative vorticity, a quick calculation from one of Shapiro's charts (1977, p. 1015) shows that high values

of ϵ' tend to be associated with high values of ζ and low values of ϵ' with low values of ζ .

Other support for the overwhelming significance of low level vorticity comes from Zehr (1976) and Erickson (1977). Both of their studies indicate more difference between the vorticities in developing and non-developing disturbances than any other factor that they studied. The differences in the lower level vorticity were 2:1 or greater in many instances.

The results of the above experiments point to the effect of lower level vorticity on intensification, but the actual formation of such initial vorticity differences still remains unclear. For some disturbances, such as easterly waves, the initiating barotropic instability mechanism may play a role in the magnitude of vorticity supplied to a newly growing wave. In other cases, as Shapiro's work might suggest, weak disturbances may acquire additional vorticity by moving through regions with high environmental vorticity. And finally, we shall see in the next section that warm sea surface temperatures and low level moisture may aid the vorticity generation and intensification process.

As mentioned before, the initial upper levels of V3 and EC11 seemed to have little impact on the relative disturbance intensities developed in the two experiments. The development seemed to be forced primarily from the lower levels and did not require one of Riehl's (1954) initiating

events in the upper atmosphere. In the V3 experiment the lower level disturbance actually created its own favorable support by the cumulus-forced transformation of an upper level cyclone into a divergent anticyclone. Although initial upper level fields may have some impact on tropical development, the results of the V3 and EC11 experiments suggest that such impact may be small relative to the impact of the lower level vorticity.

In summary, the results of this model support the hypothesis that the low level vorticity field is a very large factor in the intensification of weak tropical disturbances. We have seen that two initial states with large differences in vorticities will develop into disturbances of significantly different intensities: the larger initial vorticity being associated with the more intense disturbance. The modeling results are not totally conclusive because the V3 initial state, although still relatively weak, does contain a closed circulation and is less representative of a weak tropical disturbance than one would prefer. However, the differences in development between V3 and EC11 are so large that the vorticity effect should be a significant factor in real tropical cyclone intensification and not simply limited to the simulations discussed here.

4.3 Sea Surface Temperature and Moisture Effects

In the previous sections we discussed model experiments that all had essentially the same thermodynamic initial

conditions. Setting χ_0 and $\bar{\chi}_s$ the same in the experiments of Tables 4, 6, and 7 allowed a better comparison of dynamic factors between experiments, but this practice did not allow the relative impact of moisture and sea surface temperature to be studied.

In the EC11 and EC17 experiments, the composite easterly wave did not strongly intensify with the given χ_0 and $\bar{\chi}_s$ initial conditions, although the V3 vortex developed rapidly under the same conditions. Such weak development in the wave naturally led to questions concerning the possible impact of an enhanced thermodynamic initial state for the wave. In turn, these questions resulted in the EC23 and EC24 experiments.

Experiments EC23 and EC24 were duplicates of EC11 and EC17, respectively, in all aspects except $\bar{\chi}_s$ and the initial χ_0 fields (Table 9). All four experiments used the composite easterly wave initial conditions (Figures 14, 18), and EC17 and EC24 included diffusion whereas EC11 and EC23 did not. The change in $\bar{\chi}_s$ from 30°C in EC11 and EC17 to 40°C in EC23 and EC24 was equivalent to a sea surface temperature change from approximately 28.6°C to 30.3°C (See Table 2). In addition, the χ_0 initial field was increased from a value of 10 to a value of 20, which was equivalent to an equivalent-potential temperature change from 350 K to 360 K.

The combined new values of χ_0 and $\bar{\chi}_s$ represented a very warm, moist boundary-layer environment. They represent, in

TABLE 9

CYCLIC BOUNDARY EXPERIMENTS WITH MODIFIED
CUMULUS PARAMETERIZATION OR BOUNDARY
LAYER MOISTURE CHANGES

Designator	Comments
EC21	Same as EC14 except η , stability parameter, held at constant value of 2 throughout simulation.
EC22	Same as EC15 except η , stability parameter, held at constant value of 2 throughout simulation and integration period limited to 94 hours.
EC23	Same as EC11 except $[\bar{\chi}_s]$ set to spatially, temporally constant 40, χ_0 set to initially uniform 20, and integration period limited to 80.5 hours.
EC24	Same as EC17 except $[\bar{\chi}_s]$ set to spatially, temporally constant 40, and χ_0 set to initially uniform 20.

some sense, the most favorable thermodynamic conditions that a wave might encounter in the boundary layer. As such, these initial conditions were appropriate for testing the maximum effect that more favorable thermodynamic conditions might have on stimulating development of the easterly wave.

The expected increased intensification occurred, but the magnitude of the effect was unexpected. In EC23, the changed conditions forced very rapid development, and a maximum layer 1 wind of over 30 m/sec was achieved at 80.25 hours before the integration became unstable. This value is in sharp contrast to the EC11 experiment where the intensification peaked at only a little over 17.8 m/sec at 85.5 hours.

Even with diffusion included, the wave in EC24 greatly intensified because of the more favorable χ_0 and $\bar{\chi}_s$. In EC17, wave intensification peaked at a little over 15 m/sec for layer 1, and no closed vortex formed (Figure 32). However, the wave in EC24 formed a very definite closed vortex as Figure 38 shows, and the maximum layer 1 wind was over 26 m/sec by forecast hour 96 (Figure 39).

In the previous section, we looked at intensification as a concentration of existing vorticity. In this section, we have added another potent genesis factor, the creation of vorticity by diabatic heating. In order to illustrate this effect, we need the frictionless horizontal divergence equation for layer 1:

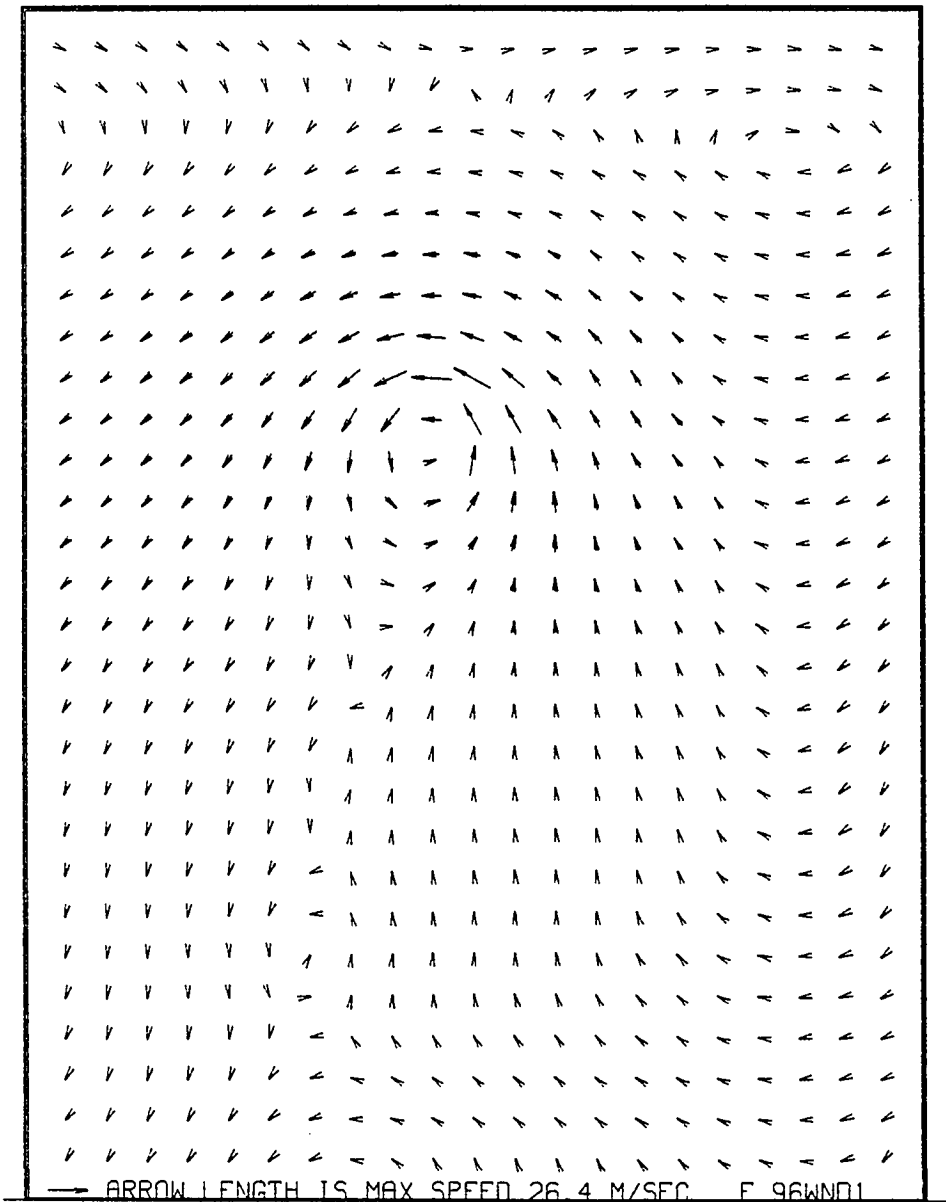


Fig. 38. EC24 experiment. Level 1 wind field at forecast hour 96.

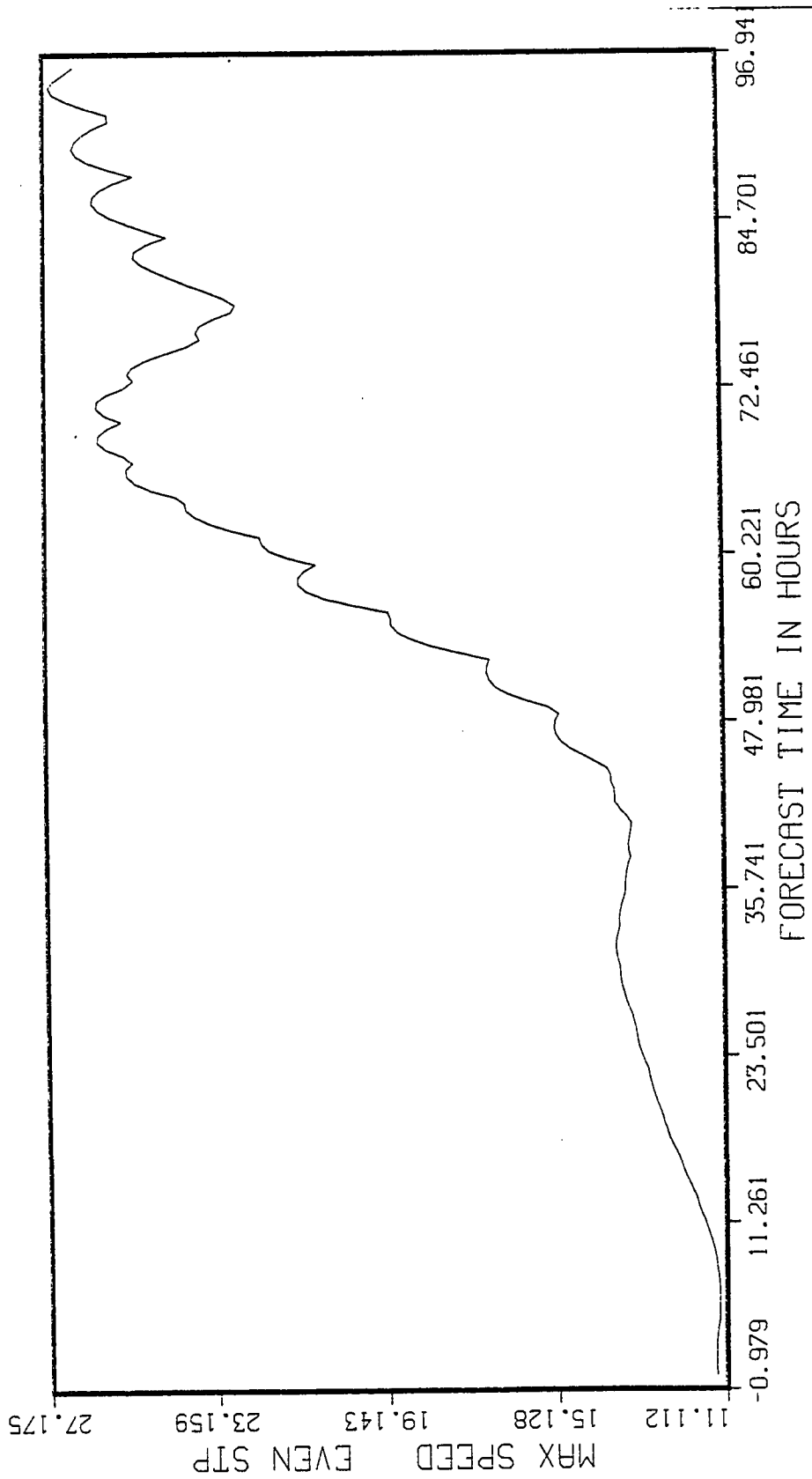


Fig. 39. EC24 experiment. Level 1 maximum wind speed (m/sec) versus even time steps.

$$\begin{aligned} \frac{d\delta_1}{dt} = & -\nabla^2 (h_1 + \epsilon h_2) - 2 \frac{\partial v_1}{\partial x} \frac{\partial u_1}{\partial y} - \left(\frac{\partial u_1}{\partial x}\right)^2 \\ & - \left(\frac{\partial v_1}{\partial y}\right)^2 + f\zeta_1 - \beta u_1 \end{aligned} \quad (93)$$

where δ_1 is the horizontal divergence in layer 1, h_1 and h_2 are layer 1 and layer 2 thickness values, u_1 and v_1 are layer horizontal wind components, ζ_1 is layer 1 vorticity, and β is $\partial f/\partial y$. Since changes in h_1 and h_2 were linked to cumulus convection in (5) and (6), we can see from (93) that changes in δ_1 are, at least, indirectly linked to the cumulus convection because of the $\nabla^2 (h_1 + \epsilon h_2)$ term. Now the changes in δ_1 are further linked to the changes in vorticity by the frictionless vorticity equation:

$$\frac{d\zeta_1}{dt} = -(\zeta_1 + f)\delta_1 - \beta v_1 \quad (94)$$

With (94), the conceptual chain is complete:

- (1) changes in cumulus convection cause changes in h_1 and h_2 through the Q term,
- (2) resulting in changes in $\nabla^2 (h_1 + \epsilon h_2)$ and consequently in δ_1 through (93), and
- (3) which further results in changes in ζ_1 through (94).

Thus, favorable thermodynamic conditions that enhance convection indirectly change the vorticity field. The strong intensification in EC23 and EC24 attest to the very strong positive nature of such a diabatic effect.

From the model results above, it is quite evident that favorable thermodynamic conditions can dramatically enhance the development of weak tropical disturbances. The effect is so large that even small changes in $\bar{\chi}_s$ or χ_0 would have a significant effect on development. If the real atmosphere is as sensitive to such effects, then some of the difficulty in isolating developing from non-developing disturbances may stem from the difficulty in observing small changes of moisture and sea surface temperature in the real world.

4.4 Vertical Wind Shear Effects

Several studies have associated vertical shear of the horizontal wind with tropical cyclogenesis. In particular, Gray (1975), Zehr (1976), and Lopez (1968) have stressed the idea that motion of a disturbance through a field with a large vertical wind shear ventilates the disturbance core and prevents the enthalpy concentration necessary for genesis or intensification. However, these studies and others like them failed to isolate the wind shear effect from other dynamical factors statistically associated with weak or strong wind shear; and it was not clear that the wind shear was a destructive factor, in and of itself.

The desire to isolate this wind shear effect led to a series of experiments combining 700 mb GATE-composite wave initial conditions in layers 0 and 1 with different mean u flows in layer 2. Integration of these different states should have led to decreased genesis with increasing wind

shear, if the shear hypothesis were true.

The results show a different story. Looking at Table 10, we see that all of the vertical wind shear cases develop vortices (see also Figures 40, 41, 42, and 43) of about the same intensity. The only consistent relationship is one between increasing easterly vertical wind shear and an increasing intensification rate (see also Figures 44, 45, 46, and 47), but the final magnitude of the developed vortex does not appear to be affected very much.

These results are contrary to the generally accepted effect, but they are not necessarily contrary to observations concerning shear effects on cumulus clouds. For many years strong vertical wind shears have often been associated with the development of severe storms in mid-latitudes. These storms, which include tornados, are often more intense than the tropical convection in cloud clusters and tropical cyclones; yet they develop in the presence of high vertical wind shear.

Several control experiments verified that the CISK shear results were due to a combination of CISK and the initial state rather than reflecting solely the properties of the initial state. These controls, EC6, EC7, and EC8, each had the same initial conditions as its respective mate in the trio of EC13, EC14, and EC15;¹ but the integrations of the controls

¹The basic effect was confirmed by the first three experiments. There was little need to run a control on the EC12 experiment.

TABLE 10

EFFECTS OF UPPER LEVEL WIND SHEAR ON CYCLONE GENESIS

Experiment	Initialization		Formation of Vortex by 96 hrs.		Max. speed within 96 hrs	Time ¹ to exceed 16m/sec (hr.)	Time ¹ to Reach max. spd. (hr.)
	level 0,1	level 2	level 0	level 1			
EC11	700mb composite wave	300mb composite wave	yes	yes	18.0	69.5	82.5
EC12	700mb composite wave	u2 =+9.5 v2 = 0	yes	yes	17.9	85.0	88.5
EC13	700mb composite wave	u2 = 0 v2 = 0	yes	yes	20.5	67.0	81.5
EC14	700mb composite wave	u2 =-10 v2 = 0	yes	yes	19.4	63.0	82.5
EC15	700mb composite wave	u2 =-20	yes	yes	20.6	59.5	76.0

¹Relative to the even time steps.

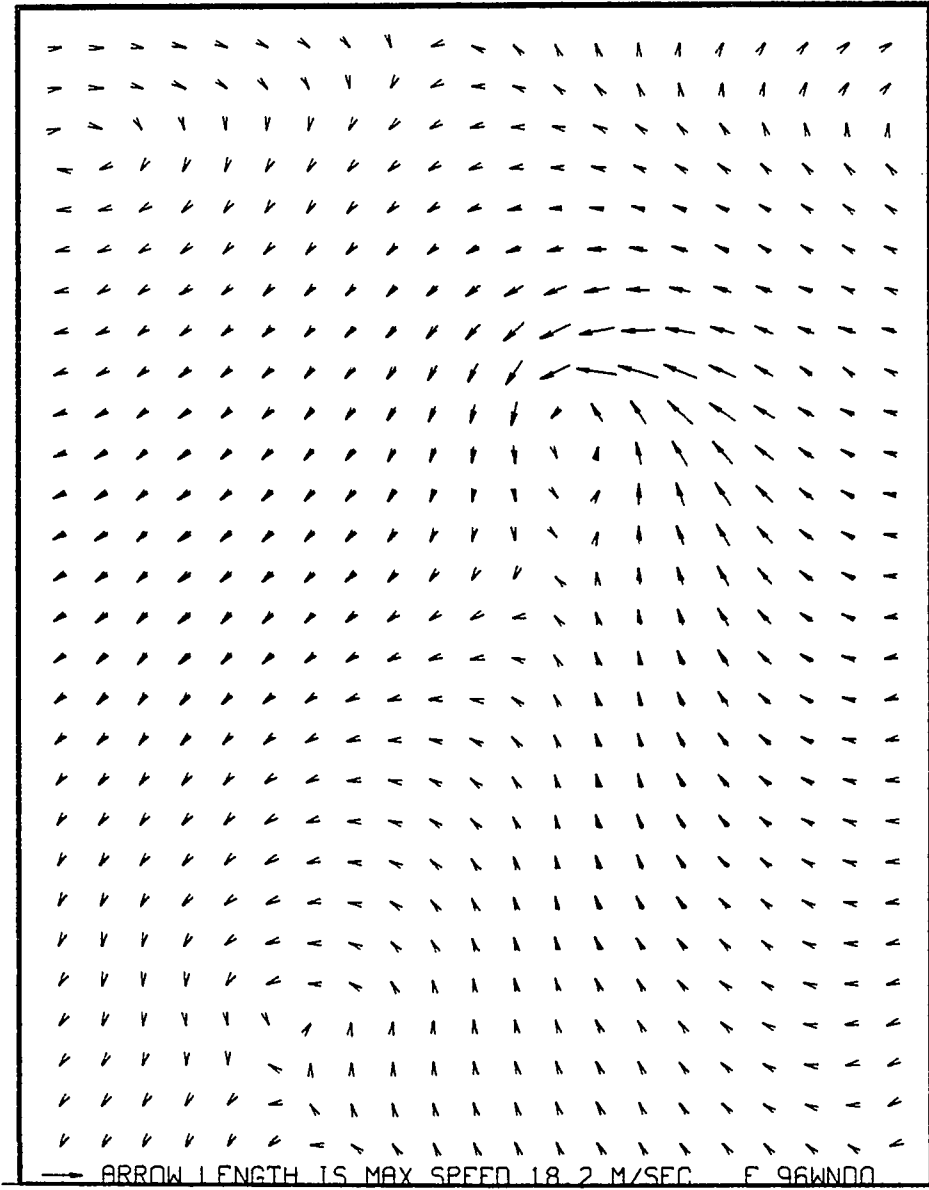


Fig. 40. EC12 experiment. Level 0 wind at forecast hour 96.

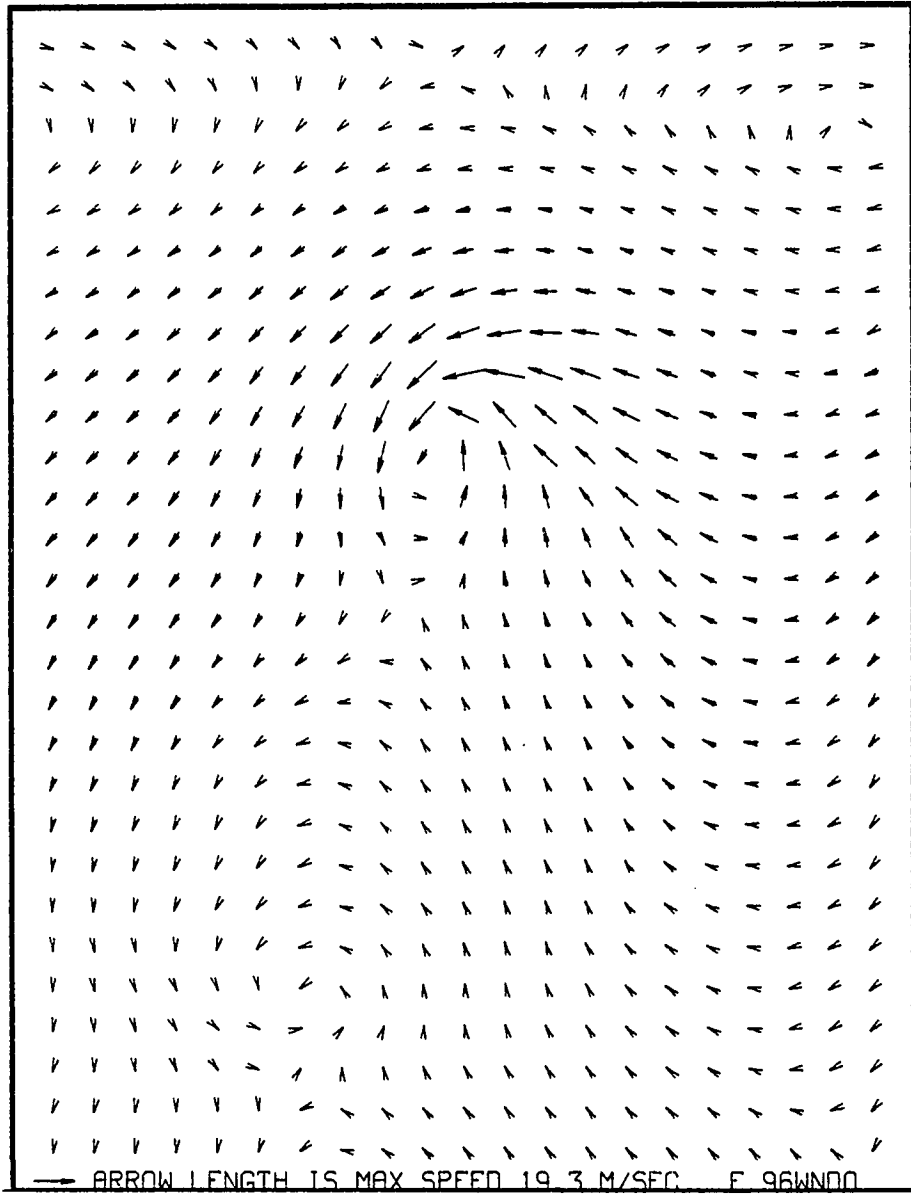


Fig. 41. EC13 experiment. Level 0 wind field at forecast hour 96.

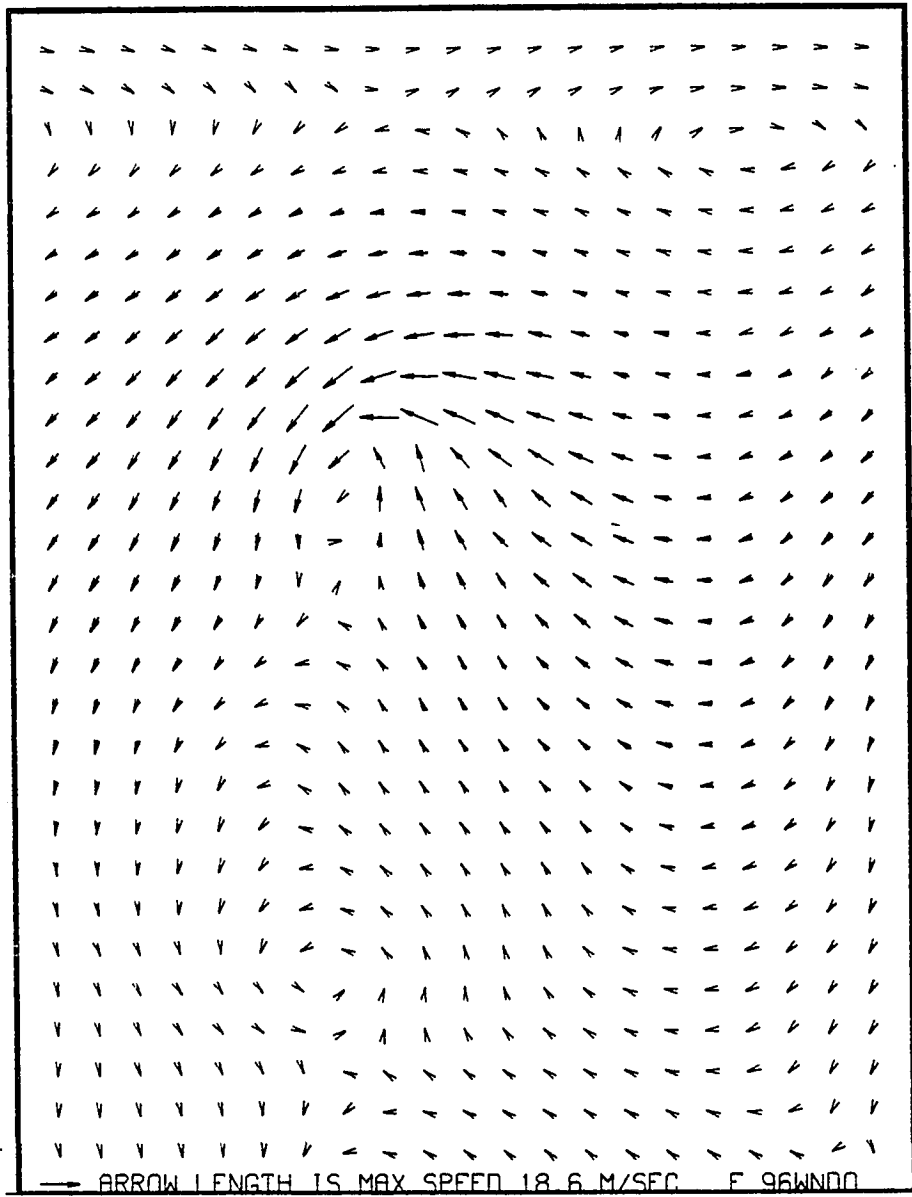


Fig. 42. EC14 experiment. Level 0 wind field at forecast hour 96.

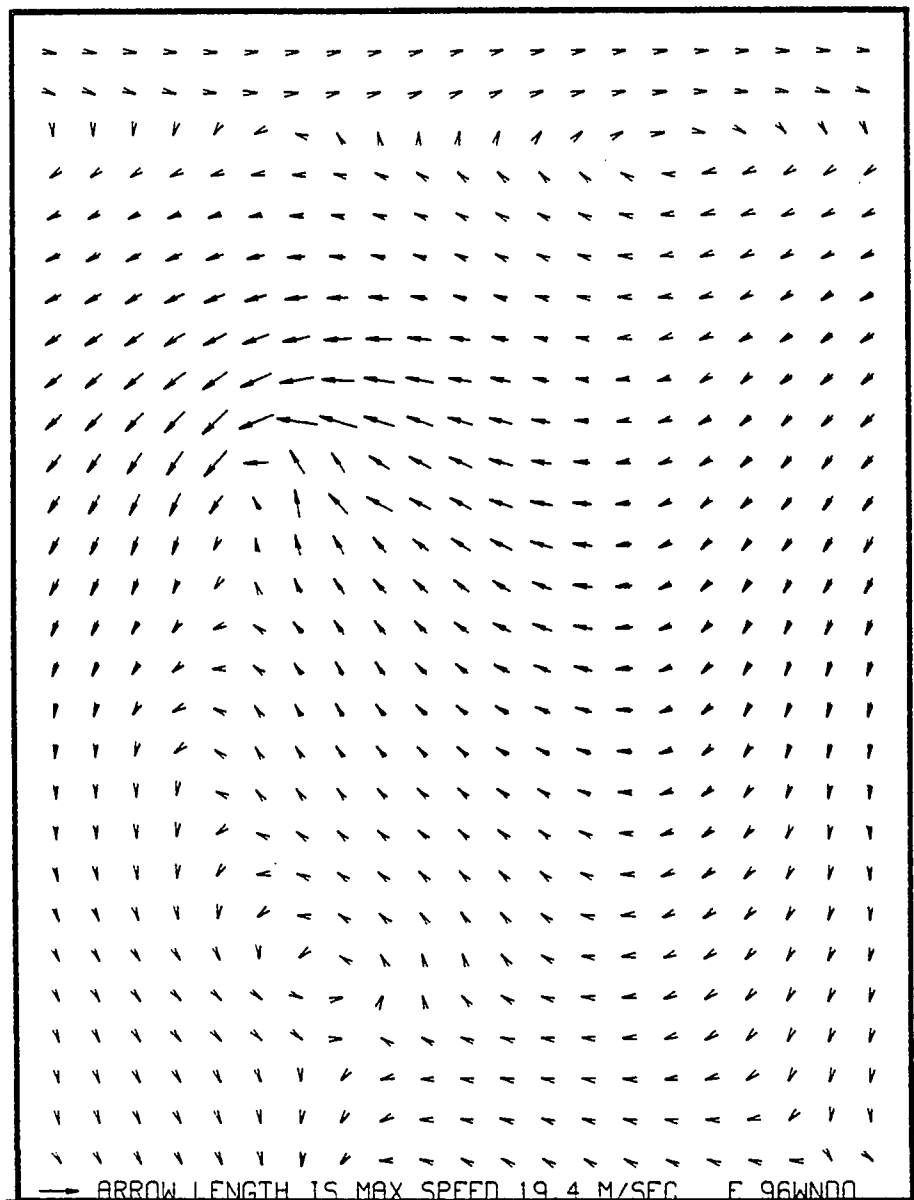


Fig. 43. EC15 experiment. Level 0 wind field at forecast hour 96. Closed vortex above is not evident because of u, v averaging to display on ϕ grid points. Actual data shows positive u necessary to close vortex.

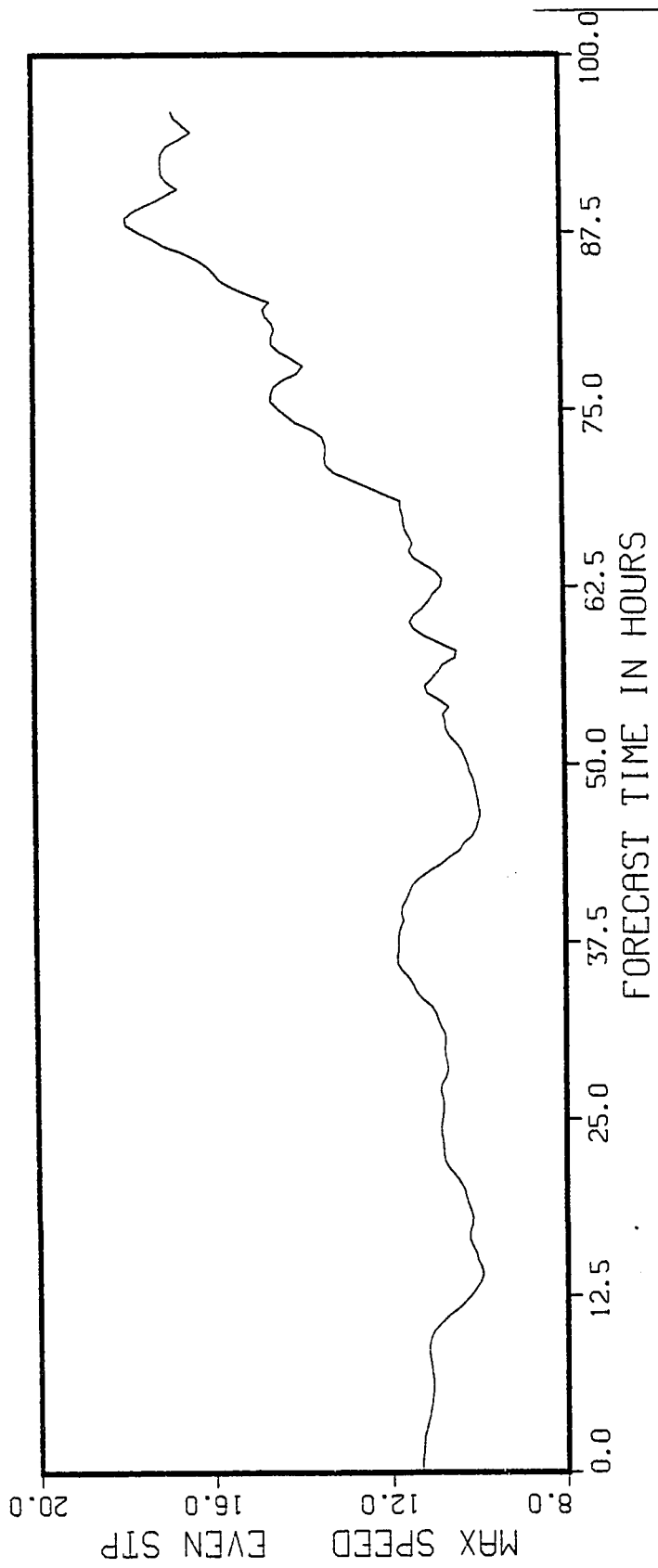


Fig. 44. ECl2 experiment. Level 1 maximum wind speed versus even time steps.

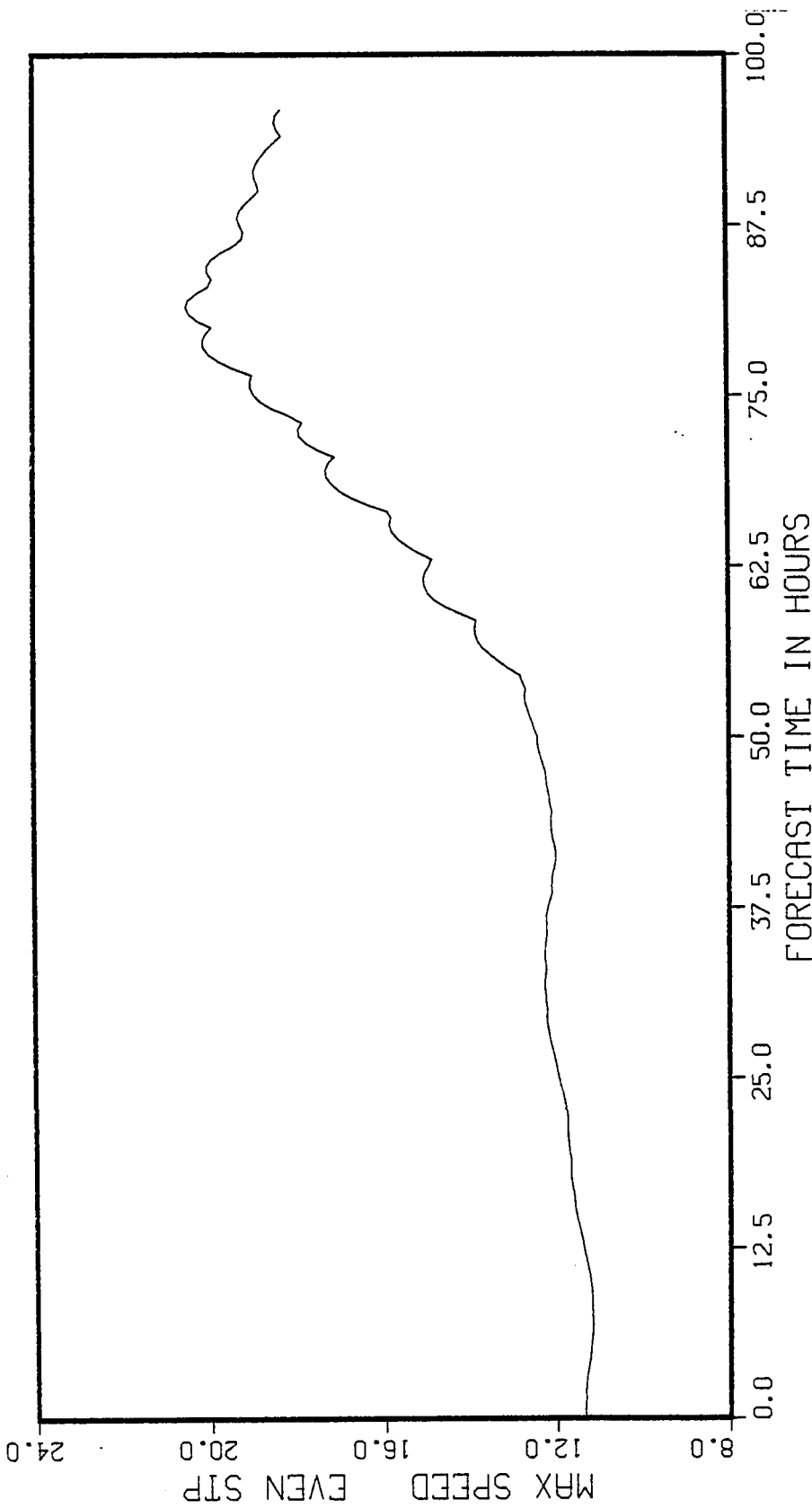


Fig. 45. ECL3 experiment. Level 1 maximum wind speed versus even time steps.

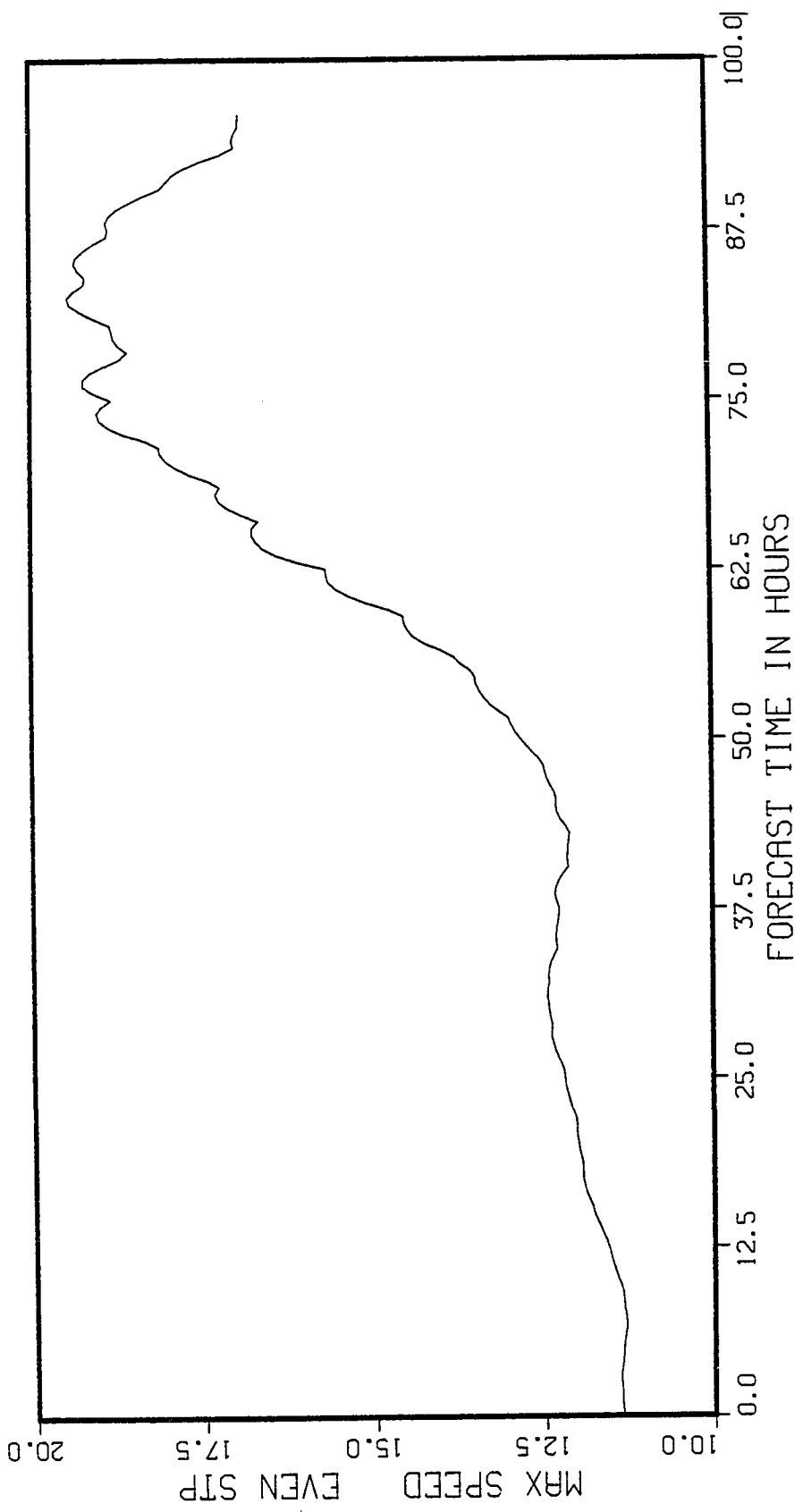


Fig. 46. EC14 experiment. Level 1 maximum wind speed versus even time steps.

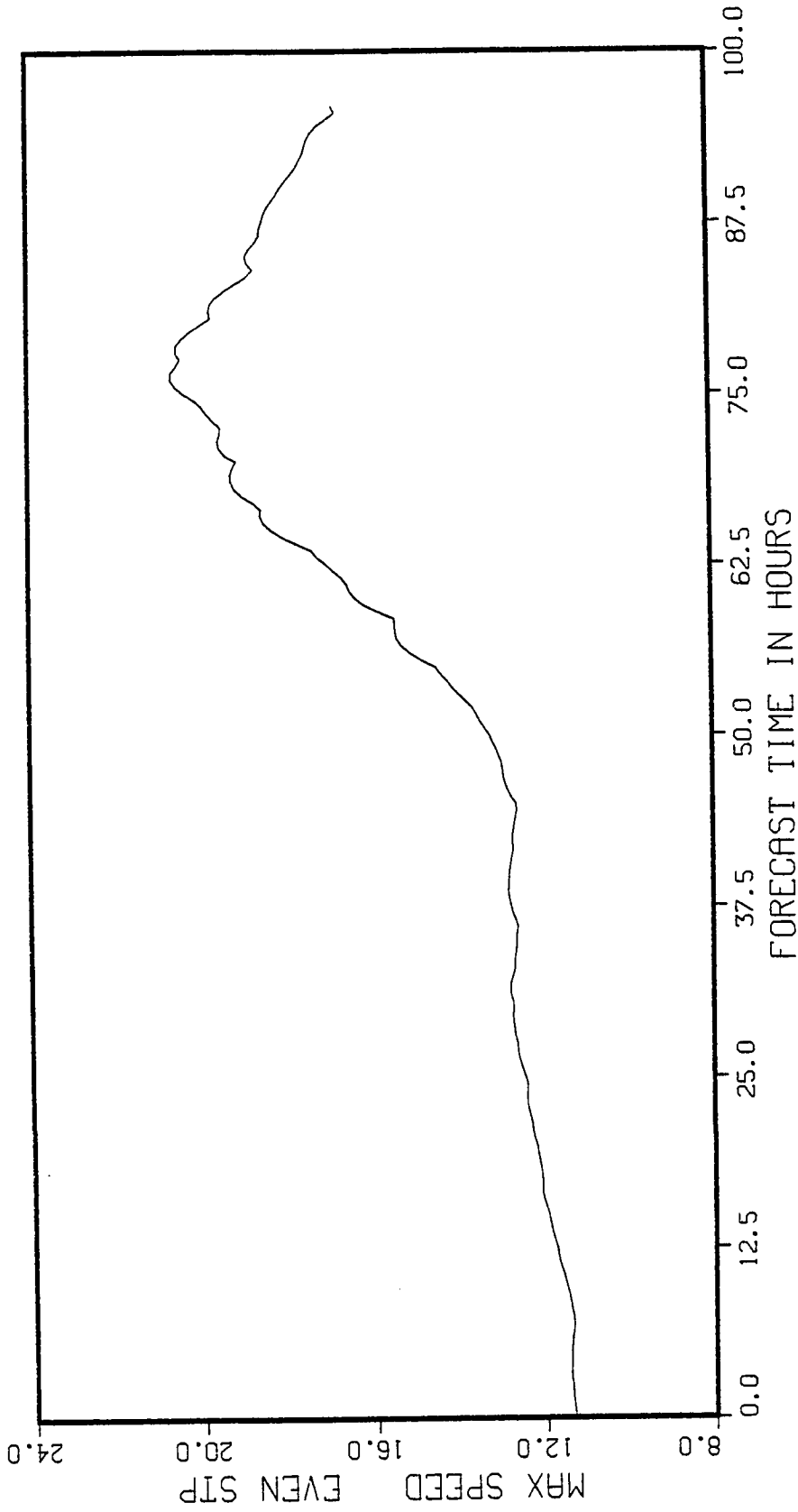


Fig. 47. EC15 Experiment. Level 1 maximum wind speed versus even time steps.

proceeded with all sources and sinks turned off.

Unlike the diabatic experiments, the controls above produced no closed cyclonic circulations. The results, as shown in Figures 48, 49, and 50, are generally rather undramatic and emphasize that the basic initial shear fields, by themselves, were not unstable or capable of development without added diabatic forcing.

One interesting observation was the monotonically increasing southeast-to-northwest tilt as the easterly vertical wind shear was increased. This effect is very obvious when Figures 48, 49, and 50 are compared, and it basically can be explained by the cyclic southern boundary that separates easterly mean flow from westerly (see also section 4.2). Because flow is not discontinuous at this boundary, the easterly flow must begin to decrease as it approaches the southern boundary, thus creating a negative meridional gradient in u near the southern boundary. Such a gradient, with stronger mean easterlies to the north and weaker to the south, allows the northern wave portion to move eastward faster than the southern portion, leading to the reversed tilt. With stronger easterlies, the gradient toward the southern boundary becomes larger and the tilting is accentuated. Thus, the wave in EC8 is tilted more than that of EC7, which is in turn tilted more than the EC6 wave.

Another example of the effect of the cyclic boundary can be seen by comparing Figures 51 and 52. In EC7 the

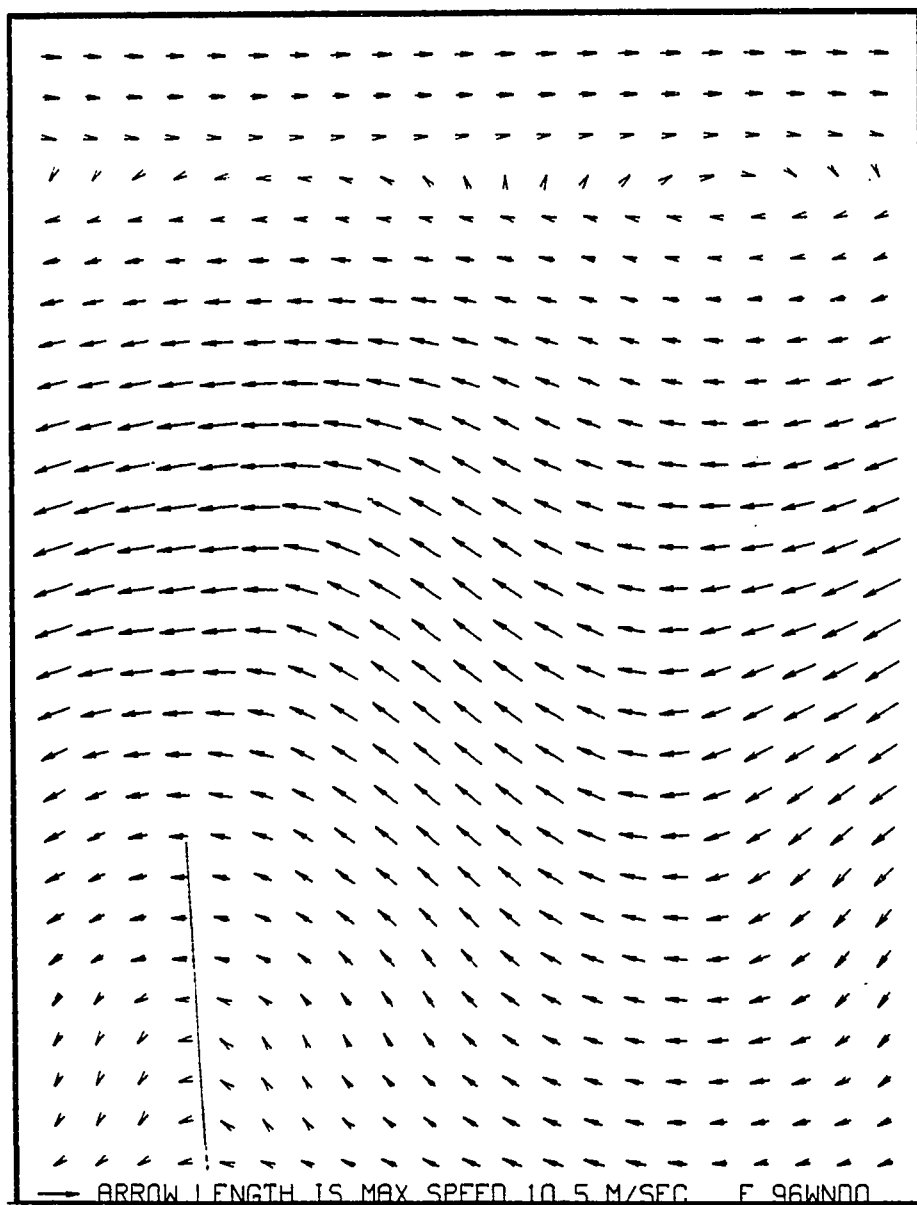


Figure 48. EC6 experiment. Levels 0 and 1 wind field at forecast hour 96.

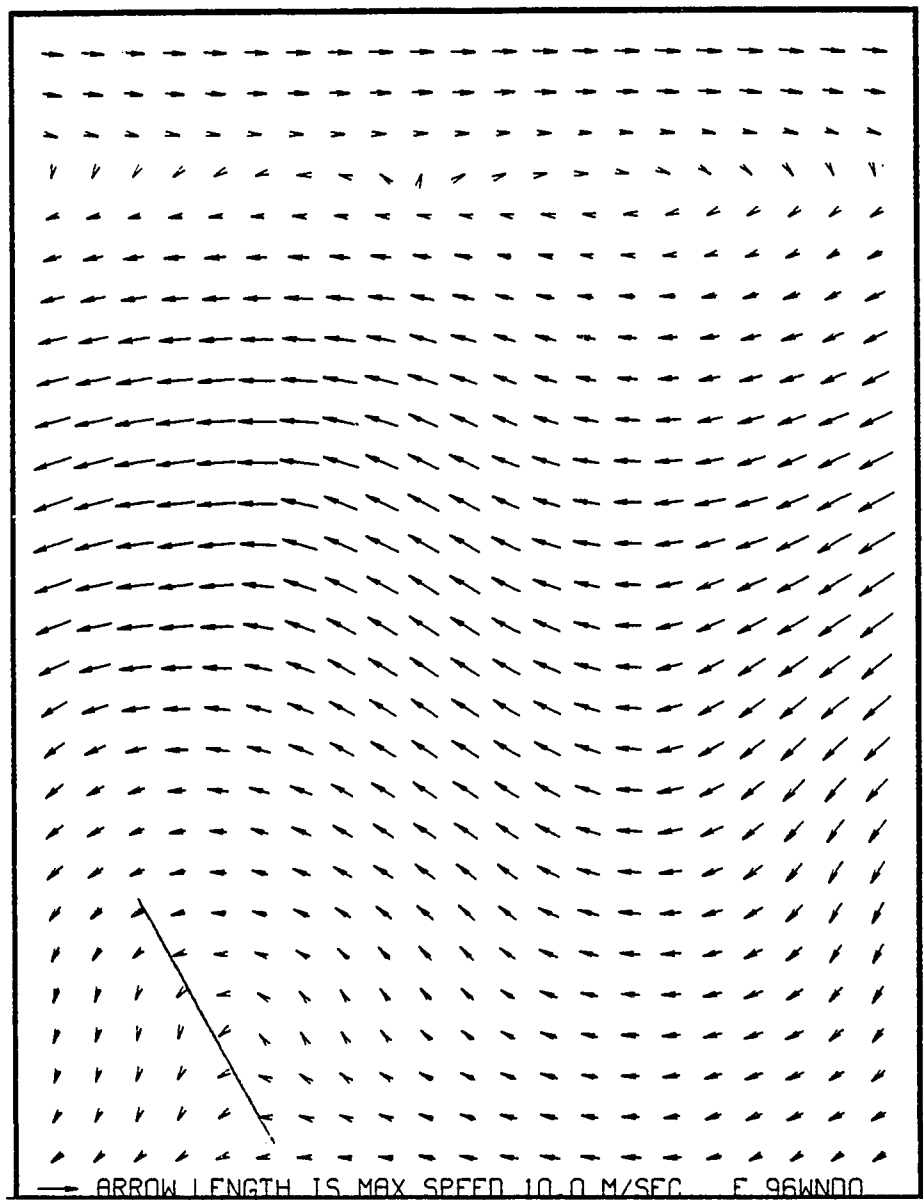


Fig. 49. EC7 experiment. Levels 0 and 1 wind field at forecast hour 96.

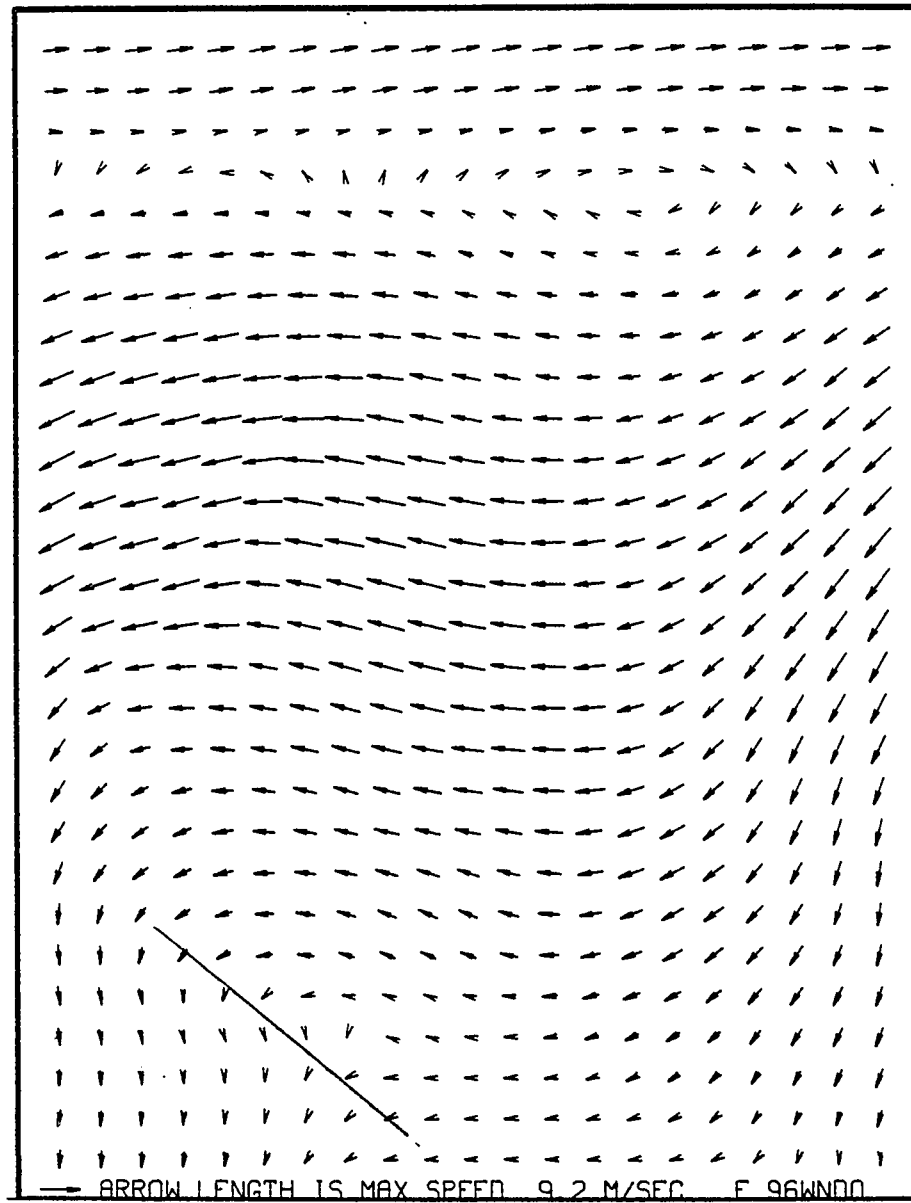


Fig. 50. EC8 experiment. Levels 0 and 1 wind field at forecast hour 96.

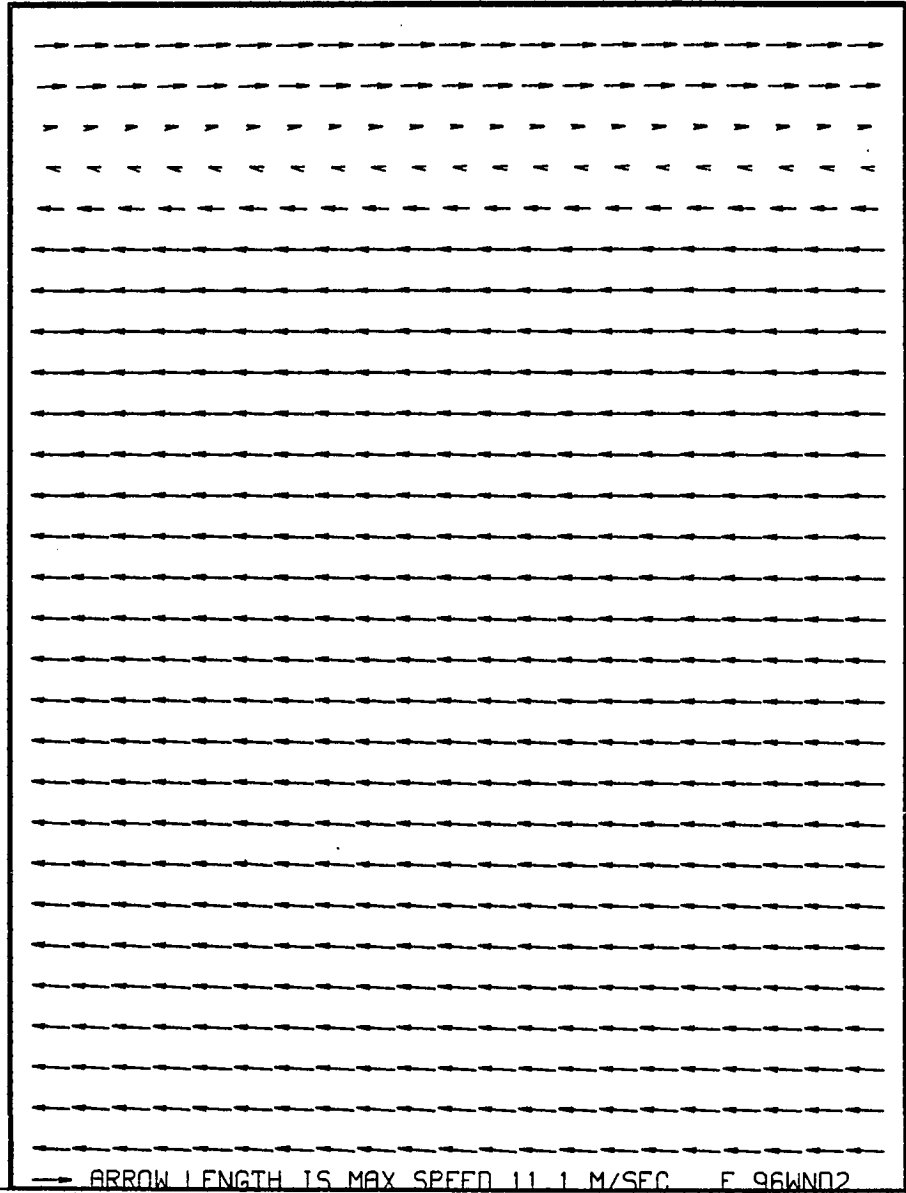


Fig. 51. EC7 experiment. Level 2
wind field at forecast hour 96.

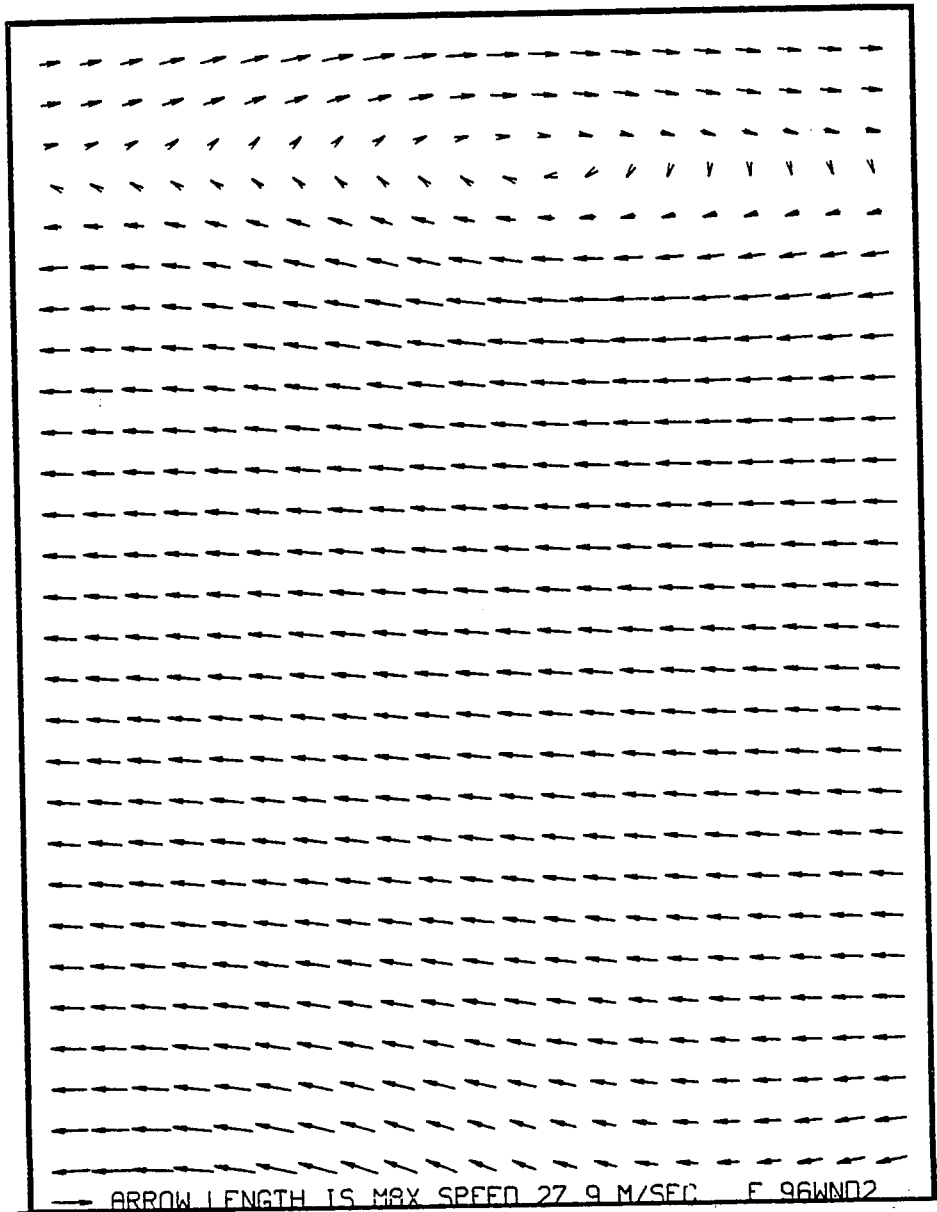


Fig. 52. EC8 experiment. Level 2 wind field at forecast hour 96.

initial mean u for level 2 is approximately -10 m/sec, and the gradient across the southern boundary does not cause much distortion in the 96 hour forecast field. However, with an increase in the initial mean u to -20 m/sec in EC8, the gradient across the southern boundary becomes much greater; and the slight turning of the wind near the southern boundary in Figure 52 probably reflects the impact of the increased gradient across the southern boundary.

An interesting illustration of dynamical effects is seen in the level 2 forecast for EC6. This experiment initially had a quiescent upper level field, but the baroclinic initial state forced a circulation to develop in level 2. This is particularly clear at the 48 hour point where a weak upper level anticyclone is positioned east of the lower wave trough and a weak cyclone positioned just west of the wave trough (Figures 53 and 54).

Energy and wind speed are other factors to note in the control experiments. In all of the control experiments, the total area kinetic energies did not vary significantly over the 96 hour period, although there were some small oscillations similar to those in EC4. However, the level 1 maximum winds did decrease slightly in all three controls, with the most decrease being in EC8 and the least in EC6.

As noted before, the intensification in the diabatically-forced experiments appeared to be somewhat greater as the initial vertical wind shear was increased. A possible

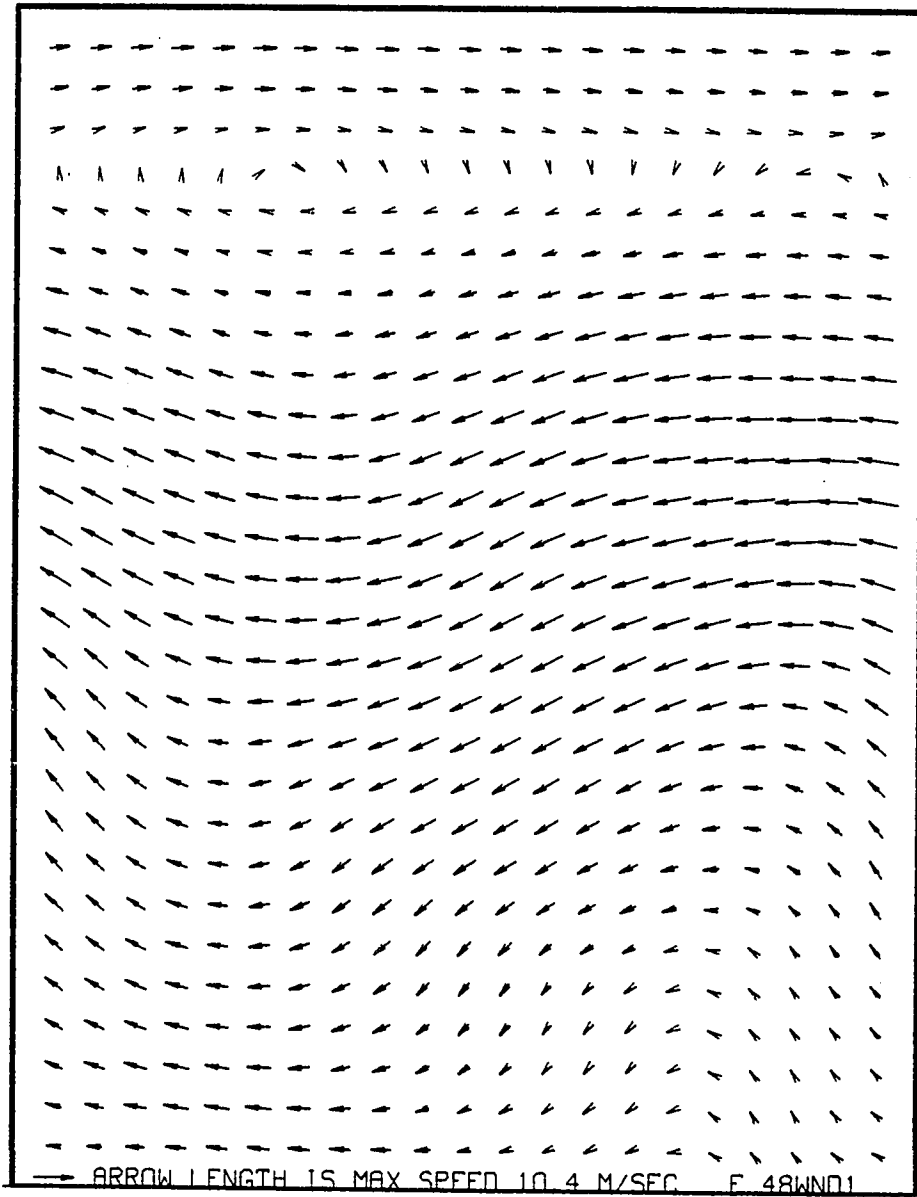


Fig. 53. EC6 experiment. Level 1 wind field at forecast hour 48.

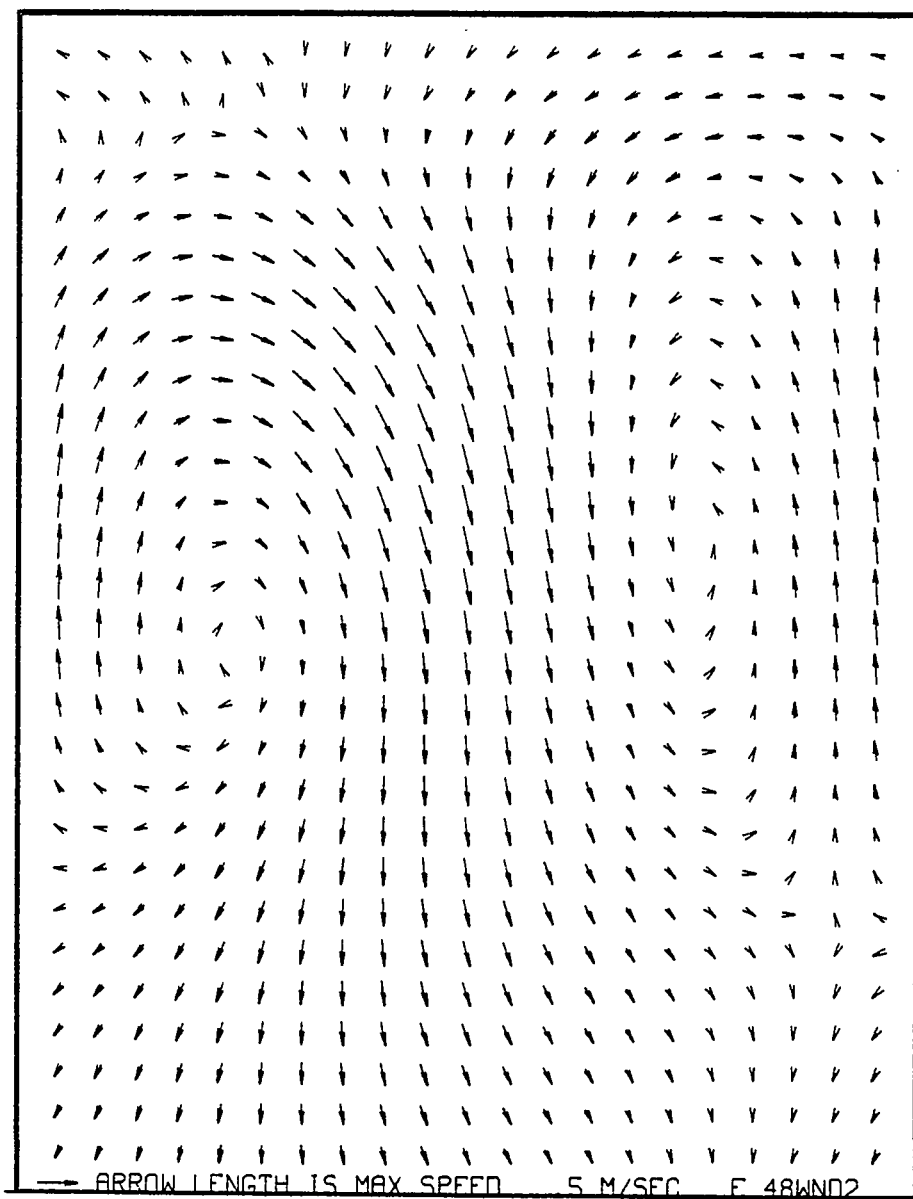


Fig. 54. EC6 experiment. Level 2 wind field at forecast hour 48.

explanation of this phenomenon lies in the indirect effect of increased initial easterlies on the magnitude of the initial stability parameter field.

On the surface, the initial thermodynamic fields for experiments EC12-EC15 were the same. This was definitely true of χ_0 , $\bar{\chi}_s$, and χ_1 , which were explicitly set with the same values in each experiment. However, χ_2 , the upper level thermodynamic variable, is diagnosed from the layer 2 thickness (eq. 34) and is not independent of the layer 2 wind field.

Setting a layer 2 wind field also implicitly sets the geopotential field through the non-linear balance initialization procedure of section 3.2. In this procedure, a stronger easterly layer 2 wind produces stronger geopotential gradients. Because the layer 2 thickness is initially diagnosed from the layer 2 and layer 1 geopotential (ϕ_2 and ϕ_1) via (87b), changed layer 2 initial geopotential fields produce changed layer 2 thickness fields.

Use of the above implies that differences in the initial level 2 wind fields in EC12-EC15 produced differences between their level 2 thickness fields. This, in turn, created differences in their χ_2 fields and stability parameter fields (η). The latter differences arose because η is diagnosed from (23), which uses χ_2 as an input variable. The magnitude of the net effect on η can be seen by comparing Figures 55 and 56 from the EC14 and EC15 experiments, respectively.

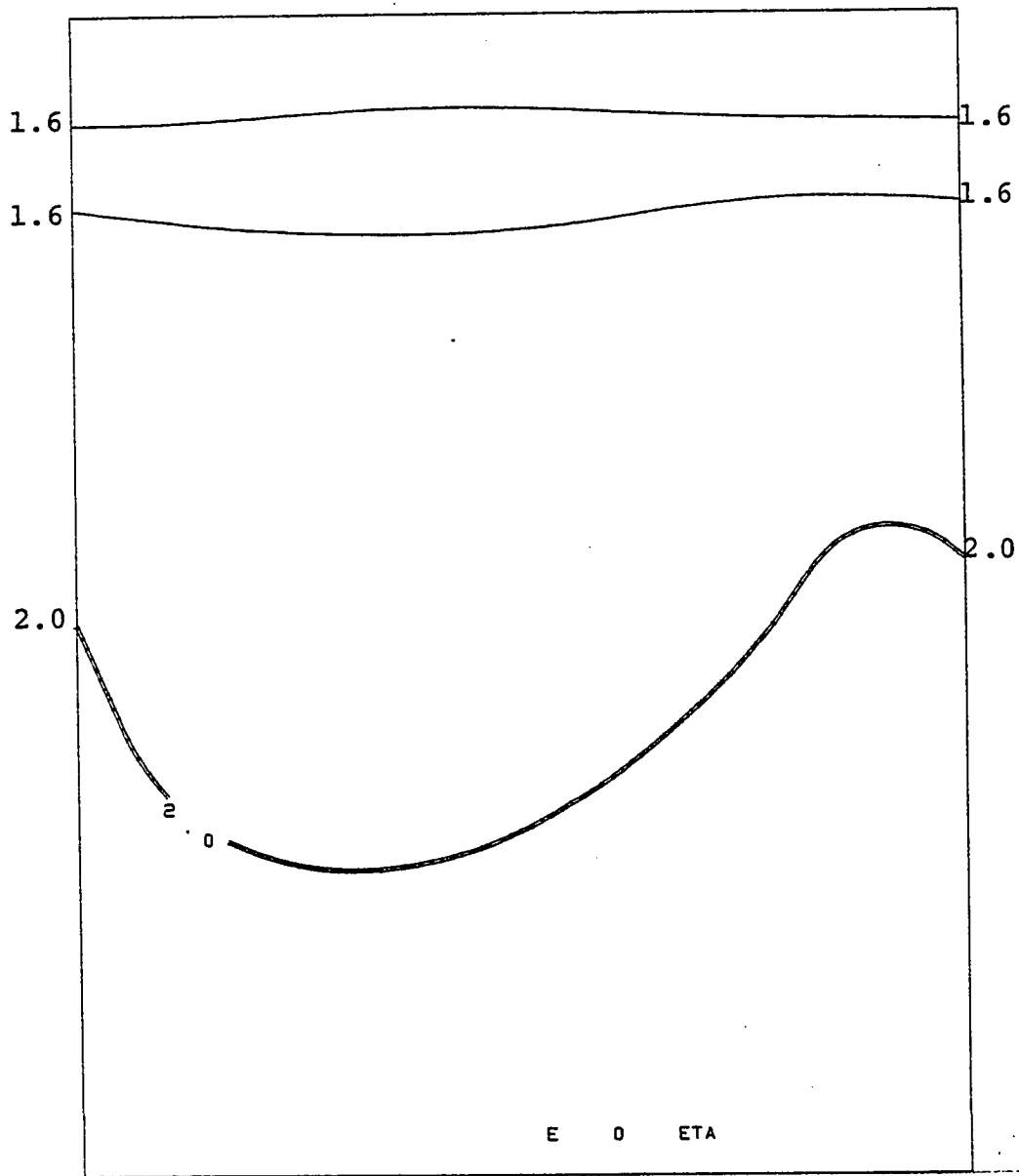


Fig. 55. ECl₄ experiment. Stability factor η at initial time.

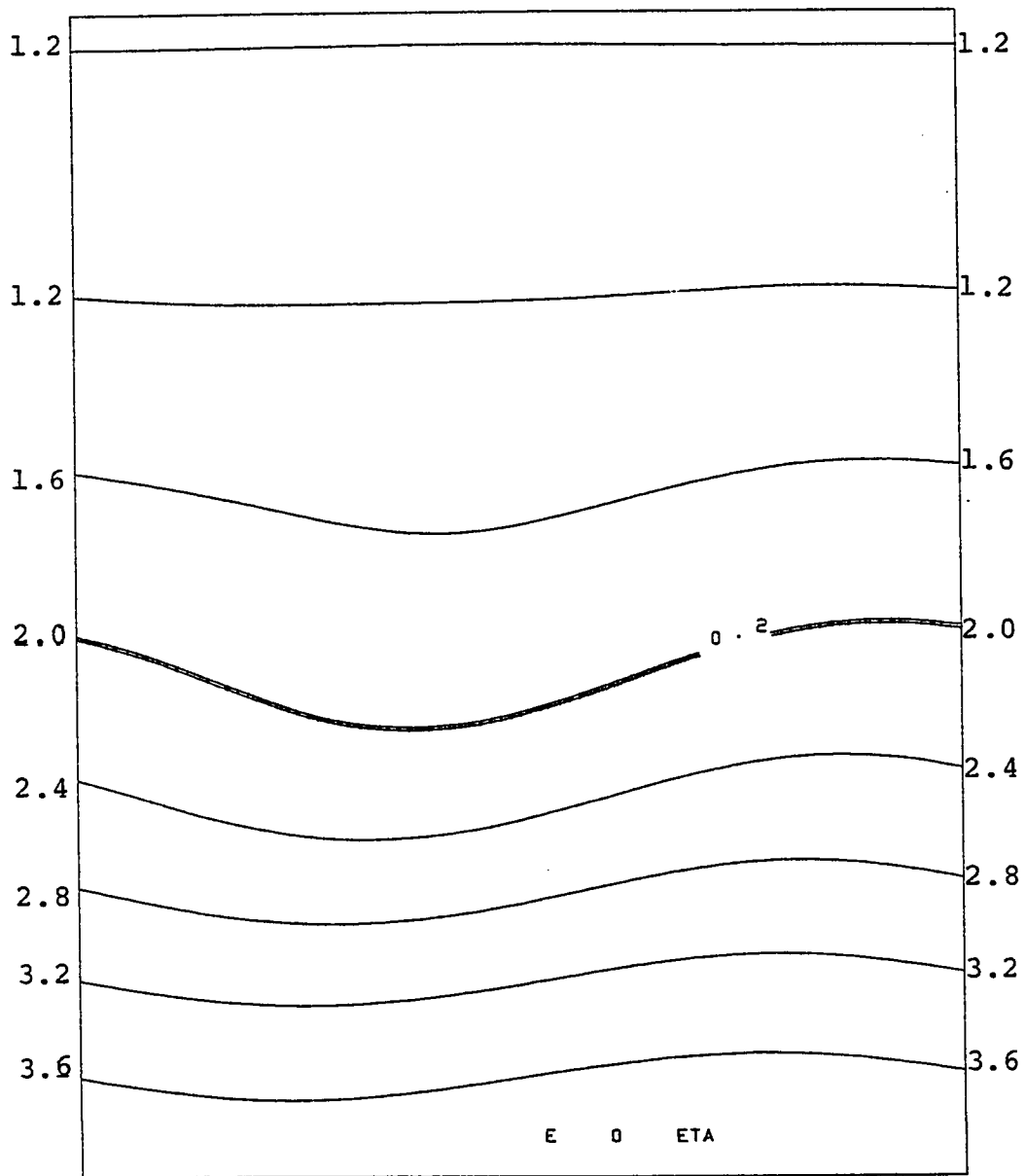


Fig. 56. EC15 experiment. Stability factor η at initial time.

Through the above mechanism, the set of wind shear experiments had not only different initial upper level winds but also somewhat different initial stability parameter fields. Increases in the magnitude of the level 2 easterlies gave consistent increases in the magnitude of the associated η fields. Thus, EC15 η values were typically larger than those of EC14 (see Figures 55 and 56), the values of EC14 larger than those of EC13, and so on. The monotonically increasing magnitude of the η fields from EC12 to EC15 imply a monotonically increasing convection effect from EC12 to EC15. This boost in convection is then the final link that tentatively explains why EC15 intensified slightly more than EC14, EC14 more than EC13, and EC13 more than EC12.

Some additional experiments were run to confirm that the different η fields above were not masking a significant detrimental vertical shear effect. EC21 and EC22 (Table 9) used the same initial fields as EC14 and EC15, respectively. However, in the forecast model, the value of the stability parameter (η) was set to a constant value of 2 throughout the forecast. This constant η eliminated the effect of the different initial η fields of EC14 and EC15, and it should have allowed any significant vertical wind shear effects to surface.

The results of EC21 and EC22 still showed that vertical shear of the horizontal wind does not have a large effect on development. In Table 11, we can see that both

TABLE 11
 LAYER 1 MAXIMUM SPEED FOR
 CONSTANT η EXPERIMENTS

EC21 experiment (upper level wind= -10 m/sec)		EC22 experiment (upper level wind= -20 m/sec)
Forecast Hour	Max. Speed in Layer 1 (m/sec)	Max. Speed in Layer 1 (m/sec)
0	11.34	11.34
24	11.59	11.70
48	10.98	11.02
72	13.20	13.86
87		14.24 (peak)
94	14.66	14.10
95	14.79 (peak)	

experiments intensified to nearly the same extent. The maximum wind speed in the experiment with larger shear did peak slightly earlier than in the experiment with less shear, and the smaller shear EC21 produced a slightly higher maximum wind speed than the larger shear EC22. However, these small differences are not indicative of the strong shear effect hypothesized by Gray and others.

The essentially null effect of wind shear in the current experiments can be qualitatively compared to the magnitude of the effect expected from Gray's (1975) results. In his study, Gray discussed the climatological frequency of tropical cyclone genesis. Among other factors, Gray hypothesized that genesis frequency was inversely proportional to a vertical shear parameter:

$$G \propto \frac{1}{\left[\left| \frac{\bar{V}_{950} - \bar{V}_{200}}{750} \right| + 3 \right]} \quad (95)$$

where G is the genesis frequency, \bar{V}_{950} is the 950 mb horizontal wind vector, and \bar{V}_{200} is the 200 mb wind vector.

Although the current model does not have 950 and 200 mb levels per se, we can adapt Gray's shear parameter to estimate the impact on genesis frequency from the different shear environments of EC21 and EC22.. Use of (95) and mean u values from layer 1 and layer 2 of both EC21 and EC22 gives:

$$\frac{G_{21}}{G_{22}} \propto \frac{\sqrt{[-5.27 - (-20)]^2 + 3}}{\sqrt{[-5.27 - (-10)]^2 + 3}} \approx 2.3$$

where G_{21} and G_{22} are genesis frequencies for EC21 and EC22 type shear cases, respectively, -5.27 is the initial level 1 mean u component in both EC21 and EC22, -20 is the level 2 mean u in EC22, and -10 is the level 2 mean u in EC21. One would infer from the above calculation that genesis frequency in EC21 shear conditions should be over twice that in EC22 shear conditions and that large differences should exist between the intensification observed in the EC21 and EC22 experiments. As we have seen, such differences do not exist, and the model results do not support the hypothesis that vertical wind shear has a large negative effect on tropical cyclone genesis.

In addition to vertical shear effects, EC21 provided some data on thermodynamic effects as a by-product. In EC14 the maximum level 1 wind peaked at approximately 19.4 m/sec. However, in EC21, although the initial η field was somewhat larger in magnitude (uniform 2 compared to Figure 48), the layer 1 maximum wind speed peaked at only 14.8 m/sec. The decreased intensification in EC21 was undoubtedly caused by the exclusion of χ_0 effects in the integration (i.e., constant η). In EC14 the χ_0 field was concentrated by the wave, and air-sea transfer also increased the magnitude of χ_0 . Such increases in χ_0 in EC14 produced increased η values and consequently enhanced convection in parts of the wave. In EC21, these effects were not present, thus at least

partially explaining the lesser intensification of EC21 compared to EC14.

Another sidenote from the shear experiments concerns the CISK mechanism. The large effect of CISK on development is readily observed by a comparison of the experiments with CISK included to those without. When CISK was an included mechanism in a wave forecast, the initial wave in the lower level typically formed a lower level vortex by the end of a 96 hour integration period. Such waves did not form vortices in any experiments that excluded the CISK. The inference from these observations is that CISK probably is a necessary part of real tropical cyclone genesis and intensification.

4.4 Cumulus Momentum Transfer

As discussed in the introduction, several observational studies have pointed toward the importance of vertical momentum transfer by cumulus clouds. Two easterly wave experiments were run to explore the impact of this transfer upon the easterly wave.

The first experiment, EC19, determined the effect of cumulus momentum transfer, by itself, on a coasting easterly wave. In this experiment the boundary layer was still driven by the layer 1 geopotential, but the heating effect of the clouds¹ was shut off. However, the Q term from the

¹The Q term in the equation of continuity multiplied by 0. See Chapter II, eq. (5) and (6).

boundary layer convergence was still allowed to function in the momentum equation (see Chapter II; eq. (1) and (2) and F_{1x} , F_{1y} , F_{2x} , F_{2y} terms).

As observations suggested, the cumulus momentum served as a lower level sink and an upper level energy source. Figure 57 and Figure 58 show a complementary decline in the level 1 kinetic energy as the level 2 energy rises. The level 1 easterly wave retained the wave form over the 96 hour forecast period, and the streamlines were very similar to the EC4 totally-coasting wave fields. However, the cumulus momentum transfer has drastically weakened the EC19 wave, a fact both confirmed by the level 1 areal kinetic energy loss and by the large drop in maximum wind speed over the forecast period (Figure 59).

The EC18 experiment is exactly the same as EC11 except that cumulus momentum transfer is turned on. The cumulus momentum transfer very efficiently debilitates the wave and prevents any significant intensification. The CISK heating was still working as shown by Figure 60, which reveals a pattern similar to, but much weaker than the analogous EC11 field. However, no vortex formed (Figure 61), and the level 1 maximum wind speed plot (Figure 62) reveals a profile much closer to that of EC4, the coasting wave, than to the profile of EC11, the CISK-driven wave. A comparison with EC17, which used diffusion damping, shows that damping is greater in the cumulus momentum transfer experiment.

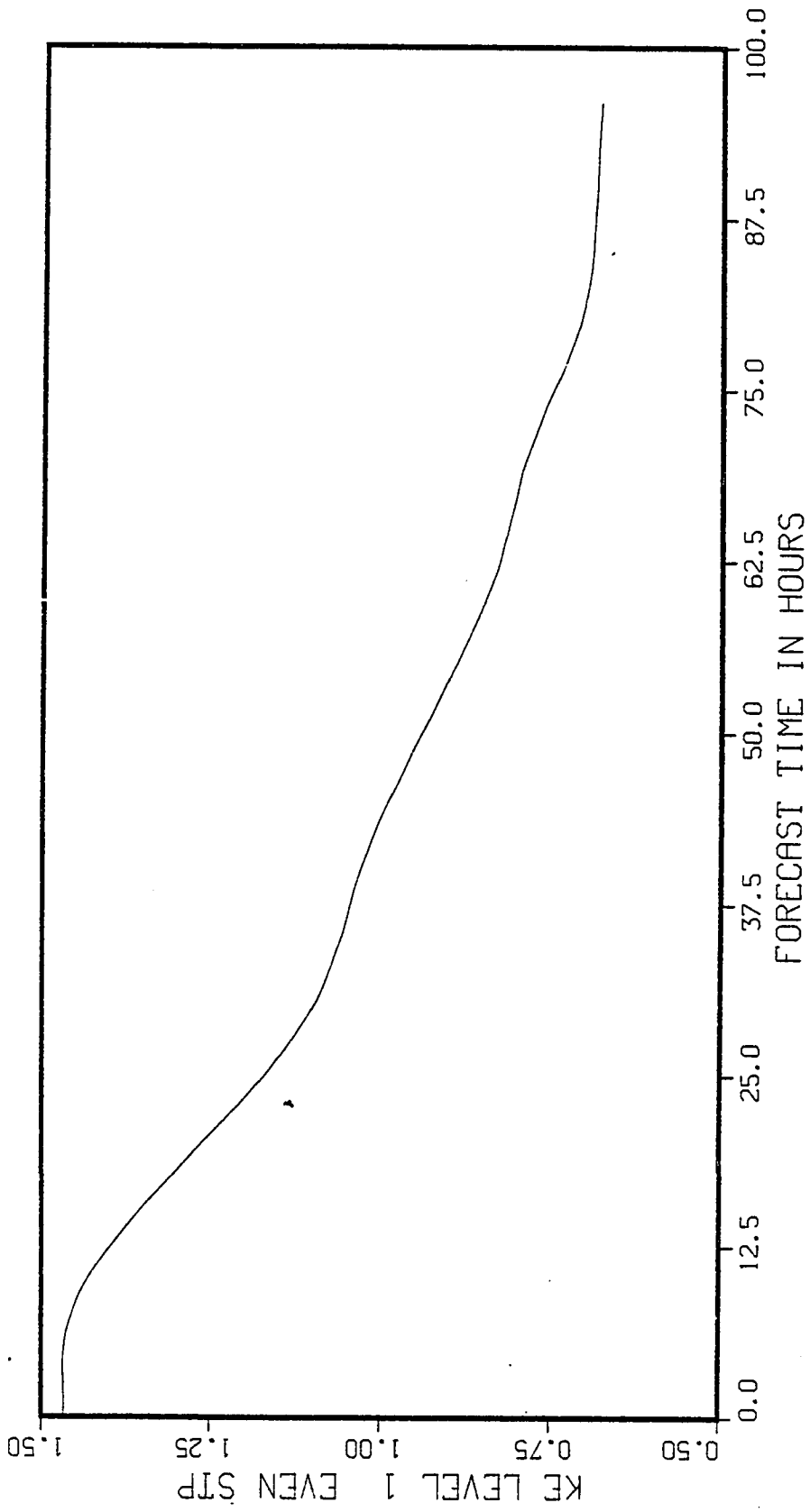


Fig. 57. EC19 experiment. Level 1 total area kinetic energy versus even time steps.

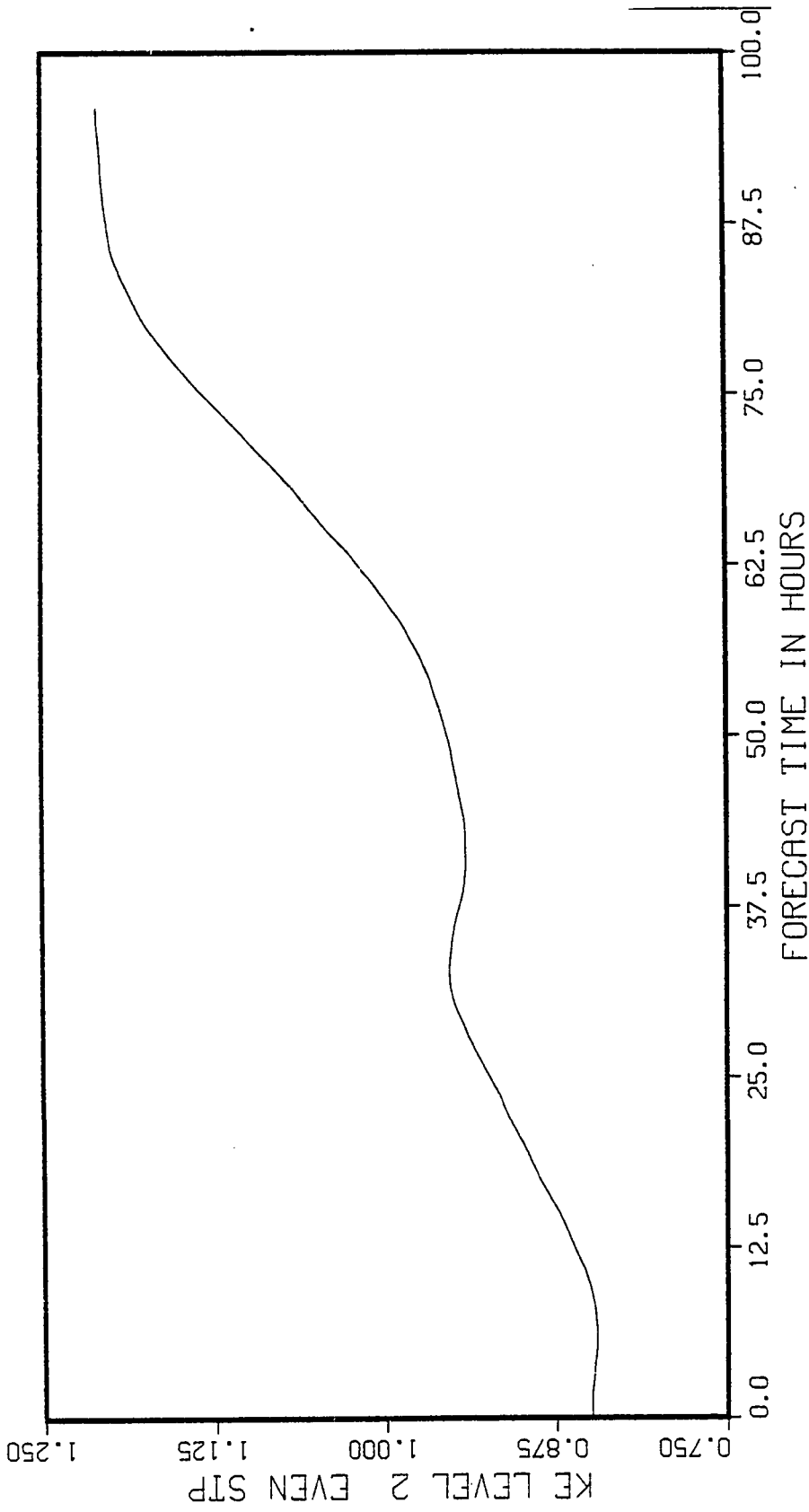


Fig. 58. EC19 experiment. Level 2 total area kinetic energy versus even time steps.

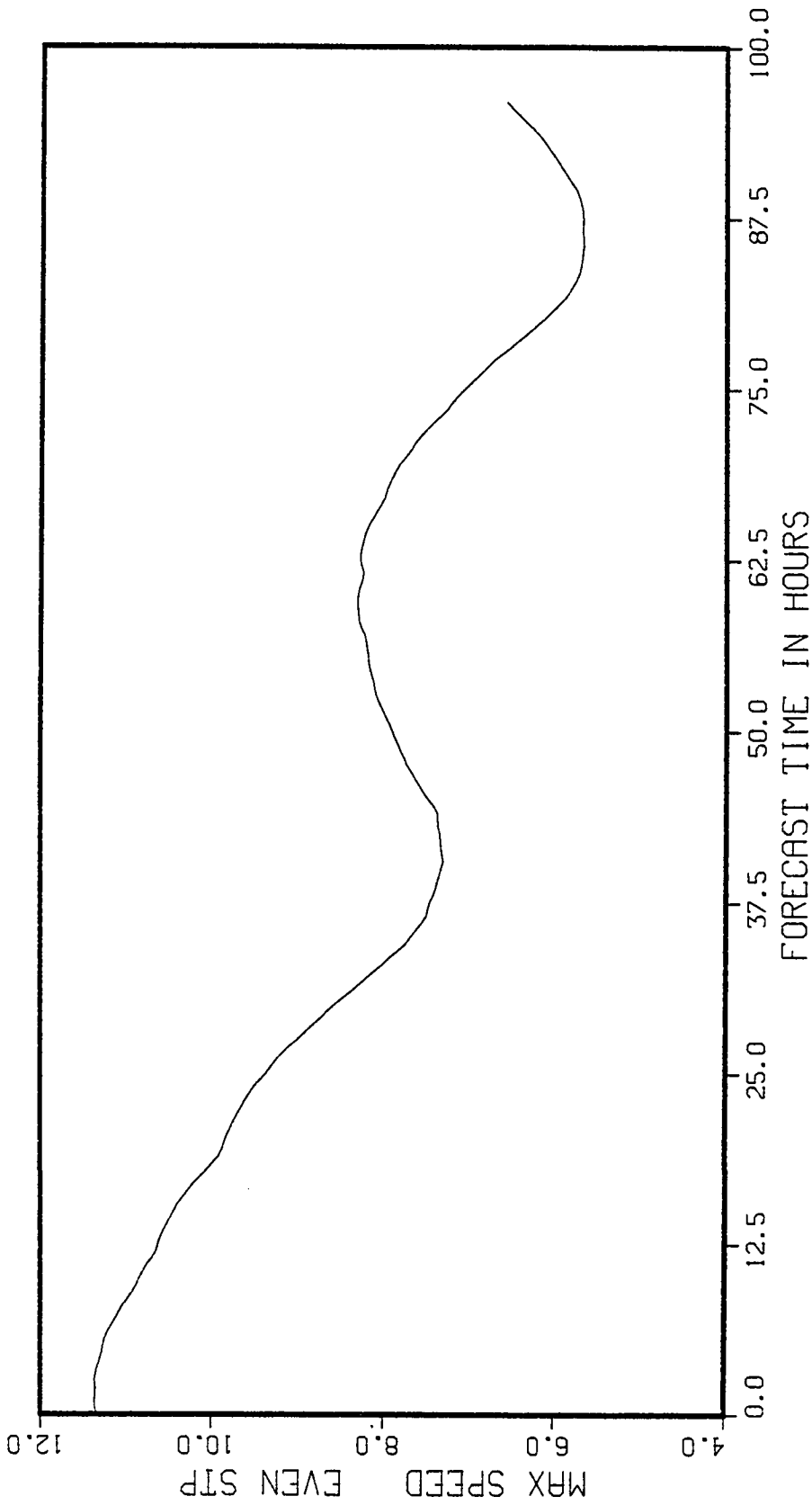


Fig. 59. ECl9 experiment. Maximum wind speed versus even time steps.

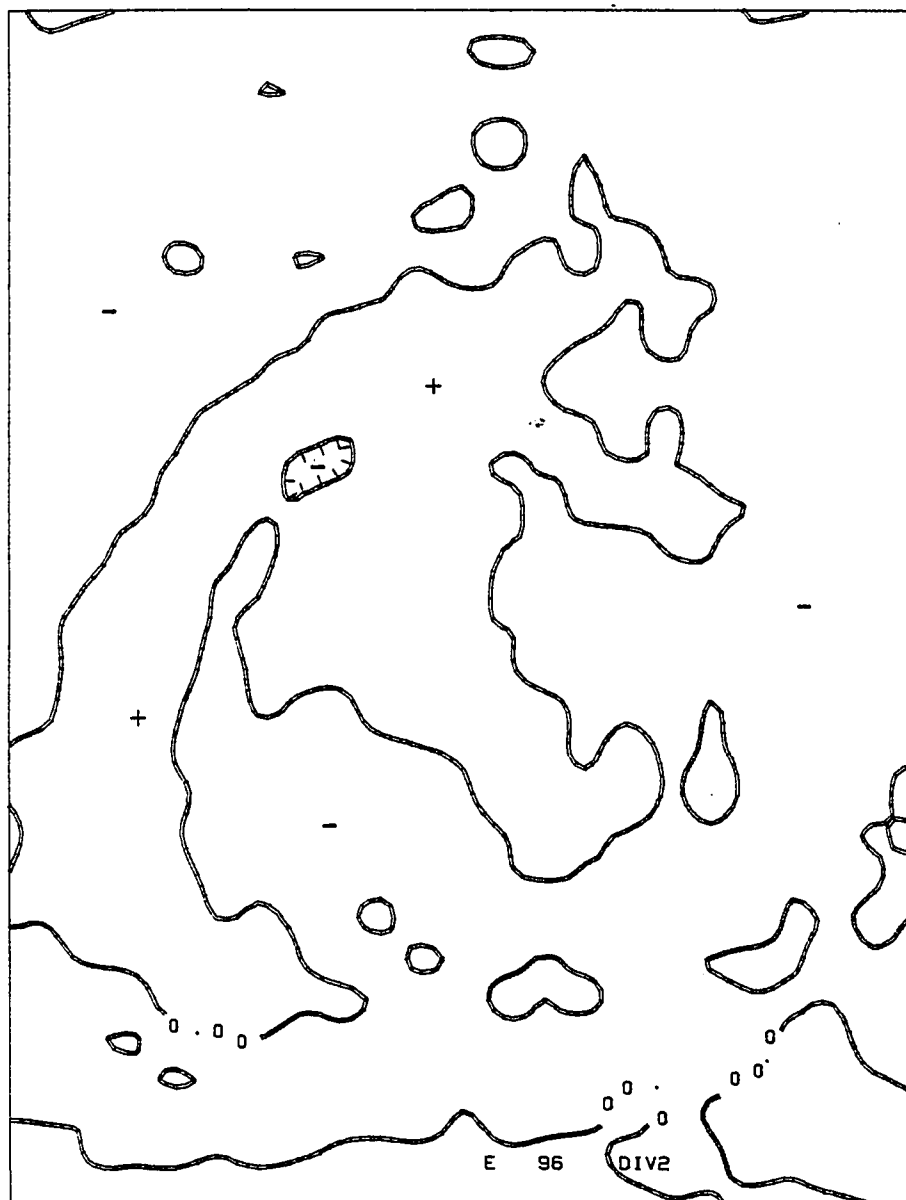


Fig. 60. EC18 experiment. Level 2 divergence at forecast hour 96.

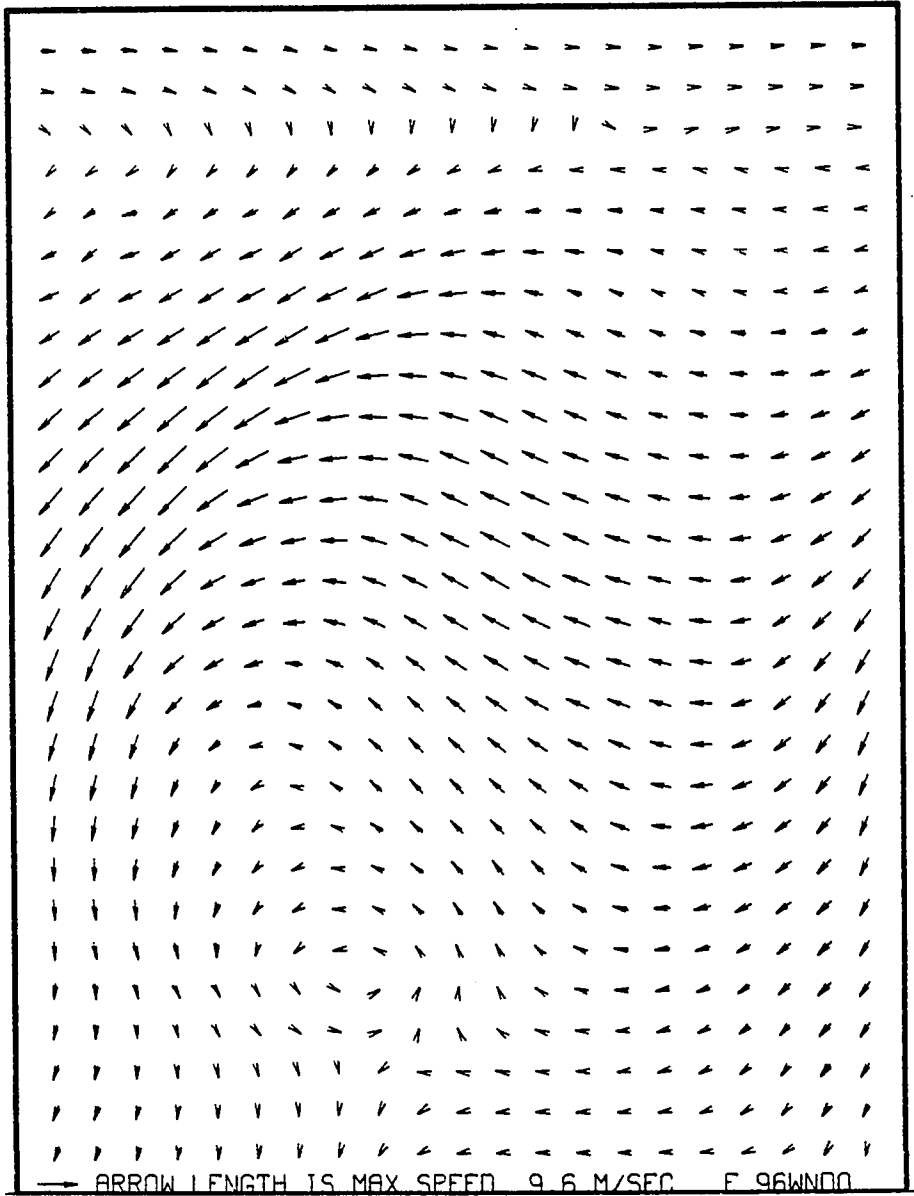


Fig. 61. EC18 experiment. Level 0 wind field at forecast hour 96.

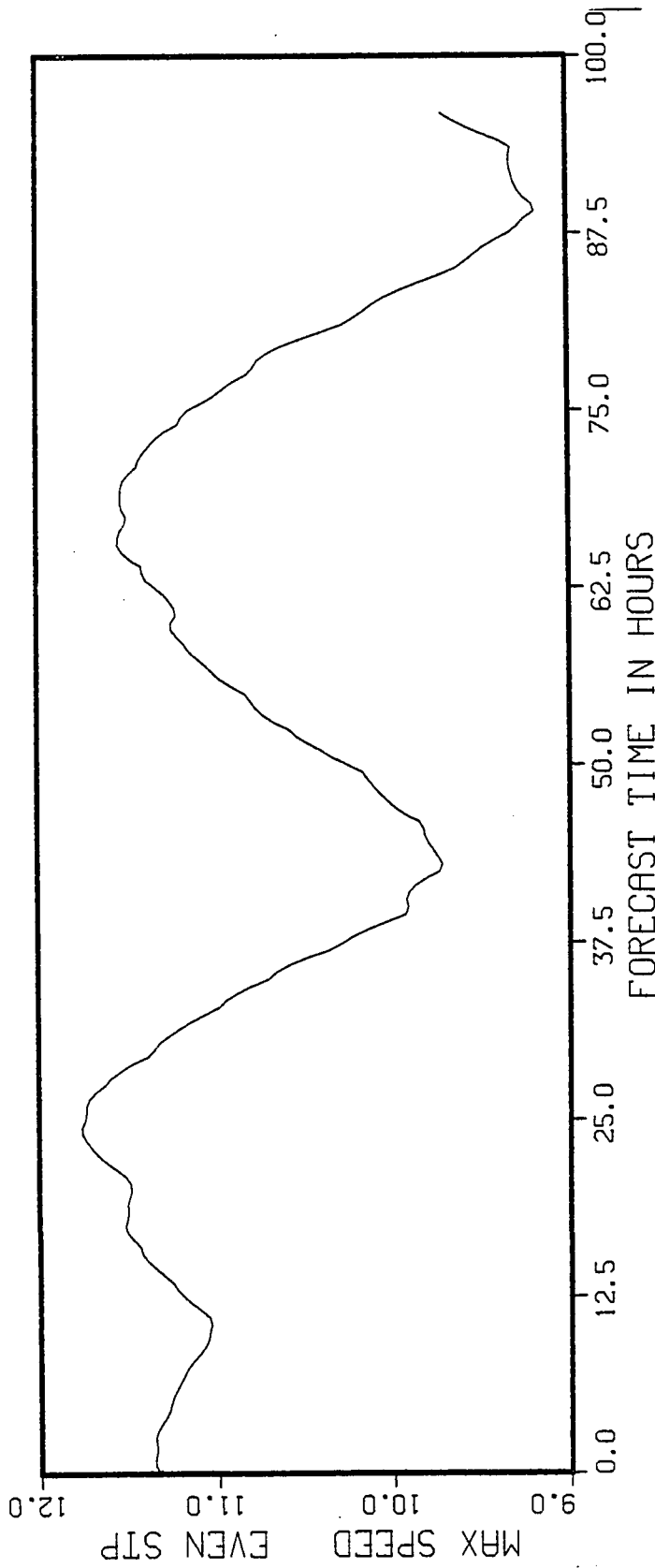


Fig. 62. ECL8 experiment. Maximum wind speed versus even time steps.

McBride (1979) has proposed a tropical cyclone genesis mechanism that invokes cumulus momentum transfer as a primary forcing. The cumulus momentum experiments here do not support such a hypothesis because the momentum transfer serves to weaken, not to strengthen cyclone genesis. The experiments, however, do confirm the results of Estoque, et al. (1977), who also found such a damping effect in their model.

4.5 Wave-CISK

As discussed in the introduction, wave-CISK depends upon internal wave convergence rather than friction to drive the boundary layer. Using a divergent easterly wave as an initial state, one could nicely test the strength of wave-CISK by running and comparing two forecasts that included only one difference: $C_D = .0015$ or $C_D = 0$. However, even using a non-divergent initial wave might allow a weak test of wave-CISK.

The use of a non-divergent initial state for a wave-CISK experiment meant that the wave must first internally redevelop a divergence field before the wave-CISK mechanism could be expected to produce boundary-layer convergence and subsequent cumulus feedback to the disturbance. We saw, in looking at the no-source or sink experiment EC4, that the initially non-divergent easterly wave regained a weakly organized internal divergence field by 96 hours. If wave-

CISK were an extremely effective mechanism, it should have begun to affect the easterly wave by the 96 hour point. However, if wave-CISK were a weak or moderate mechanism, it would not be expected to change the wave structure by the end of 96 hours because of the initial non-divergent wave state.

What are the results? Basically, experiment EC20, with heating turned on but $C_D = 0$, is not much different from EC4 with no friction or heating. The 96 hour wind field of EC4 (Figure 19) looks almost exactly the same as the 96 hour wind field for EC20 (Figure 63). One small difference to be noted is that at 96 hours, the maximum wind speed is slightly less in the EC20 field than in the EC4 field (10.2 versus 10.4). Also, the 96 hour organized weak convergence field of EC4 (Figure 20) has become disorganized noise in EC20 (Figure 64). Because EC20 started with a non-divergent wave, strong intensification was not expected; however, at most, one would expect to see no difference. That EC20 actually appears to be very slightly weaker than EC4 is surprising.

The results of the EC20 experiment really do not demonstrate much. Without an initial patterned convergence field in the wave, the wave-CISK probably acted more as minor noise in the integration than anything else. Moreover, we cannot use the insignificant differences between EC4 and EC20 to conclude that wave-CISK is either important or not important.

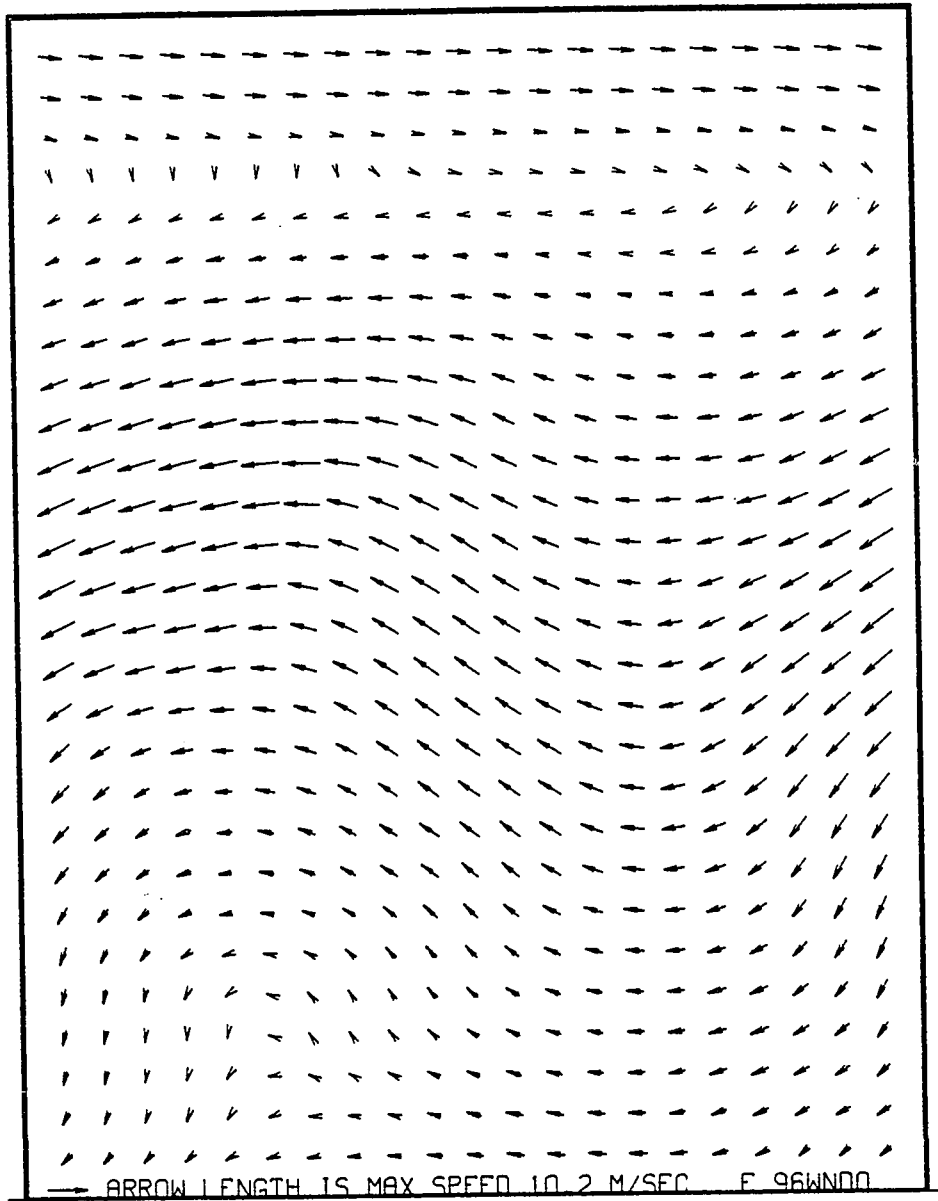


Fig. 63. EC20 experiment. Level 0 and
1 wind fields at forecast hour 96.

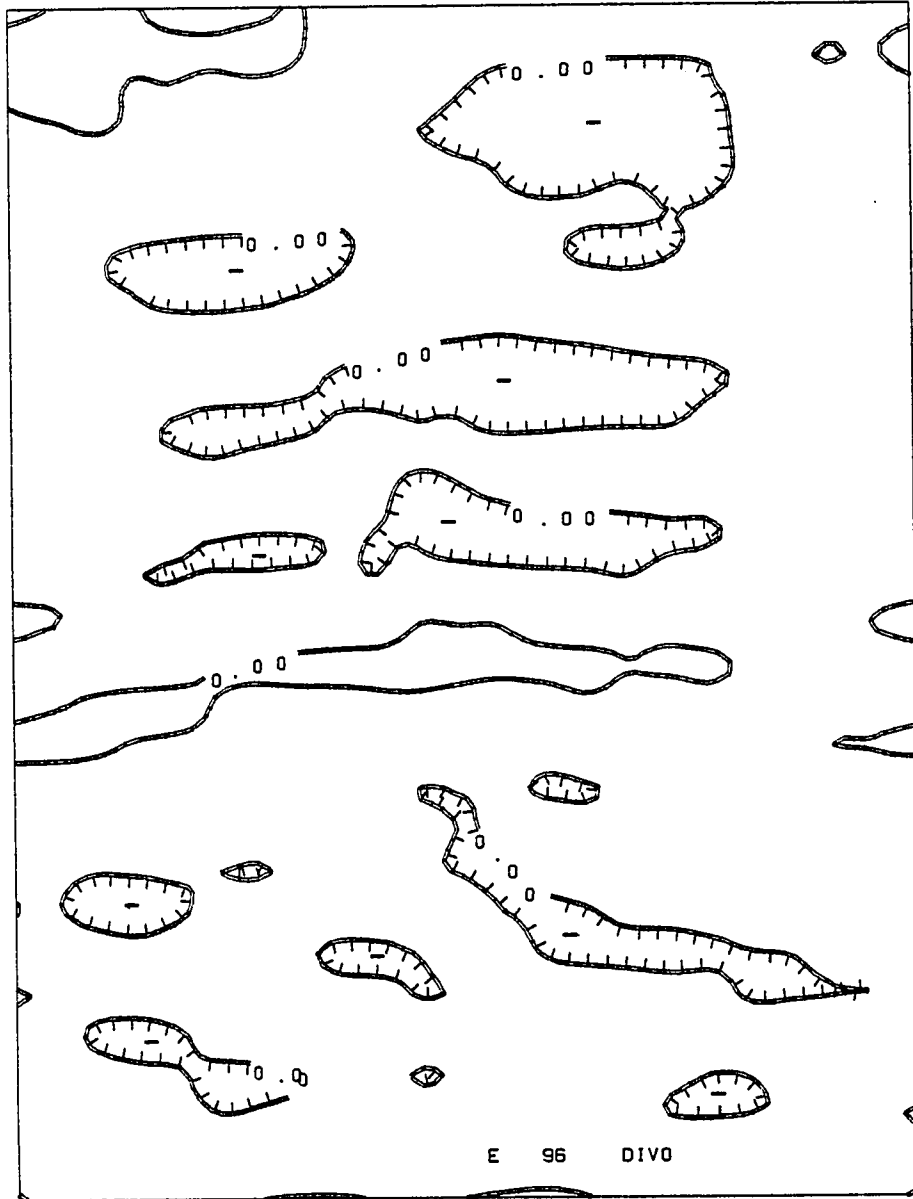


Fig. 64. EC20 experiment. Levels 0 and 1 divergence at forecast hour 96.

The idea of a wave-CISK test is good, but the EC20 conditions were not a fair test. One possible remedy would be to take the fields of EC11 after 24 hours, set $C_D = 0$, and continue the run to 96 hours. With the initial organized convergence forced by frictional CISK, the wave-CISK would have a chance to truly show its effect. Such an experiment, however, is not part of this study and is left to future work.

CHAPTER V

CONCLUSIONS

5.1 Summary

This research has used relatively simple model simulations to study tropical cyclone genesis and intensification. Some of the more significant model characteristics are as follows:

1. Primitive equations.
2. Three layers of incompressible fluid.
3. Constant thickness boundary layer.
4. Boundary layer friction using a drag coefficient.
5. Latent and sensible heat exchange with the sea surface by bulk parameterization.
6. Cumulus parameterization (CISK) as a function of both vertical velocity in the boundary layer and a stability factor based on the vertical profile of equivalent-potential temperature. Convection was basically treated as a mass source in the upper layer and a mass sink in the lower layer.
7. Mid-tropospheric equivalent-potential temperature held constant.

Numerical solution of the model was by finite differences. The scheme used time and space staggered grids and semi-implicit time differencing. Boundary conditions were Dirichlet in one model version and cyclic in another.

The wind was the basic field for model initialization. Three different types of flow fields were used among the model experiments. The first was a simple symmetric vortex with a maximum wind speed of 10 m/sec (Ooyama, 1969). The

second was the wind field of an easterly wave from composited GATE data (Reed, et al., 1977), and the third wind field was simply one of east-west flow. In conjunction with initialized thermodynamic fields, these three wind fields in various combinations were the basic inputs for the model simulations.

The simulation results support the following conclusions about some aspects of tropical cyclone genesis and intensification:

1. The CISK mechanism is a highly important, integral part of the genesis and intensification process. With CISK included, simulations often produced closed, cyclonic vortices from initial easterly wave states. When CISK was excluded, vortices did not develop from these same wave states.
2. The magnitude of the lower level vorticity field in a weak disturbance is extremely important in determining how much intensification occurs. On a relative basis, the lower level disturbance seems to be more significant in the intensification process than any organization of the upper levels.
3. Genesis and intensification are extremely sensitive to sea surface temperature and low level moisture. Model experiments that used an easterly wave initial wind field intensified weakly when the initial boundary-layer equivalent-potential temperature was 350° K and the sea surface temperature was 28.6° C. The same initial wave intensified strongly, with formation of a closed cyclonic vortex and a maximum wind of about 26 m/sec, when the above temperatures were changed to 360K and 30.3° C, respectively.
4. Large values of vertical shear of the horizontal wind do not appear to inhibit tropical cyclone genesis or intensification. Simulations involving initial states with different shears did not differ significantly in intensification or development.

5. Cumulus momentum transport acts to reduce genesis and development. Simulations including a crude momentum transport were severely damped.

5.2 Limitations and Suggestions

The results of this research are only suggestive because of limitations in the simulations. A list of some of these deficiencies might include the simple physics in the Ooyama model, the low vertical resolution of the model, the non-divergent initialization, and the initial tropical wind fields selected for study.

Certainly, the model in this study does not attempt to simulate a vast number of atmospheric mechanisms. It is possible, although not probable, that the addition of some of the absent mechanisms might change the qualitative results cited above. With that in mind, future models exploring the development phenomena should contain additional model physics such as true thermodynamics, radiation, a more realistic boundary layer, and a somewhat more sophisticated cumulus parameterization.

Coupled with model physics is the vertical resolution of the model. Many tropical disturbances probably require more than two vertical layers for a good representation of dynamics. Future models should include such higher resolution in order to better capture the vertical interactions in the tropics.

The initialization could also be improved to include some divergence. This would help because, although the large-scale, dry tropical atmosphere tends to be quasi-non-divergent, the smaller scale, cloudy disturbance areas tend to be areas where convergence is concentrated. Including this effect in an initialization should produce better meso-scale simulations.

Finally, the initial fields used for simulating development should more closely resemble the weak disturbances discussed by Gray as quoted in section 1.7. Representative disturbances would preferentially include several real, well-observed cases of both development and non-development. Such cases will be difficult to find, but they are necessary because composite and artificial initial data can carry simulation only so far.

The conclusions of this study also suggest that new observational studies may be useful. Sophisticated statistical techniques might be able to isolate the wind shear effect from the impact of any correlation effects between low-level vorticity and low vertical shear of the horizontal wind. If successful, such a study might confirm or contradict some of the results of this study.

In addition, observational studies might constructively look at the comparative effect of low level moisture and sea surface temperature versus the effect of upper level conditions. This study suggests a much greater influence on

development by the moisture and sea temperature, but a specific observational study would provide more evidence one way or the other.

REFERENCES

- Adams, J. C., et al., 1975. NCAR Software Support Library Volume 2. Nat. Center Atmos. Res., Boulder, Col., 257 pp.
- Anthes, R. A., 1972. Development of asymmetries in a three-dimensional numerical model of the tropical cyclone. Mon. Wea. Rev., 100, 461-476.
- Anthes, R. A., S. L. Rosenthal, and J. W. Trout, 1971a. Preliminary results from an asymmetric model of the tropical cyclone. Mon. Wea. Rev., 99, 744-758.
- Anthes, R. A., F. W. Trout, and S. L. Rosenthal, 1971b. Comparisons of tropical cyclone simulations with and without the assumption of circular symmetry. Mon. Wea. Rev., 99, 759-766.
- Aspliden, C. I., 1976. A classification of the structure of the tropical atmosphere and related energy fluxes. J. Appl. Meteor., 15, 692-697.
- Asselin, R., 1972. Frequency filter for time integrations. Mon. Wea. Rev., 100, 487-490.
- Benwell, G. R. R. and Bretherton, F. P., 1968. A pressure oscillation in a ten-level atmospheric model. Quart. J. Roy. Meteor. Soc., 94, 123-131.
- Barrett, E. C., 1974. Climatology from Satellites. Methuen & Co., Ltd., London, 418 pp.
- Betts, A. K., 1974. Thermodynamic classification of tropical convective soundings. Mon. Wea. Rev., 102, 760-764.
- Ceselski, B. F., 1974. Cumulus convection in weak and strong tropical disturbances. J. Atmos. Sci., 31, 1241-1255.
- Charney, J. G., and A. Eliassen, 1964. On the growth of the hurricane depression. J. Atmos. Sci., 21, 68-75.
- Chen, J. H., 1973. Numerical boundary conditions and computational modes. J. Comp. Phys., 13, 522-535.

- Chen, J. H. and K. Miyakoda, 1974. A nested grid computational for the barotropic free surface atmosphere. Mon. Wea. Rev., 102, 181-190.
- Cho, H. R. and Y. Ogura, 1974. A relationship between the cloud activity and low-level convergence as observed in Reed-Recker's composite easterly waves. J. Atmos. Sci., 31, 2058-2065.
- Elsberry, R. L. and E. J. Harrison, Jr., 1971. Height and kinetic energy oscillations in a limited region prediction model. Mon. Wea. Rev., 99, 883-888.
- Elvius, T. and Sundstrom, 1973. Computationally efficient schemes and boundary conditions for a fine mesh barotropic model based on the shallow water equations. Tellus, 25, 132-156.
- Erickson, C. O., 1963. An incipient hurricane near the West African Coast. Mon. Wea. Rev., 91, 61-68.
- Erickson, S. L., 1977. Comparison of developing vs non-developing tropical disturbances. Master's Thesis, Dept. Atmos. Sci., Col. State Univ., Fort Collins, CO, 80 pp.
- Estoque, M. A., et al., 1977. Vorticity budget of the easterly wave in relation to cumulus transport. J. Atmos. Sci., 34, 77-86.
- Fett, R. W., 1968. Typhoon formation within the zone of the inter-tropical convergence. Mon. Wea. Rev., 96, 106-117.
- Fingerhut, W. A., 1978. A numerical model of a diurnally varying tropical cloud cluster disturbance. Mon. Wea. Rev., 106, 255-264.
- Frank, N. L., 1963. Synoptic case study of tropical cyclogenesis utilizing TIROS data. Mon. Wea. Rev., 91, 355-366.
- Frank, W. M., 1977a. The structure and energetics of the tropical cyclone II. Dynamics and energetics. Mon. Wea. Rev., 105, 1136-1150.
- Frank, W. M., 1977b. Convective fluxes in tropical cyclones. J. Atmos. Sci., 34, 1554-1568.
- Frank, W. M., 1978. The life cycles of GATE convective systems. J. Atmos. Sci., 35, 1256-1264.

- Gerrity, J. P. and R. D. McPherson, 1970. Noise analysis of a limited area fine mesh prediction model. ESSA Tech. Memo., WBTM NMC 46, 81 pp.
- Gerrity, J. P. and R. D. McPherson, 1971. On an efficient scheme for the numerical integration of a primitive-equation barotropic model. J. Appl. Meteor., 10, 353-363.
- Gray, W. M., 1967. The mutual variation of wind shear, and baroclinicity in the cumulus convective atmosphere of the hurricane. Mon. Wea. Rev., 95, 55-73.
- Gray, W. M., 1975. Tropical cyclone genesis. Atmos. Sci. Paper No. 234, Dept. Atmos. Sci., Col. State Univ., Fort Collins, CO., 121 pp.
- Gray, W. M., 1977. Tropical disturbance to cyclone transformation. Draft paper, Dept. Atmos. Sci., Col. State Univ., Boulder, CO., 50 pp.
- Gray, W. M. and R. W. Jacobson, Jr., 1977. Diurnal variation of deep cumulus convection. Mon. Wea. Rev., 105, 1171-1188.
- Gray, W. M., and J. McBride, 1976. The Role of frictional convergence in tropical cyclone genesis, in Atmos. Sci. Paper No. 259, Dept. Atmos. Sci., Col. State Univ., Fort Collins, CO., 76-86.
- Haltiner, G. J., 1971. Numerical Weather Prediction. John Wiley & Sons, Inc., New York, 317 pp.
- Hawkins, H. F. and D. T. Rubsam, 1968. Hurricane Hilda 1964. I genesis, as revealed by satellite photography, conventional and aircraft data. Mon. Wea. Rev., 96, 428-452.
- Hebert, P. J., 1978. Intensification criteria for tropical depressions of the Western Northern Atlantic. Mon. Wea. Rev., 106, 831-840.
- Hess, S. L., 1959. Introduction to Theoretical Meteorology. Holt, Rinehart, and Winston, New York, 362 pp.
- Holton, J. R., 1972. An Introduction to Dynamic Meteorology. Academic Press, New York, 319 pp.

- Hope, J. R., and C. J. Neumann, 1977. A survey of world wide tropical cyclone prediction models. Proceedings of 11th Tech. Conf. Hurr. and Trop. Meteor. 13-16 Dec. 1977, Miami Beach, FL, 367-374.
- Iribane, J. V., and W. L. Godson, 1973. Atmospheric Thermodynamics. D. Reidel Publishing Co., Boston, 222 pp.
- Jones, R. W., 1977a. A nested grid for a three-dimensional model of a tropical cyclone. J. Atmos. Sci., 34, 1528-1553.
- Jones, R. W., 1977b. Vortex motion in a tropical cyclone model. J. Atmos. Sci., 34, 1518-1527.
- Jordan, C. L., 1958. Mean soundings for the West Indies area. J. Meteor., 15, 91-97.
- Kasahara, Y. and R. E. Tuleya, 1974. Structure of a tropical cyclone developed in a three-dimensional model. J. Atmos. Sci., 31, 893-919.
- Kurihara, Y. and R. E. Tuleya, 1974. Structure of a tropical cyclone developed in a three-dimensional numerical simulation model. J. Atmos. Sci., 31, 893-919.
- Lewis, B. M. and D. P. Jorgensen, 1978. Study of the dissipation of hurricane Gertrude (1974). Mon. Wea. Rev., 106, 1288-1306.
- Kanamitsu, M., 1975. On Numerical Prediction over a Global Tropical Belt, Dept. of Meteor., Florida State U., Report No. 75-1, July 1975, 282 pp.
- Lilly, D. K., 1960. On the theory of disturbances in a conditionally unstable atmosphere. Mon. Wea. Rev., 88, 1-17.
- Lindzen, R. S., 1974. Wave-CISK in the tropics. J. Atmos. Sci., 31, 156-179.
- Lopez, R. E., 1968. Investigation of the importance of cumulus convection and ventilation in early tropical storm development. Atmos. Sci. Paper No. 124, Dept. Atmos. Sci., Col. State Univ., Fort. Collins, CO, 86 pp.
- Madala, R. V. and S. A. Piacsek, 1975. Numerical simulation of asymmetric hurricanes on a β -plane with vertical shear. Tellus, 27, 453-468.

- Madala, R. V., 1978. An efficient direct solver for separable and non-separable elliptic equations. Mon. Wea. Rev., 106, 1735-1741.
- Mathur, M. B., 1974. A multiple-grid primitive equation model to simulate the development of an asymmetric hurricane (Isbell, 1964). J. Atmos. Sci., 31, 371-393.
- McBride, J. L., 1979. Observational analysis of tropical cyclone formation. Atmos. Sci. Paper No. 308, Dept. of Atmos. Sci., Col. State Univ., Fort Collins, CO, 230 pp.
- McGregor and L. M. Leslie, 1977. On the selection of grids for semi-implicit schemes. Mon. Wea. Rev., 105, 236-238.
- Mesinger, F. and A. Arakawa, 1976. Numerical methods used in atmospheric models. GARP Pub. Ser. No. 17, UNIPUB, N. Y., 64 pp.
- Mihok, W. F., and D. E. Hinsman, 1977. Tropical storm forecasts during 1977 using the Fleet Numerical Weather Central tropical cyclone model. Proceedings of 11th Tech. Conf. Hurr. and Trop. Meteor. 13-16 Dec. 1977, Miami Beach, FL, 401-404.
- Miller, B. I., P. P. Chase, and B. R. Javinen, 1972. Numerical prediction of tropical weather systems, Mon. Wea. Rev., 100, 825-835.
- Norquist, D. C., E. E. Recker, and R. J. Reed, 1977. The energetics of African wave disturbances as observed during phase III of GATE. Mon. Wea. Rev., 105, 334-342.
- Ooyama, K., 1964a. A dynamical model for the study of tropical cyclone development. Proceed. Symp. on Trop. Meteor., Rotura, New Zealand, 5-13 Nov. 1963, New Zealand Meteor. Service, Wellington, New Zealand, p. 678.
- Ooyama, K., 1964b. A dynamical model for the study of tropical cyclone development. Geofis. Intern., 4, 187-198.
- Ooyama, K., 1969. Numerical simulation of the life cycle of tropical cyclones. J. Atmos. Sci., 26, 3-40.
- Palmen, E. and C. W. Newton, 1969. Atmospheric Circulation Systems. Academic Press, New York, 603 pp.

- Payne, S. W. and M. M. McGarry, 1977. The relationship of satellite inferred convective activity to easterly waves over West Africa and the adjacent ocean during phase III of GATE. Mon. Wea. Rev., 105, 413-420.
- Ramage, C. S., 1974. The typhoons of October 1970 in the South China Sea: intensification, decay and ocean interaction, J. Appl. Meteor., 13, 739-751.
- Reed, R. J. and R. H. Johnson, 1974. The vorticity budget of synoptic scale wave disturbances in the tropical Western Pacific, J. Atmos. Sci., 31, 1784-1790.
- Reed, R. J., D. C. Norquist and E. E. Recker, 1977. The structure and properties of African wave disturbances as observed during phase III of GATE. Mon. Wea. Rev., 105, 317-333.
- Riehl, H., 1954. Tropical Meteorology. McGraw Hill Book Co., Inc., New York, 392 pp.
- Rosenthal, S. L., 1970a. A circularly symmetric primitive equation model of tropical cyclone development containing an explicit water vapor cycle. Mon. Wea. Rev., 98, 643-663.
- Rosenthal, S. L., 1970b. Experiments with a numerical model of tropical cyclone development--some effects of radial resolution. Mon. Wea. Rev., 98, 106-120.
- Rosenthal, S. L., 1971a. A circularly symmetric primitive-equation model of tropical cyclones and its response to artificial enhancement of the convective heating functions. Mon. Wea. Rev., 99, 414-426.
- Rosenthal, S. L., 1971b. The response of a tropical cyclone model to variations in boundary layer parameters, initial conditions, lateral boundary conditions, and domain size. Mon. Wea. Rev., 99, 767-777.
- Rosenthal, S. L., 1978. Numerical simulation of tropical cyclone development with latent heat release by the resolvable scales I: model description and preliminary results. J. Atmos. Sci., 35, 258-271.
- Sadler, J. C. 1976. A role of the tropical upper tropospheric trough in early season typhoon development. Mon. Wea. Rev., 104, 1266-1278.

- Sadler, J. C., 1978. Mid-season typhoon development and intensity changes and the tropical upper tropospheric trough. Mon. Wea. Rev., 106, 1137-1152.
- Sela, J. and S. Scolnik, 1972. Method for solving simultaneous Helmholtz equations. Mon. Wea. Rev., 100, 644-645.
- Shapiro, L. J., 1977a. Tropical storm formation from easterly waves: a criterion for development. J. Atmos. Sci., 34, 1007-1021.
- Shapiro, L. J., 1977b. A criterion for the development of tropical storms from easterly waves. Proceedings of 11th Tech. Conf. Hurr. Trop. Meteor. 13-36 Dec 1977, Miami Beach, FL, 9-14.
- Shapiro, L. J., 1978. The vorticity budget of a composite African tropical wave disturbance. Mon. Wea. Rev., 106, 806-817.
- Stevens, D. E., 1979. Vorticity momentum, and divergence budgets of synoptic-scale wave disturbances in the tropical Eastern Atlantic, Mon. Wea. Rev., 107, 535-550.
- Sundquist, E. J., 1970a. Numerical simulation of the development of tropical cyclones with a ten-level model, Part I. Tellus, 22, 359-390.
- Swartztrauber, P. N. and R. A. Sweet, 1975. Efficient FORTRAN subprograms for the solution of elliptic partial differential equations. NCAR Technical Note TN/IA-109, 139 pp.
- Syono, S., 1960. A numerical experiment of the formation of tropical cyclones. Proc. Intern. Symposium on Num. Wea. Pred., Tokyo, 1960, 405-418. Meteor. Soc. of Japan, 1962.
- Thompson, R. M., Jr., et al., 1979. Structure and properties of synoptic-scale disturbances in the intertropical convergence zone of the Eastern Atlantic. J. Atmos. Sci., 36, 53-72.
- Ulanski, S. L. and M. Garstang, 1978. The role of surface divergence and vorticity in the life cycle of convective rainfall. J. Atmos. Sci., 35, 1047-1062.
- Yamasaki, M., 1968a. Numerical simulation of tropical cyclone development with the use of primitive equations. J. Meteor. Soc. Japan, 46, 178-201.

- Yamasaki, M., 1968b. A tropical model with parameterized vertical partition of released latent heat. J. Meteor. Soc. of Japan, 46, 202-214.
- Yamasaki, M., 1977. The role of surface friction in tropical cyclones. J. Meteor. Soc., Japan, 55, 559-572.
- Yanai, M., et al., 1976. Response of deep and shallow tropical maritime cumuli to large-scale processes. J. Atmos. Sci., 33, 976-991.
- Zehr, R., 1976. Tropical disturbance intensification. Atmos. Sci. Paper No. 259, Dept. Atmos. Sci., Col. State Univ., Fort Collins, CO, 1-75.

APPENDIX A: COMPUTER PROGRAMS

In most of today's atmospheric science research, the computer plays a large role. Particularly in any kind of numerical modeling or complex numerical solutions, the computer program that directs the solution is a major part of the research effort and should preferably be an integral part of the ensuing research report.

Unfortunately, the mere bulk of the programs written for this research prevents listing them in this dissertation. However, I will try to honor any requests for copies of the actual FORTRAN listings and to answer any specific questions dealing with the programs. Inquiries concerning the programs should initially be addressed either to my advisor, Professor Holton, or to me in care of his office:

Vernon L. Bliss
c/o Professor James R. Holton
Department of Atmospheric Sciences, AK-40
University of Washington
Seattle, WA 98195

APPENDIX B: DISPLAY NOTES

Model fields in this dissertation were generally displayed by specialized computer programs. Most were either already calculated at or transformed to geopotential grid points (see Figures 4 and 5) in order to facilitate overlays for comparison purposes.

The wind field was transformed to the geopotential grid because u and v were not directly calculated at geopotential points. This transformation used linear interpolation to obtain u and v on the inner geopotential grid points. For example, on the even grid of Figure 4, u and v were calculated at the $\phi_{2,2}$ position by averaging the two neighboring u components in the x direction and the two neighboring v components in the y direction. This process, although necessary, did smooth the displayed wind field in comparison to contoured fields such as geopotential.

The wind vector and the contoured plots generally have slightly different scales. This occurs because the wind vector displays were calculated using one set of system subroutines while contouring was, by local necessity, done with a completely different systems program. However, the actual display scale differences are generally less than 1%, and one may still adequately match the overlays in most cases.

The boundary layer vertical velocity (w) fields are somewhat eccentric and deserve comment. Because of the way w was used, the forecast model calculated and output w at points for the same time level as the other fields but on the geopotential space grid indicative of an alternate time level. These fields could have been interpolated back to the other time grid for display. However, the w in the forecast model were already implicitly smoothed, and any additional interpolating or regridding for display would have

only further smoothed the fields. Thus, these fields were displayed on their own output grid as in Figure 4. However, they can still be aligned on overlays of other fields by centering.

The vorticity was calculated at the same points as w in order to minimize smoothing. Contour plots of vorticity, like w , can still be compared with other fields by centering the overlaid plots.

The contour and wind vector plots have no inherent distance markings on them. For any measurements or comparisons of distances, the reader may use the following table as a guide for scales.

TABLE 12

SCALES FOR CONTOUR AND WIND VECTOR PLOTS

Experiment	Geographical Distance of Bottom Edge of Plot (km)	Scale (km/in)
all V	3800	794.8
all E	4834,667	765.9
EC1-EC3	2486.40	476.4
EC4-EC9, EC11-EC20 (abbreviated plots)	2509.21	528.25
EC4-EC9, EC11-EC20	2509.21	955.9

The geographical distances in Table 12 apply specifically to a geopotential plot. However, the scales would apply to all contour or wind vector plots within a given experiment or set of experiments.

A final note involves the energy plots, which were internally normalized for display. Thus, the displays present the relative deviations from the average energy within a given energy history. This was necessary to insure automated, presentable plots without extensive manual tinkering. Such normalization does not prevent use of the plots for their major purpose, monitoring energy changes within a given integration; but it does complicate easy comparison of energy levels between different model runs.

APPENDIX C: MODEL TESTING

C.1 Dirichlet Boundary Forecast Model

The first testing used a simple barotropic initial state and turned off sources and sinks in the model. The reasoning behind this was that the model must perform well in this situation if it is expected to produce physical results in much more complex simulations. Thus, if the model fared poorly in the V2 experiments of Table 4, it would not be expected to do well in the easterly wave case with friction and CISK turned on.

Experiment V2A was the basic test of the above type and was run with a time step well below the maximum

time step that was permitted by the linear stability criterion. One can compare Figure 65 and Figure 66 with Figure 9 and see that the vortex has changed insignificantly after ten days of forecast integration. Since the initial vortex was barotropic and the forecast used no sources or sinks, the vortex should have simply continued to rotate without change just as it apparently did. The only detectable change in the ten-day wind field from the initial field is that the maximum wind speed has increased from 9.6 to 9.8 m/sec.

A look at the geopotential fields of the V2A experiment shows a few more changes. When compared to the initial field of Figure 10, Figures 67 and 68 do show some boundary distortion and some slight changes in the positioning of the isopleths, but the smooth, circular contour shape in the center of the domain is well-preserved. Both the similarity of these fields to the initial field and their smoothness--there was no explicit smoothing--are quite remarkable for a result from a ten day primitive equation model.

In the V2A no-sink-or-source integration, the area averaged energies should be conserved. Figures 69 to 74 show at most a variation of .8% in kinetic energy and .08% in potential energy over the ten day forecast period. These minor variations are quite acceptable because the model was not constrained to conserve these quantities by the numerical scheme.

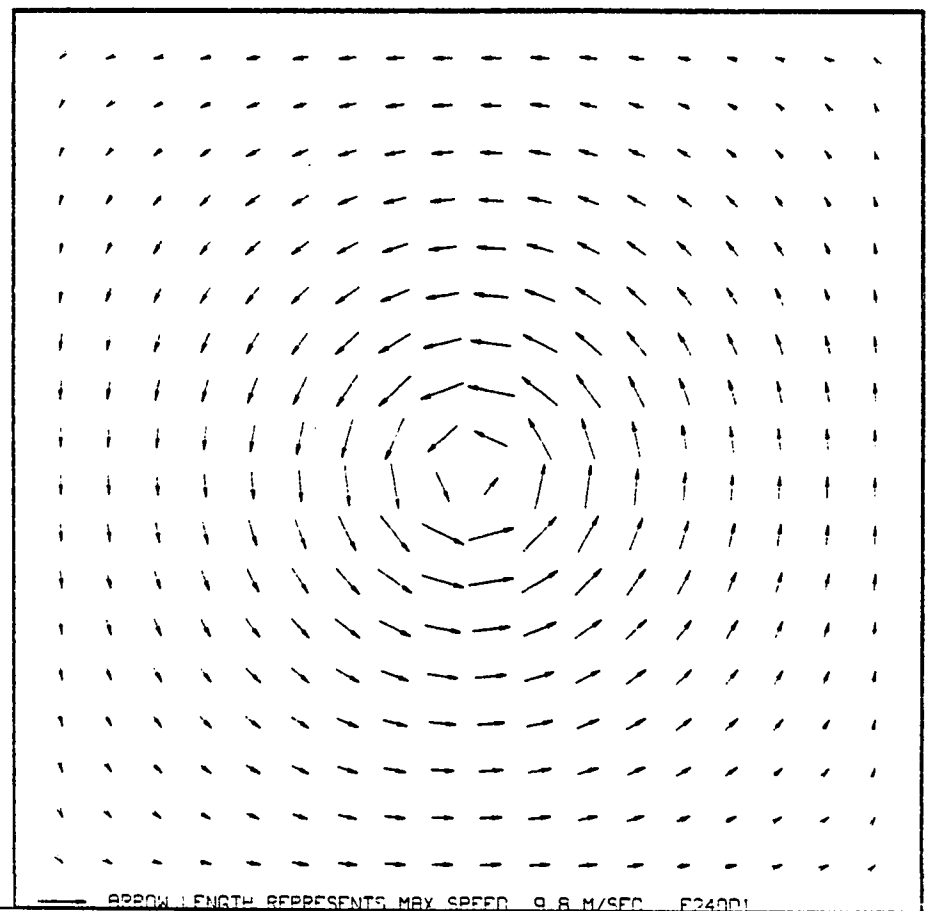


Fig. 65. V2A experiment. Level 1 wind field at forecast hour 240.

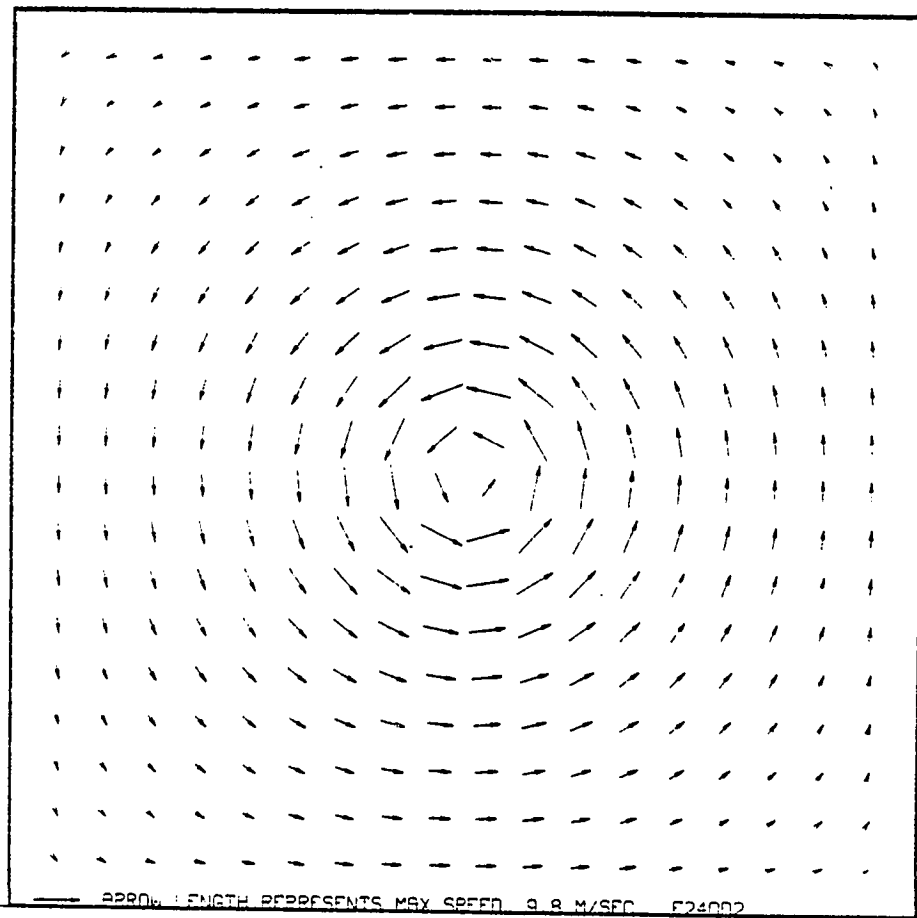


Fig. 66. V2A experiment. Level 2 wind field at forecast hour 240.

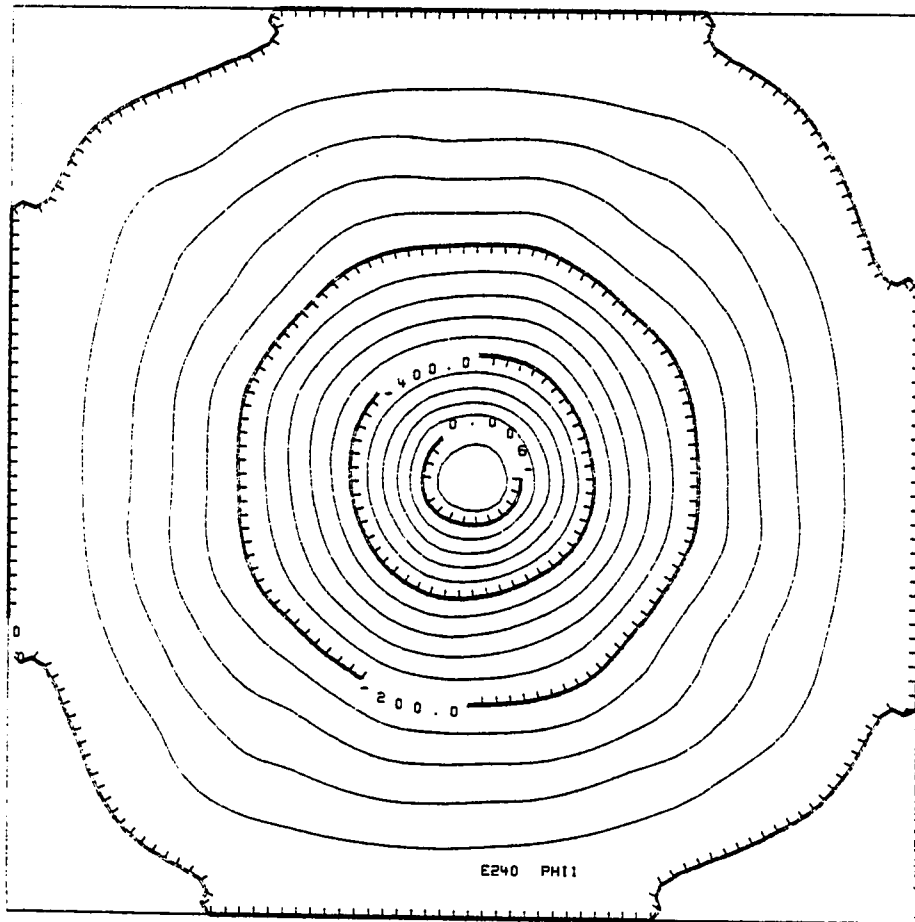


Fig. 67. V2A experiment. Level 1 geopotential (m^2/sec^2) at forecast hour 240.

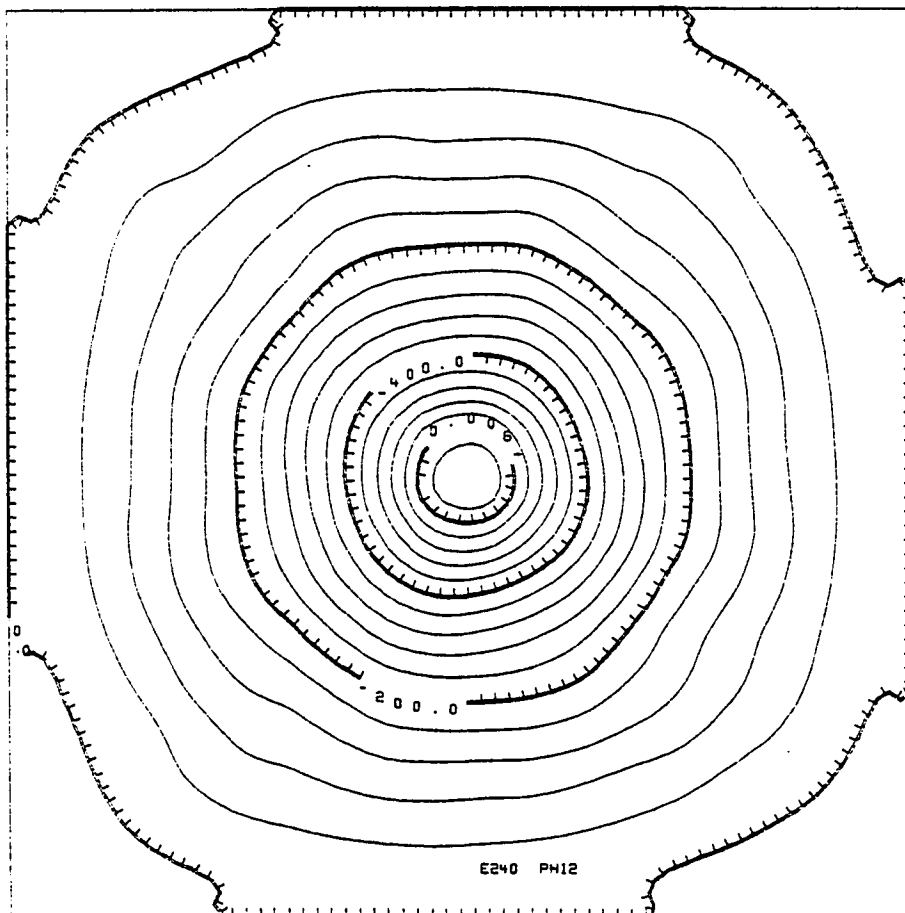


Fig. 68. V2A experiment. Level 2 geopotential (m^2/sec^2) at forecast hour 240.

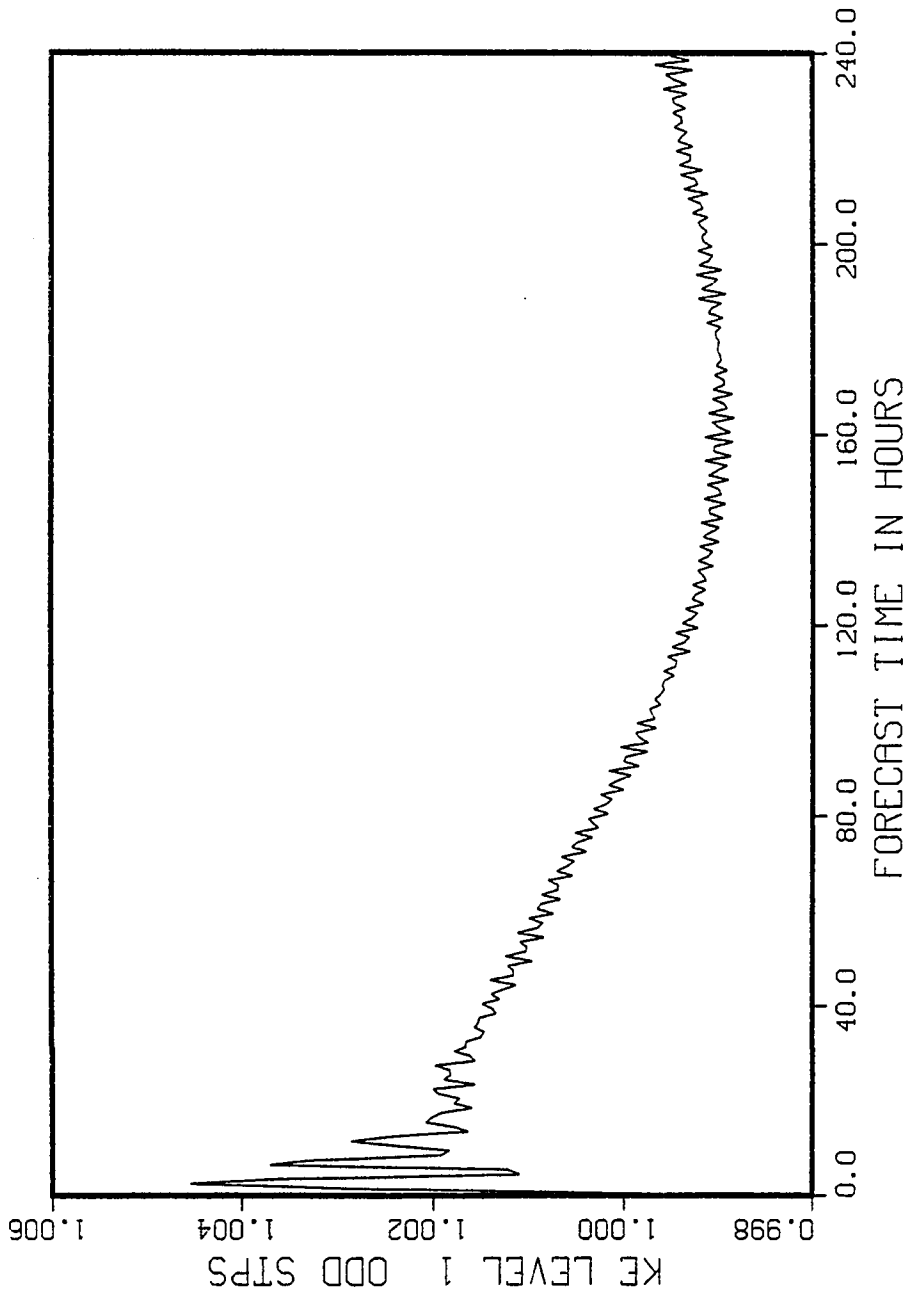


Fig. 69. V2A experiment. Level 1 total kinetic energy versus odd time steps.

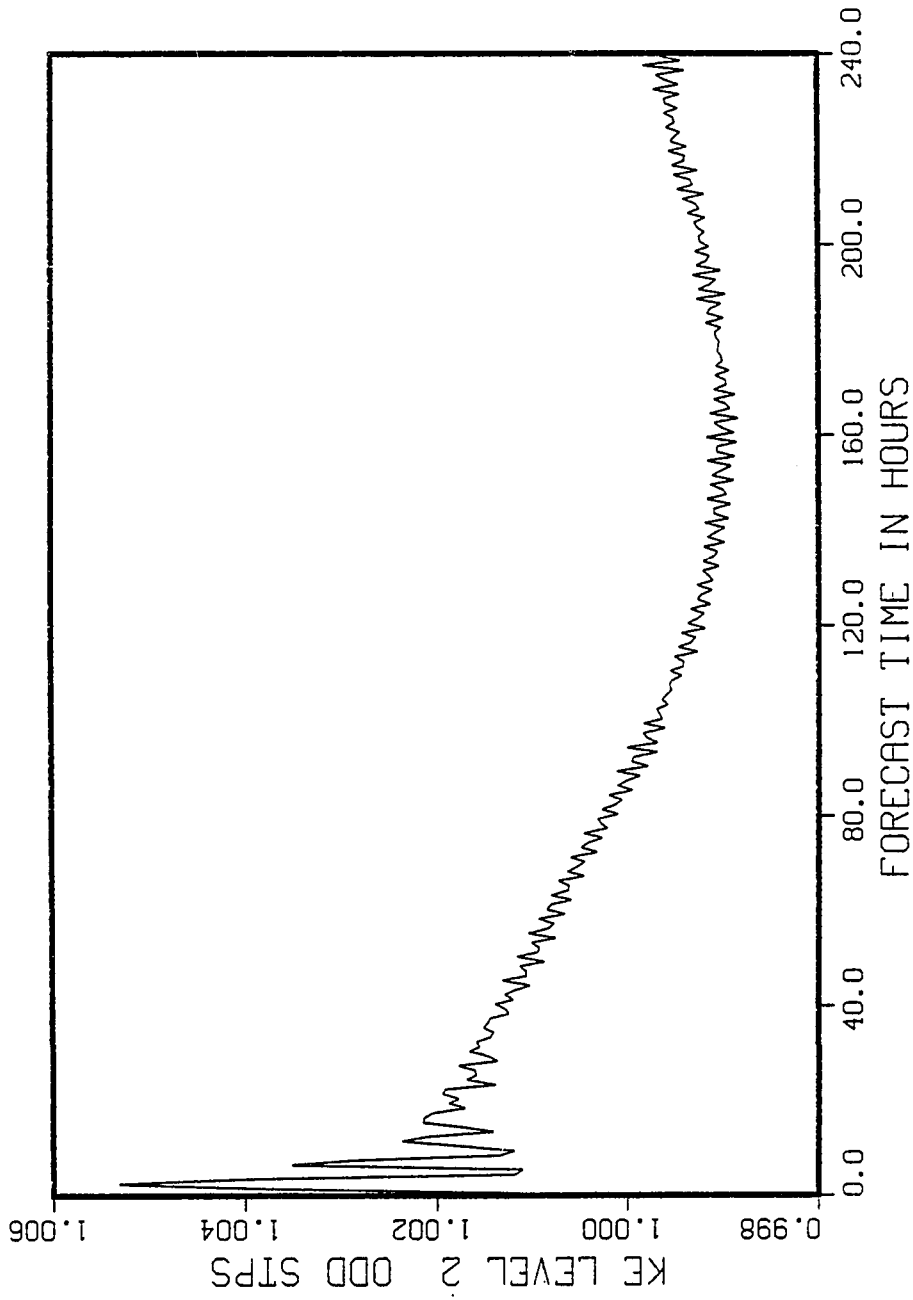


Fig. 70. V2A experiment. Level 2 total area kinetic energy versus odd time steps.

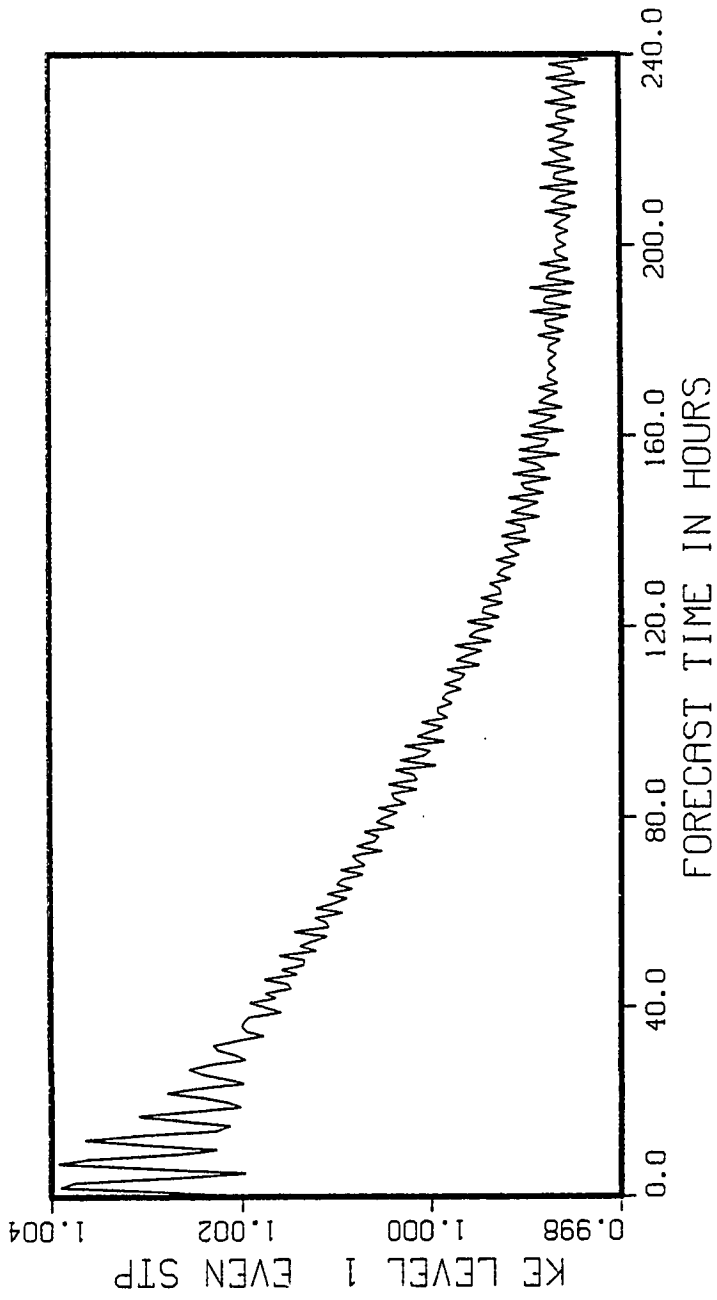


Fig. 71. V2A experiment. Level 1 total area kinetic energy versus even time steps.

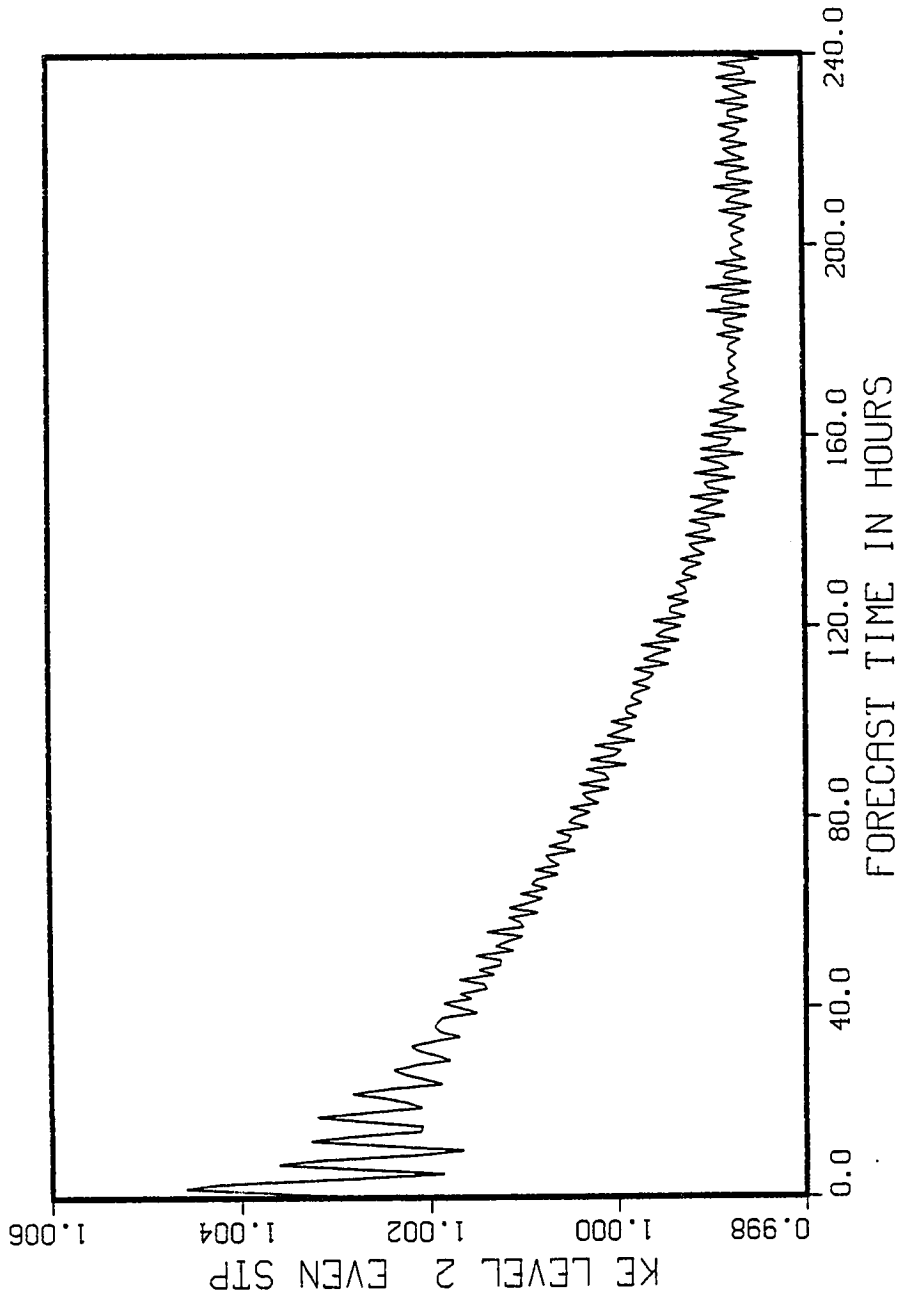


Fig. 72. V2A experiment. Level 2 total area kinetic energy versus even time steps.

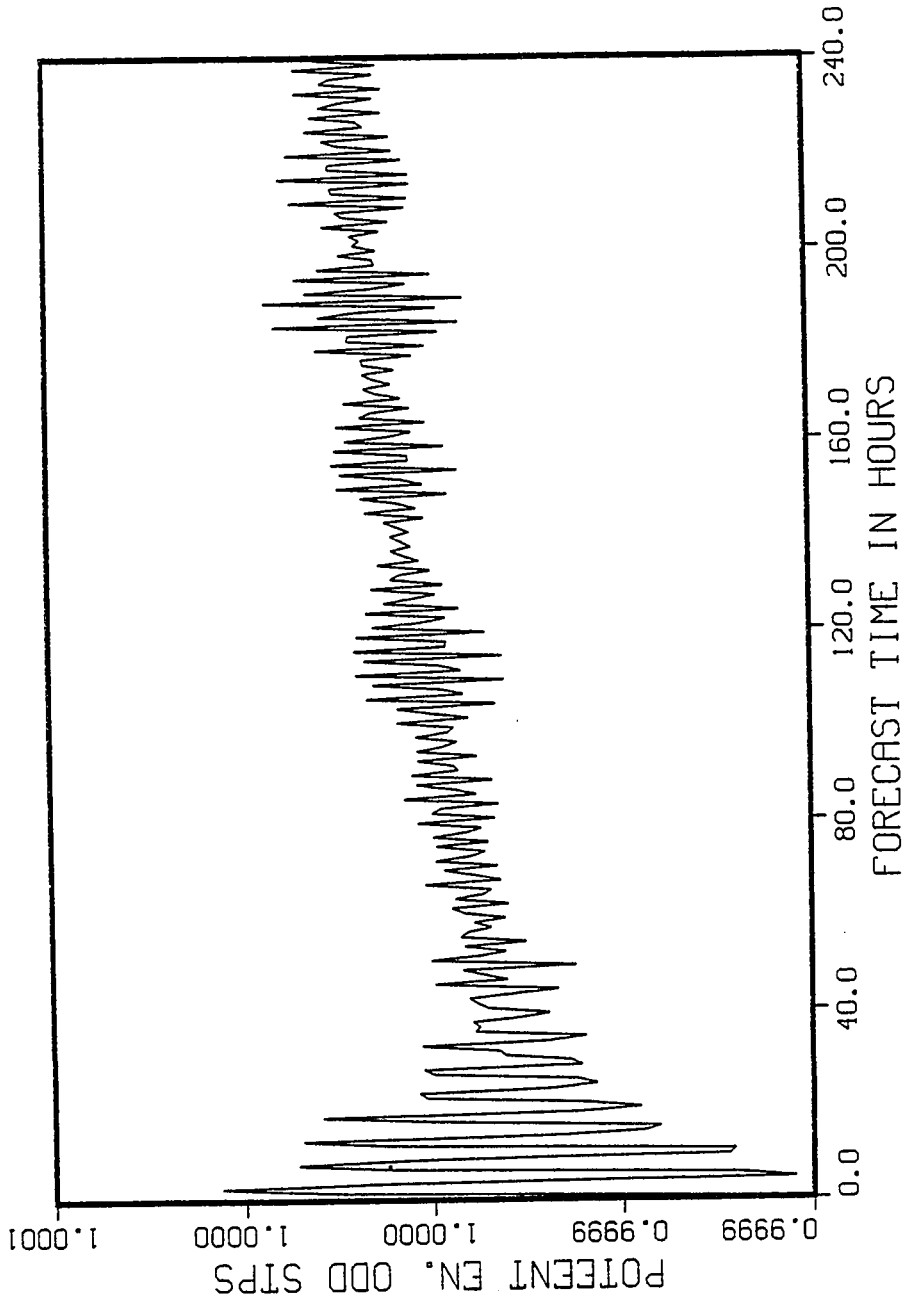


Fig. 73. V2A experiment. Total area potential energy versus odd time steps.

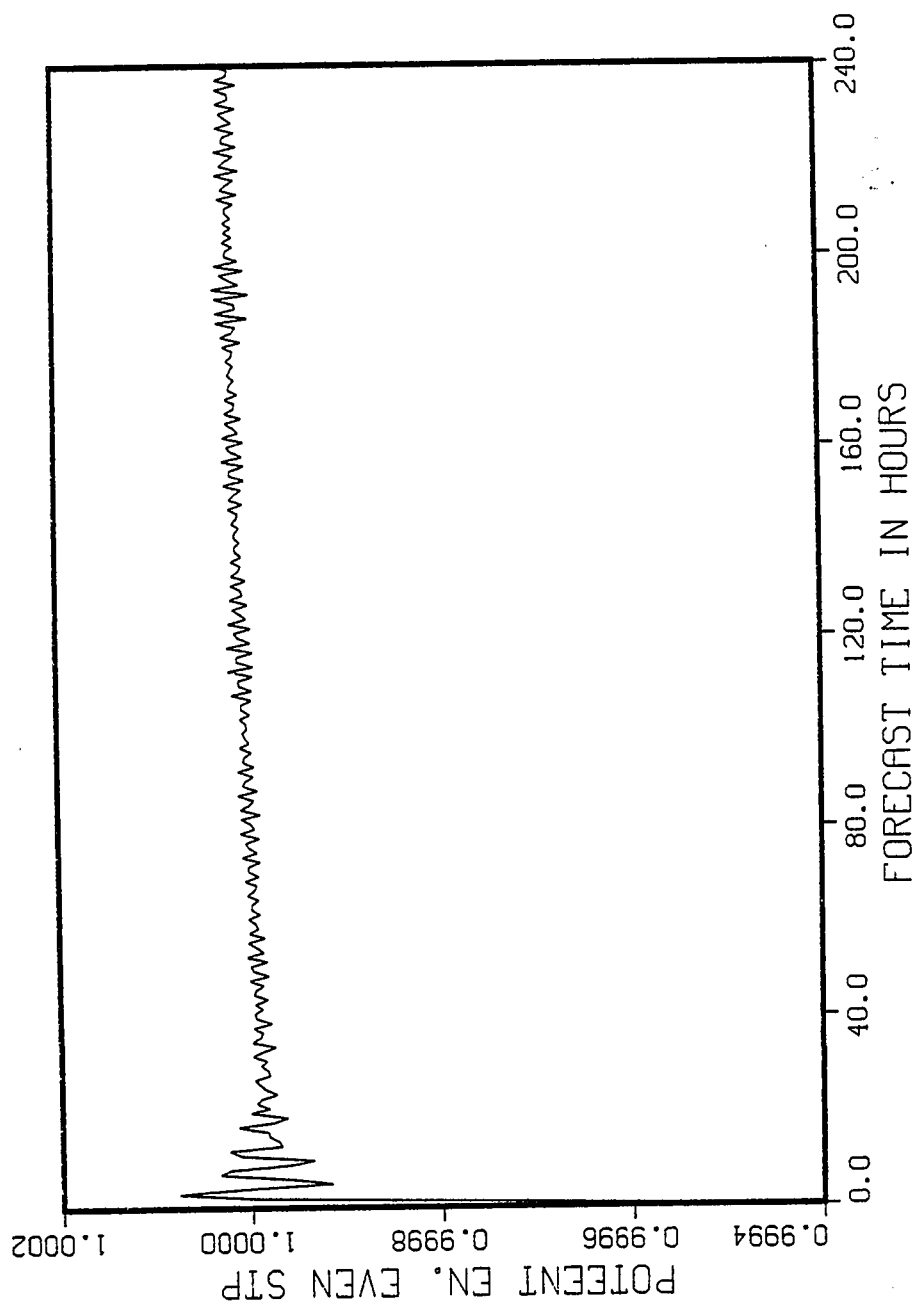


Fig. 74. V2A experiment. Total area potential energy versus even time steps.

With no sources or sinks, the vortex should neither significantly fill nor deepen. The time histories of minimum surface pressure in Figure 75 and Figure 76 confirm such a characteristic for this experiment. The exhibited surface pressures are in Pa units,¹ but conversion to mb shows that there is less than one mb variation in the minimum surface pressure throughout the integration.

A look back at the previous time histories reveals some apparent periodic variations in the fields. Benwell and Bretherton (1968) and Elsberry and Harrison (1971) have investigated similar phenomena for other limited area models and concluded that the oscillations are probably manifestations of standing inertial-gravity waves. However, the causes, amplitudes, and periods of the waves are model and initialization dependent; and their investigation would be lengthy. The low amplitude of these waves in experiment V2A suggests that they probably do not seriously mask or change the results of additional experiments with the forecast model. Thus, their detailed causes or methods to ameliorate their effect were not investigated.

¹The plotted pressures are calculated by $P = g\rho(h_0 + h_1' + \epsilon h_2')$ where g is gravitational acceleration, h_0 is the boundary layer thickness, h_1' is the layer 1 thickness deviation from standard, h_2' is the layer 2 deviation from standard, and ϵ is the ratio of layer 2 density to layer 1. For assumptions of $\epsilon = .9$, $\rho = 1 \text{ kg/m}^3$ in the lower layers, and a standard thickness of 5 km for both layer 1 and layer 2, one can obtain an actual total surface pressure by

$$P_{\text{sfc}} = P + g\rho(\bar{h}_1 + \epsilon\bar{h}_2) = P + 93100.$$

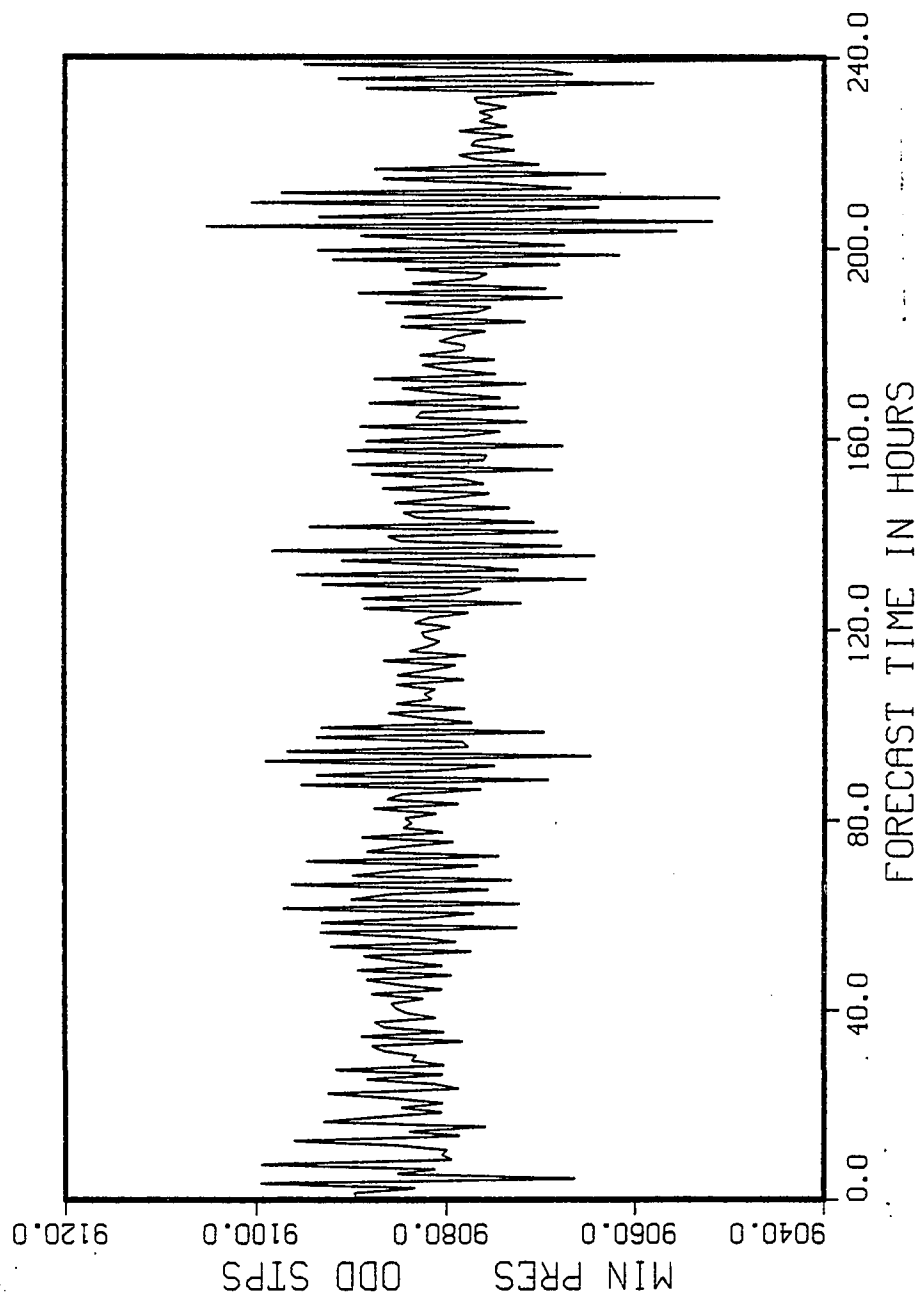


Fig. 75. V2A experiment. Minimum surface pressure deviations versus odd time steps.

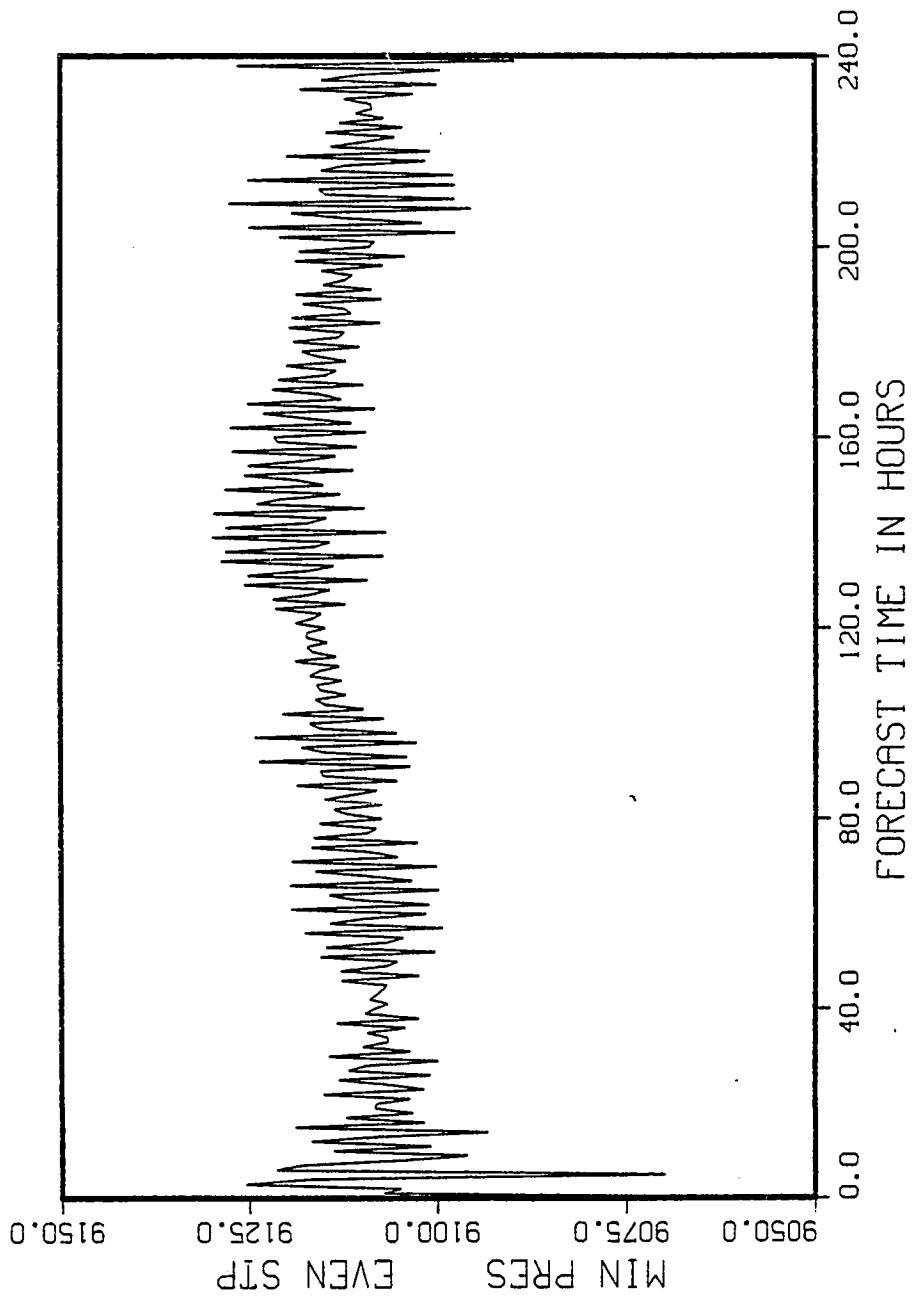


Fig. 76. V2A experiment. Minimum surface pressure deviation ($P_{sfc} - 93100$) versus even time steps. Units are in Pa.

Companions to the V2A experiment are the V2B and V2C experiments, which tested the basic model performance as a function of time step. Elvius and Sundstrom (1973) derived the linear stability criterion for a barotropic, single layer model with a numerical scheme similar to the one used here (see section 3.1.7). For the 10 m/sec vortex and the Δs of 100 km ($\Delta x = 200$ km) of experiments V2A, V2B, and V2C, this stability criterion would allow a maximum time step of about 2.78 hours. Experiments V2A, V2B, and V2C are all exactly the same except for respective time steps of .5, 1, and 2 hours. Comparisons among the following groups of figures show that all three time steps give comparable results and stability: V2A, Figs. 67, 74, 77-78; V2B, Figs. 79-81; and V2C, Figs. 82-84. This implies that the Elvius and Sundstrom criterion is reasonably valid for this model and also confirms the stability and programming correctness of the semi-implicit algorithm.

A first examination of boundary layer interaction in the model began with spin-down tests. Experiment V1, initialized with the same barotropic vortex as experiments V2A, V2B, and V2C was integrated with no source or sink except that provided by the boundary-layer-drag-generated vertical velocity. During the four-day integration, the vortex slowly decayed as Table 13 shows, and the boundary layer and layer 1 kinetic energies fell to about half their initial values. Crude analytical models can also provide estimates of these

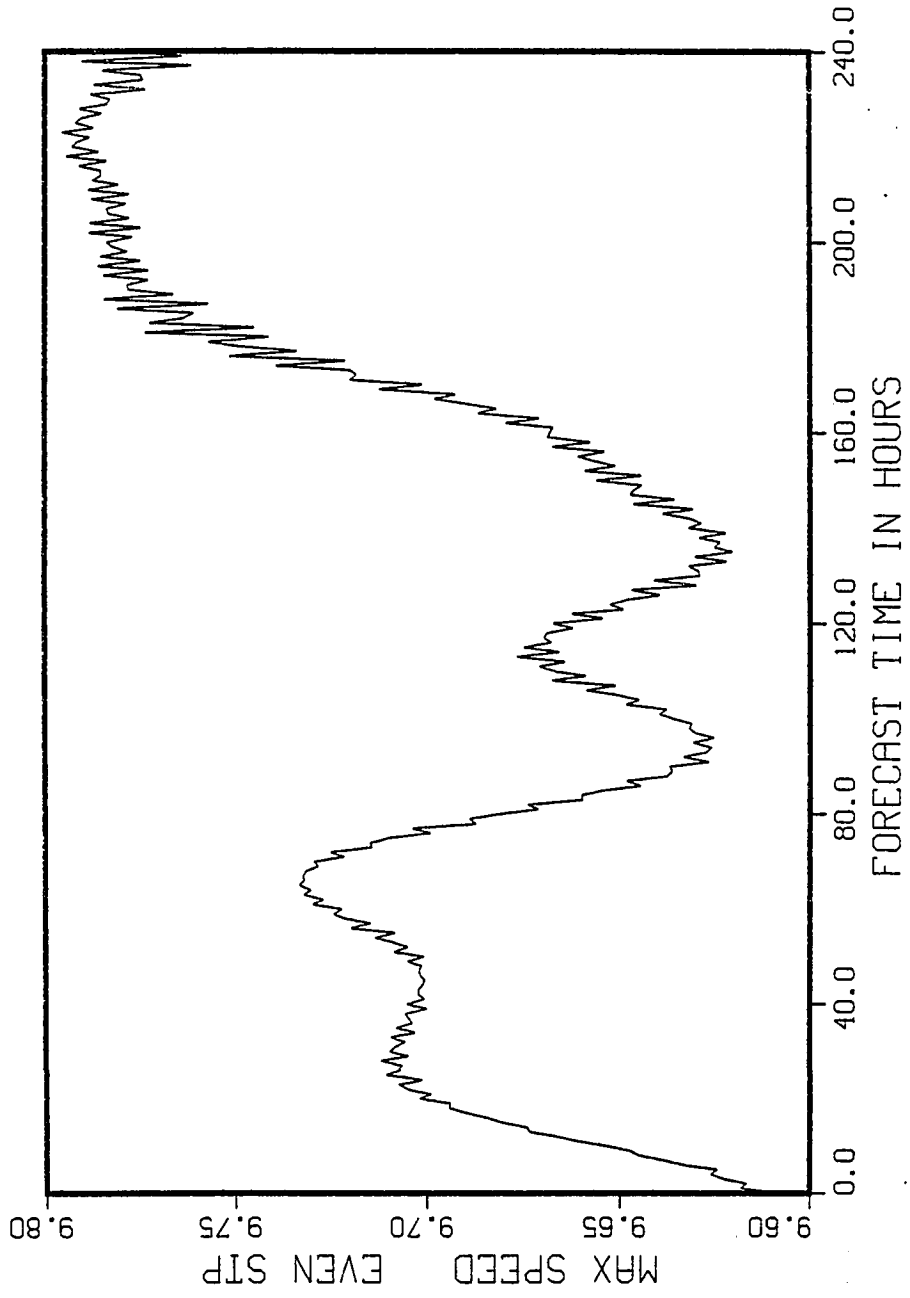


Fig. 77. V2A experiment. Maximum speed versus even time steps.

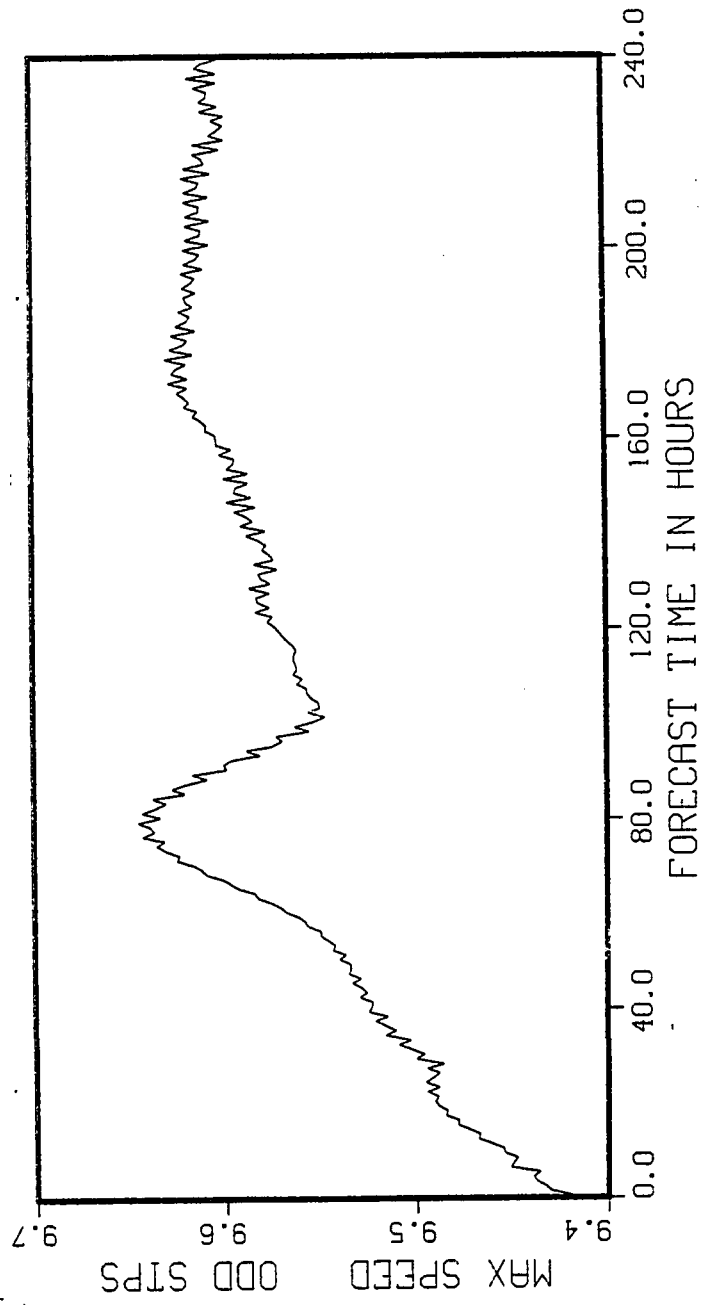


Fig. 78. V2A experiment. Maximum speed versus odd time steps.

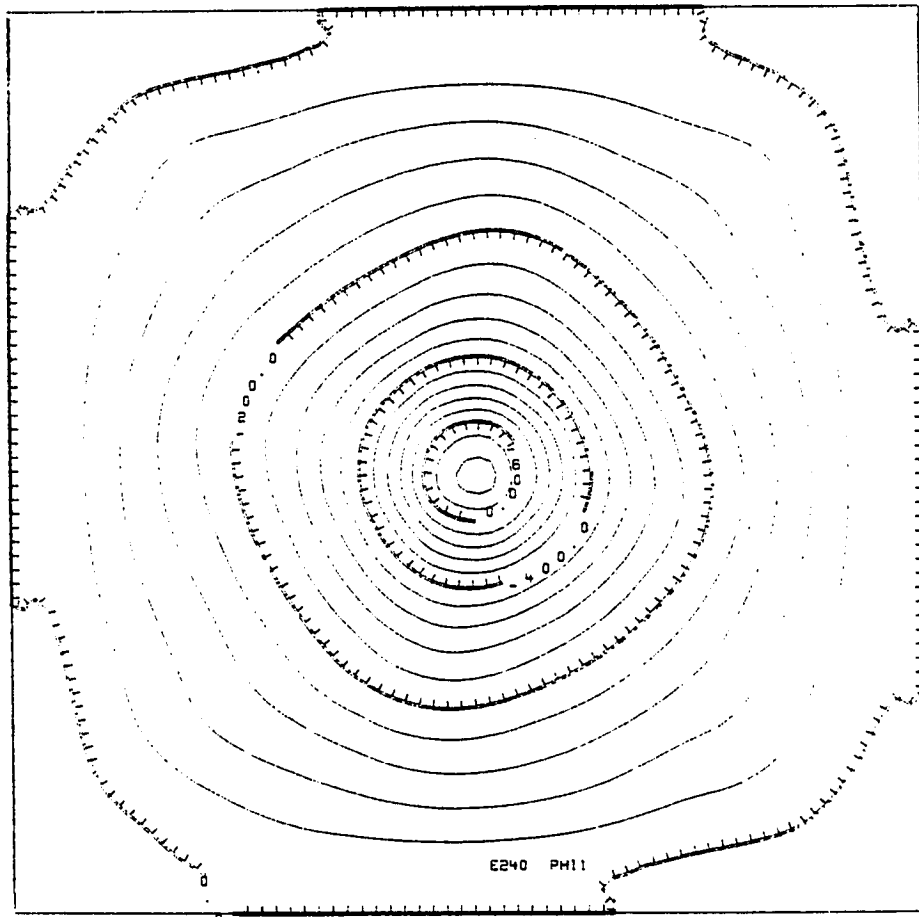


Fig. 79. V2B experiment. Layer 1 geopotential (m^2/sec^2) at forecast hour 240.

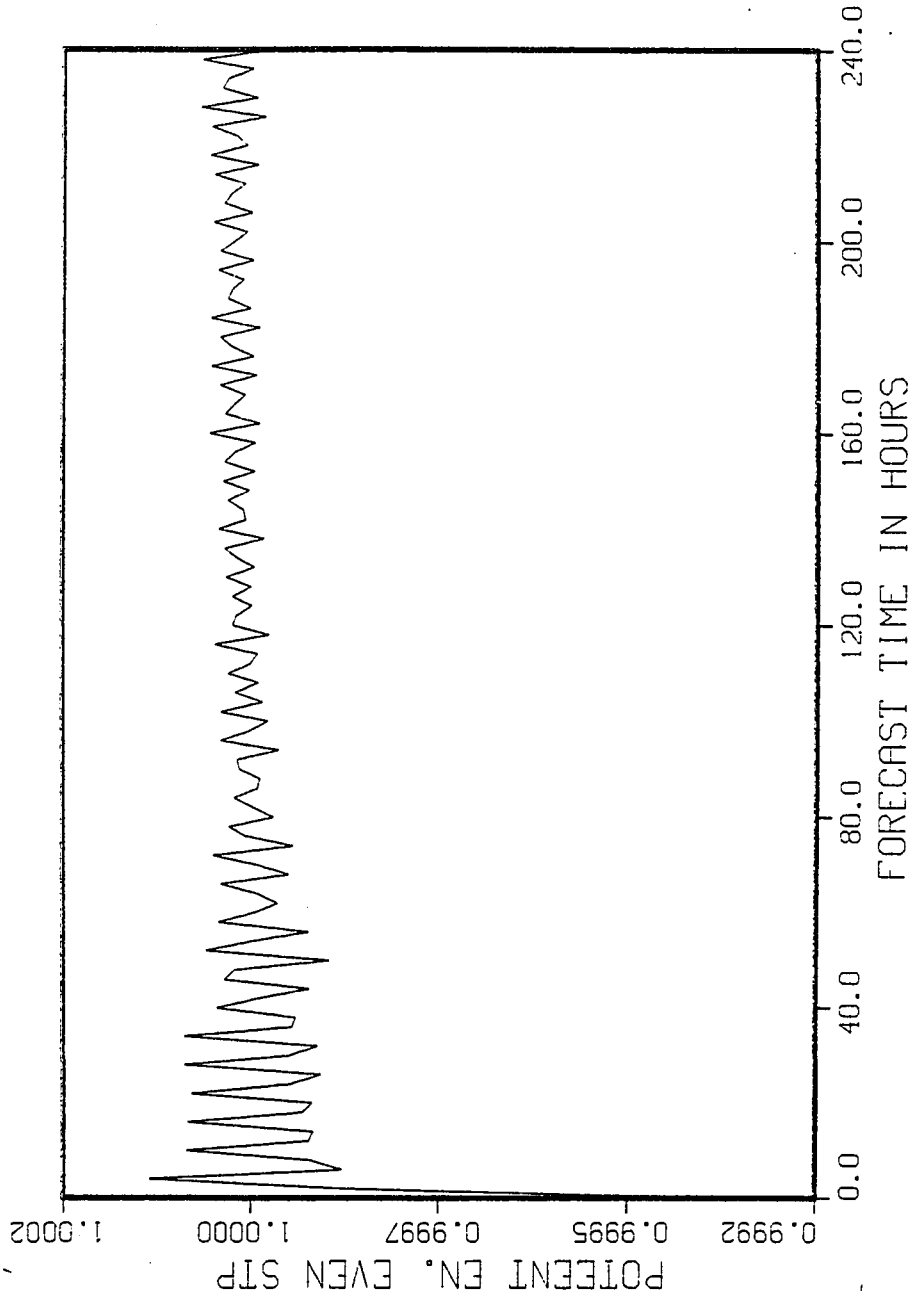


Fig. 80. V2B experiment. Total area potential energy versus even time steps.

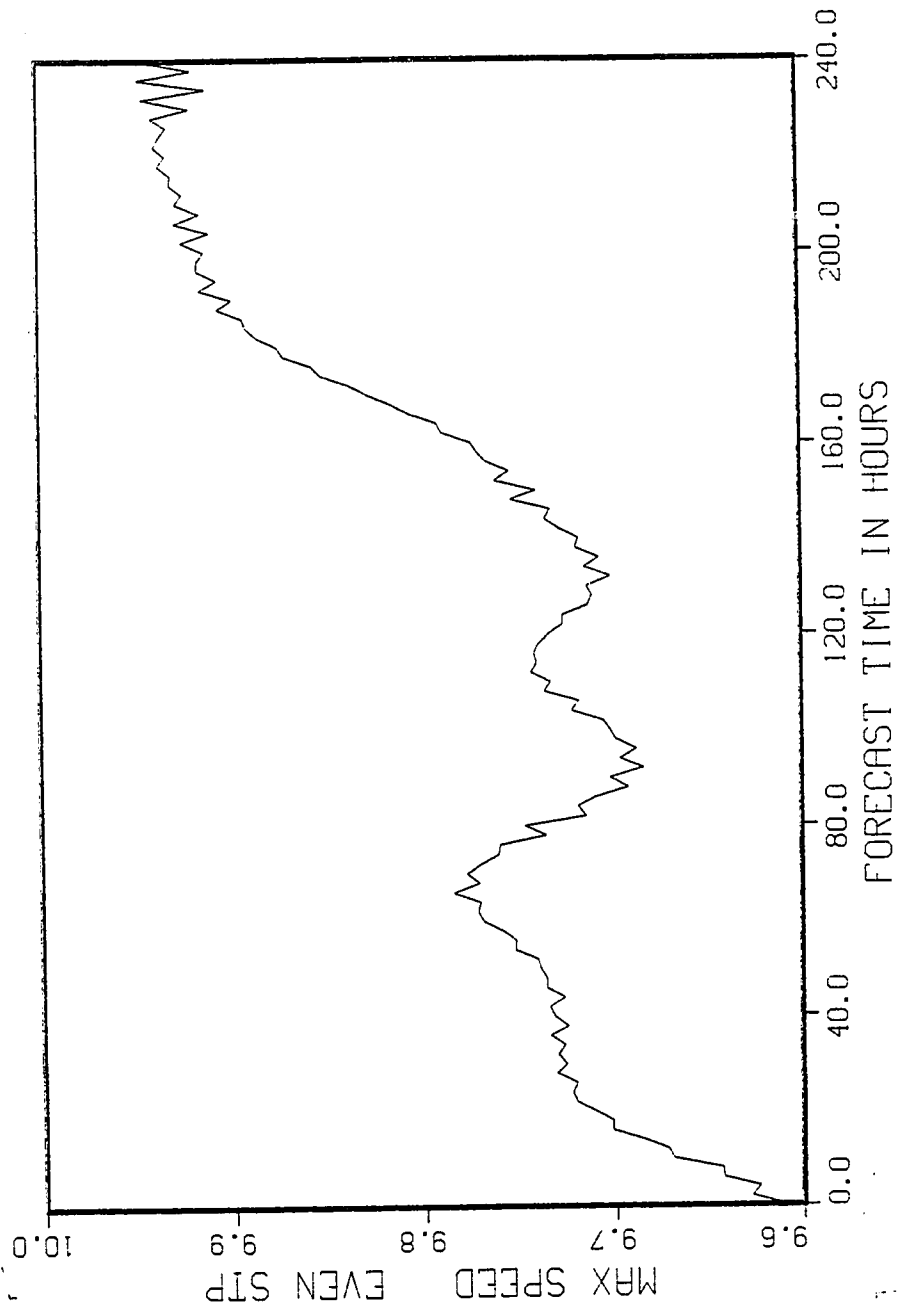


Fig. 81. V2B experiment. Maximum speed versus even time steps.

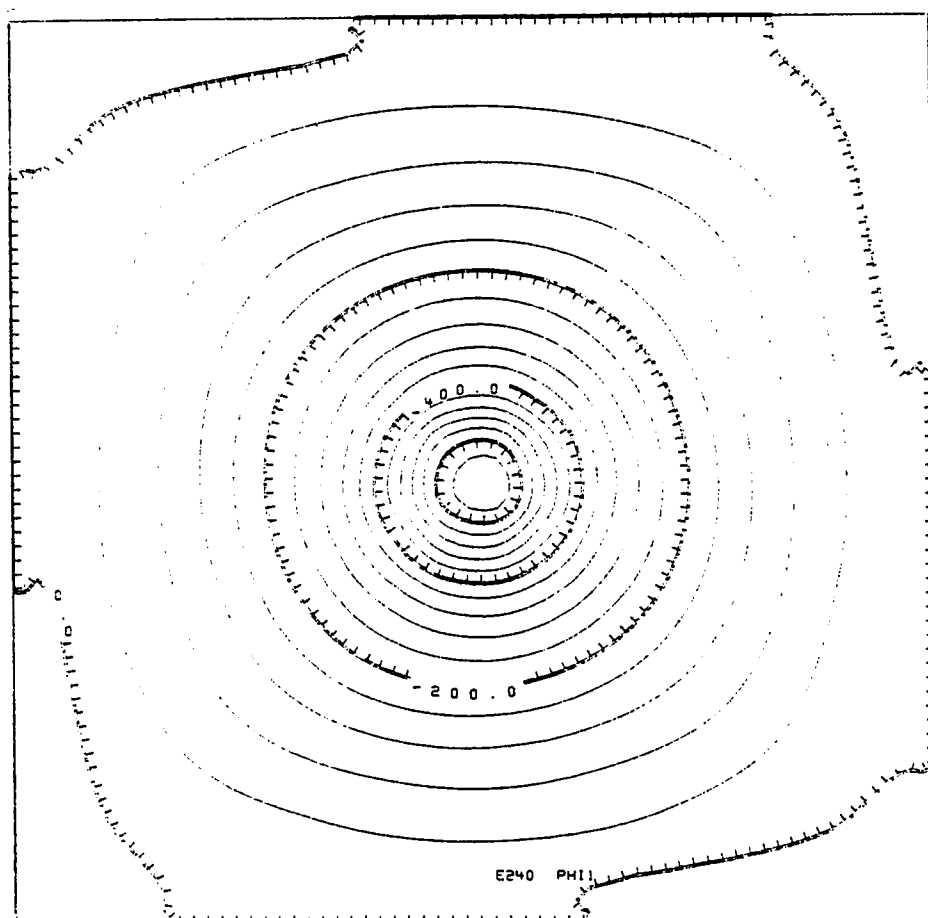


Fig. 82. V2C experiment. Layer 1 geopotential (m^2/sec^2) at forecast hour 240.

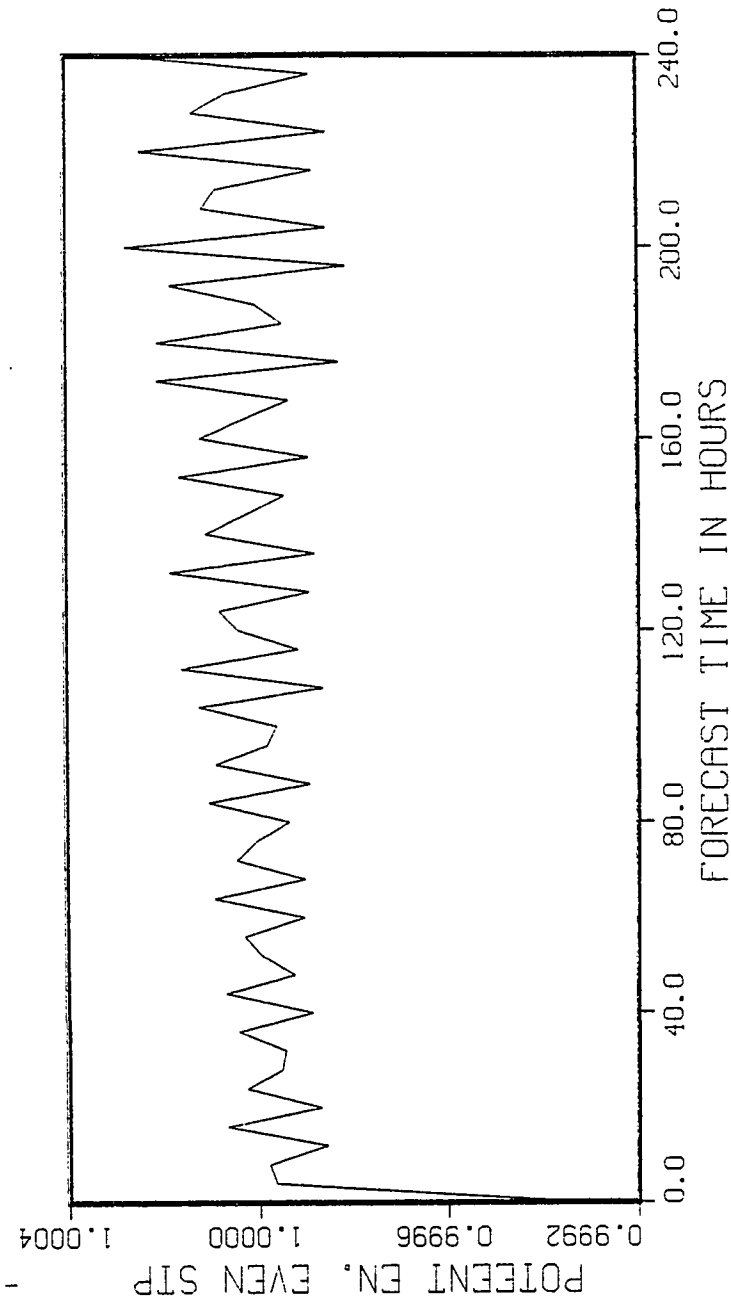


Fig. 83. V2C experiment. Total area potential energy versus even time steps.

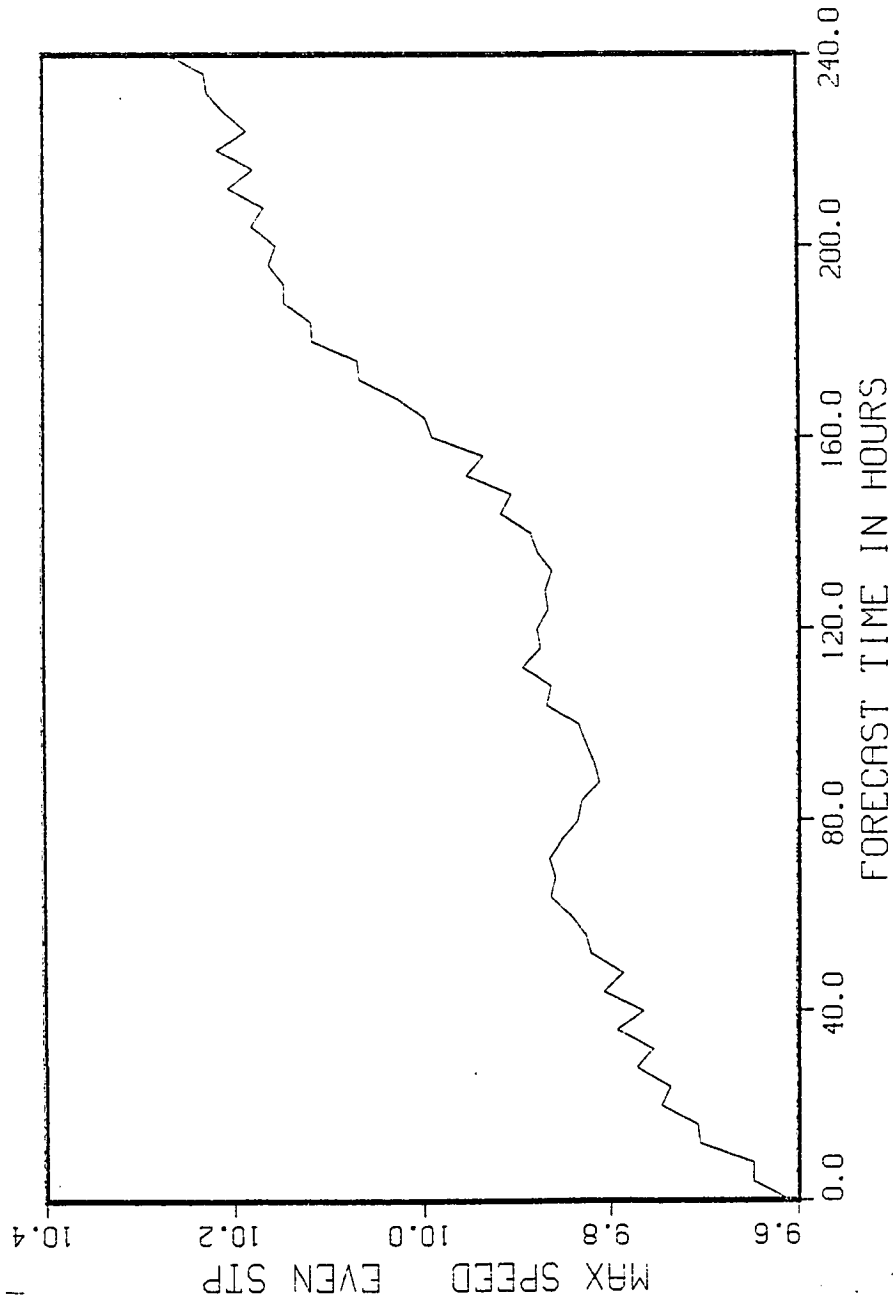


Fig. 84. V2C experiment. Maximum speed versus even time steps.

TABLE 13
SPIN-DOWN RATIOS

A final ÷ A initial where A is	Experiment VI		Experiment EC3	
	Even Step (used data)	Odd Step (used data)	Even Step (used data)	Odd Step (used data)
Area KE level 0	.513	.504	.581	.581
Area KE level 1	.524	.513	.582	.583
Area KE level 2	.865	.863	.956	.956
Min. Pressure	1.035	1.035	1.004	1.004
Max. Speed	.581	.572	.699	.694

numbers, and one such model (Holton, 1972) yields the following time constant for Ekman spin-down decay of a barotropic atmosphere:

$$\tau_E = H(2/fK)^{1/2} \quad (96)$$

where H is the barotropic atmosphere thickness, f is the Coriolis parameter, and K is the eddy coefficient. When pertinent values ($f = .00005 \text{ sec}^{-1}$, H = the combined thickness of layers 1 and 0 of 6000 m, $K = 10 \text{ m}^2/\text{sec}$) are entered into (96), one obtains a time constant of about 105 hours and a consequent estimated decay to about 40% of the initial energy after four days. This 40% decay rate does not exactly match the approximately 50% values of Table 13, but the correspondence is close when one recognizes the wide differences in method used to arrive at the two sets of values.

This reasonable correspondence supports the models capability, at least, to grossly simulate boundary layer interaction.

Although layer 1 and the boundary layer spin-down rather rapidly, layer 2 decays much more slowly. This is physically understandable because layer 1 is directly connected to the boundary layer by the boundary-layer vertical velocity, but there is no such direct connection between layers 1 and 2. The lack of a direct connection between layer 1 and 2 means that it takes longer for layer 2 to feel the effect of the boundary layer than for layer 1 to feel the same effect. Hence, the layer 2 vortex decays much more slowly than layer 1.

V3 is the first model experiment that attempted to simulate a hurricane-like disturbance. The experiment turned on the boundary layer friction, sea surface interaction, and the basic cumulus parameterization mechanism. For economy in computer testing, a grid spacing Δs of 100 km and Δx of 200 km (distance between points on display) was chosen to define the fields. This rather coarse mesh could not resolve the details normally found near the center of a hurricane, but the mesh was fine enough to pick out the major large scale hurricane development for model testing purposes.

The results were dramatic. By 48 hours the upper layer vortex was gone and was replaced by the developing anti-cyclone of Figure 17. By 96 hours the original barotropic vortex with a 10 m/sec maximum wind developed into a tropical

cyclone with a 33.4 m/sec (about 64.9 kt) maximum wind in the boundary layer and 33.3 m/sec in layer 1. Figure 16 shows the distinctive spiral inflow of the hurricane boundary layer, while Figure 85 exhibits the more symmetrical cyclone structure in the middle atmosphere above the boundary layer. Figures 86 and 87 confirm the boundary layer convergence near the center, and Figure 88 shows weak convergence near the center of the disturbance in the middle layer. In the upper layer, the anticyclone is now fully developed and Figure 89 and Figure 90 show its outflow and divergence away from the center. The forecast tropical cyclone appears to simulate several characteristics of the real world rather well.

During the integration, the geopotential fields changed smoothly and show little noise at the 96 hour point. When compared to the Figure 10 initial fields, the (Figure 91) lower layer geopotential field shows greatly increased gradients in order to support the increased velocity field. The upper layer geopotential field of Figure 92 presents a completely different picture and shows a reversed gradient that balances the upper level hurricane anticyclone. In both the upper and the lower level fields, the gradients seem very smooth, and they exhibit no significant extraneous noise.

The moisture parameter χ_0 and the convection parameter η are linked to the developing hurricane, and their fields became significantly altered during the integration. At the 96 hour stage, the χ_0 field of Figure 93 shows an increase

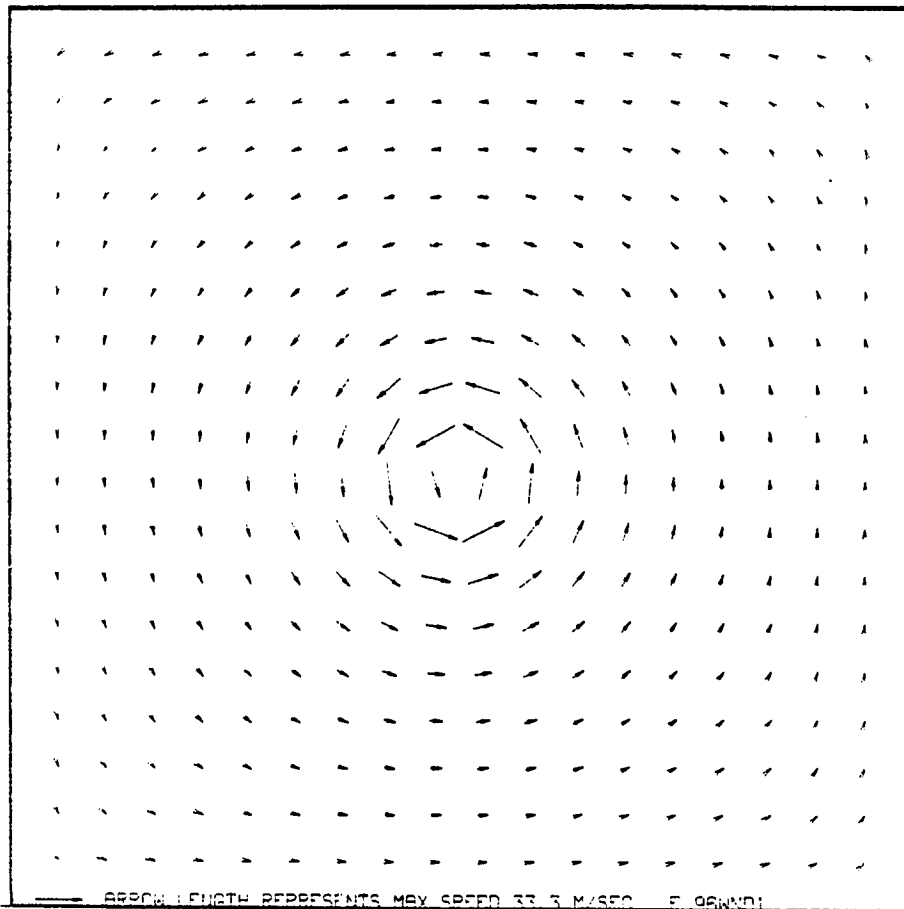


Fig. 85. V3 experiment. Level 1 wind field at forecast hour 96.

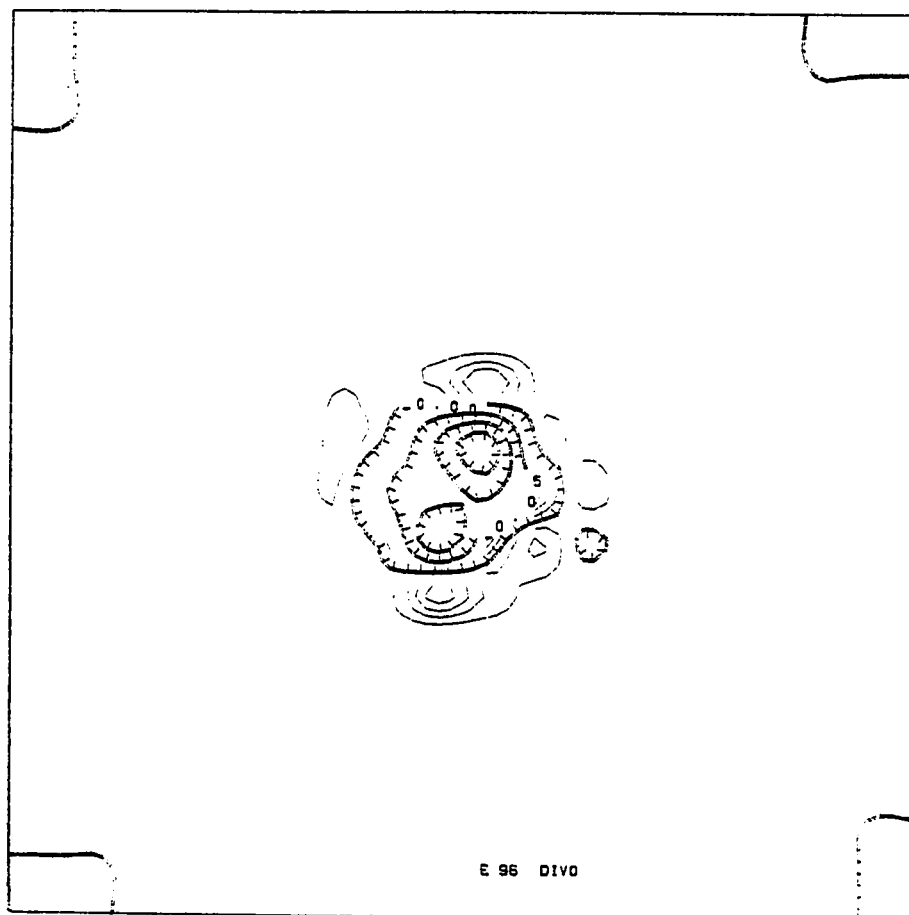


Fig. 86. V3 experiment. Level 0 divergence ($\times 10^3 \text{sec}^{-1}$) at forecast hour 96.

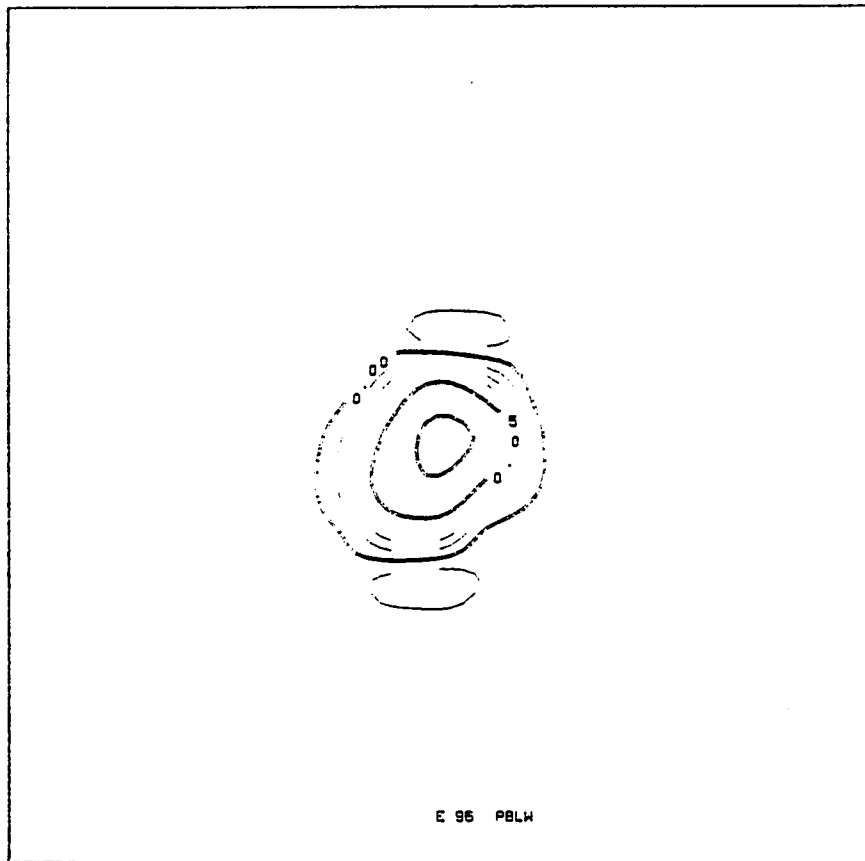


Fig. 87. V3 experiment. Boundary layer vertical velocity (m/sec) at forecast hour 96.

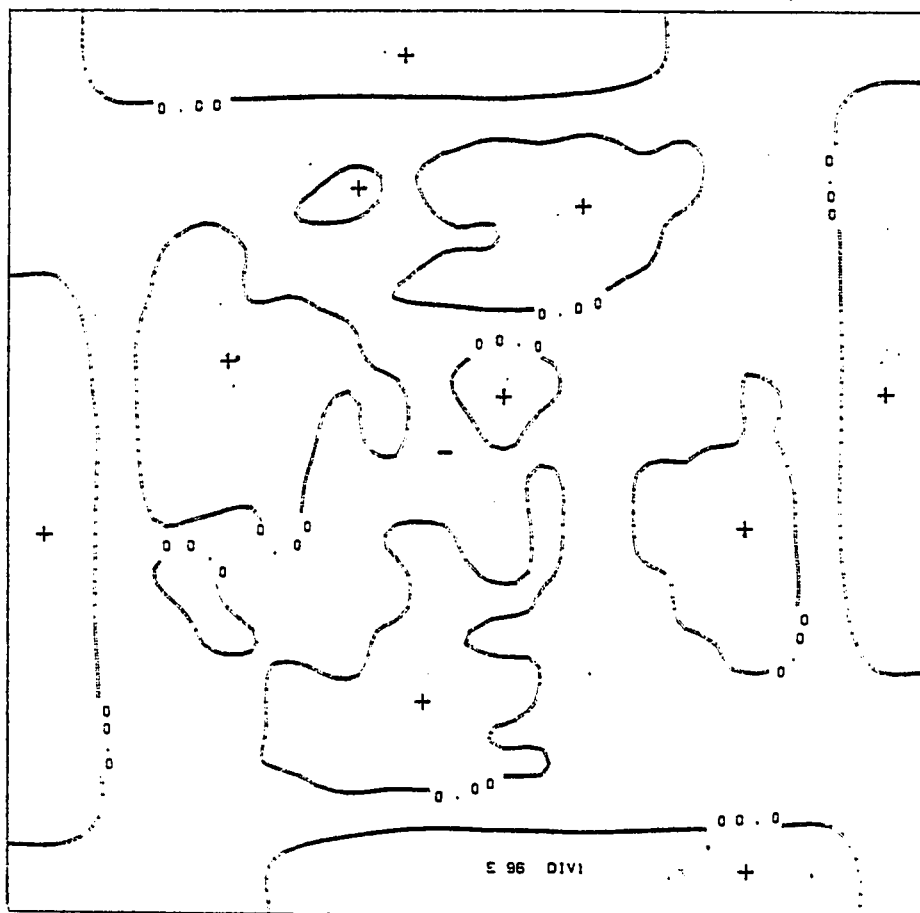


Fig. 88. V3 experiment. Level 1 divergence ($\times 10^3 \text{sec}^{-1}$) at forecast hour 96.

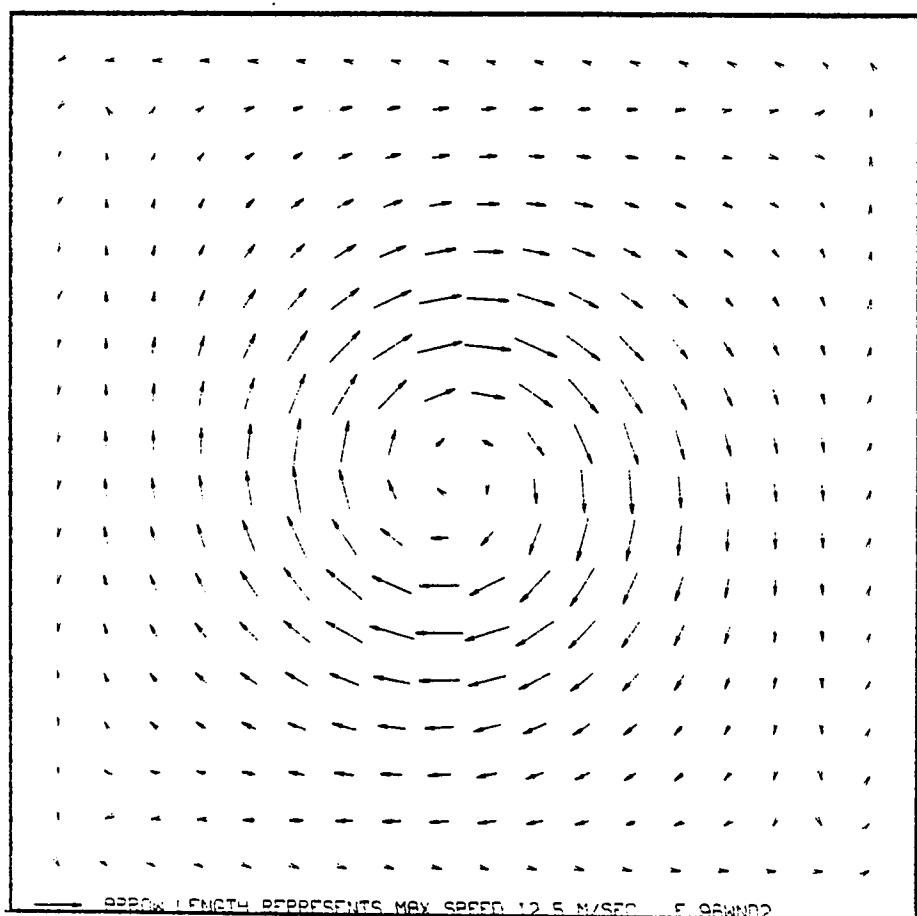


Fig. 89. V3 experiment. Level 2 wind field at forecast hour 96.

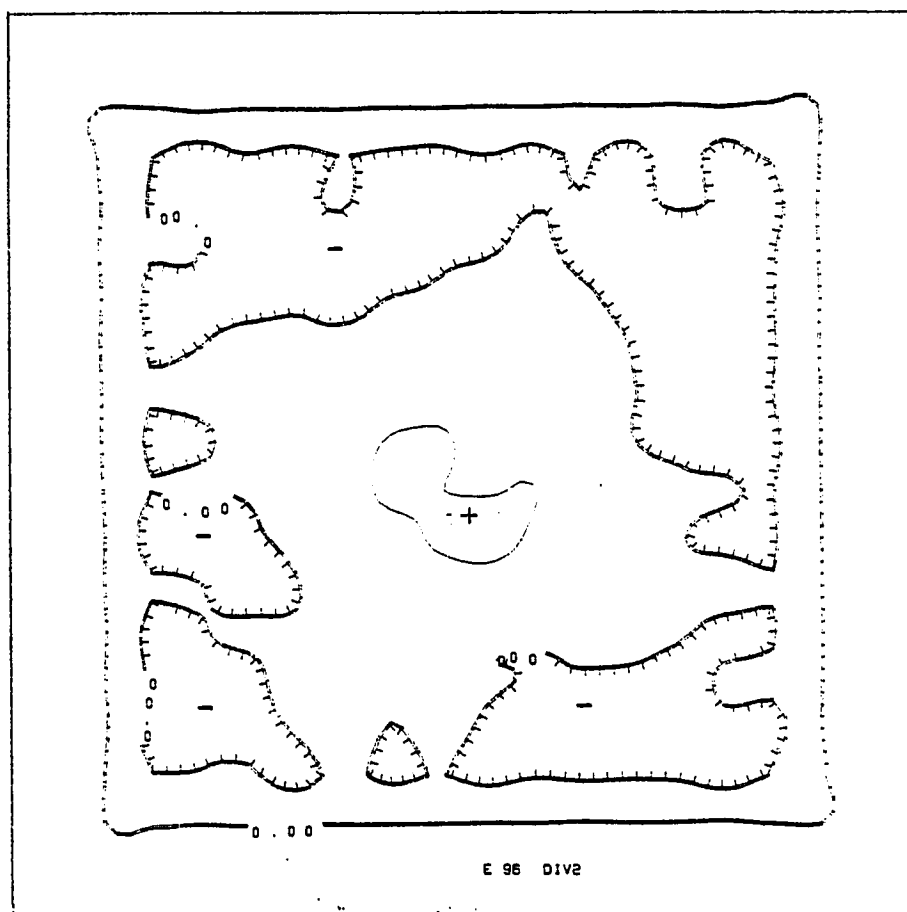


Fig. 90. V3 experiment. Level 2 divergence ($\times 10^3 \text{sec}^{-1}$) at forecast hour 96.

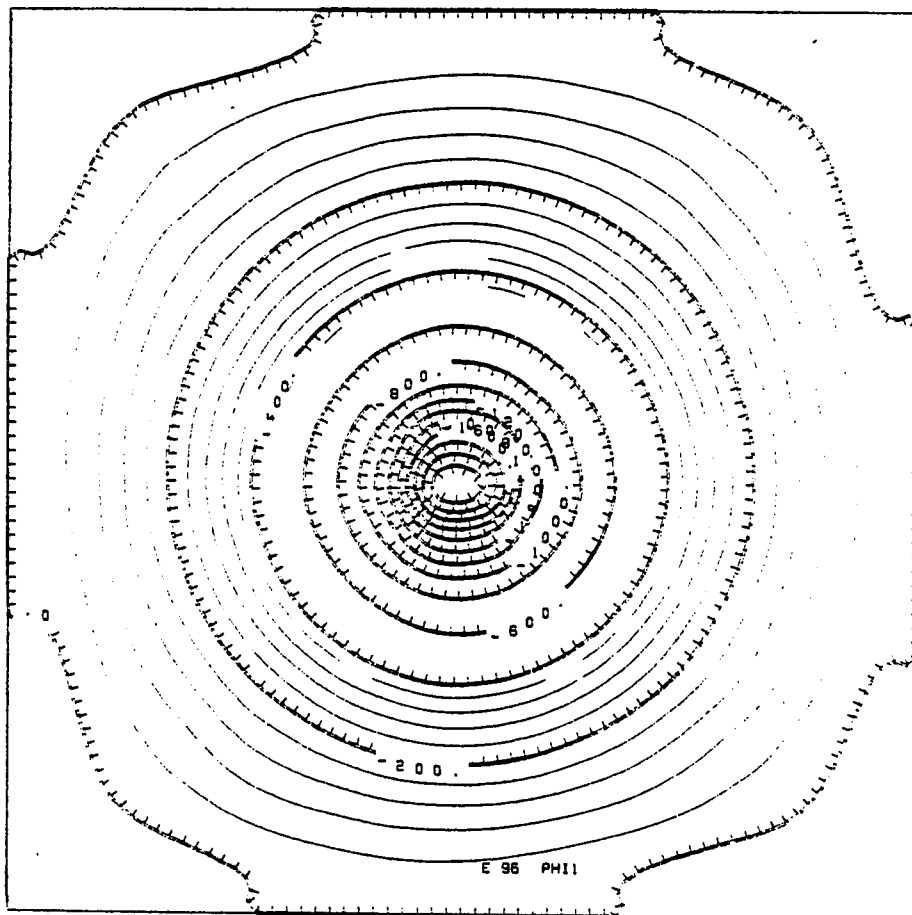


Fig. 91. V3 experiment. Level 1 geopotential (m^2/sec^2) at forecast hour 96.

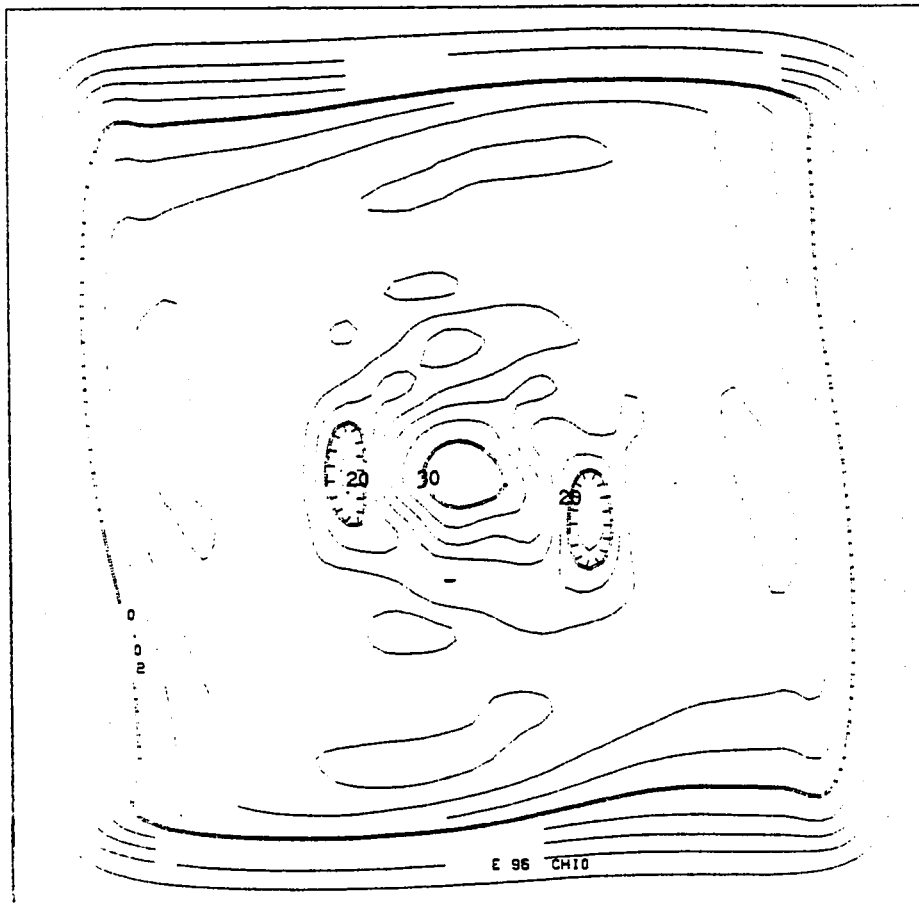


Fig. 93. V3 experiment. Boundary layer X_0 (K) at forecast hour 96.

in χ_0 and a concentration near the hurricane center when compared to the initial χ_0 field, which had a uniform value of 10. This concentration is undoubtedly due both to advection into the interior by the converging boundary layer wind field and by transfer of moisture from the sea surface.

The convective parameter field of Figure 34 stands in opposition to the centrally concentrated χ_0 field. The η field has a minimum in the central region at the 96 hour point, and this is probably a major factor in the decreasing intensification rate displayed in the maximum speed plot of Figure 93.

With diabatic sources included, the model is not indefinitely stable. Although the wind field at 144 hours (Figure 96), still appears reasonable, the accompanying geopotential field of Figure 97 is already showing signs of instability, and the integration finally completely blows up by hour 168. The plots in Figures 94, 95, 98, and 99 all show the same story. The integration proceeds smoothly to about the hour 135 stage and then begins to develop increasing noise followed by a final catastrophic failure.

Fortunately, the model functions well for at least the first 96 hours, which is the particular period of interest in this research. While more inherent, long-term stability in the model would be desirable, its absence does not severely impact experiments that remain within the stable period of integration.

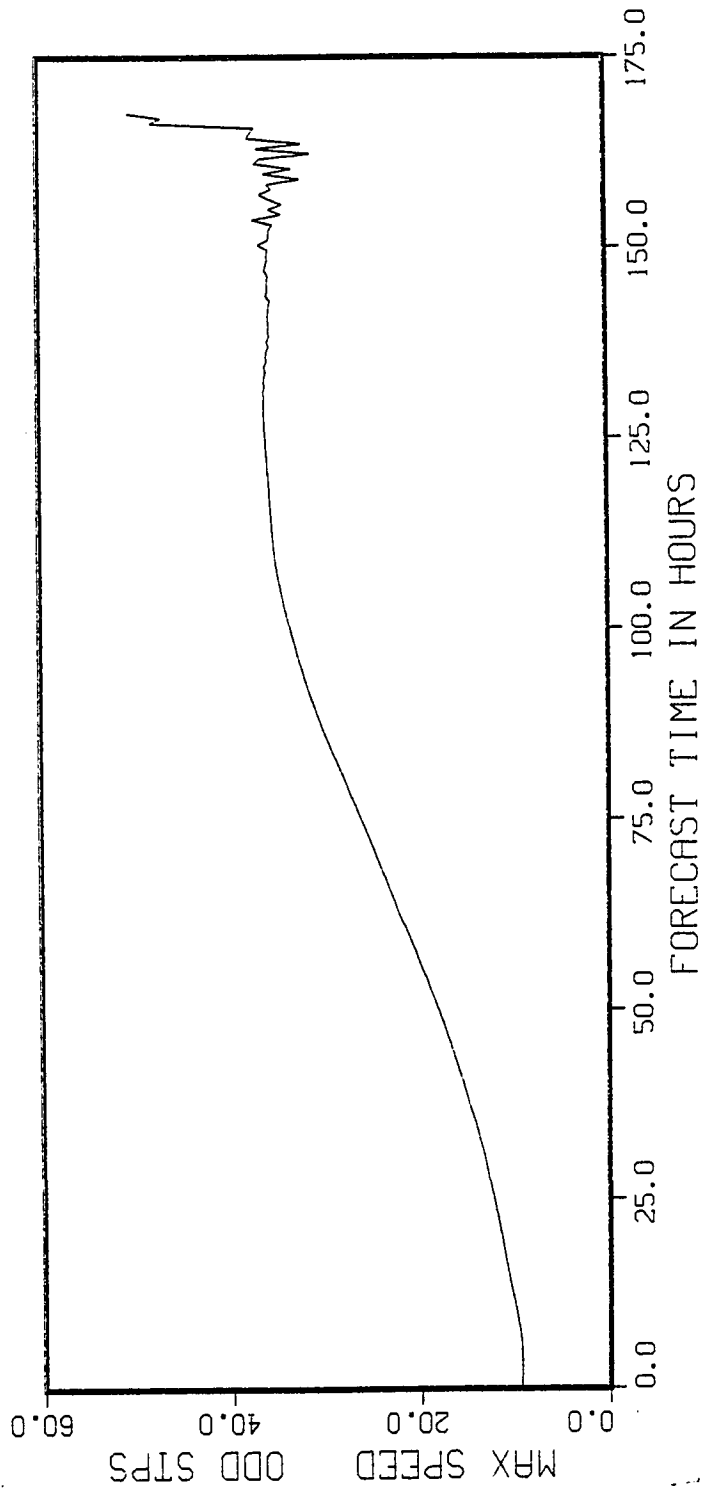


Fig. 94. V3 experiment. Level 1 maximum wind speed versus odd time steps.

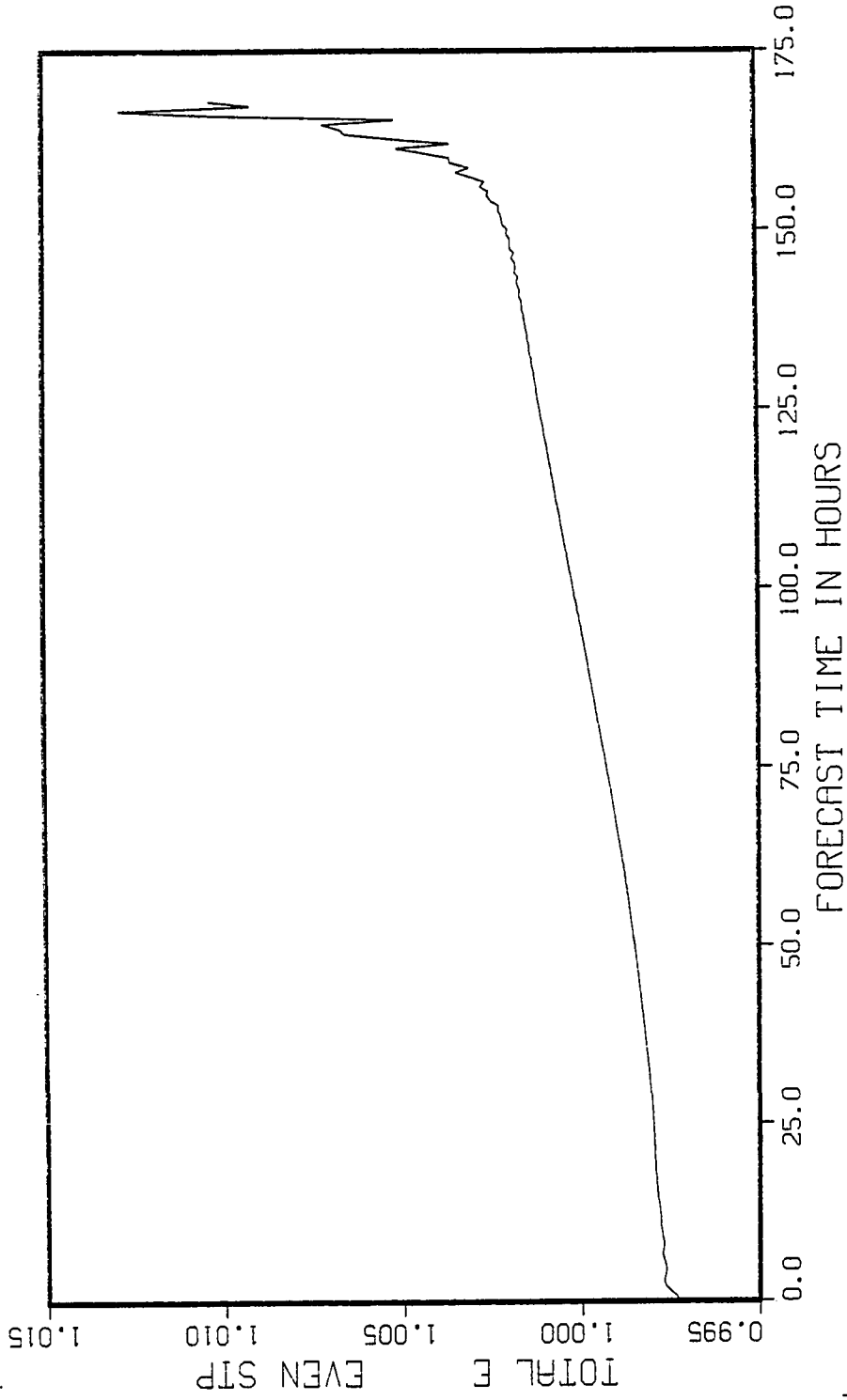


Fig. 95. V3 experiment. Total energy versus even time steps.

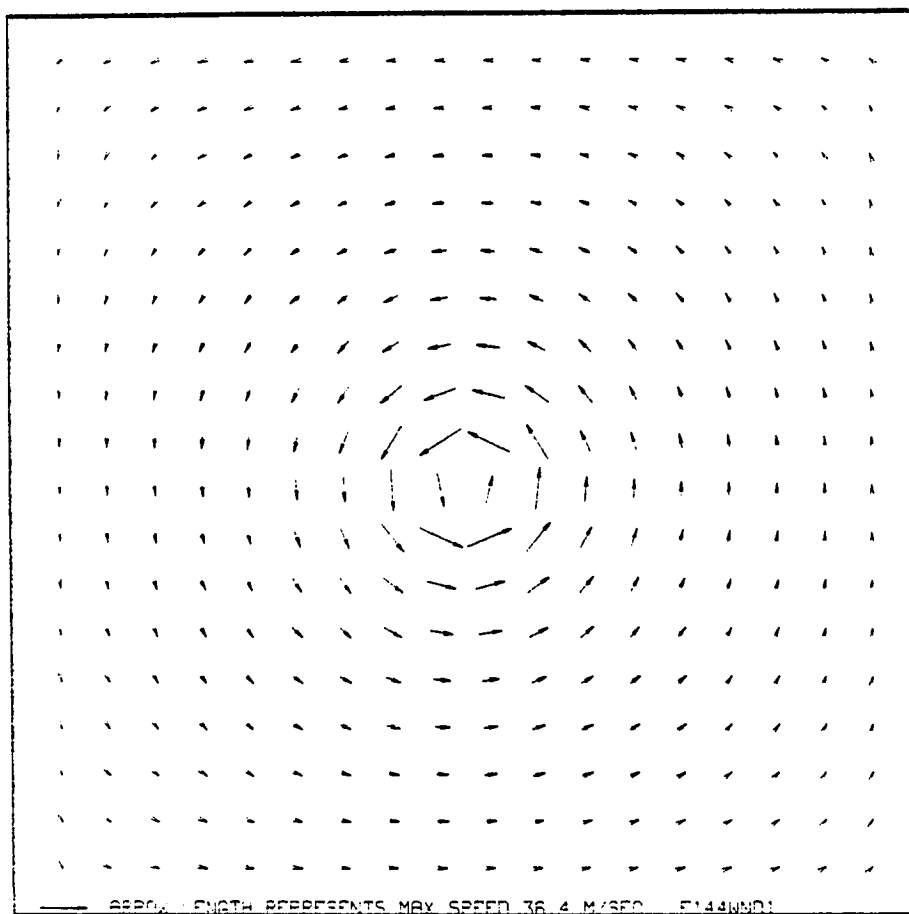


Fig. 96. V3 experiment. Level 1 wind field at forecast hour 144.

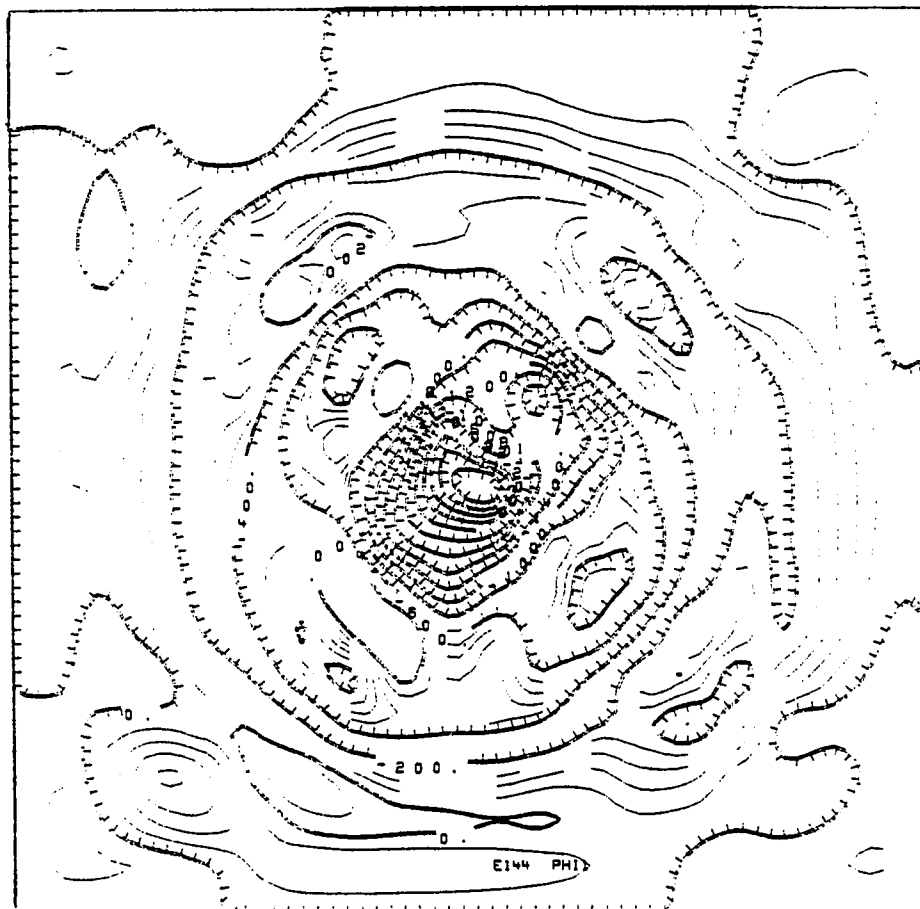


Fig. 97. V3 experiment. Level 1 geopotential (m^2/sec^2) at forecast hour 144.

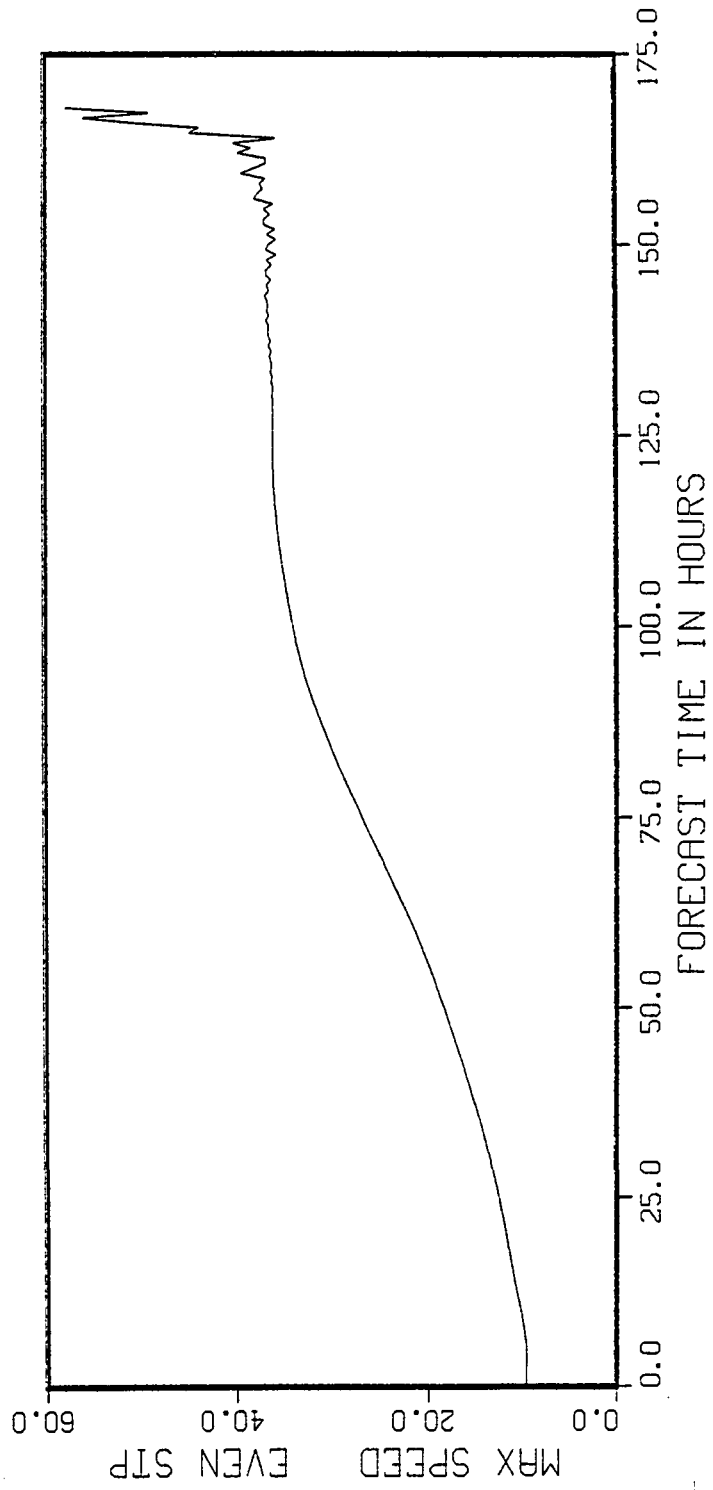


Fig. 98. V3 experiment. Level 1 maximum wind speed versus even time steps.

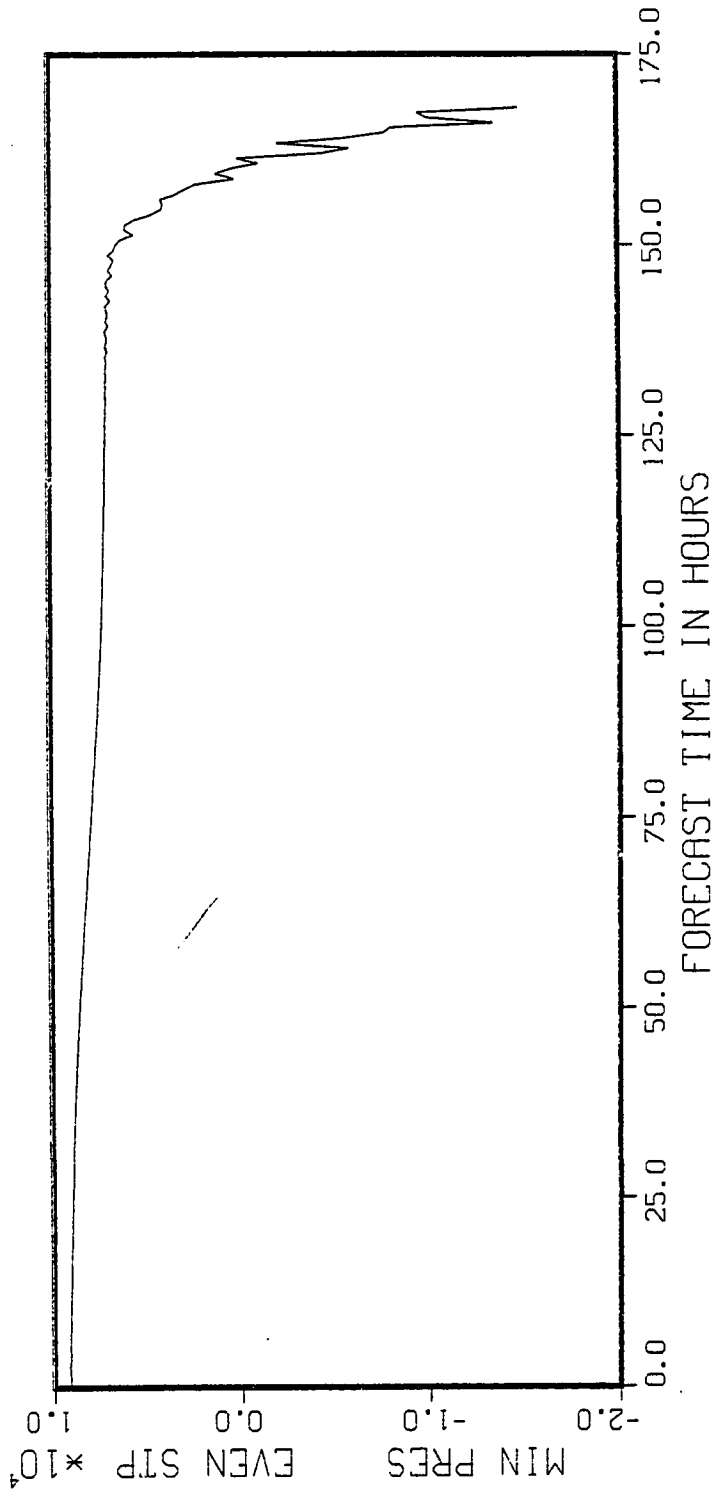


Fig. 99. V3 experiment. Minimum surface pressure deviation versus even time steps.

C.2 Cyclic Boundary Forecast Model

In the previous section we examined several experiments that tested the behavior of the fixed boundary forecast model. The basic physics remained the same in the cyclic version, but it was still necessary to test the behavior of the new version for several reasons: (1) check for program bugs, (2) investigate any eccentricities of the cyclic boundary conditions, and (3) test some of the available model parameters that had not been previously used.

In the first experiment, ECl, the integration of the initial barotropic easterly wave perturbation proceeded for ten days. All diabatic sources and sinks were turned off, and the fields were initialized and integrated using a constant Coriolis parameter and a zero mean u field.

With no sources or sinks and a constant f , we should expect no drastic changes in the barotropic initial state over the integration period. Comparing the initial wind and geopotential fields of Figures 100 and 101 with the forecast fields of Figures 102 and 103, we note that the orientation of the low has changed from SW-NE to SE-NW. Otherwise the fields are very similar and both the geopotential gradients and the wind speed are well preserved. Other charts (not shown) indicate that the areal kinetic energy does begin to increase slightly after the 50 hour point, but the total increase after 10 days is less than .45% for layer 0, layer 1, or layer 2; and the total range of the maximum wind speed

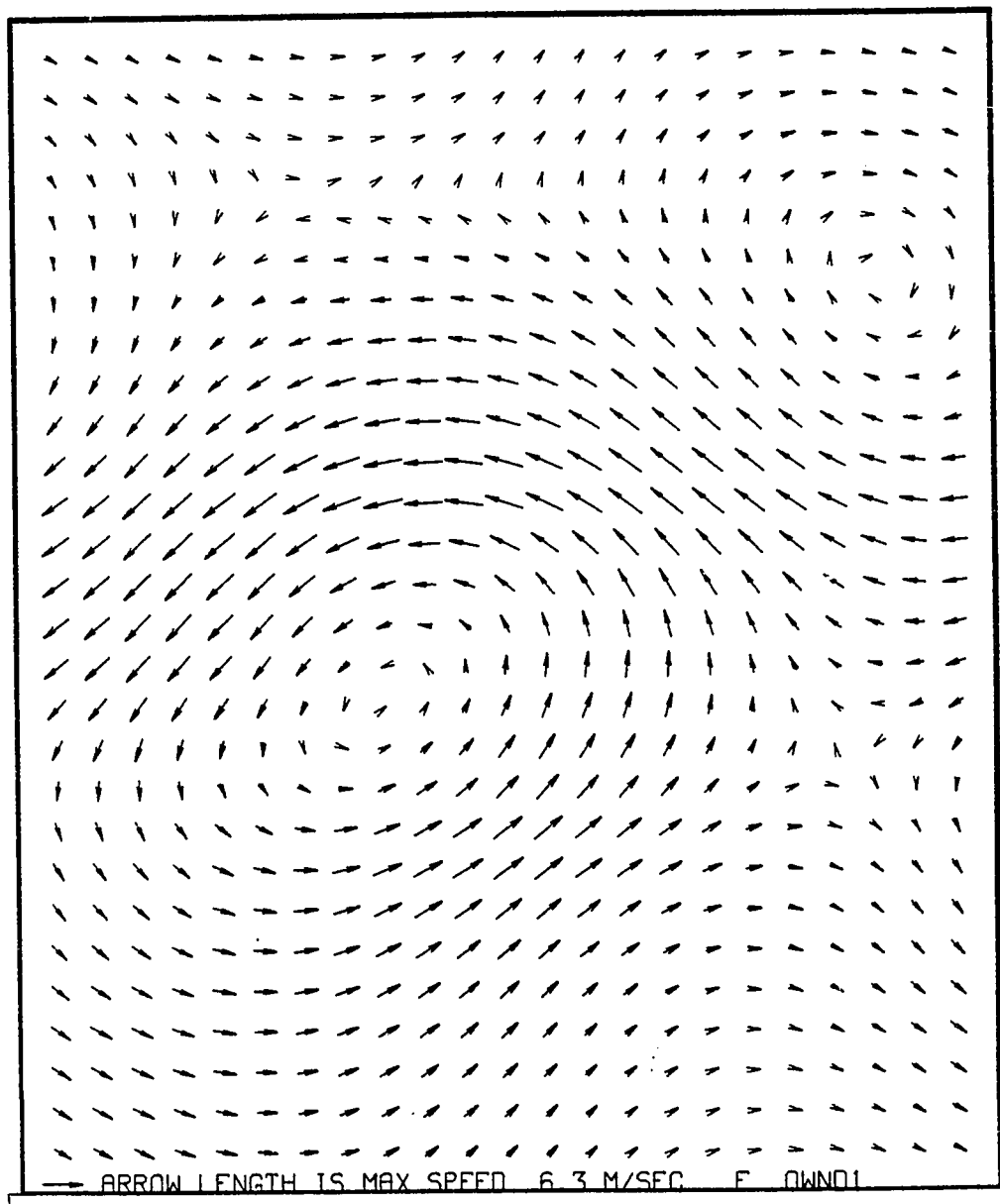


Fig. 100. ECl experiment. Levels 0, 1, and 2 initialized wind field.

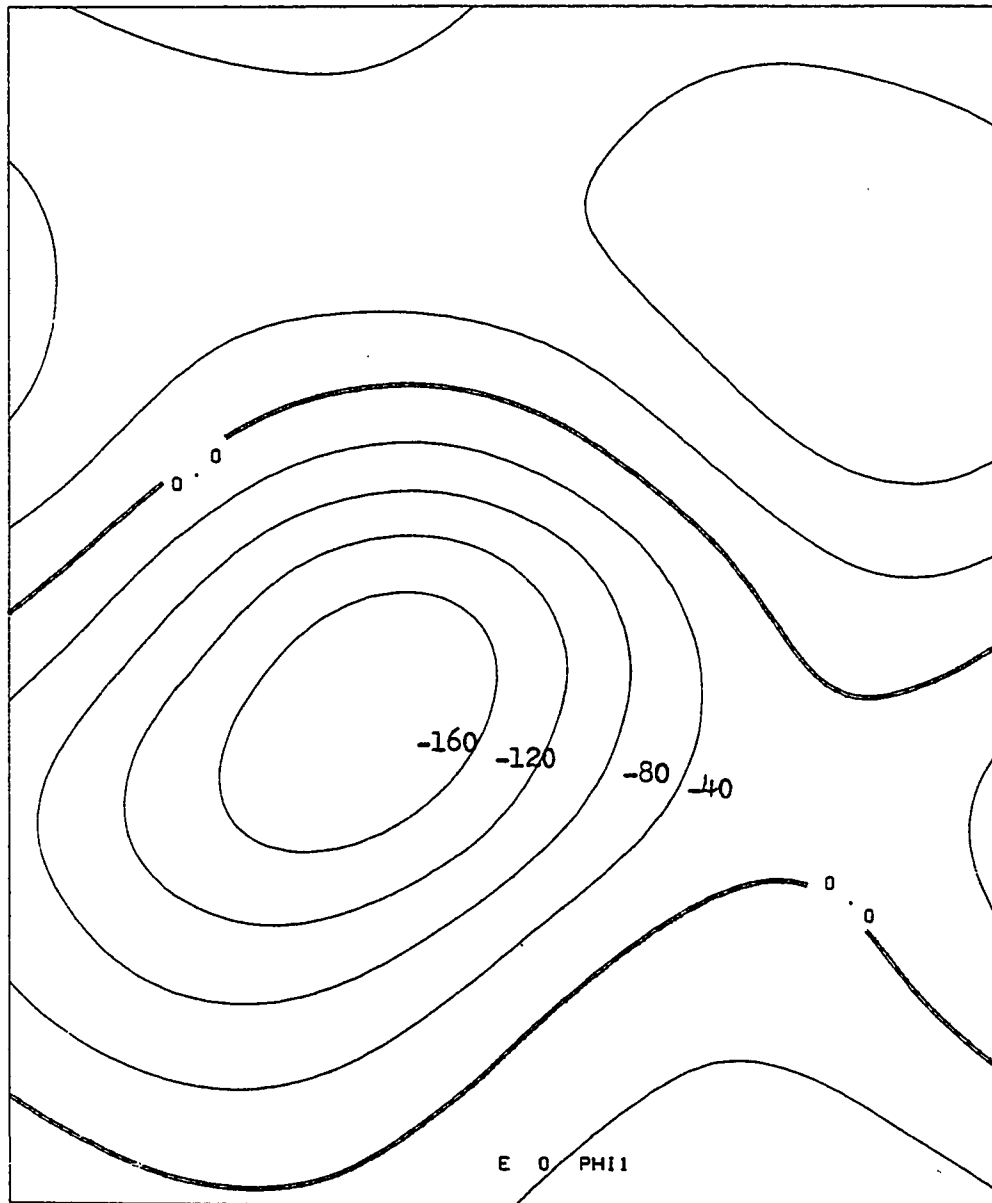


Fig. 101. ECI experiment. Levels 0, 1, and 2 initialized geopotential (m^2/sec^2).

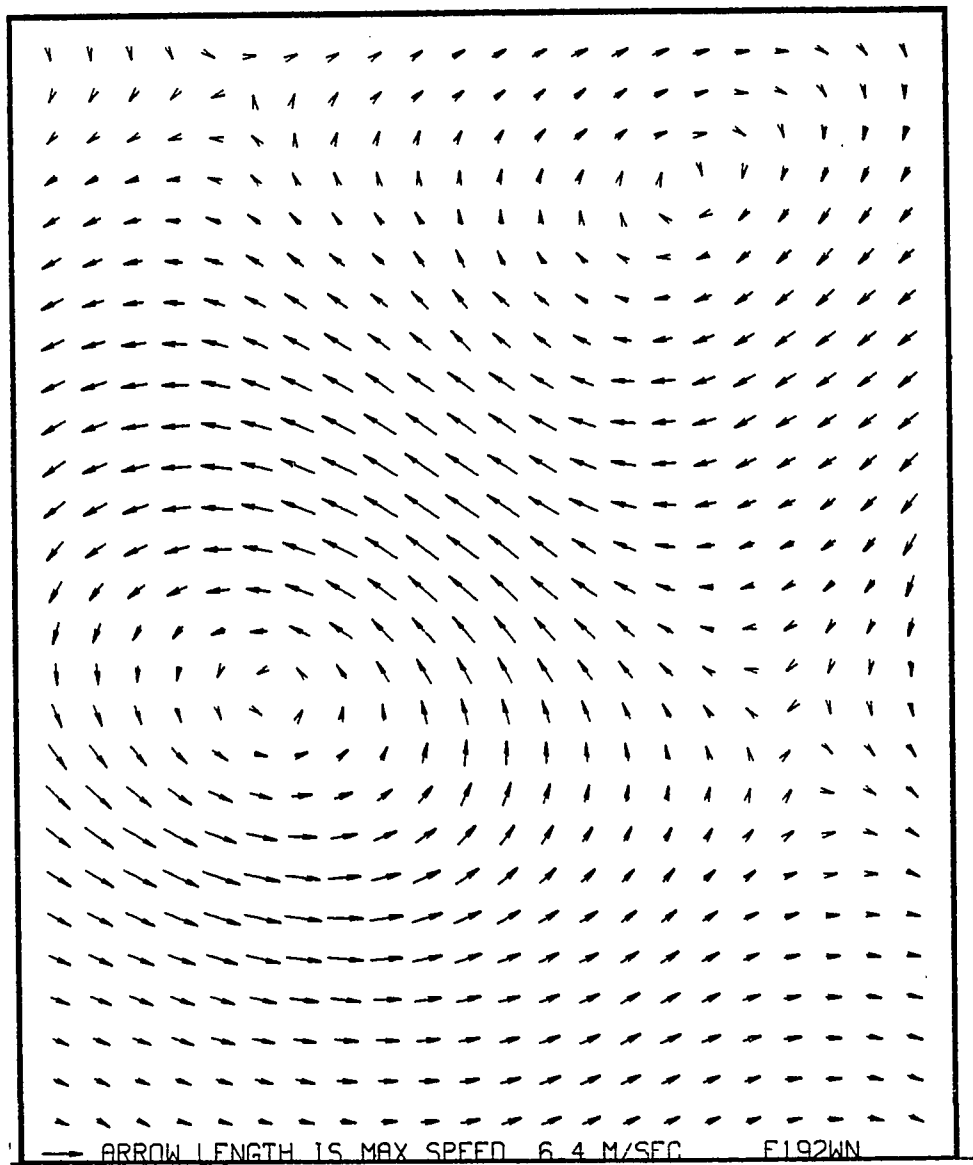


Fig. 102. ECl experiment. Level 1 wind field at forecast hour 192.

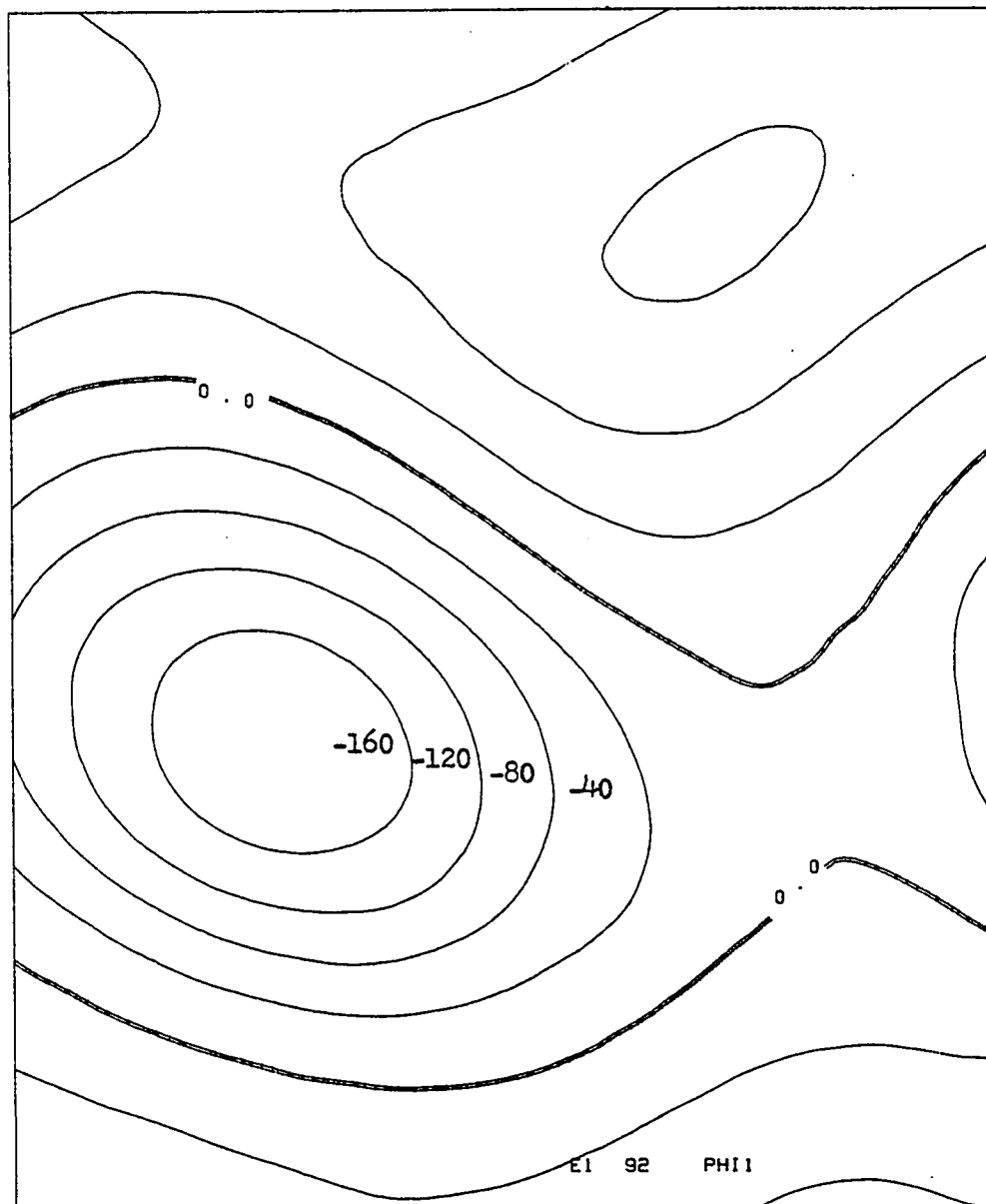


Fig. 103. ECl experiment. Level 1 geopotential at forecast hour 192.

falls between about 6.3 and 5.75 m/sec. The minimum surface pressure has a small amplitude fluctuation of about .15 mb, indicating that the wave is not filling or deepening significantly. These observations all tend to verify the original forecast of little change for these initial conditions.

Experiment EC2 used the same initial state and forecast conditions as EC1 except that the geometry was no longer an f -plane but rather an equatorial β -plane. The presence of the east-west cyclic boundary is physically natural, since we are dealing with an easterly wave that is pseudo-periodic in the east-west direction. However, the use of the north-south cyclic boundary cannot be physically explained, and its use is justified only as a lesser numerical evil than fixed north-south boundaries. This experiment investigated the impact of a large Coriolis gradient at this artificial N-S boundary.

In EC2 there was a sawtooth-like discontinuity in the Coriolis parameter at the north-south cyclic boundary. The Coriolis parameter was specified to increase monotonically northward as in the real world. However, the cyclic boundary condition implies that just north of the north boundary, the Coriolis parameter drops to zero, and just south of the equatorial boundary, the Coriolis parameter rises to a subtropical value.

Unfortunately, this boundary condition appeared to create several deleterious effects. Comparing Figure 104

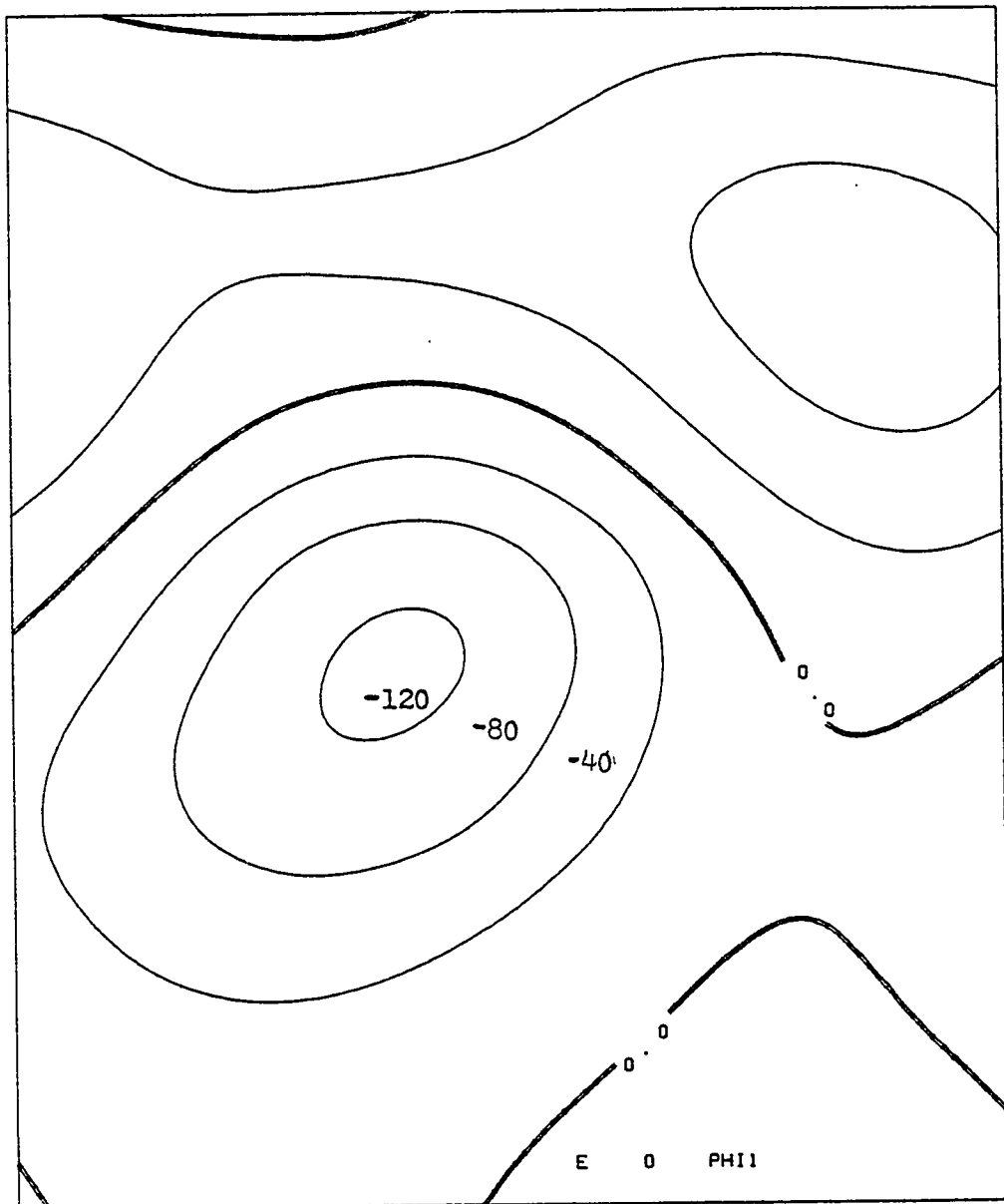


Fig. 104. EC2 experiment. Levels 0, 1, and 2 initialized geopotential.

with Figure 105, we see that the geopotential is much more ragged in the EC2 forecast field than in the EC1 fields; and, in addition, the EC2 geopotential appears to have weakened. The 240 hour wind field in Figure 106 does not at first appear to be as affected as the geopotential field, although the maximum wind speed is down from an initial 6.3 to 5.7 m/sec. EC2, however, has a much wider variation in the wind field than EC1 as we can see by looking at Figures 107 and 108. These figures reveal a significant oscillation in both areal kinetic energy (KE) and maximum speed, although there is no large underlying trend toward either increased KE or maximum wind speed. These results point toward the boundary discontinuity in the Coriolis parameter as a major causative agent because a similar experiment with a constant Coriolis parameter did not exhibit such characteristics.

EC1 and EC2 do demonstrate the role of the β -effect. In EC1 (constant f) the cyclone drifted very slowly westward at a speed of about .5 m/sec. With the introduction of the β -effect in EC2, this westward drift increased to an average of 3.23 m/sec over the 240 hours. This increased propagation speed was undoubtedly due to the β -effect. Additional confirmation of the source of the drift comes from the Rossby wave formula which yields a phase speed of -3.96 m/sec ($L = 2642$ km, $\beta = 2.2389 \times 10^{-1} \text{sec}^{-1} \text{m}^{-1}$), a value that is in reasonable agreement with the actual observed propagation speed.

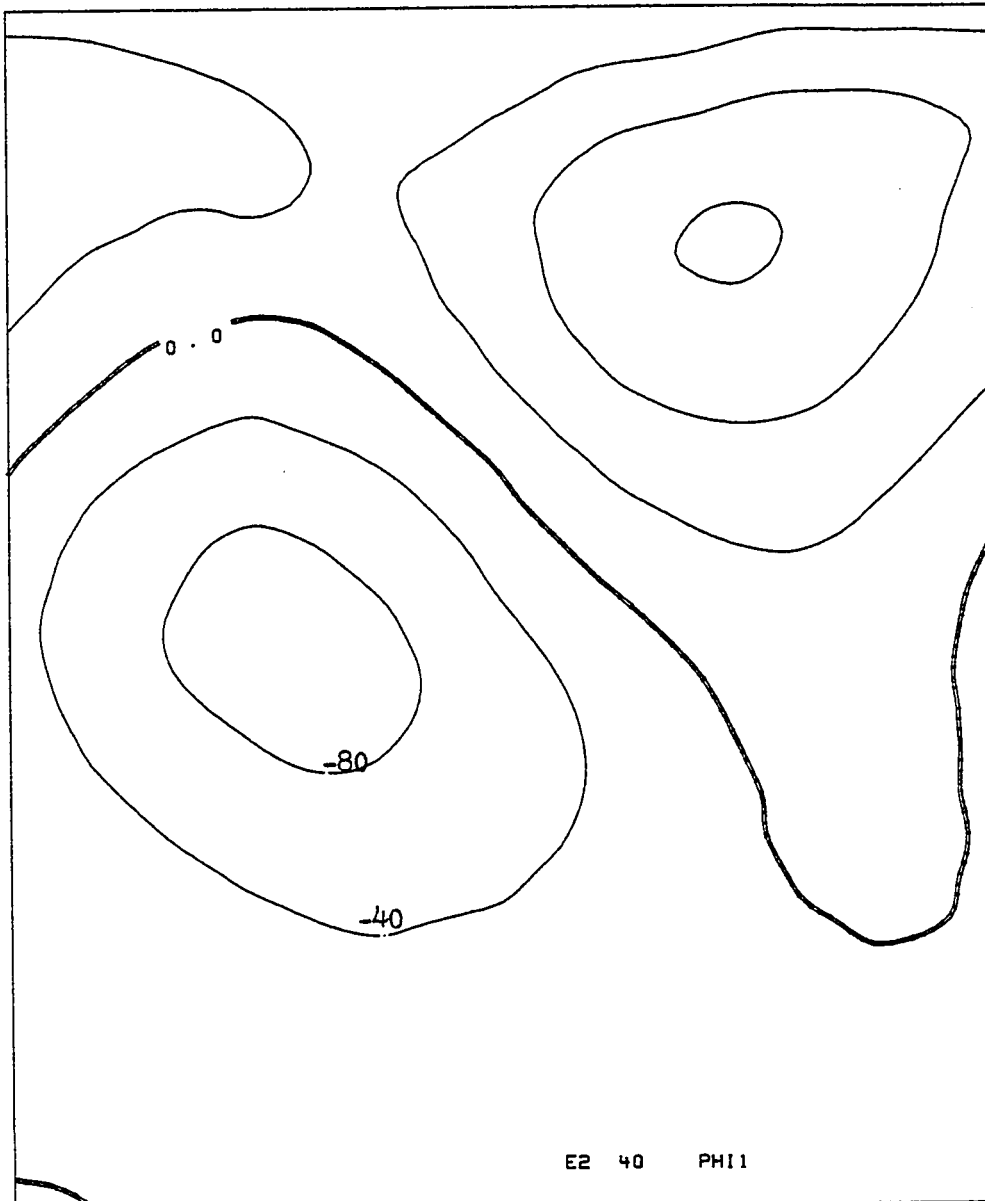


Fig. 105. EC2 experiment. Level 1 geopotential at forecast hour 240.

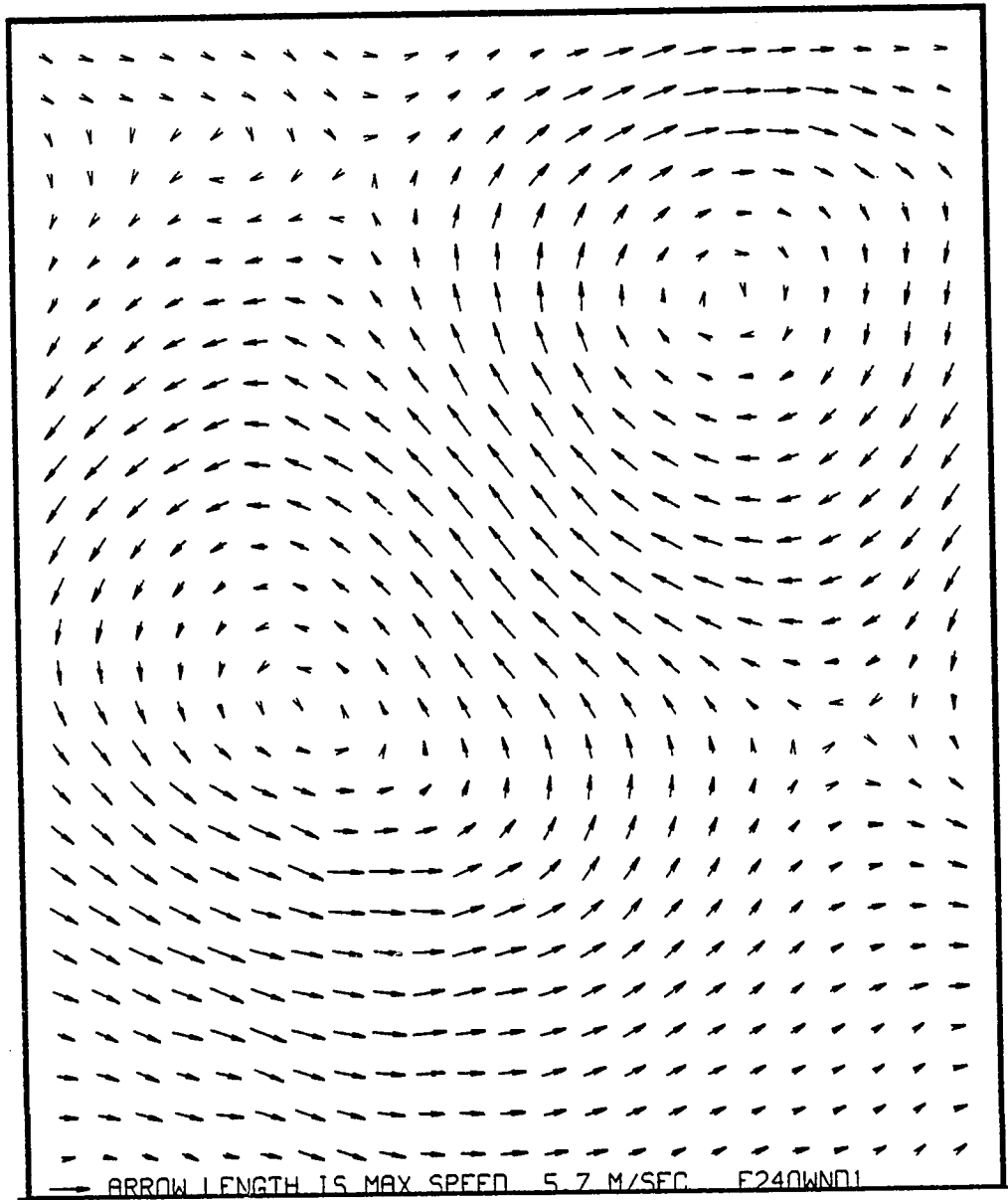


Fig. 106. EC2 experiment. Level 1 wind field at forecast hour 240.

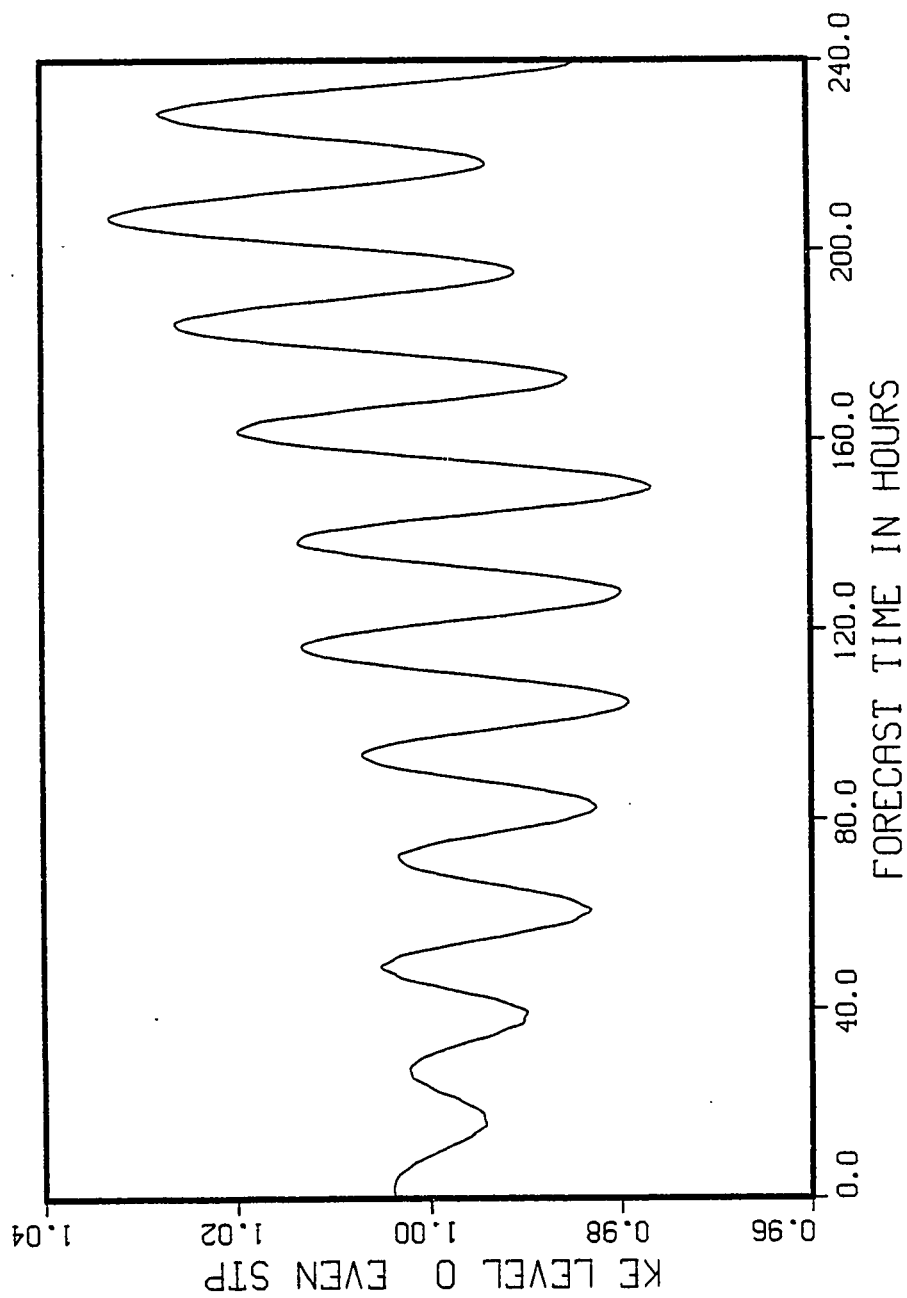


Fig. 107. EC2 experiment. Level 0 normalized kinetic energy versus even time steps.

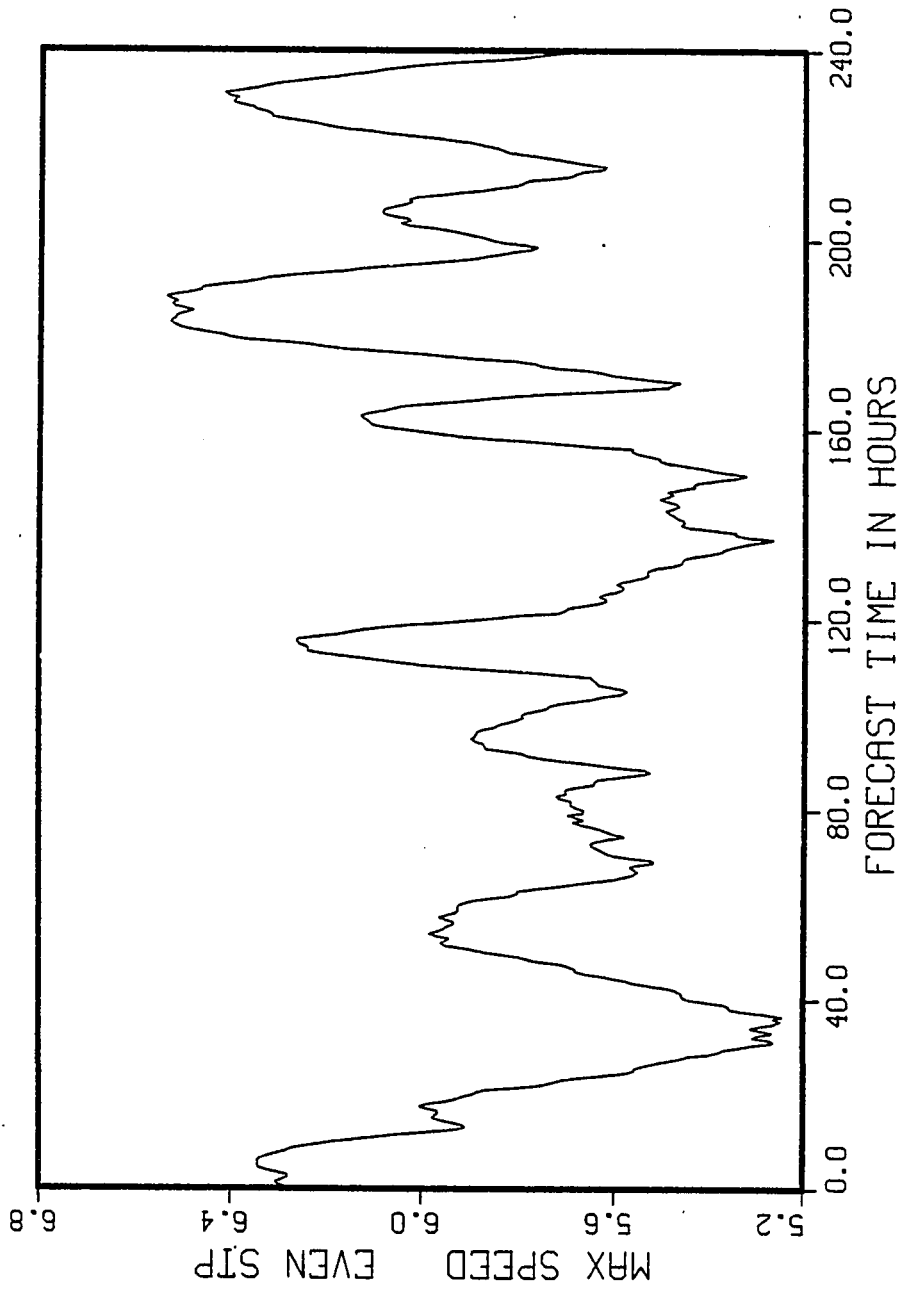


Fig. 108. EC2 experiment. Level 1 maximum wind speed versus even time steps.

The cyclic version forecast model was run in a spin-down test from IECEB/5 initialized fields. As shown in Table 13 and Figures 109 to 112 in this test (EC3), the vortex slowly decayed as expected. The test again adds confidence that another piece of the model works correctly.

Experiment EC9 (Table 6) was a test of the diffusion terms, and all options were turned off except for the diffusion terms λ_1 , λ_2 , and μ . We can see that the diffusion terms are working by comparing the EC9 results with the completely source-and-sink-free EC4 experiment. The EC9 energy plots, Figures 113, 114, and 115, all show decreased energy with time when compared to the analogous EC4 energy plots of Figures 23, 24, and 25. The maximum wind speed in EC9 (Figure 116) also shows a small decrease when compared against EC4 (Figure 22). The decay is weak because the diffusion constants are small. Such small coefficients were retained from Ooyama (1969) in the interest of consistency. They were adequate in magnitude to show that the model diffusion processes worked as expected.

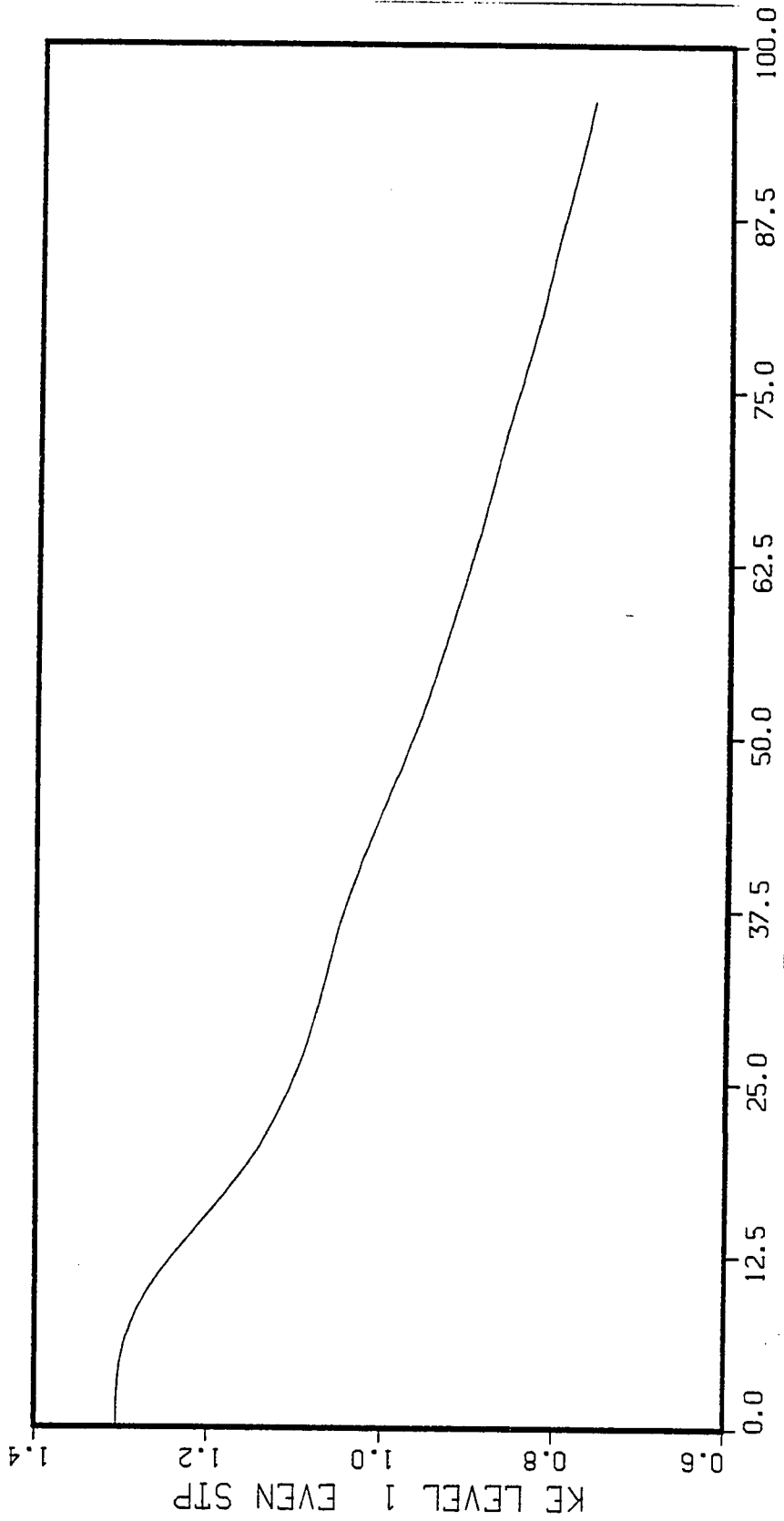


Fig. 109. EC3 experiment. Level 1 kinetic energy versus even time steps.

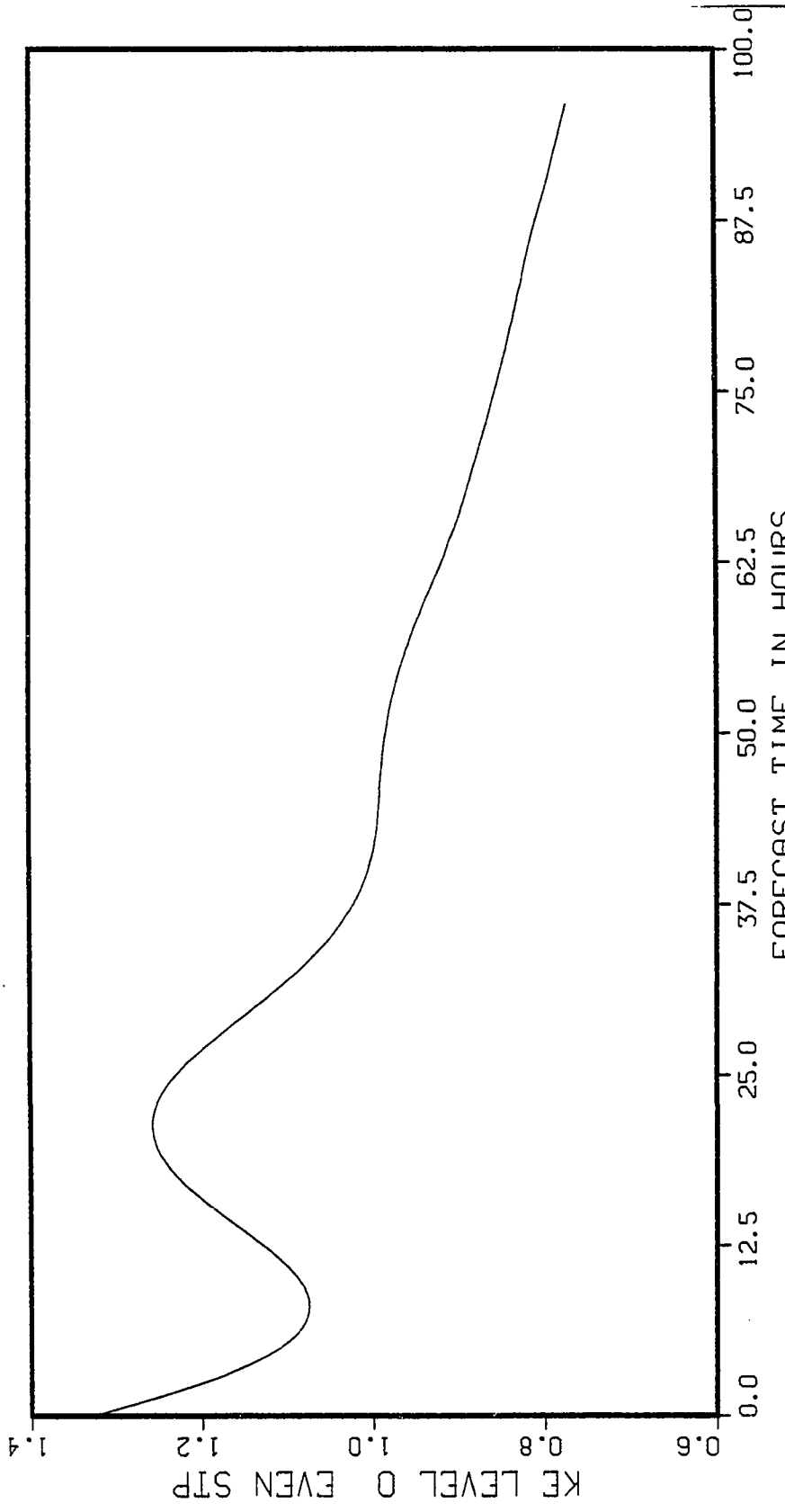


Fig. 110. EC3 experiment. Level 0 kinetic energy versus even time steps.

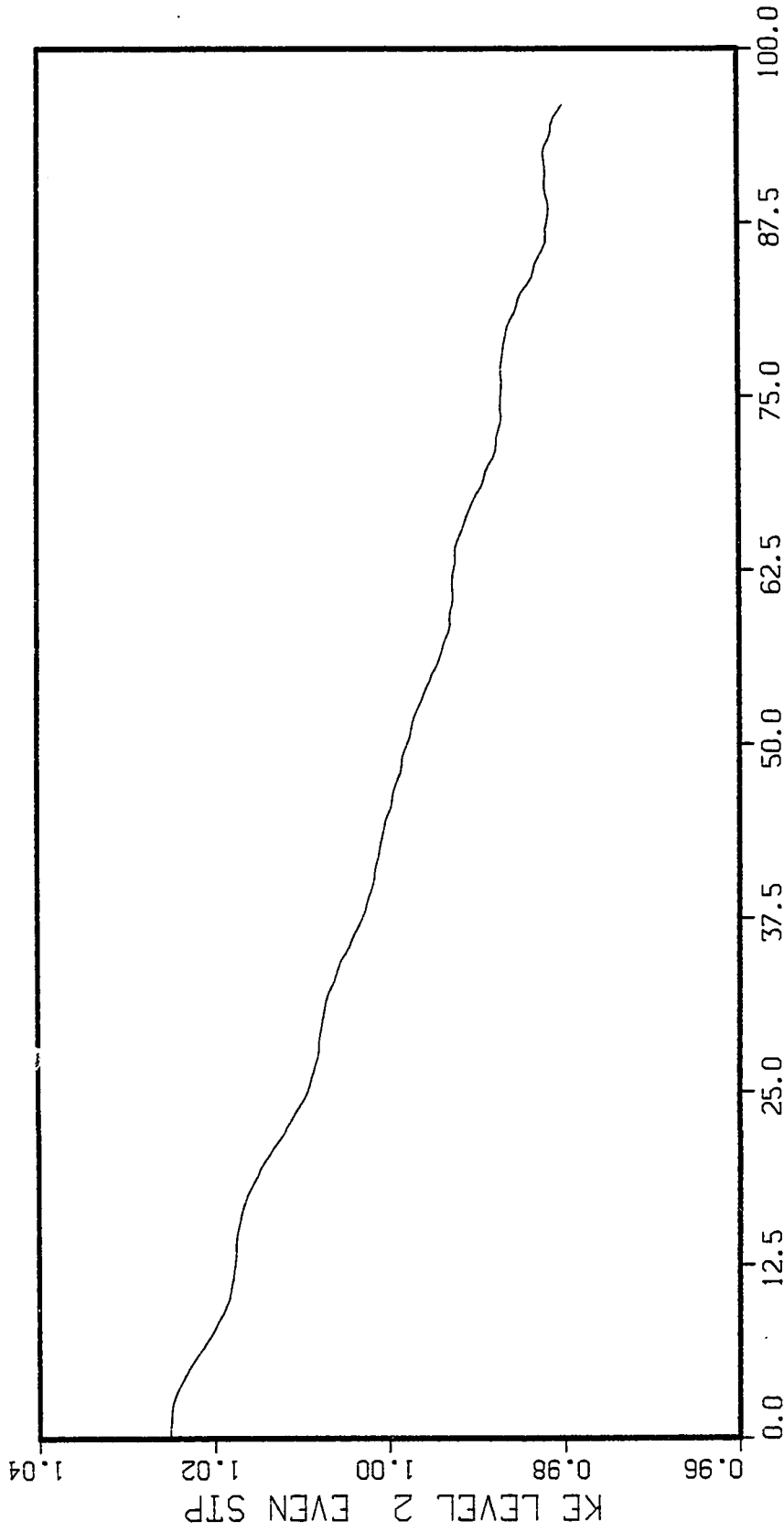


Fig. 1.11. EC3 experiment. Level 2 kinetic energy versus even time steps.

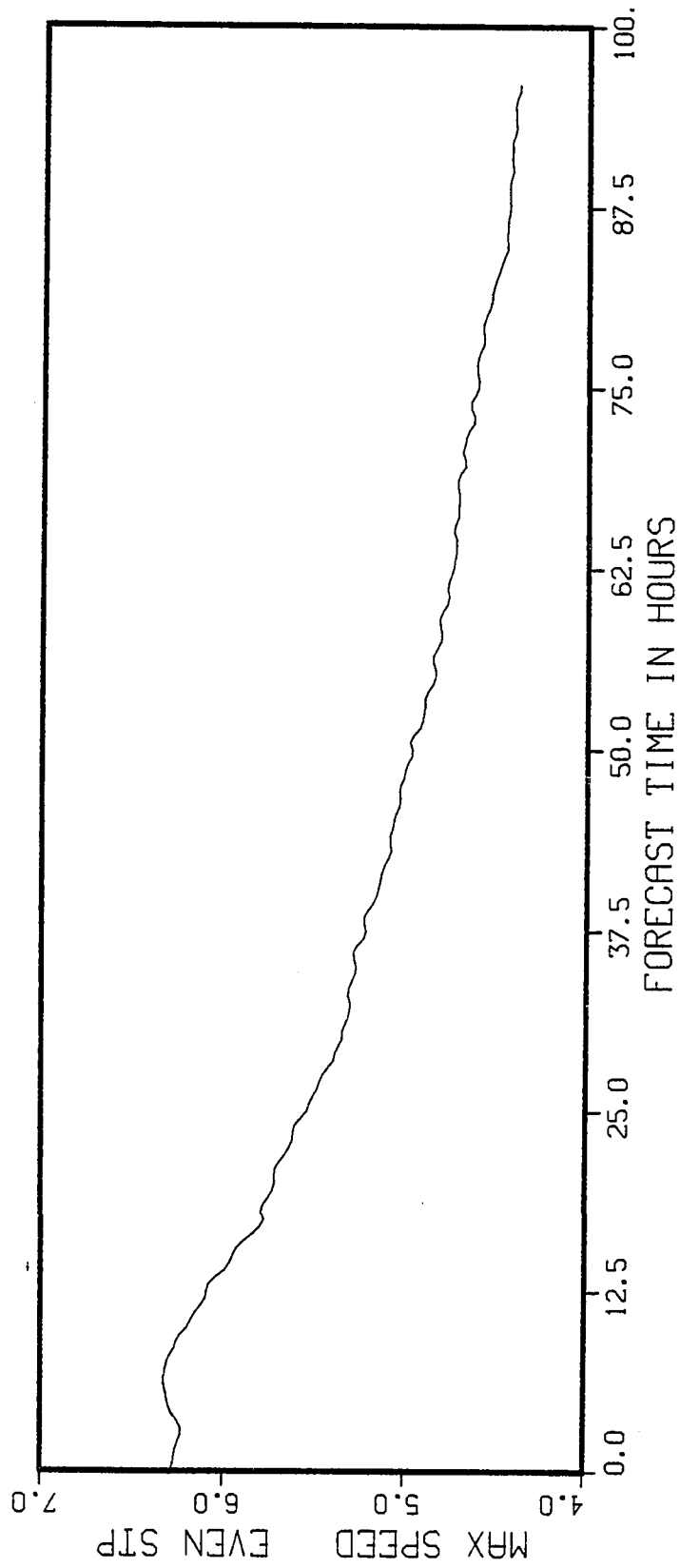


Fig. 112. EC3 experiment. Level 1 maximum wind versus even time steps.

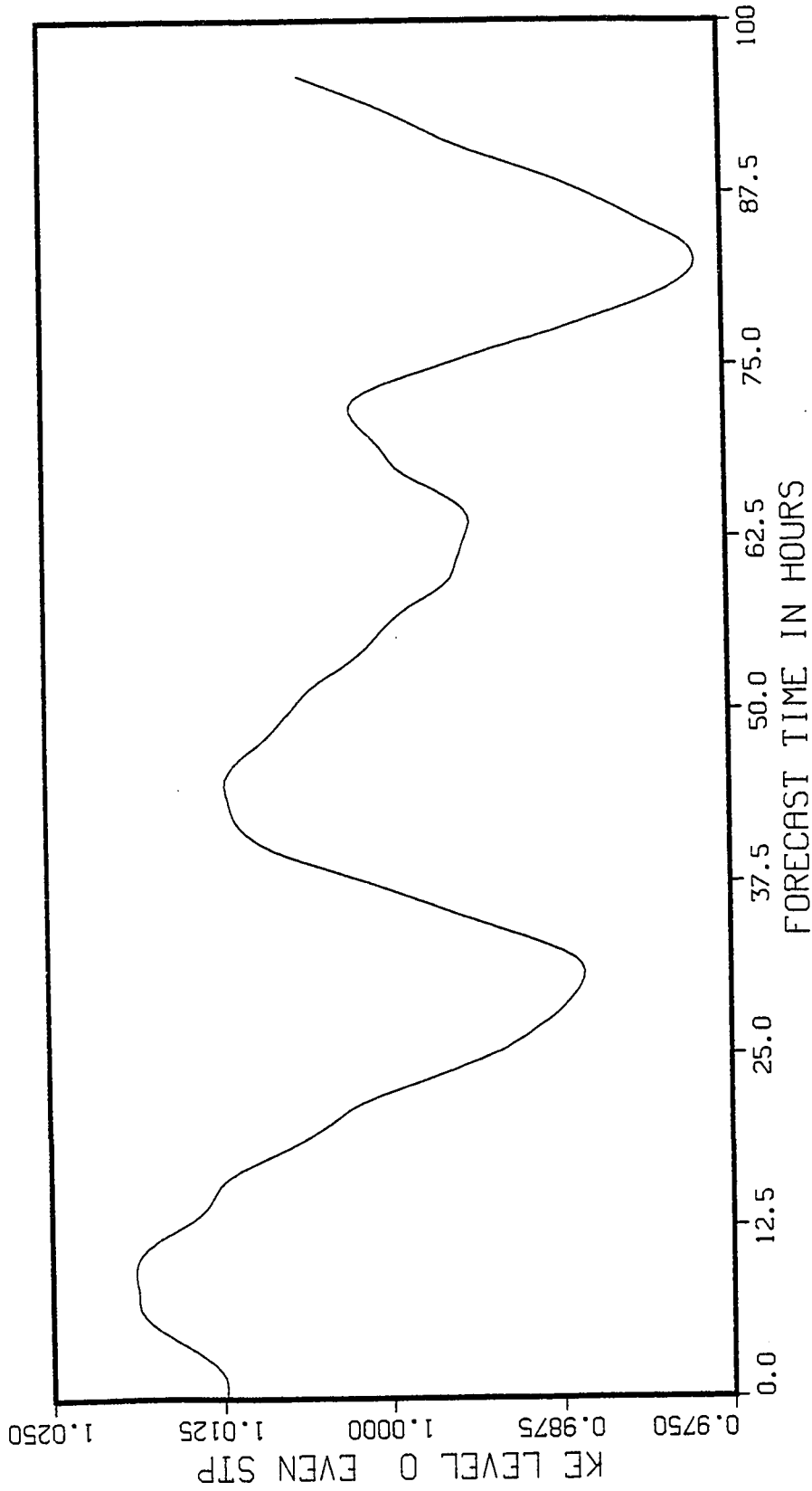


Fig. 113. EC9 experiment. Level 0 total area kinetic energy versus even time steps.

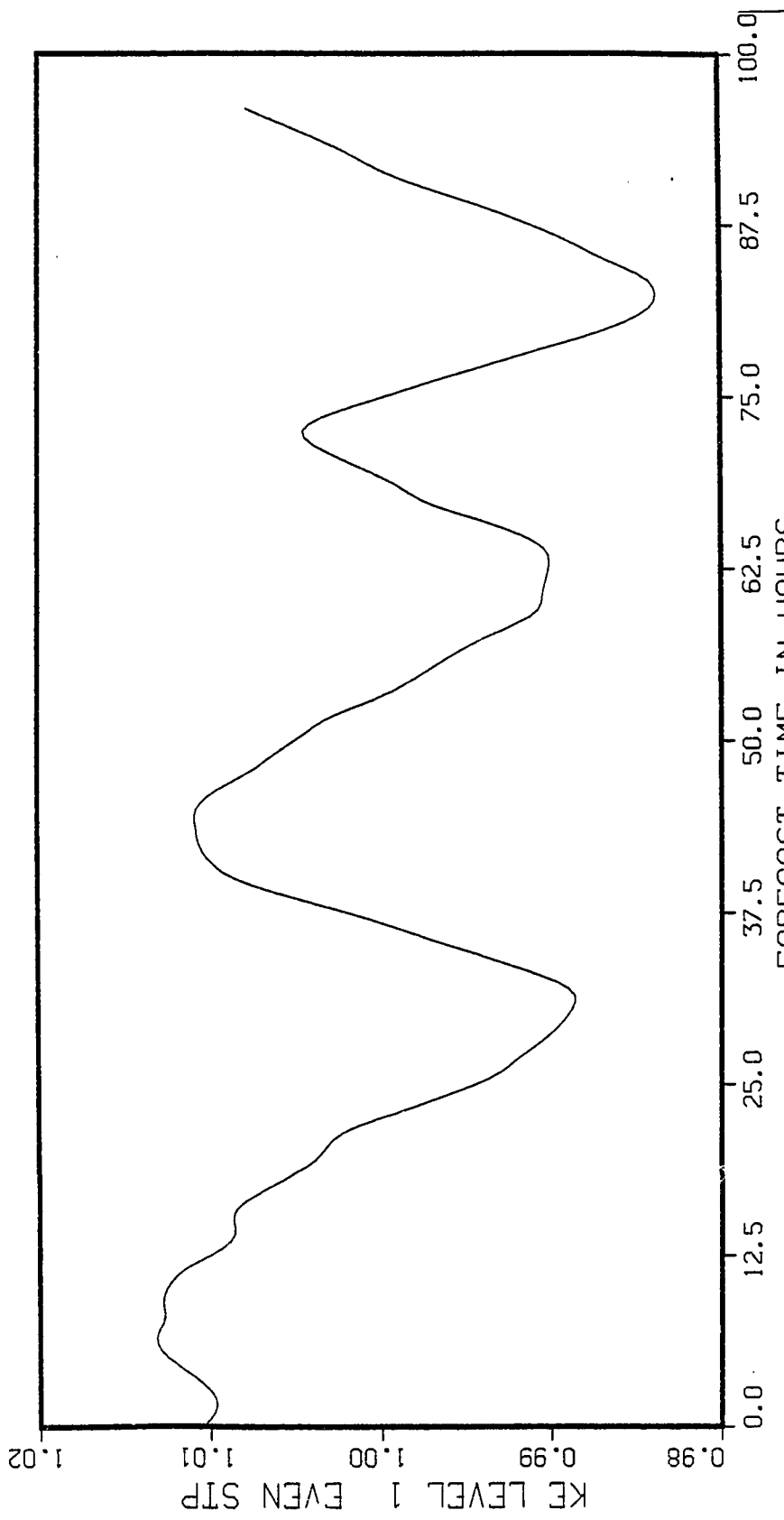


Fig. 114. EC9 experiment. Level 1 total area kinetic energy versus even time steps.

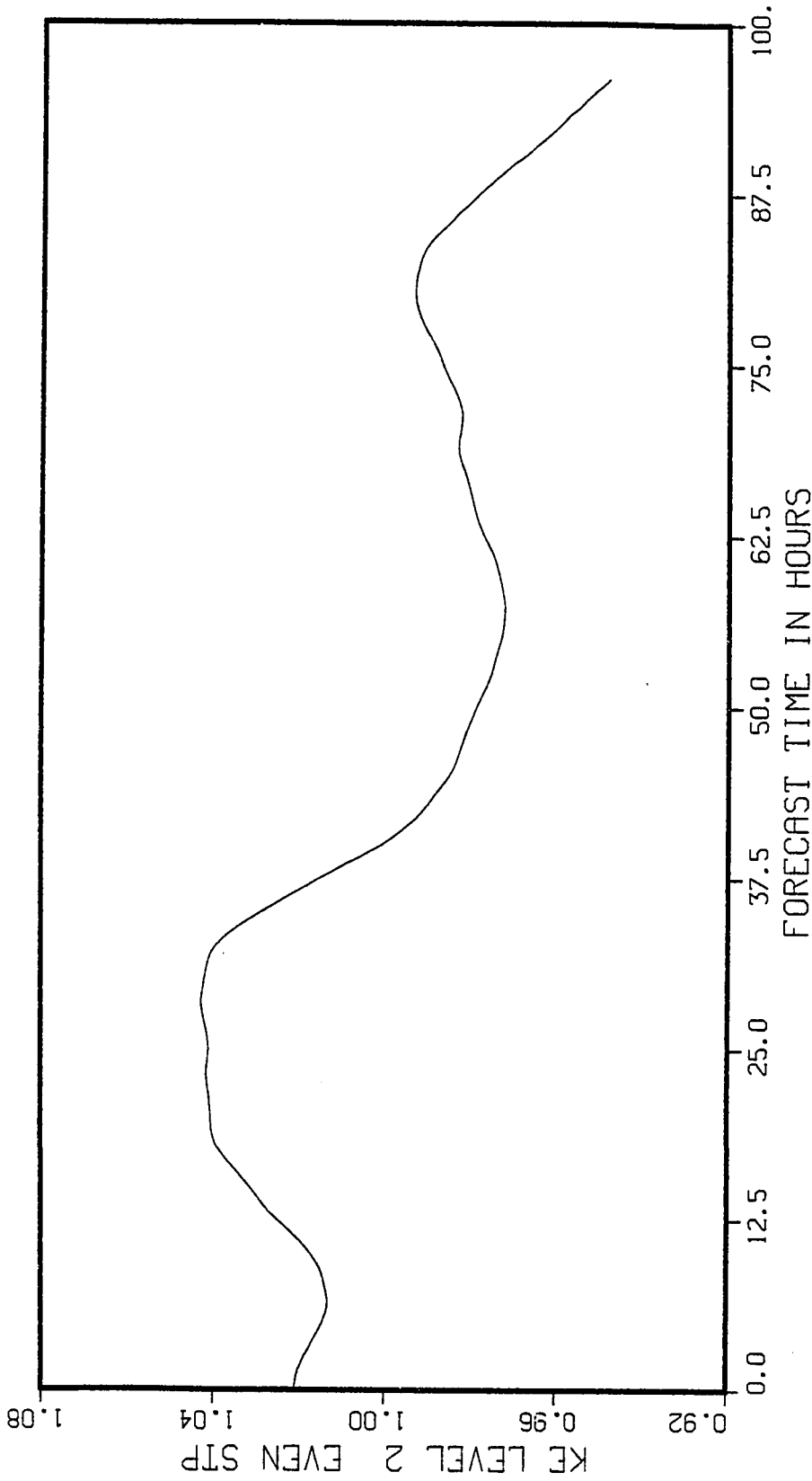


Fig. 115. EC9 experiment. Level 2 total area kinetic energy versus even time steps.

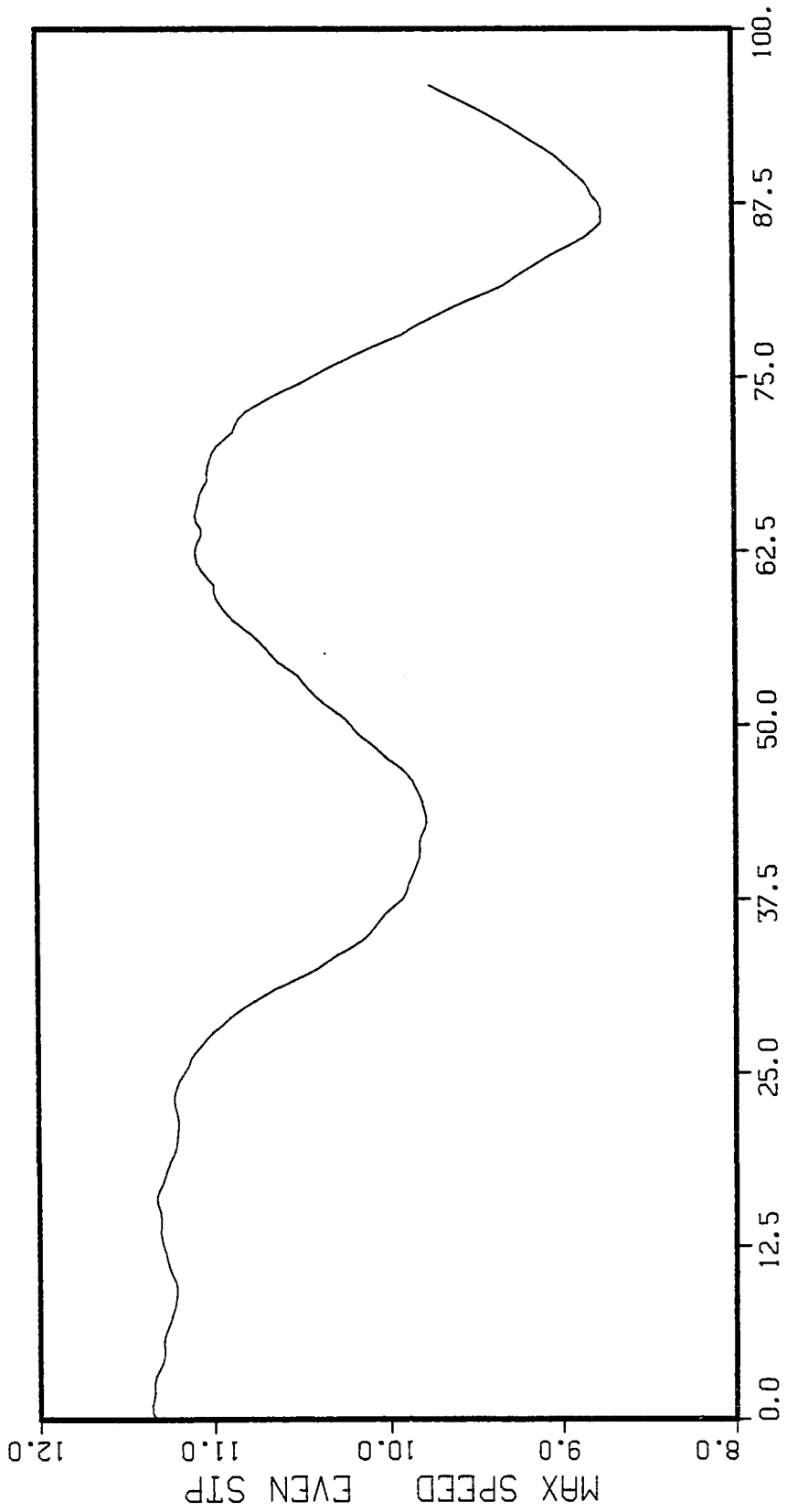


Fig. 116. EC9 experiment. Level 1 maximum speed (m/sec) versus even time steps.

VITA

Author's Name	Vernon LeRoy Bliss
Date of Birth	31 July 1943
Place of Birth	Bakersfield, California
Parents	Lester A. Bliss Dorothy M. Bliss
Secondary Education	East Bakersfield High School Bakersfield, California
Degrees	Bachelor of Science: 1965 California Institute of Technology. Master of Science: 1970 University of Hawaii.